Westerduinweg 3
1755 LE Petten
P.O. Box 15
1755 ZG Petten
The Netherlands

www.tno.nl

T +31 88 866 50 65

TNO report

TNO 2020 R11345

Numerical analysis and validation of unsteady aerodynamics for floating offshore wind turbines

Date May 2020

Author(s) K. Boorsma and M. Caboni

Copy no
No. of copies
Number of pages 136 (incl. appendices)
Number of appendices 2
Sponsor
Project name
Project number

Acknowledgement

The main part of this work has been been executed within the framework of the IRP-Wind UNAFLOW project. The participants of this project, i.e. POLIMI (A. Zasso and S. Mancini), University of Stuttgart (T. Lutz and M. Cormier) and DTU (R. Mikkelsen), are acknowledged for their contributions.

Summary

This report deals with a numerical investigation of the unsteady aerodynamics of a floating horizontal axis offshore wind turbine and its validation against dedicated wind tunnel experiments. In the underlying UNAFLOW project, both three-dimensional and two-dimensional wind tunnel tests were conducted respectively on the rotating rotor and the airfoil used by this rotor's blades. For the rotating tests, the wind turbine base was subjected to imposed sinusoidal surge oscillations to reproduce the motions of floating platforms. The airfoil wind tunnel tests were designed based on the actual conditions under which the rotor blades operated in the experiment, by harmonically pitching the airfoil in the tunnel.

In the numerical investigation, different aerodynamic models are used to analyze the complex unsteady flow. For the airfoil simulations different lifting line models for unsteady airfoil aerodynamics are compared. Shed vorticity modeling in attached flow conditions has been validated both by means of a free vortex wake code as well as an engineering approach based on Theodorsen theory. In stalled flow the potential and shortcomings of several dynamic stall models have been assessed.

For the rotor simulations, free vortex wake and blade element momentum (BEM) approaches were used (plus a few CFD simulations). For the imposed experimental surge motion a dynamic inflow effect was hardly visible, resulting in a good agreement between experiment and simulations. However the necessity of including apparent wind velocities due to platform motion in the momentum equations was verified for the BEM simulations. A numerical study into the variation of surge frequencies and amplitudes and their impact on phase differences between surge velocity and resulting thrust force revealed the influence of airfoil aerodynamics in separated flow rather than the importance of wake aerodynamics and the associated dynamic inflow modeling. However the relevance of airfoil aerodynamics in separated flow is expected to be limited for full scale turbines in surge motion.

Contents

1 Introduction

Floating offshore wind turbines are often believed to represent the next generation of green energy. Offshore systems can overcome some of the typical wind energy limitations. Being installed at sea, they can be built bigger than onshore turbines without visual pollution or noise emission issues. Also the great distance from buildings, mountains etc. typically means higher wind speeds and lower turbulence which turns into higher energy production and lower fatigue loads. Floating offshore turbines use floating platforms of different types fixed with anchor chains to the seabed. The main advantage compared to nowadays industrial standard bottom-fixed turbines is the chance to exploit sea areas with much higher depth. This installation solution makes the system sensitive to sea movements, making big displacements in high wave condition possible. For this reason, the turbine rotor is often working in strong unsteady condition due to the platform translational and rotational motions. In the current state of art modeling there are still open questions regarding the unsteady aerodynamic response of large wind turbine rotors due to platform motion, and how accurate the engineering methods as used by industry can capture this. Although previous work has, by means of comparing to actuator disk simulations, indicated that blade element momentum simulations with the appropriate dynamic inflow engineering model are able to accurately predict dynamic loading for the expected surge motions [1], a validation exercise has never been performed.

In the IRPWind UNAFLOW project [2, 3], the unsteady aerodynamics of a floating offshore wind turbine have been investigated numerically and experimentally in POLIMI's GVPM wind tunnel and the DTU Red wind tunnel. This report presents the TNO contribution to this project, together with several additional investigations that were carried out after the project. Firstly the investigations into unsteady airfoil aerodynamics are reported in Chapter 2, followed by unsteady rotor aerodynamics in Chapter 3. Conclusions are given in Chapter 4.

2 Airfoil

Before analyzing the 3D simulations of the tested turbine model, the performance of the several sub-models covering unsteady airfoil aerodynamics (e.g. dynamic stall) are assessed using the 2D experiments performed on the airfoil used in the UNAFLOW blade, namely the 10% thick SD7030 airfoil. This is a low Reynolds number airfoil, which was also applied to the blades in the rotating wind tunnel test in an attempt to bypass the challenge of matching the large Reynolds numbers of the commercial wind turbines from nowadays. Another rationale behind this comparison is to assess how important the dynamic stall effect is in the rotating experiment, and in this way understand how much it contributes on the overall rotor dynamics analyzed below.

2.1 Experiment

The 2D experiments involved a 0.13 m chord 10% thick SD7030 airfoil in both steady and unsteady conditions, clean and tripped configurations and under different turbulence intensity levels and Reynolds numbers. Unsteady conditions were obtained

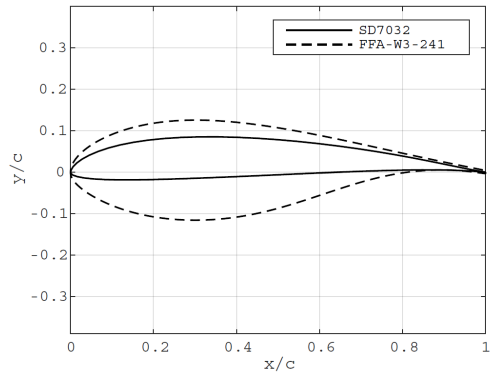

Figure 2.1: Tested airfoil (SD7032, solid line) compared against full scale reference airfoil shape (FFA-W3-240, dashed line) [4]

by harmonically pitching the airfoil (around the quarter chord location) at different reduced frequencies for different geometric angles of attack (varying both mean and amplitude). Herein the reduced frequency is defined as

$$k = \frac{\omega c}{2U} \tag{2.1}$$

with

k	[-]	reduced frequency
ω	[rad/s]	pitch frequency
c	[m]	airfoil chord
U	[m/s]	wind tunnel speed

Velocities of 5.7, 8.6, 11.5 and 17.3 m/s equivalent to chord Reynolds numbers of 50k, 75k, 100k and 150k are measured. The lift coefficient was extracted at the blade middle section using pressure taps (where the tunnel wall effect is small) as a function of the pitch angle. The drag coefficient was inferred from wake rake measurements The different turbulent intensities are created by adding three thin wires, placed in the flow about 4 chords upstream covering full span of the 2D wing. Two wire diameters were tested, d=0.15 mm and 0.30 mm. Measurement of turbulence intensity in the empty wind tunnel was conducted using single component hotwire probe at the position of the quarter chord. The idea of using three wires upstream is to slightly increase TI to bypass natural transition on the airfoil, removing unwanted laminar separation phenomena. A photo of the set-up together with some sample results are shown in Figure 2.2. More information about the test set-up can be found in the UNAFLOW report [2], although a detailed description including test matrix overview is unfortunately not available. The current investigation focusses on the Re=100k dataset for a clean blade with a 0.15 mm upstream wire, resulting in a turbulence intensity of about 0.29%, which seemed sufficient to bypass the laminar boundary layer and remove non-linear parts on the lift curve at the low Reynolds numbers.

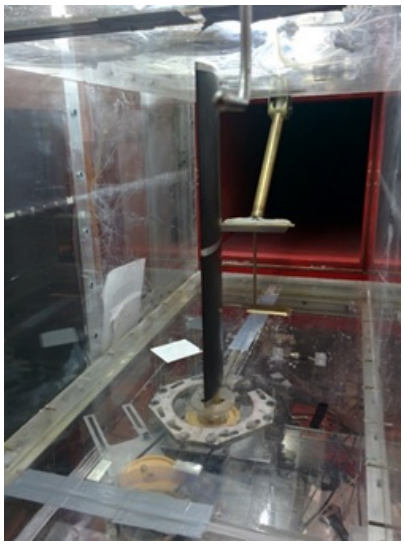

(a) Test set-up in the DTU red tunnel

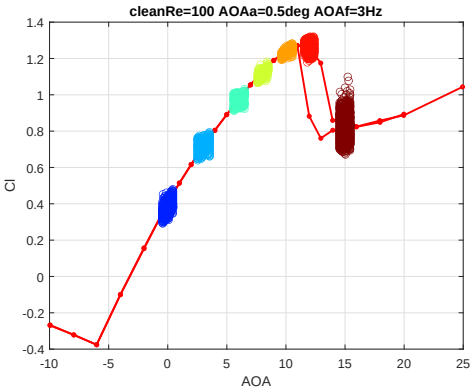

(b) Steady lift polar (red line) and unsteady lift data (colored circles, f=3Hz, $\Delta\alpha$=0.5°, mean angles of attack between 0° and 15°), Re=100k, clean conditions.

Figure 2.2: Airfoil test set-up and sample results

2.2 Simulations

2.2.1 Numerical set-up

Aero Module is a TNO software featuring current state-of-the-art wind turbine aerodynamic models [5]. The two aerodynamic models included in Aero Module are respectively a method based on the classical blade element momentum (BEM) theory similar to the implementation of Phatas [6], and a method based on a free vortex wake model coupled to the lifting line model, named Aerodynamic Wind turbine Simulation Module (AWSM) [7]. Both models need the input of airfoil data, which need to be supplied in terms of lift, drag and moment coefficients as a function of angle of attack. Simulations were performed using both BEM and AWSM, modeling a large aspect ratio blade (AR=769), pitching it in standstill (non-rotating) with the same periodic function as used in the selected experimental cases.

In rapid angle of attack variations two important unsteady airfoil aerodynamic effects are distinguished here that deserve special attention from lifting line modeling point of view. Firstly there is the shed vorticity or Theodorsen effect [8], as the airfoil circulation varies with angle of attack and thus time, leading to induced velocity variations at the airfoil location. A free vortex wake code like AWSM implicitly includes the Theodorsen effect as the wake itself is simulated (see also Figure 2.3). However a BEM simulation needs an explicit addition to model this effect. The Beddoes-Leishman model [9] features a sub-model for this effect. This also indicates that in order not to mimick this effect twice, this part of the Beddoes Leishman model should be switched off in combination with AWSM. Because the variation of airfoil circulation with angle of attack is the steepest for attached flow conditions (due to the linear lift curve slope in this region), this effect is most prominent before stall.

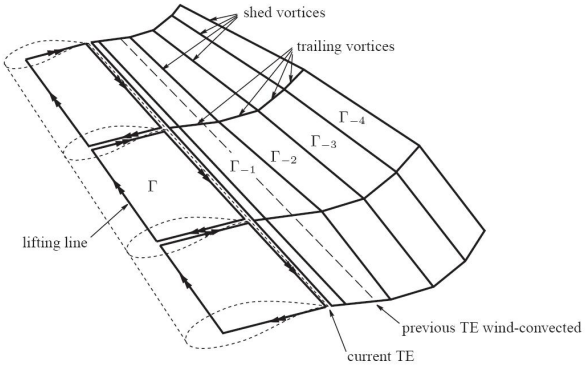

Figure 2.3: AWSM wake geometry [7]

Secondly there is the dynamic stall effect, resulting in deviation from the static airfoil characteristics for stalled conditions depending on the dynamic inflow variations. Several models exist that cover the dynamic stall effect. In Aero Module users can opt for four dynamic stall models, namely a Snel first and second order model [10], an Onera model [11] and a Beddoes-Leishman model [9]. Specific implementation details can be found in [12, 13]. The lift and drag polar input was taken from the corresponding static wind tunnel measurements. The potential flow lift curve was determined by linear regression of the specified polar between -3 ° and 5 ° angle of attack. The available experimental cases were simulated with all of these four models, plus a simulation without dynamic stall model selected. Calculations were performed with a time step of 0.01 s (100 Hz) which should be sufficient to accurately resolve the pitching motion even for the highest frequencies (3 Hz).

2.2.2 Comparison

The resulting comparisons plots showing lift coefficient variation as a function of geometric angle of attack are given in Appendix A (Figure A.1 to A.84). Several observations can be made based on these plots.

Attached flow The plots featuring a low amplitude (0.5 °) and low frequency (0.5 Hz) like Figure A.2 hardly show any deviation from the static lift curve, both experimentally and numerically. For an increasing amplitude and frequency the Theodorsen effect becomes visible in the experiment by means of a counter-clockwise loop (note the arrow in the plots), indicating the expected lag with respect to the static lift curve (e.g. Figure A.24). It can be observed that the AWSM simulations are generally capable of simulating this effect well in agreement with the measurements. As expected, for the BEM simulations this holds when the Beddoes-Leishman model is used. A closer look however at the different BEM simulations shows also the Snel methods to predict a deviation from the static lift curve. For a mean angle of attack of zero degrees the direction of the loop is in agreement with the experiment (e.g. Figure A.12), but for positive mean angles of attack a clockwise instead of counter-clockwise loop is predicted (e.g. Figure A.36). In some cases the same holds for the Onera model. Theoretically the Snel (and Onera) method should not predict dynamic variation before stall, but in case of slight deviations of the polar from the linear potential flow lift curve, the model starts to 'act' resulting in the observed loops. Using the Snel method in combination with AWSM therefore slightly reduces the size of the loop. Although the magnitude of the effect is relatively small, it is recommended to have a further look at the implementation to resolve this. In case of laminar or CFD synthesized polars, which often exhibit a non-perfectly linear lift curve in attached flow conditions, the effect could start to play a larger role.

Separated flow Having a better look at the plots for higher angles of attack ($\mu_{AOA} = 9\,^\circ$ and above) it can be observed that for the lower frequencies (f<1.5Hz) the measured stall loops are often not predicted by the simulations, irrespective of the model used (see e.g. A.43). In some cases (e.g. Figure A.44), two distinct measurement loops are visible of which the upper version of the downstroke seems predicted by the simulations. Perhaps this is related to the occurrence of leading edge stall and the difference in chordwise separation point between upstroke and downstroke even for quasi-steady conditions. Above the mentioned frequencies of 1.5 Hz the agreement seems satisfactory. For $\mu_{AOA} = 10\,^\circ$ and 12 ° the reattachment in the downstroke is predicted too early for all models (e.g. Figure A.58). The measurements sometimes feature a sudden peak in the upstroke between 15 ° and 18 ° angle of attack which is not replicated by any of the models (e.g. Figure A.68). Furthermore it can be observed that the current implementation of the combination between AWSM and the Beddoes Leishman model can result in non-physical trends for high angles of attack (e.g. Figure A.81). In these cases the same holds for the AWSM simulations without a dynamic stall model. As noted above the circulatory lift part of the Beddoes Leishman model is switched off when used together with AWSM, which probably needs further attention in terms of implementation in this indicial method.

Following the above observations it can be advised to use the Beddoes Leishman model with BEM and the Snel model together with AWSM. Looking ahead at the wind tunnel experiment with the rotating turbine we can compare reduced frequencies k and angle of attack ranges of the airfoil experiment to the values at 75% span in surge motion. Where the chord based Reynolds number at this station is around 90k, the reduced frequencies stay below 0.02 and angles of attack below 8 ° stay away

from stall. This indicates that for the rotating experiment the effects of unsteady airfoil aerodynamics are expected to be limited.

3 Rotor

3.1 Experiment

The 2.38 m diameter turbine model tested in UNAFLOW is a 1:75 scaled version of the DTU 10MW RWT [14], considering both structural and aerodynamic characteristics in the scaling process. The model was designed and engineered by POLIMI within the LIFES50+ project [15, 16]. To bypass the Reynolds number matching challenge, a low Re profile (SD7032) was applied in the blades (see also Figure 2.1) changing chord and twist distributions to fulfill compliance with full scale loads. The experimental campaign was carried out in the Boundary Layer Test Section of the Galleria del Vento POLIMI GVPM (13.84m wide x 3.84m high x 35 m long). The wind speed could be considered constant in the rotor zone with a turbulence intensity of around 2%.

The turbine model is mounted on a test rig moved by two hydraulic actuators for surge and pitch movement at the tower base respectively. Loads were measured by means of two six-component balances, mounted at the tower base and underneath the nacelle, of which only the latter was used in the post-processing. To deduce the aerodynamic thrust and torque variation, special effort was put into removing the inertial forces from the measurements, which appeared far from trivial. In this report only the measured thrust will be subject of investigation, which includes this correction. A PIV system was used for measuring the two velocity components of the turbine wake in the vertical plane behind the wind turbine. Rated conditions are studied in the present report, featuring a rotational speed of 241 rpm, an inflow velocity of 4 m/s (tip speed ratio of 7) at a blade pitch angle of zero degrees. Figure 3.1 gives a visualization of the turbine model including the set-up. A more detailed description of the experimental setup, and of the background and purposes of the project is to be found in [2].

A variety of surge motions were executed. Using equation 2.1 based on the rotor diameter and surge frequency rather than chord and airfoil pitch frequency, it is possible to translate real life surge frequencies to the wind tunnel model case assuming rated conditions. Typical real life surge frequencies are in to order of 60-120 s, which translates to 0.25-0.50 Hz at model scale using this assumption. It is noted that the relevant time scale for dynamic inflow roughly scales with the ratio of rotor diameter and wind velocity [1], which is around 15 s for modern turbines and around 0.6 seconds for the UNAFLOW turbine. This would imply that the surge motion is about 5 times slower than typical dynamic wake time scales, which could indicate this effect not to be very relevant. The test matrix however features a variety of frequencies between 0.125 Hz and 2 Hz of which the upper limit does fall in the range of interest. Apart from the frequencies it is noted that the surge amplitude is also of interest, as the product of frequency and amplitude determines the maximum surge velocity and its derivatives. From previous research [17] it is known that gradual changes in wind speed are less likely to result in dynamic wake effects compared to more abrupt wake changes e.g. due to a sudden pitch step.

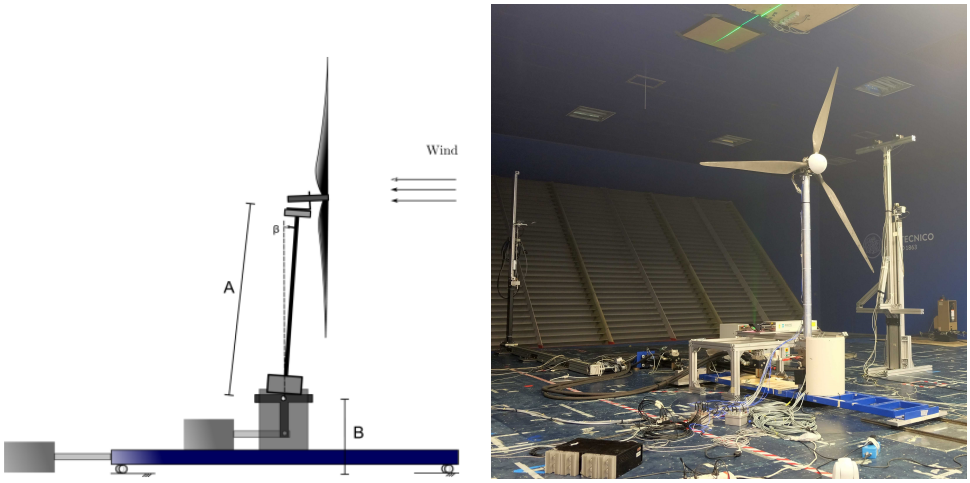

(a) Test set-up in the POLIMI tunnel

(b) Picture of the model in the tunnel

Figure 3.1: Overview of the turbine test

3.2 Simulations

3.2.1 Numerical set-up

The Aero Module, as introduced in section 2.2.1, is used to simulate the aerodynamics of the turbine undergoing surge motions. Both the AWSM and BEM model were used in this respect by specifying, as input, the rotor kinematics, wind excitation and the movement of the tower base. A rigid version of the turbine was simulated and the effect of tower stagnation on the rotor was not considered. Airfoil data was obtained from the corresponding 2D experiment (Chapter 2) for clean conditions at a Reynolds number of $1 \cdot 10^5$. The in-situ correction for rotational effects from Snel [18] was applied to the airfoil data. The Snel first order dynamic stall model [10] was used on top of that. The time step was kept at the approximate equivalent of 10 ° rotor azimuth change for both the BEM and AWSM simulations. For a surge frequency range between 0.125 Hz and 4Hz this means the corresponding resolved phase angle of the surge motion is ranging between 0.3 ° and 10 ° (assuming 360 ° for a full surge cycle).

Wake modeling The ECN dynamic inflow model [17] has been implemented for usage with the BEM solver. This model adds another term to the axial momentum equation to account for the aerodynamic rotor 'inertia' in the case of blade pitch angle variation, rotational speed variation or wind speed variation. The term is proportional to the time derivative of the annulus averaged axial rotor induction and has a dependency on the radial position.

AWSM models the wake geometry by convecting shed and trailing vorticity as depicted in Figure 2.3. Here the trailing vorticity accounts for the effects of spanwise circulation variation, whilst the shed vorticity accounts for the effects of bound vortex variation with time. As a result, effects due to dynamic inflow, shed vorticity (e.g. aeroelastic instabilities), skewed wake, non-uniformities in the rotor plane (e.g. shear, individual blade pitching, non-coherent gusts) and variation in spanwise circulation (e.g. tip and root effect), are modeled intrinsically. For a free wake, the wake convection speed at each wake point is determined by the aggregate of the induced velocities from all vortices using the law of Biot and Savart.

For the free vortex wake simulation, the number of wake points was chosen to make sure that the wake length was developed over at least 3 rotor diameters downstream of the rotor plane. The wake convection was free for approximately 2 rotor diameters downstream. For the remaining diameter in the far wake, the blade average induction at the free to fixed wake transition is applied to all wake points. This choice is based on experience obtained e.g. within the Vortexloads projects [19], which showed that these parameters hardly influence dynamic loading and that the effect on average load levels is less than a percent.

This report includes also some results obtained by means of Unsteady Reynolds-Averaged Navier-Stokes equations (URANS) numerical simulations. These calculations were performed with the block-structured, finite-volume flow solver FLOWer developed by the German Aerospace Center (DLR) [20], with extensions for wind turbines simulations by the University of Stuttgart ([21], [22]). A more detailed description of these calculations can be found in the dedicated UNAFLOW paper [2]

Steady validation Prior to the unsteady investigation, a validation for steady conditions is carried out. Although only rotor global quantities are available as measurements, it is deemed useful to compare these to the numerical result at the chosen

Table 3.1: Comparison of steady model performance at 4 m/s wind and 241 rpm

	Experiment	CFD	AWSM	BEM
Thrust T [N]	35.9	34.2	35.0	34.7
Δ wrt exp [%]	/	-4.8	-2.5	-3.5
Power P [W]	83.8	73.4	75.5	74.0
Δ wrt exp [%]	/	-12.4	-9.9	-11.8

operational condition of 4 m/s wind and 241 rpm (zero degree pitch angle). The results are given in Table 3.1. The results indicate a slight under prediction of the thrust

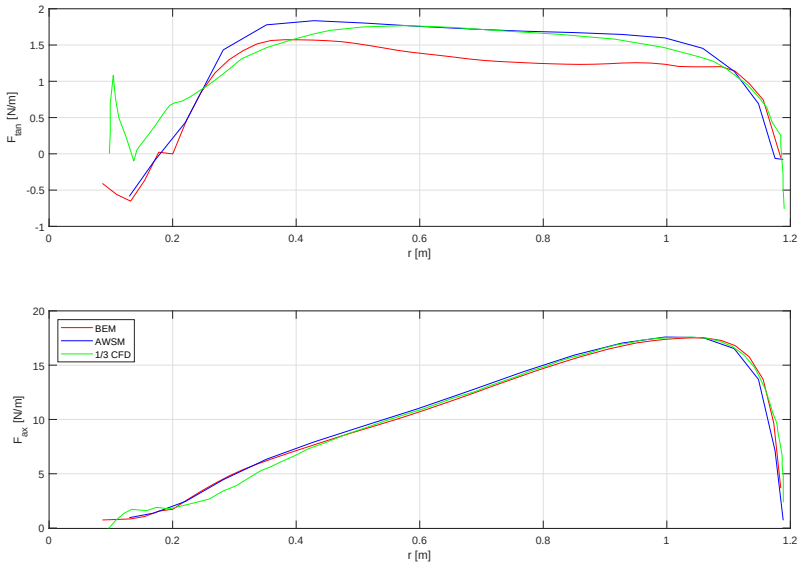

Figure 3.2: Comparison of force distributions in steady conditions, 4 m/s and 241 rpm

by the codes, probably within the error band of the experimental values. The power discrepancy however is in the range of 10%. The underlying simulated force distributions are given in Figure 3.2, which reveal a good agreement between the different codes also on a sectional level. The observed difference led to an investigation into the possible causes arising from the tunnel environment. The ceiling of the tunnel is closest to the rotor and for an upward pointing blade the difference between blade tip and ceiling was around 60 cm. In AWSM it is possible to model a ground (or ceiling) effect by mirroring the whole system of vortices with respect to a defined horizontal plane. A simulation mimicking the tunnel ceiling was performed, taking into account an estimate of the tunnel ceiling boundary layer displacement thickness, which effectively places the ceiling closer to the rotor in an equivalent inviscid situation. Although this simulation reveals the expected variation of thrust and power with azimuth angle (or varying distance of the rotating blades with respect to the ceiling), the differences of the revolution averaged power with respect to the free air simulation are below 0.4%. Hence this cannot explained the observed differences between measurements and simulations.

In a next step the tunnel velocity measurements which were obtained from a pitot tube 5 m (about 2.1 diameters) upstream of the rotor plane were verified. From an AWSM simulation it is possible to obtain rotor induced velocities at a specified point in space. It appears that the rotor induced velocity 5 m upstream of the rotor center is about -0.06 m/s for the investigated 4 m/s case. Re-running the AWSM simulation for 4.06 m/s instead of 4 m/s freestream wind it was confirmed that the velocity 5 m upstream now equals to 4 m/s. The output of this run resulted in an increase in thrust and power of respectively 1.6% and 4.2%. So it appears that this discrepancy can

compensate for about half of the observed difference in power between simulations and measurements. Unfortunately this investigation was performed after performing the unsteady simulations. As the underlying difference due to this effect is small and mainly affecting the absolute levels predicted by the codes rather than the unsteady behavior, this effect is not compensated for in the unsteady simulations of this report.

3.2.2 Apparent wind

A turbine subject to surge or pitching motion experiences apparent wind velocities at the rotor due to the movements of the tower base. Since these wind velocities are adding energy to the system (as they are induced by the waves) it can be argued to incorporate these in the effective wind speed used in the momentum part of the BEM equations. This in addition to the obvious implementation of this relative motion in the element part of the BEM equations, which should anyhow be present. See also the below displayed axial momentum equation 3.1 to clarify this point (for the sake of simplicity a rigid turbine is assumed and the tangential induction and a correction for the finite number of blades have been removed here).

$$2\mathsf{a}(1-\mathsf{a})\rho(\mathsf{U}_w-\mathsf{U}_s)^2 2\pi r dr = \sum_B c 0.5\rho W^2 c_l(\alpha)\cos(\phi) dr \quad , \tag{3.1}$$

where

$\phi = atan2((\mathsf{U}_w - \mathsf{U}_s)(1-\mathsf{a}), \Omega r), \quad \alpha = \phi - \epsilon$ and $W = \sqrt{((\mathsf{U}_w - \mathsf{U}_s)(1-\mathsf{a}))^2 + (\Omega r)^2}$

with

U_w	[m/s]	wind speed
U_s	[m/s]	surge motion velocity (apparent wind)
a	[-]	axial induction factor (related to U_w - U_s)
r	[m]	radius of element considered
c	[m]	local blade chord at radius r
ρ	[kg/m^3]	air density
W	[m/s]	effective velocity at element
c_l	[-]	lift coefficient
α	[$^\circ$]	angle of attack
ϕ	[$^\circ$]	inflow angle wrt rotor plane
Ω	[rad/s]	rotor speed
ϵ	[$^\circ$]	twist plus pitch angle.

In this equation the blade element part is on the right hand side, in which the surge velocity U_s is included in the velocity triangle by subtracting it from the wind speed U_w (thereby affecting effective velocity term W, the inflow angle ϕ and angle of attack α). The momentum part is on the left hand side of equation 3.1, and the discussed proposition is to replace the U_w term with (U_w-U_s) as shown in the equation.

The validity of this statement is verified by comparing a simulation in surge with a moving rotor (which is used in the present work) to a simulation with a 'fixed' rotor featuring a (sinusoidal) wind variation in agreement with the surge motion. See also Figure 3.3 for the resulting plot of axial force versus surge motion. The free vortex wake simulations give nearly identical results for both approaches, indicating that the main effect the wind turbine rotor experiences is the apparent wind effect rather than the rotor moving into and out of its own wake (at least for this case). For the BEM simulations it is observed that the shape of the force response is off if apparent wind velocities are not taken into account in the momentum equations.

Implementation wise this can result in a challenge since an aero-elastic code is not always aware whether motion of the blade is due to flexible nature of the turbine (e.g.

tower fore-aft bending) or due to platform motion induced by waves. Recommended practice here is to register translational and rotational movement at the tower base and extrapolate the resulting apparent wind velocities to the designated rotor plane locations. For a pitching movement this would imply a linear variation with height of apparent wind velocity over the rotor disk, and hence a non-uniform inflow condition which anyhow is a challenge for BEM simulations.

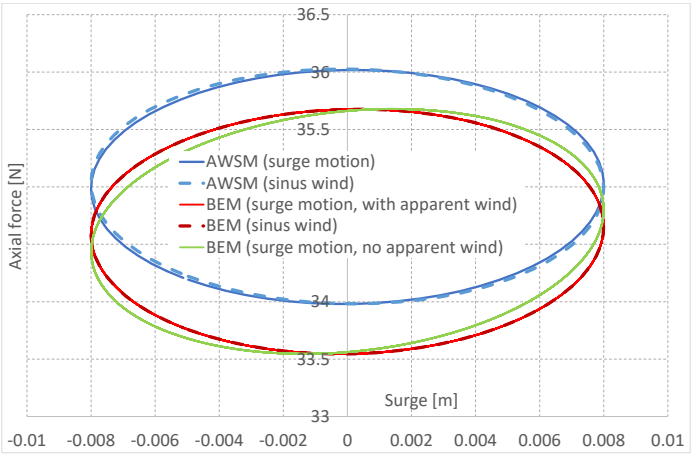

Figure 3.3: Comparison of BEM and AWSM predicted axial force as function of surge, f=2 Hz, Δx=0.008 m, U=4 m/s and 241 rpm. Applying surge excitation by means of prescribing actual surge motion or harmonic wind variation are compared, as well as the effect of incorporating the apparent wind variations in BEM for the first approach.

3.2.3 Unsteady comparison

Firstly a comparison between experiment and simulations in surge is presented. Then two sets of surge simulations are calculated to investigate differences between BEM and AWSM simulations. One set is characterized by a constant frequency and varying amplitude while the other features a constant amplitude and varying frequency. Investigated are the response of the angle of attack at 75% blade span (numerical cases only), the rotor thrust and the rotor torque. The results of these simulations are presented by means of Bode plots, showing the magnitude and phase of the above mentioned output rotor signals with respect to the surge motion. This allows to evaluate unsteady effects in the rotor aerodynamic response. The data reported in the Bode plots are evaluated by processing the simulated signals in the time domain, by calculating the peak to peak distances. For the constant frequency and constant amplitude investigations, the rotor signals as a function of time and hysteresis plots are given in Appendix B.

Comparison to experiments A comparison between experimental and numerical response of the rotor is performed for three selected surge cases. An overview of these cases is given in Table 3.2, also including the steady case. Figures 3.4, 3.5, 3.6 and 3.7 show the comparison between experimental rotor thrust and that predicted by AWSM and BEM in the time domain. Figures 3.4 shows that for the steady case the AWSM simulation has not yet fully converged, illustrated by the small decrease of torque with time. CFD results are also included for the surge case at amplitude of

0.008 m and frequency of 2 Hz (Figure 3.5). The measurement results are characterized by highly noisy signals. To be treatable, these signals have been post-processed by selecting the component of the signal at the same frequency of the surge motion using Fourier transforms. This processing was performed using the “fft” function in Matlab taking 6 surge cycles in one bock (hence without window function and overlap). The same processing applied to the CFD data, as it contains high frequency contributions due the modeling of tower shadow. As indicated above, AWSM and BEM results are instead processed unfiltered using peak to peak distances. The measurement data being reported in the resulting Bode plot in Figure 3.8 have been obtained directly from the Fourier transforms of the experimental data.

Both the magnitude and phase show a generally good agreement between measurements and simulations. To verify the importance of the dynamic inflow model, also BEM simulations without this engineering model are included in Figure 3.8. These results indicate that dynamic inflow effects are not significantly affecting the dynamic response of the rotor for these cases. Because the magnitude of the thrust amplitude is divided by the surge amplitude, an almost linear trend of this variable follows as a function of frequency. In general, the rotor thrust follows the surge velocity (product of frequency and amplitude) which has a -90 $^\circ$ phase with respect to the surge motion. It is noted that the 10 $^\circ$ azimuth timestep of the simulations influences the accuracy of the phase angle estimate as it limits the phase angle resolution to 5 $^\circ$ for example for the 2 Hz surge motion. Therefore phase differences below this number should be treated with care.

Table 3.2: Surge experimental cases.

case No.	amplitude [m]	frequency [Hz]
1	0	0
2	0.035	1
3	0.008	2
4	0.125	0.125

Figure 3.4: Comparison between experimental rotor thrust and that predicted by AWSM and BEM with fixed turbine rotor.

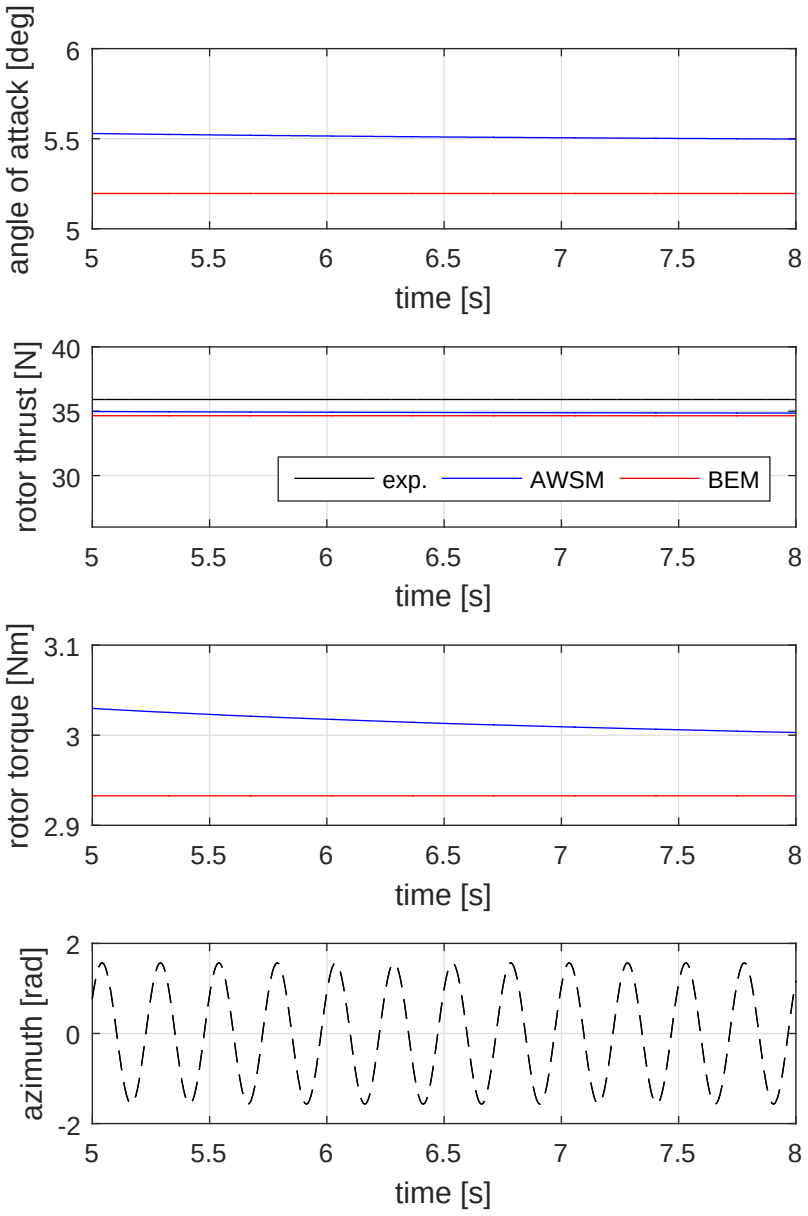

Figure 3.5: Comparison between experimental rotor thrust and that predicted by CFD, AWSM and BEM for a surge motion characterized by frequency of 2 Hz and amplitude 0.008 m.

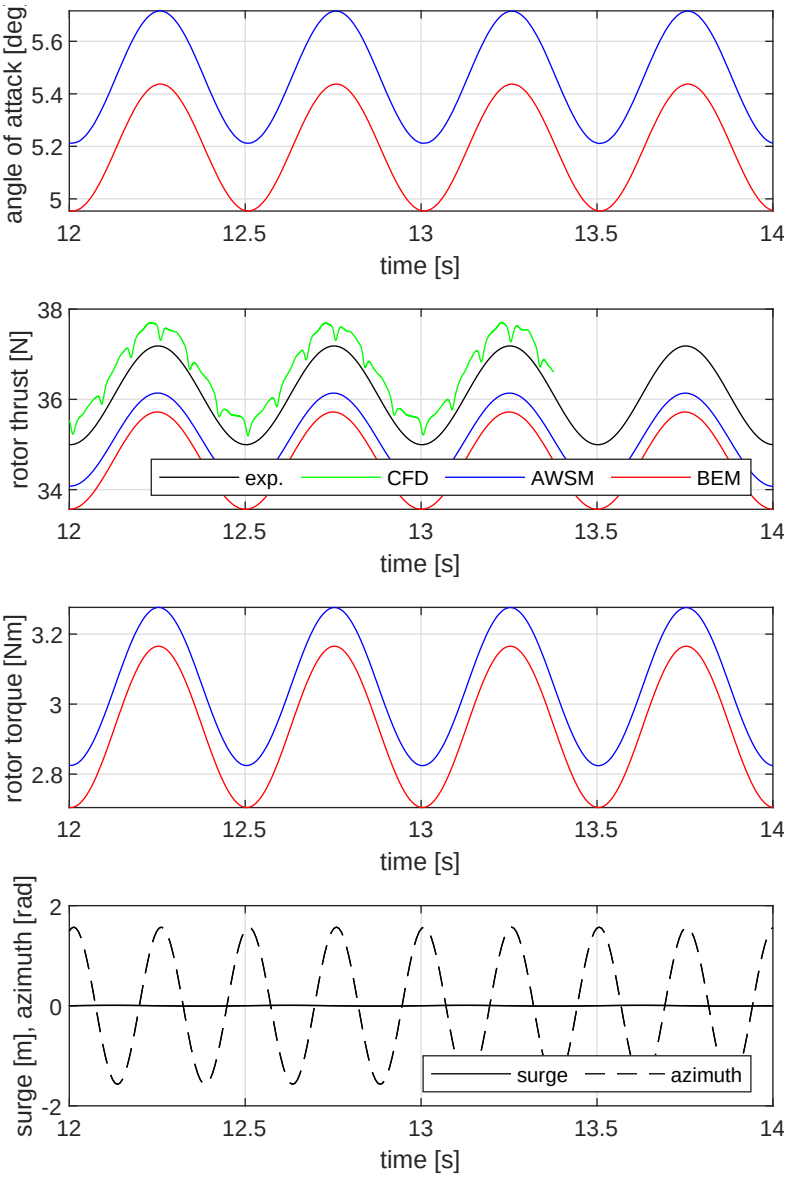

Figure 3.6: Comparison between experimental rotor thrust and that predicted by AWSM and BEM for a surge motion characterized by frequency of 1 Hz and amplitude 0.035 m.

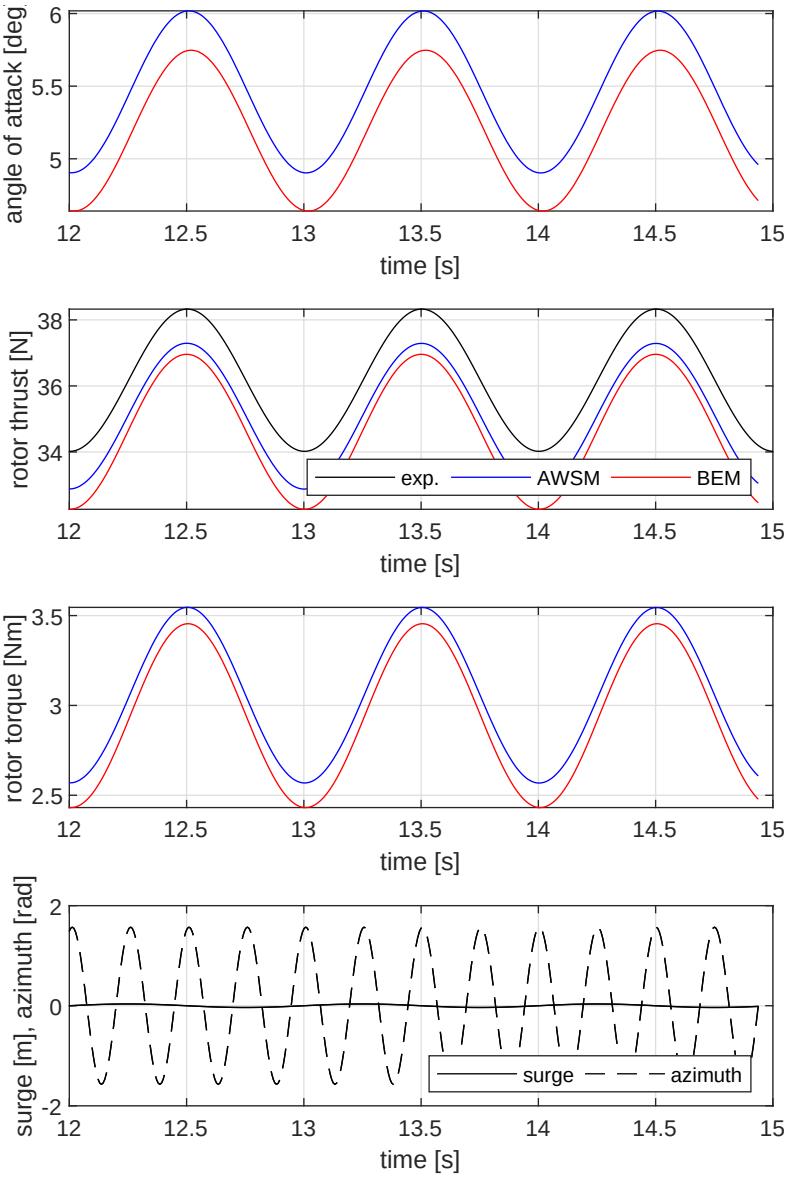

Figure 3.7: Comparison between experimental rotor thrust and that predicted by AWSM and BEM for a surge motion characterized by frequency of 0.125 Hz and amplitude 0.125 m.

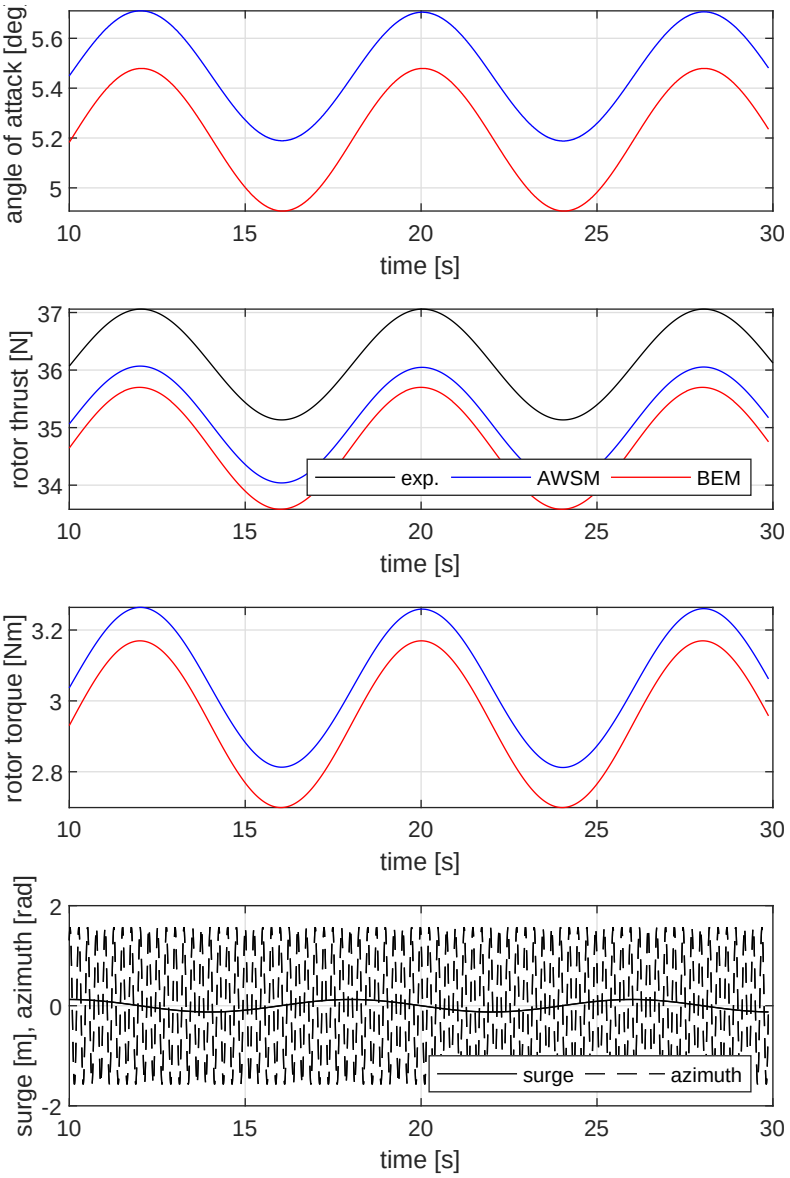

Figure 3.8: Response of the rotor thrust to surge motion for the experimental cases from Table 3.2. The response is evaluated by showing the ratio of the rotor thrust amplitude to the surge amplitude (left subplot) and the phase between these two signals (right subplot).

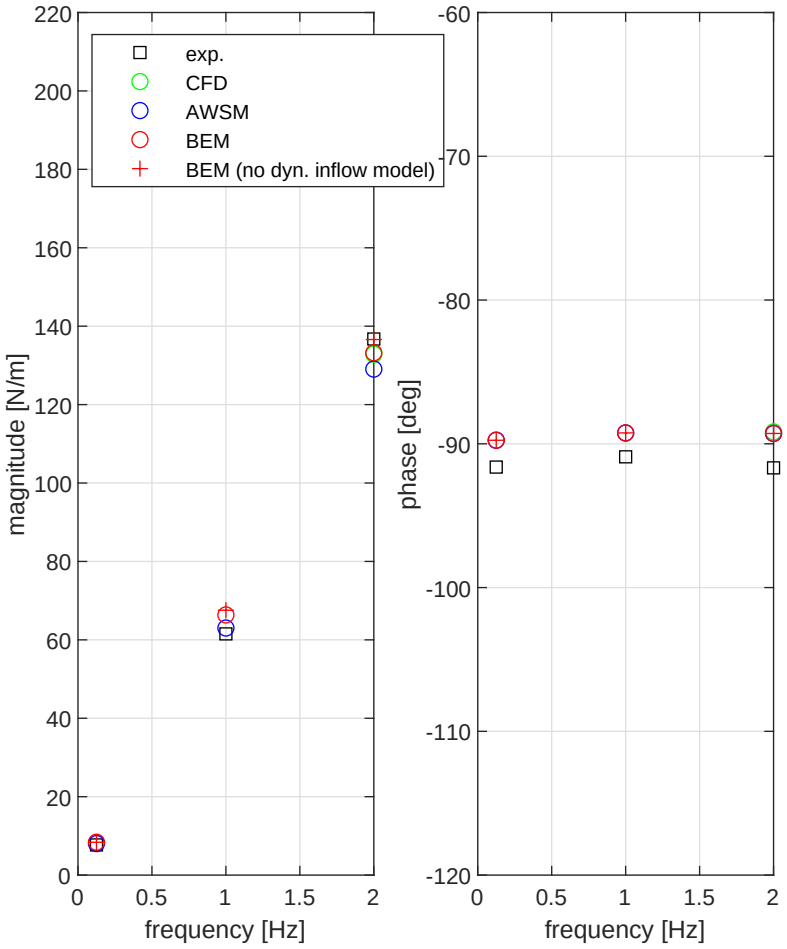

Amplitude variation for constant frequency An overview of the surge cases with constant frequency and varying amplitude are given in Table 3.3. Figures 3.9, 3.10 and 3.11 shows the Bode plots of the aforementioned rotor signals. Looking at the Bode plots for the rotor thrust in Figure 3.10 it is noted that a 5 to 10% magnitude differences exist between BEM and AWSM. The verify whether this difference could be caused by the modeling of shed vorticity, BEM simulations were executed with the Beddoes Leishman model and without a model for unsteady airfoil aerodynamics. The results showed a negligible influence (<1%) on the predicted magnitude and phase, pointing in the direction of differences in rotor rather than airfoil aerodynamic modeling as origin for the observed differences.

The predicted trend with surge amplitude is very similar between BEM and AWSM. Since the magnitude is visualized by dividing the thrust amplitude by the applied surge amplitude this yields a relatively constant value for these constant frequency cases. A slight decrease of the magnitude is observed for increasing surge amplitude. The highest amplitude case of 0.52 m shows a more sudden decrease, caused by the angle of attack approaching 10 $^\circ$ for which the lift curve slope of the airfoil starts to fall off more steeply. See also the hysteresis plot of the thrust in Figure B.10 which starts to deviate from the symmetric ellipsoid shape because of this. The phase of the thrust signal remains clustered around -90 $^\circ$ phase. Roughly the same observations can be made for the torque signal in Figure 3.11.

Table 3.3: Surge cases with constant frequency.

case No.	amplitude [m]	frequency [Hz]
1	0.0325	0.5
2	0.065	0.5
3	0.13	0.5
4	0.26	0.5
5	0.52	0.5

Figure 3.9: Response of the angle of attack at 75% of the blade span to surge motion. Simulations are here performed with a fixed surge frequency of 0.5 Hz and amplitude ranging from 0.0325 m to 0.52 m (x-axes). The response is evaluated by showing the ratio of the angle of attack amplitude to the surge amplitude (left subplot) and the phase between these two signals (right subplot).

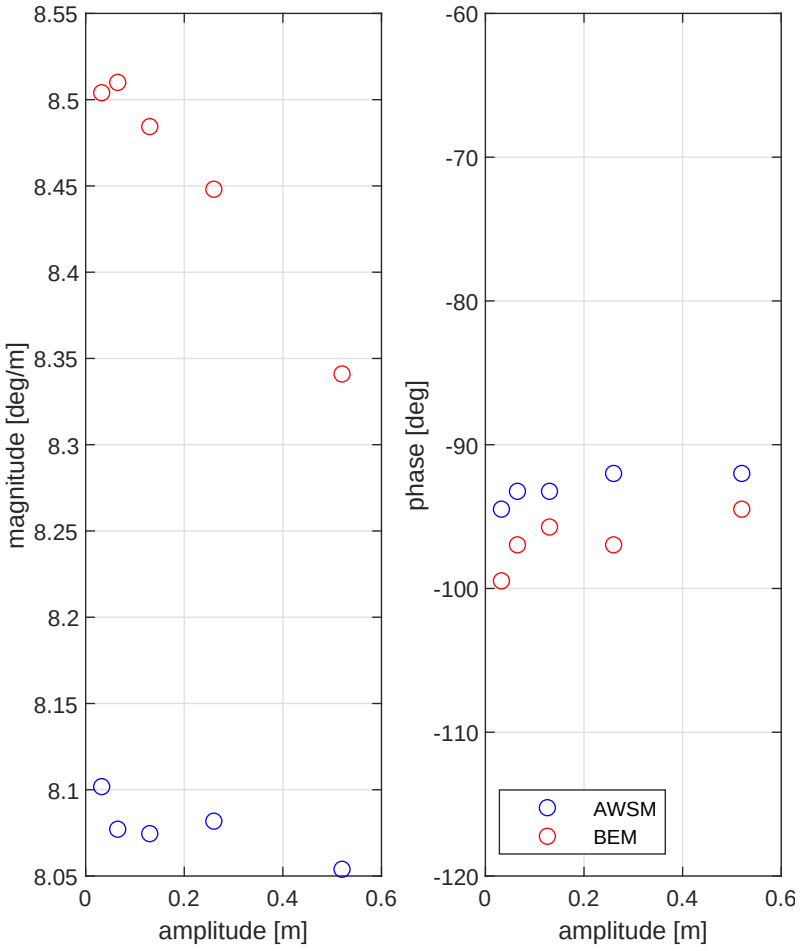

Figure 3.10: Response of the rotor thrust to surge motion. Simulations are here performed with a fixed surge frequency of 0.5 Hz and amplitude ranging from 0.0325 m to 0.52 m (x-axes). The response is evaluated by showing the ratio of the rotor thrust amplitude to the surge amplitude (left subplot) and the phase between these two signals (right subplot).

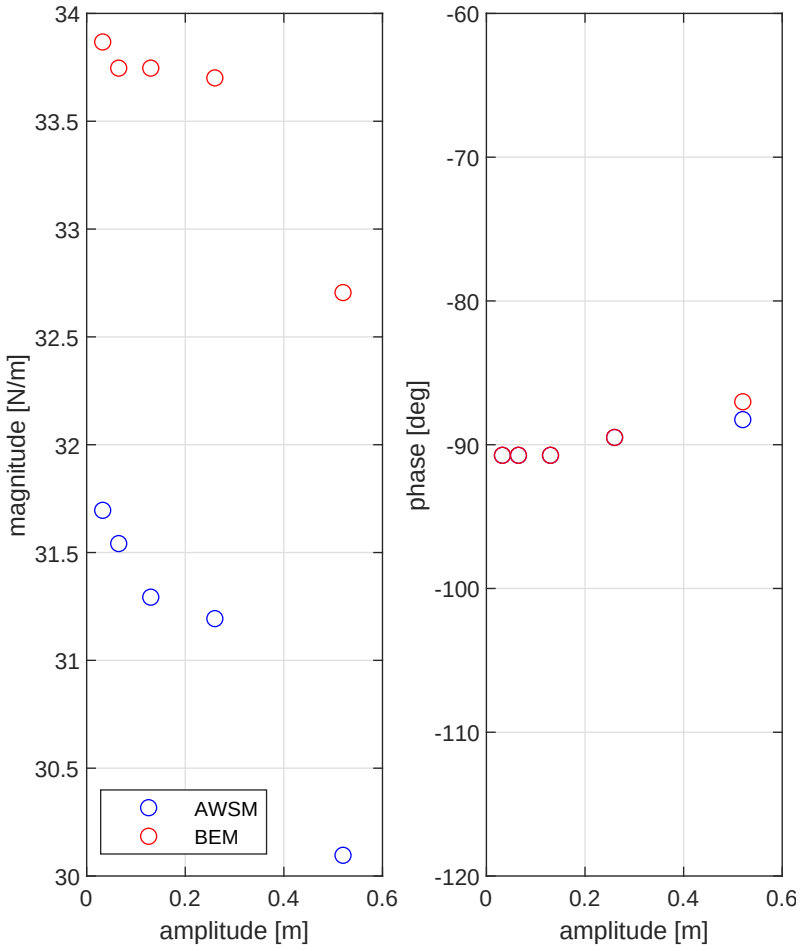

Figure 3.11: Response of the rotor torque to surge motion. Simulations are here performed with a fixed surge frequency of 0.5 Hz and amplitude ranging from 0.0325 m to 0.52 m (x-axes). The response is evaluated by showing the ratio of the rotor torque amplitude to the surge amplitude (left subplot) and the phase between these two signals (right subplot).

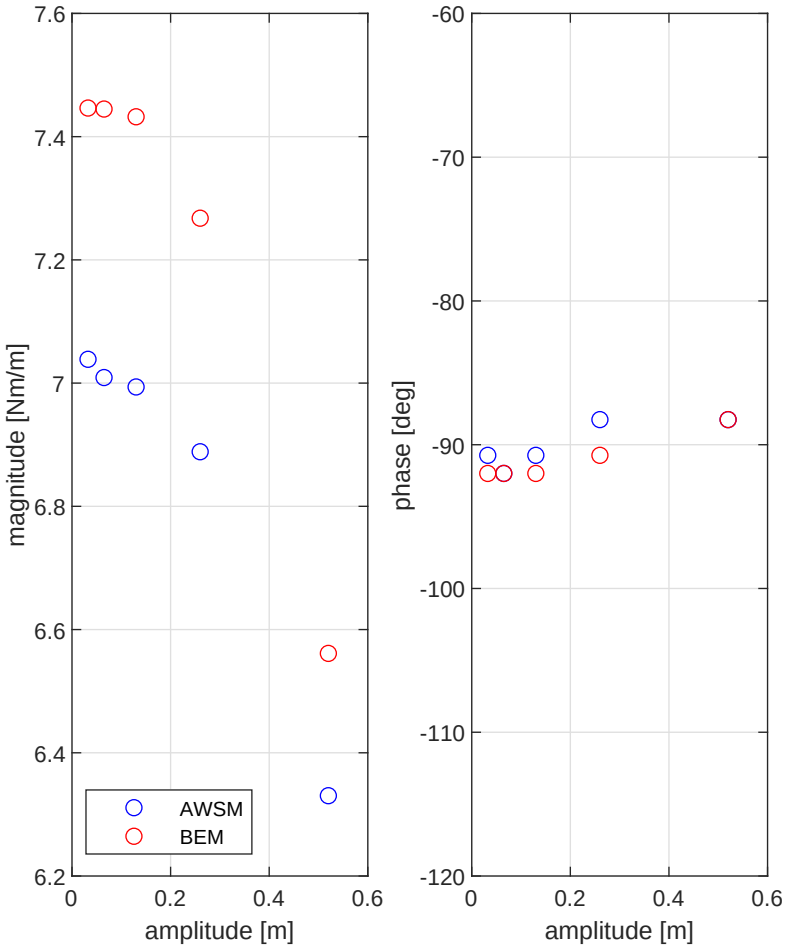

Frequency variation for constant amplitude An overview of the surge cases with constant amplitude are given in Table 3.4. Figures 3.12, 3.13 and 3.14 show the Bode plots of the aforementioned rotor signals. From the thrust variation in Figure 3.13 it can be observed that the magnitude is increasing as expected for the constant amplitude variable frequency cases. The trend of the magnitude with frequency is similar between BEM and AWSM, although the AWSM predicted amplitudes are slightly lower in agreement with the constant frequency cases. The phase is clearly departing the $-90\,^\circ$ offset for surge frequencies above 2 Hz, indicating the thrust to lead by approximately $10\,^\circ$ with respect to the maximum surge velocity. The fact that the phase of the thrust is leading the surge velocity is unexpected as a dynamic inflow effect is expected to result in a lag due to the inertia of the wake. A deeper investigation revealed that switching off the Snel dynamic stall model instead results in a lag of approximately $5\,^\circ$ for both the BEM and AWSM simulations. Indeed the angle of attack at the 75% span station reaches about $10\,^\circ$ for this case (see Figure B.15), where the lift curve slope starts to fall off. Together with the relatively high surge frequency this results in reduced frequencies with respect to the chord and apparent velocity (equation 2.1), where dynamic stall modeling becomes important. However, also referring to the discussion in section 2.2.2 on this topic, the questions remains whether the calculated response is in agreement with real life physics. It should also be noted that for full scale turbines, surge frequencies are not expected to approach values that result in reduced frequencies typical for dynamic stall phenomena.

The 4 Hz case displays an even larger difference with the $-90\,^\circ$ phase offset for both BEM and AWSM simulations. As now the angle of attack tops around $15\,^\circ$ (see Figure B.17), a more abrupt stall results in a sudden drop of the lift coefficient which results in a highly asymmetric hysteresis plot in Figure B.18. As such this case is dominated by airfoil aerodynamics rather than rotor wake aerodynamics. Similar conclusions can be drawn for the corresponding Bode plot of the rotor torque.

Table 3.4: Surge cases with constant amplitude.

case No.	amplitude [m]	frequency [Hz]
1	0.13	0.25
2	0.13	0.5
3	0.13	1
4	0.13	2
5	0.13	4

Figure 3.12: Response of the angle of attack at 75% of the blade span to surge motion. Simulations are here performed with a fixed surge amplitude of 0.13 m and frequency ranging from 0.25 Hz to 4 Hz (x-axes). The response is evaluated by showing the ratio of the angle of attack amplitude to the surge amplitude (left subplot) and the phase between these two signals (right subplot).

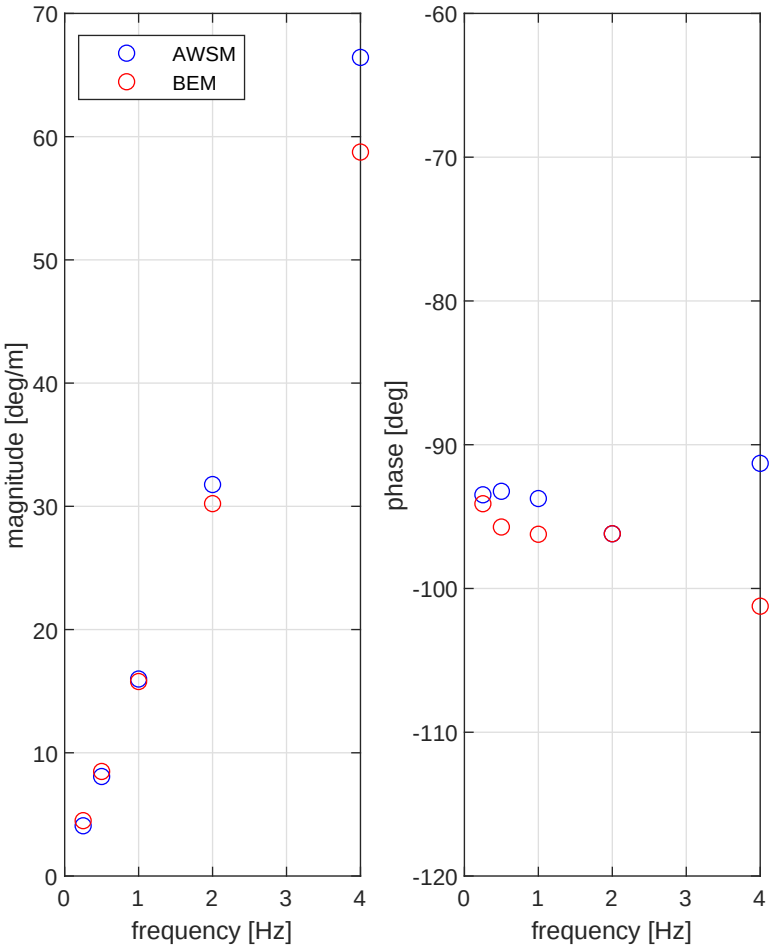

Figure 3.13: Response of the rotor thrust to surge motion. Simulations are here performed with a fixed surge amplitude of 0.13 m and frequency ranging from 0.25 Hz to 4 Hz (x-axes). The response is evaluated by showing the ratio of the rotor thrust amplitude to the surge amplitude (left subplot) and the phase between these two signals (right subplot).

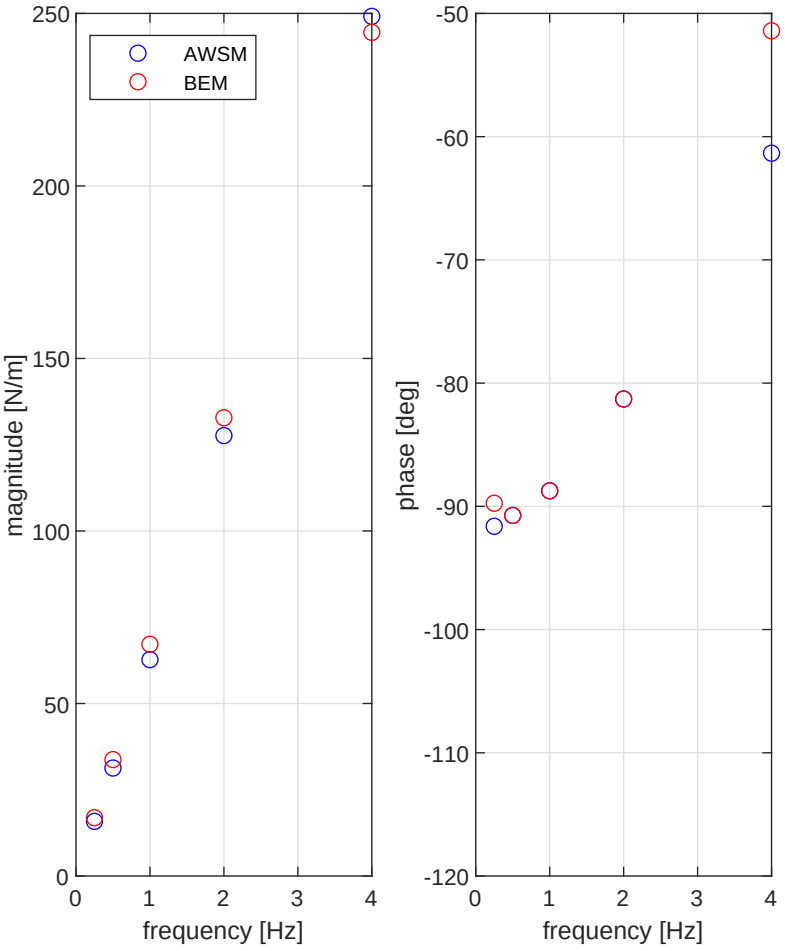

Figure 3.14: Response of the rotor torque to surge motion. Simulations are here performed with a fixed surge amplitude of 0.13 m and frequency ranging from 0.25 Hz to 4 Hz (x-axes). The response is evaluated by showing the ratio of the rotor torque amplitude to the surge amplitude (left subplot) and the phase between these two signals (right subplot).

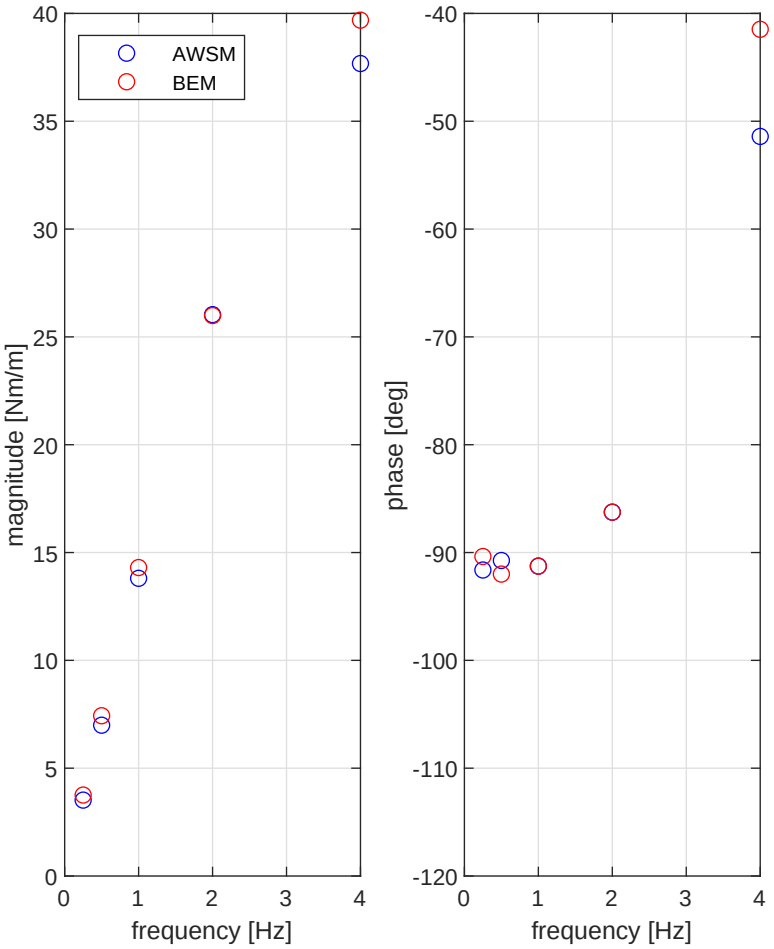

4 Conclusions and recommendations

Concluding it can be stated that a very successful comparison exercise has been performed to validate the unsteady aerodynamic modeling of floating offshore wind turbines using both airfoil and rotor wind tunnel test data. More specifically the dynamic stall models used by the Aero Module have been validated using 2D airfoil experiment results in pitching motion. The modeling of shed vorticity effects by a free vortex code and the Beddoes Leishman model was found to be in good agreement with the airfoil experiment. Following the observations it is advised not to use the current implementation of the Beddoes Leishman model in combination with AWSM. In addition to that it was found that the implementation of some dynamic stall modeling requires attention to prevent the prediction of non-physical hysteresis loops in attached flow for non-linear lift curve slopes. For the turbine test, the imposed experimental surge motion did not reveal the dynamic inflow effect to play a large role, resulting in a good agreement between experiment and simulations. However the necessity of including apparent wind velocities due to platform motion in the momentum equations was verified for the BEM simulations. A numerical study into the variation of surge frequencies and amplitudes and their impact on phase differences between surge velocity and resulting thrust force revealed the influence of airfoil aerodynamics in separated flow rather than the importance of wake aerodynamics and the associated dynamic inflow modeling. However the relevance of airfoil aerodynamics in separated flow is expected to be limited for full scale turbines in surge motion.

It is recommended to further explore the experimental database (both rotor and airfoil), as only a small portion of the available data has been touched upon. For the rotor experiments it is recommended to also focus on pitching motion, which brings in addition to the dynamic inflow effect also yaw modeling effects. In addition to that the incorporation of apparent wind velocities is less trivial as these are not uniformly distributed over the rotor plane. Comparison to measurements and free vortex wake code results can shed light on this topic.

5 References

[1] J. B. de Vaal, M. O. L. Hansen, and T. Moan. Effect of wind turbine surge motion on rotor thrust and induced velocity. *Wind Energ.*, 17:105–121, 2014.

[2] I. Bayati, M. Belloli, L. Bernini, K. Boorsma, M. Caboni, M. Cormier, R. Mikkelsen, M. Serdeczny, T. Lutz, and A. Zasso. Unaflow project: Unsteady aerodynamics of floating wind turbines. 2018.

[3] S. Mancini, K. Boorsma, M. Caboni, M. Cormier, T. Lutz, P. Schito, and A. Zasso. Characterization of the unsteady aerodynamic response of a floating offshore wind turbine. *Wind Energ. Sci. Discuss. (in review)*, 2020. `https://doi.org/10.5194/wes-2020-94`.

[4] I. Bayati, M. Belloli, L. Bernini, R. Mikkelsen, and A. Zasso. On the aero-elastic design of the dtu 10mw wind turbine blade for the lifes50+ wind tunnel scale model. *J. Phys.: Conf. Ser.*, 753(022028), 2016.

[5] K. Boorsma, F. Grasso, and J.G. Holierhoek. Enhanced approach for simulation of rotor aerodynamic loads. In *Proceedings of EWEA Offshore 2011*, Amsterdam, The Netherlands, 2011.

[6] C. Lindenburg and J.G. Schepers. Phatas-iv aeroelastic modelling, release ”dec-1999” and ”nov-2000”. Technical Report ECN-CX–00-027, ECN, 2000.

[7] A. Van Garrel. Development of a wind turbine aerodynamics simulation module. Technical Report ECN-C–03-079, ECN, 2003.

[8] T. Theodorsen. General theory of aerodynamic instability and the mechanism of flutter. Technical Report NACA Report 496, NACA, 1935.

[9] J. G. Leishman and T. S. Beddoes. A generalized model for airfoil unsteady aerodynamic behaviour and dynamic stall using the indicial method. In *Proceedings of 42nd Annual Forum of the American Helicopter Society*, Washington, USA, 1986.

[10] H. Snel. Heuristic modelling of dynamic stall characteristics. In *Conference proceedings European Wind Energy Conference*, pages 429–433, Dublin, Ireland, October 1997.

[11] K. W. McAlister, O. Lambert, and D. Petot. Application of the onera model of dynamic stall. Technical Report 84-A-3, NASA, 1984.

[12] J.G. Holierhoek, J.B. De Vaal, A. H. Van Zuijlen, and H. Bijl. Comparing different dynamic stall models. *Wind Energy*, online 2012, 2012.

[13] M.A. Khan. Dynamic stall modeling for wind turbines. Master’s thesis, Delft University of Technology, Delft, the Netherlands, 2018.

[14] Christian Bak, Frederik Zahle, Robert Bitsche, Taeseong Kim, Anders Yde, Lars Christian Henriksen, Morten Hartvig Hansen, José Pedro Albergaria Amaral Blasques, Mac Gaunaa, and Anand Natarajan. The dtu 10-mw reference wind turbine. *Danish Wind Power Research 2013*, 2013.

[15] I. Bayati, M. Belloli, L. Bernini, and A. Zasso. Wind tunnel validation of aerodyn within lifes50+ project: imposed surge and pitch tests. *J. Phys.: Conf. Ser.*, 753(092001), 2016.

[16] I. Bayati, M. Belloli, L. Bernini, H. Giberti, and A. Zasso. Scale model technology for floating offshore wind turbines. *IET Renew. Power Gener.*, 11:1120–1126, 2017.

[17] H. Snel and J.G. Schepers. Joule1: Joint investigation of dynamic inflow effects and implementation of an engineering model. Technical Report ECN-C–94-107, ECN, 1994.

[18] B.O.G. Montgomerie, A.J. Brand, J. Bosschers, and R.P.J.O.M Van Rooij. Three-dimensional effects in stall. Technical Report ECN-C–96-079, ECN, 1996.

[19] K. Boorsma and F. Wenz and M. Aman and C. Lindenburg and M. Kloosterman. TKI WoZ VortexLoads Final report. Technical Report TNO 2019 R11388, TNO, September 2019. http://publications.tno.nl/publication/34634923/tbIASC/TNO-2019-R11388.pdf.

[20] N. Kroll and J.K. Faßbender. Megaflow - numerical flow simulation for aircraft design. 2005.

[21] C Schulz, L Klein, P Weihing, and Th Lutz. Investigations into the interaction of a wind turbine with atmospheric turbulence in complex terrain. *Journal of Physics: Conference Series*, 753(3):032016, 2016.

[22] Pascal Weihing, Christoph Schulz, Thorsten Lutz, and Ewald Krämer. Comparison of the actuator line model with fully resolved simulations in complex environmental conditions. *Journal of Physics: Conference Series*, 854(1):012049, 2017.

A Airfoil plots

Figure A.1: Comparison between SD7032 airfoil's experimental dynamic lift coefficient (incuding the bin average) and that predicted by means of different unsteay airfoil aerodynamic models for a Reynolds number of 100000. Geometric angle of attack mean, μ_{AoA}, and amplitude, A, are respectively equal to 0° and 0.5°, while frequency, f, is 0.25 Hz. In the figure, k denotes the reduced frequency.

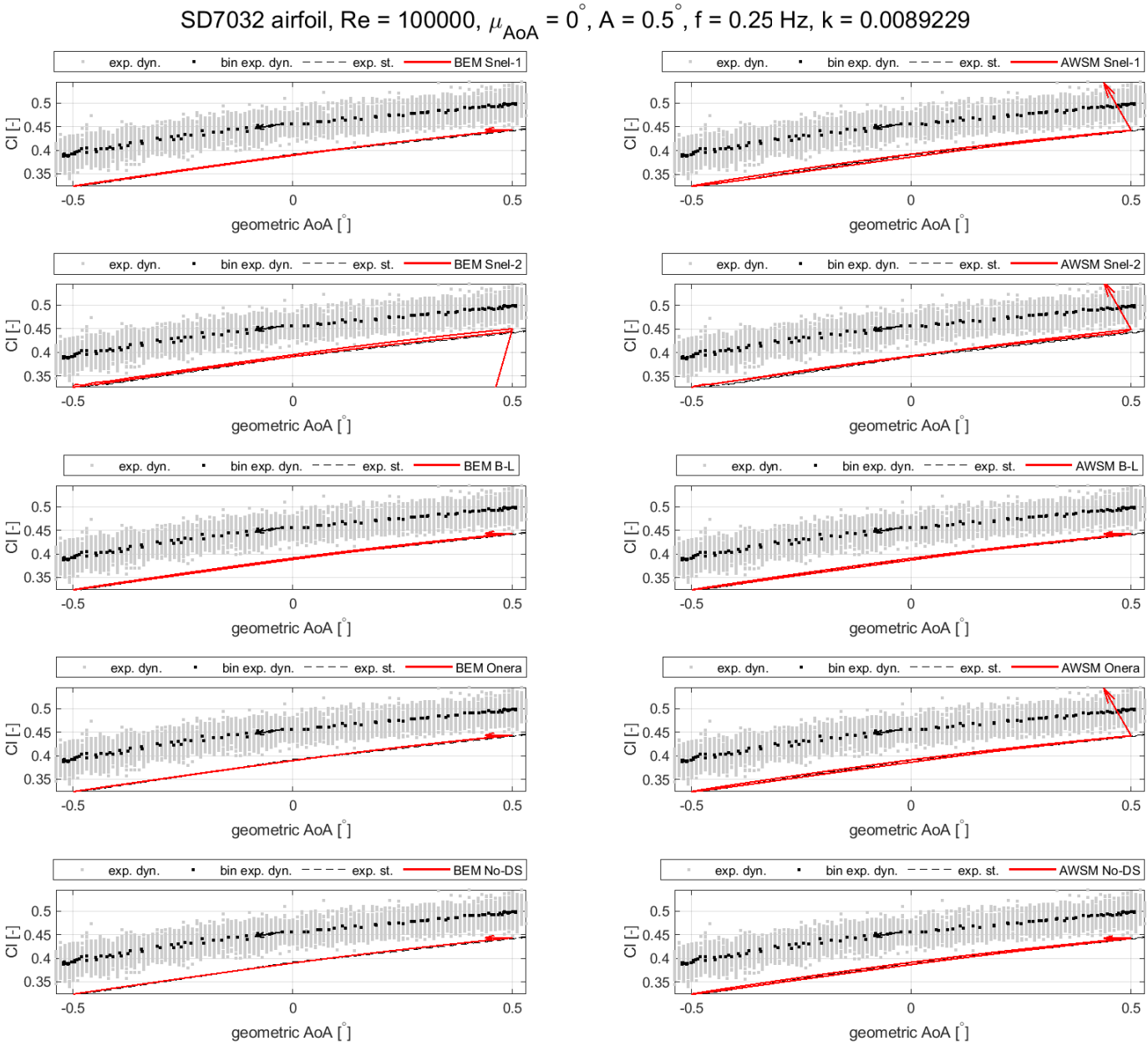

Figure A.2: Comparison between SD7032 airfoil's experimental dynamic lift coefficient (incuding the bin average) and that predicted by means of different unsteay airfoil aerodynamic models for a Reynolds number of 100000. Geometric angle of attack mean, μ_{AoA}, and amplitude, A, are respectively equal to 0° and 0.5°, while frequency, f, is 0.50 Hz. In the figure, k denotes the reduced frequency.

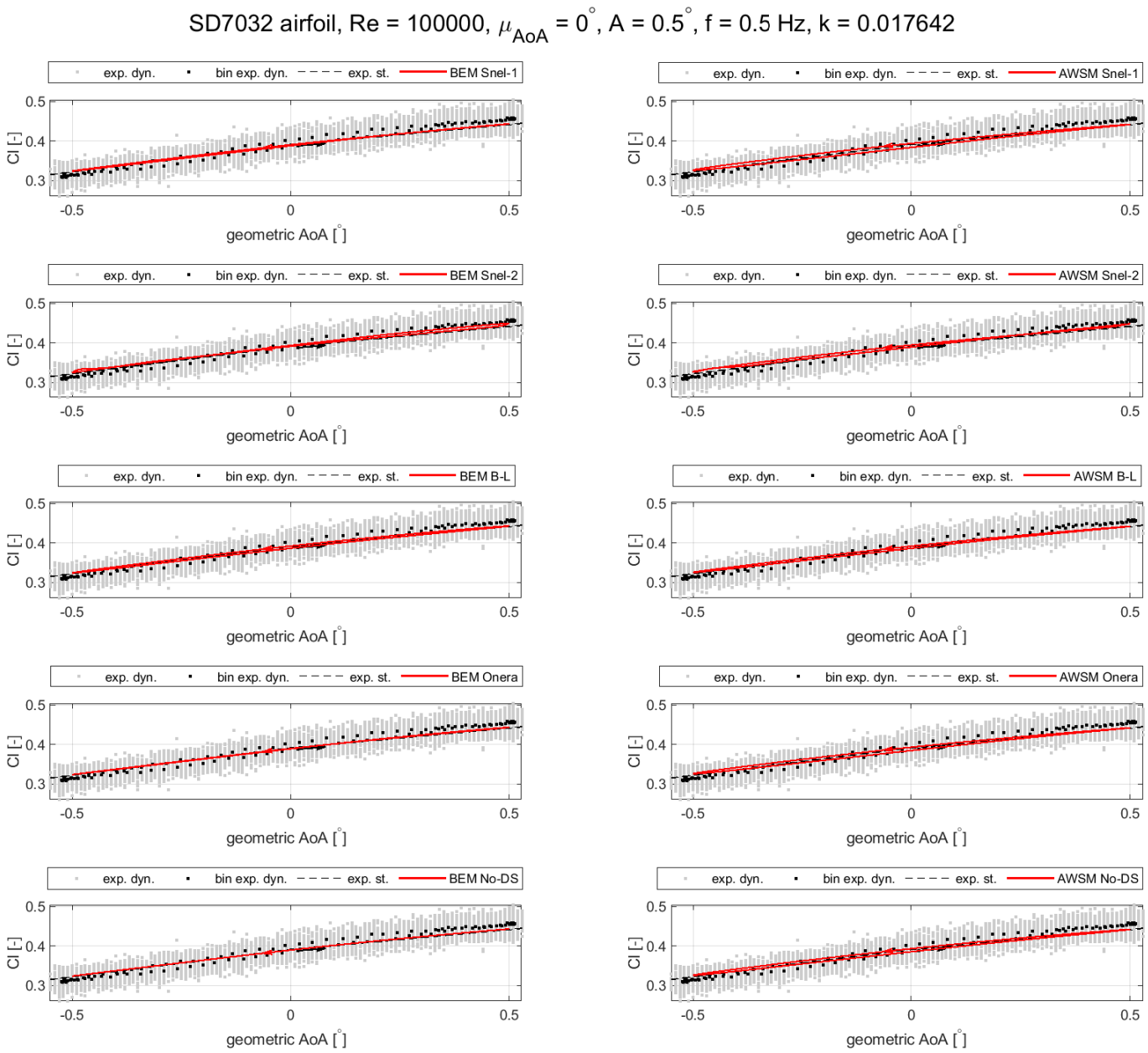

Figure A.3: Comparison between SD7032 airfoil's experimental dynamic lift coefficient (incuding the bin average) and that predicted by means of different unsteay airfoil aerodynamic models for a Reynolds number of 100000. Geometric angle of attack mean, μ_{AoA}, and amplitude, A, are respectively equal to 0° and 0.5°, while frequency, f, is 1.50 Hz. In the figure, k denotes the reduced frequency.

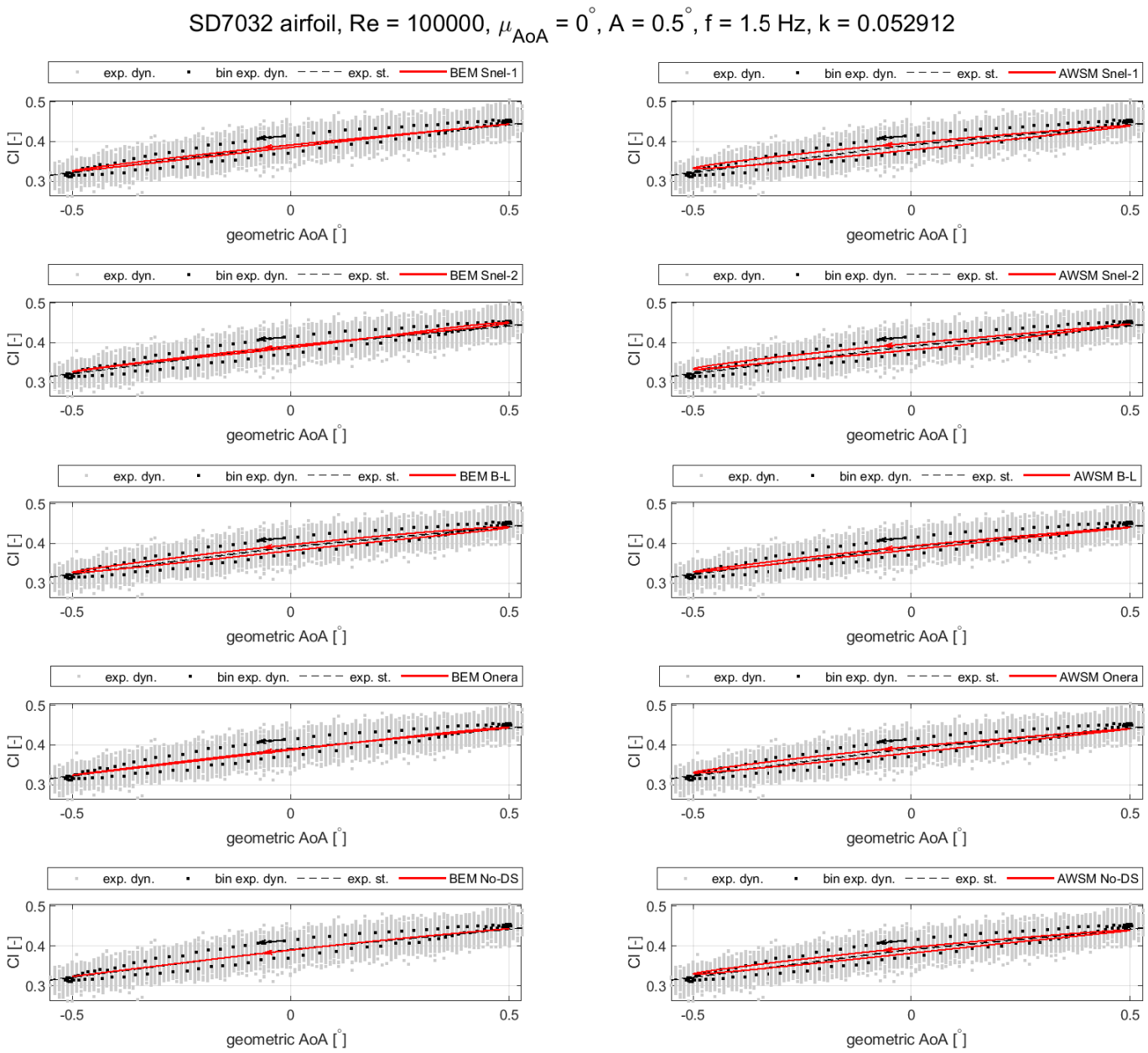

Figure A.4: Comparison between SD7032 airfoil's experimental dynamic lift coefficient (incuding the bin average) and that predicted by means of different unsteay airfoil aerodynamic models for a Reynolds number of 100000. Geometric angle of attack mean, μ_{AoA}, and amplitude, A, are respectively equal to 0° and 0.5°, while frequency, f, is 1.00 Hz. In the figure, k denotes the reduced frequency.

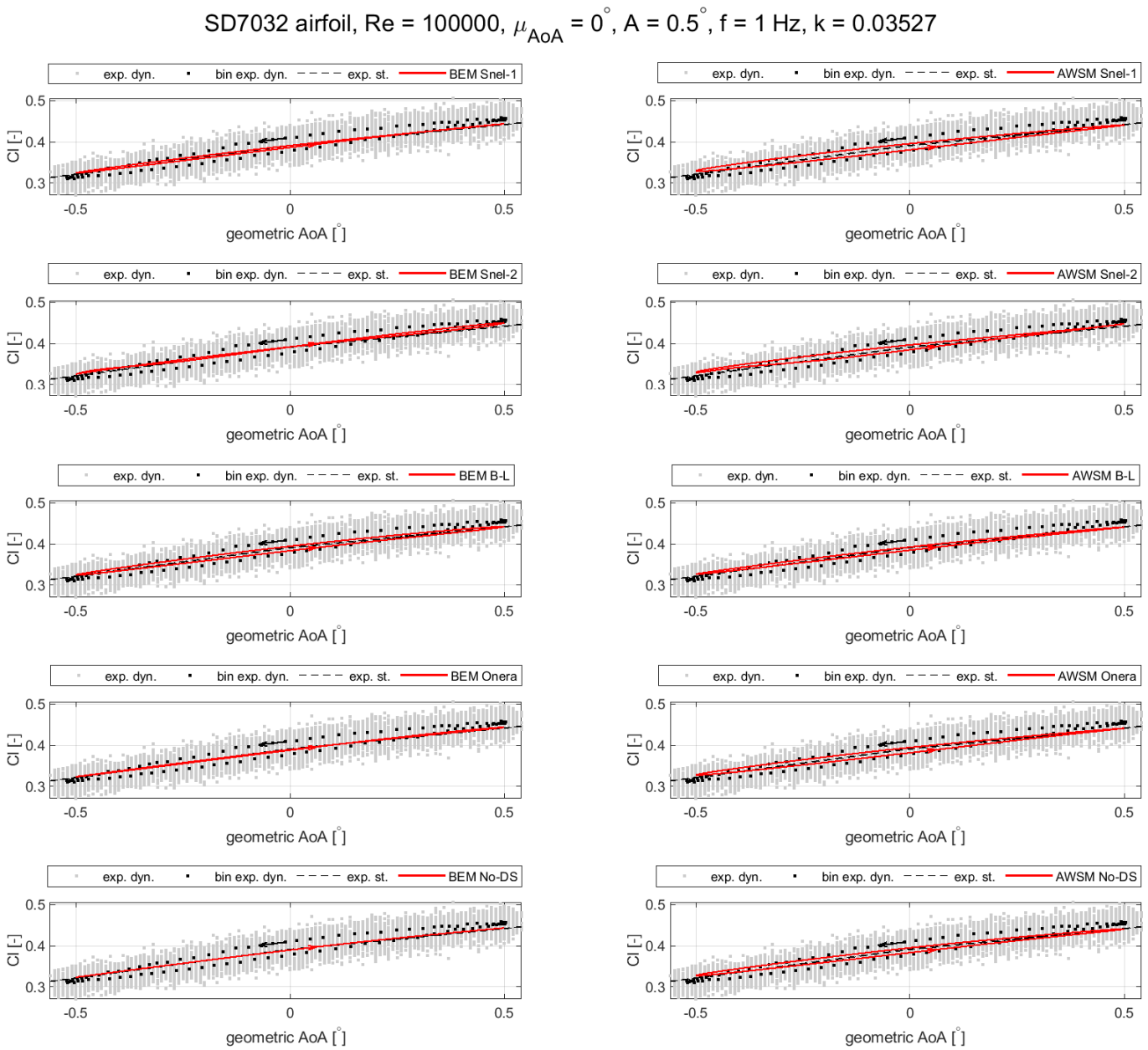

Figure A.5: Comparison between SD7032 airfoil's experimental dynamic lift coefficient (incuding the bin average) and that predicted by means of different unsteay airfoil aerodynamic models for a Reynolds number of 100000. Geometric angle of attack mean, μ_{AoA}, and amplitude, A, are respectively equal to 0° and 0.5°, while frequency, f, is 2.00 Hz. In the figure, k denotes the reduced frequency.

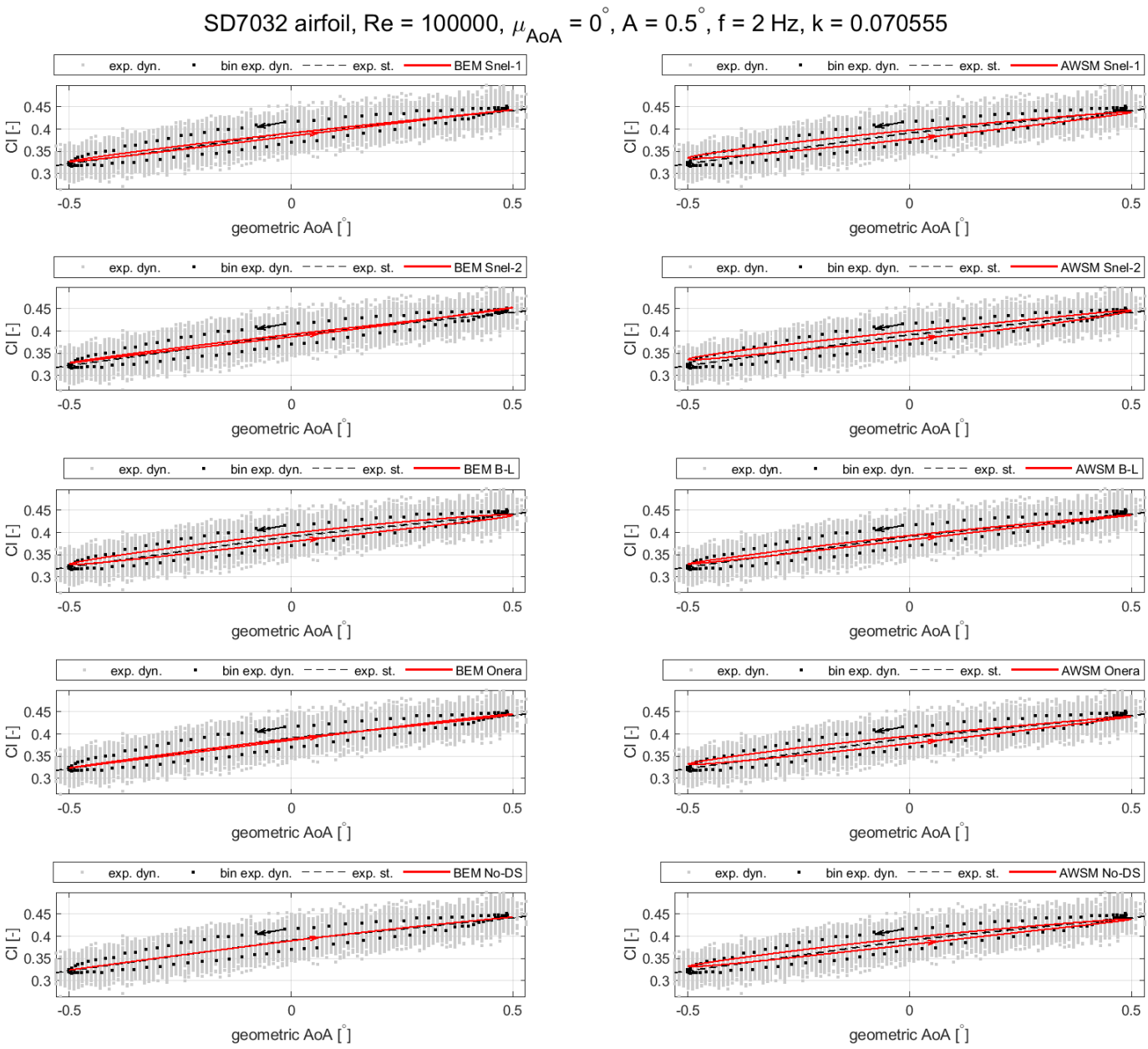

Figure A.6: Comparison between SD7032 airfoil's experimental dynamic lift coefficient (incuding the bin average) and that predicted by means of different unsteay airfoil aerodynamic models for a Reynolds number of 100000. Geometric angle of attack mean, μ_{AoA}, and amplitude, A, are respectively equal to 0° and 0.5°, while frequency, f, is 3.00 Hz. In the figure, k denotes the reduced frequency.

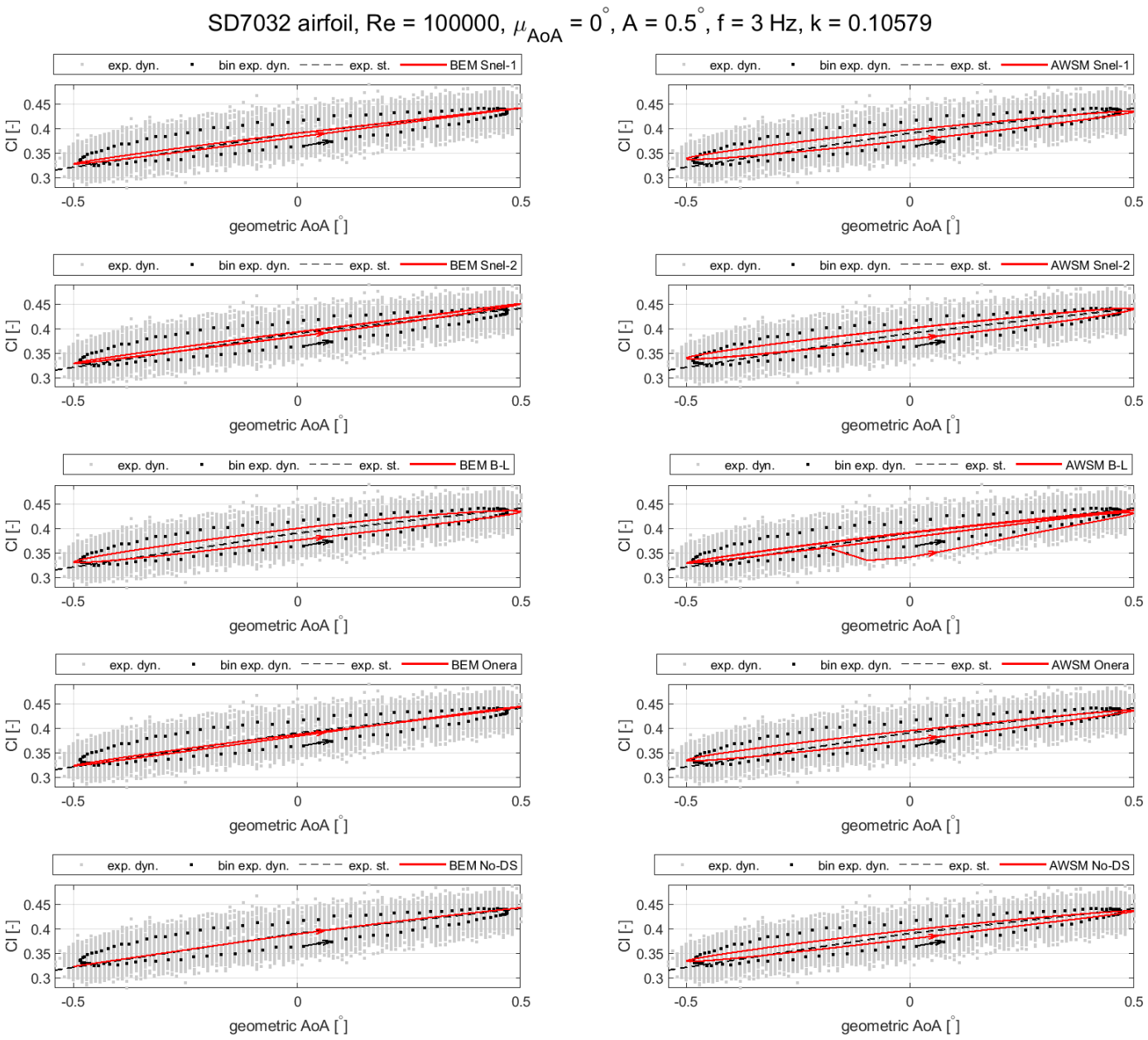

Figure A.7: Comparison between SD7032 airfoil's experimental dynamic lift coefficient (incuding the bin average) and that predicted by means of different unsteay airfoil aerodynamic models for a Reynolds number of 100000. Geometric angle of attack mean, μ_{AoA}, and amplitude, A, are respectively equal to 0° and 5.0°, while frequency, f, is 0.25 Hz. In the figure, k denotes the reduced frequency.

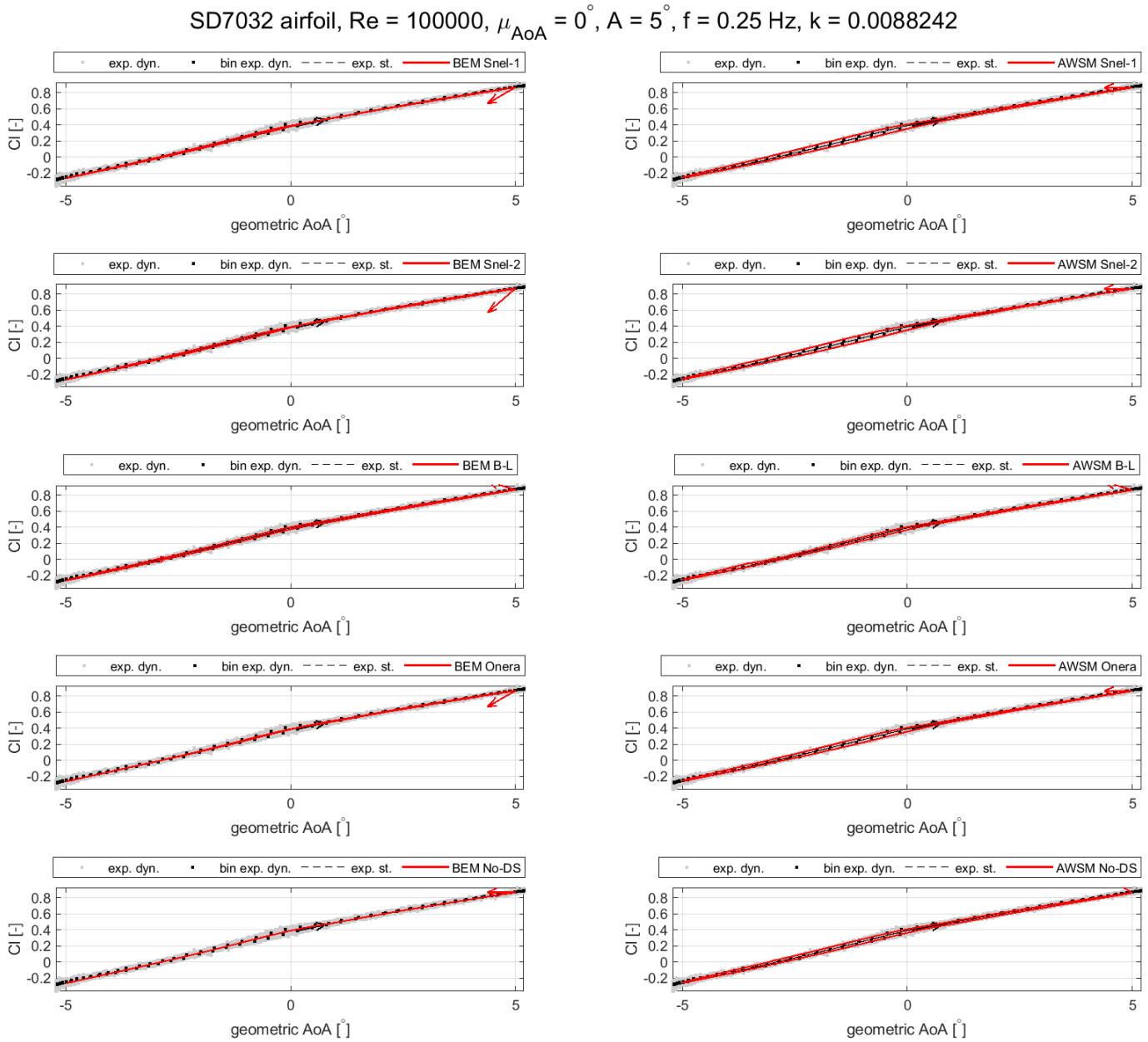

Figure A.8: Comparison between SD7032 airfoil's experimental dynamic lift coefficient (incuding the bin average) and that predicted by means of different unsteay airfoil aerodynamic models for a Reynolds number of 100000. Geometric angle of attack mean, μ_{AoA}, and amplitude, A, are respectively equal to 0° and 5.0°, while frequency, f, is 0.50 Hz. In the figure, k denotes the reduced frequency.

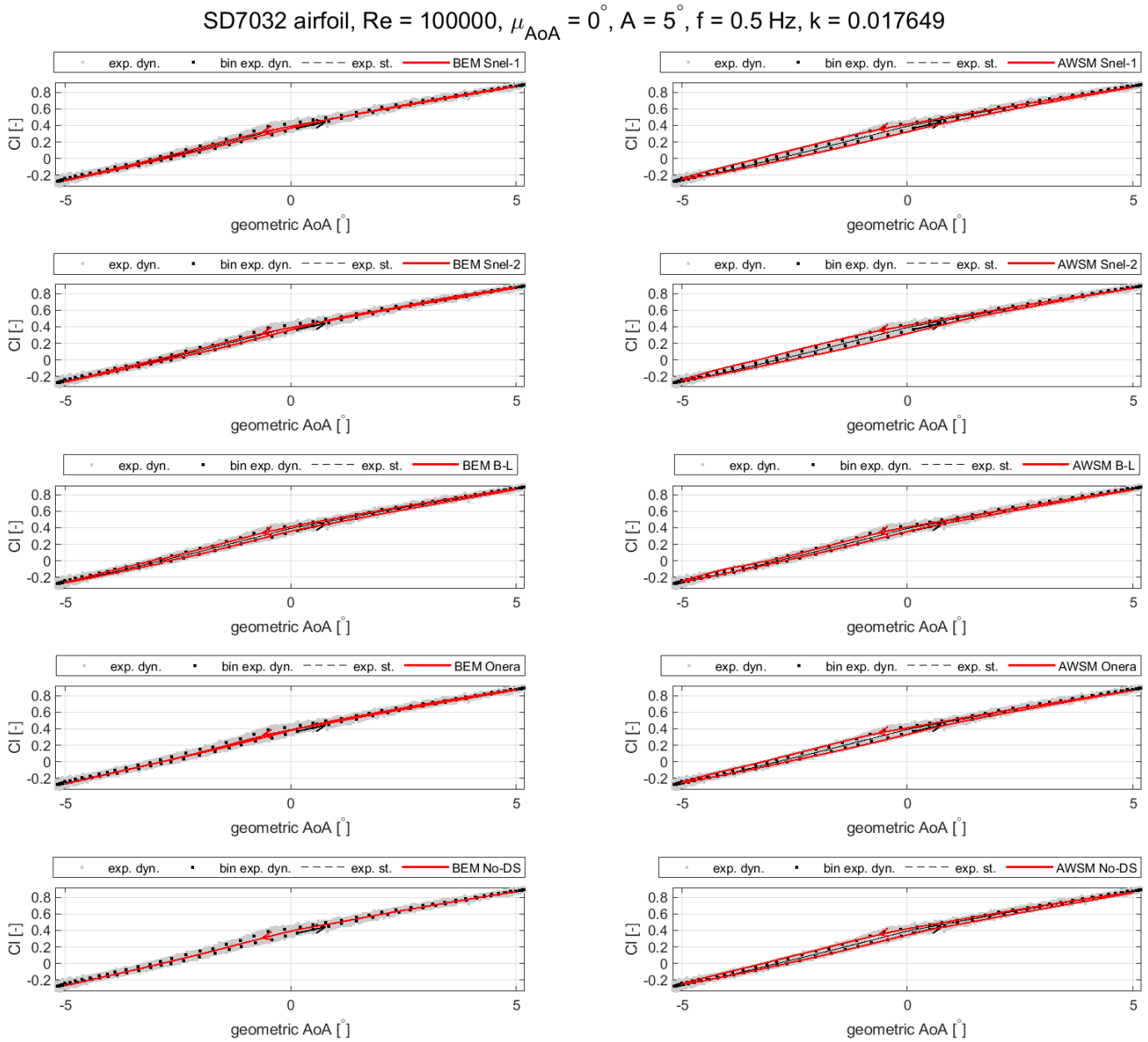

Figure A.9: Comparison between SD7032 airfoil's experimental dynamic lift coefficient (incuding the bin average) and that predicted by means of different unsteay airfoil aerodynamic models for a Reynolds number of 100000. Geometric angle of attack mean, μ_{AoA}, and amplitude, A, are respectively equal to 0° and 5.0°, while frequency, f, is 1.50 Hz. In the figure, k denotes the reduced frequency.

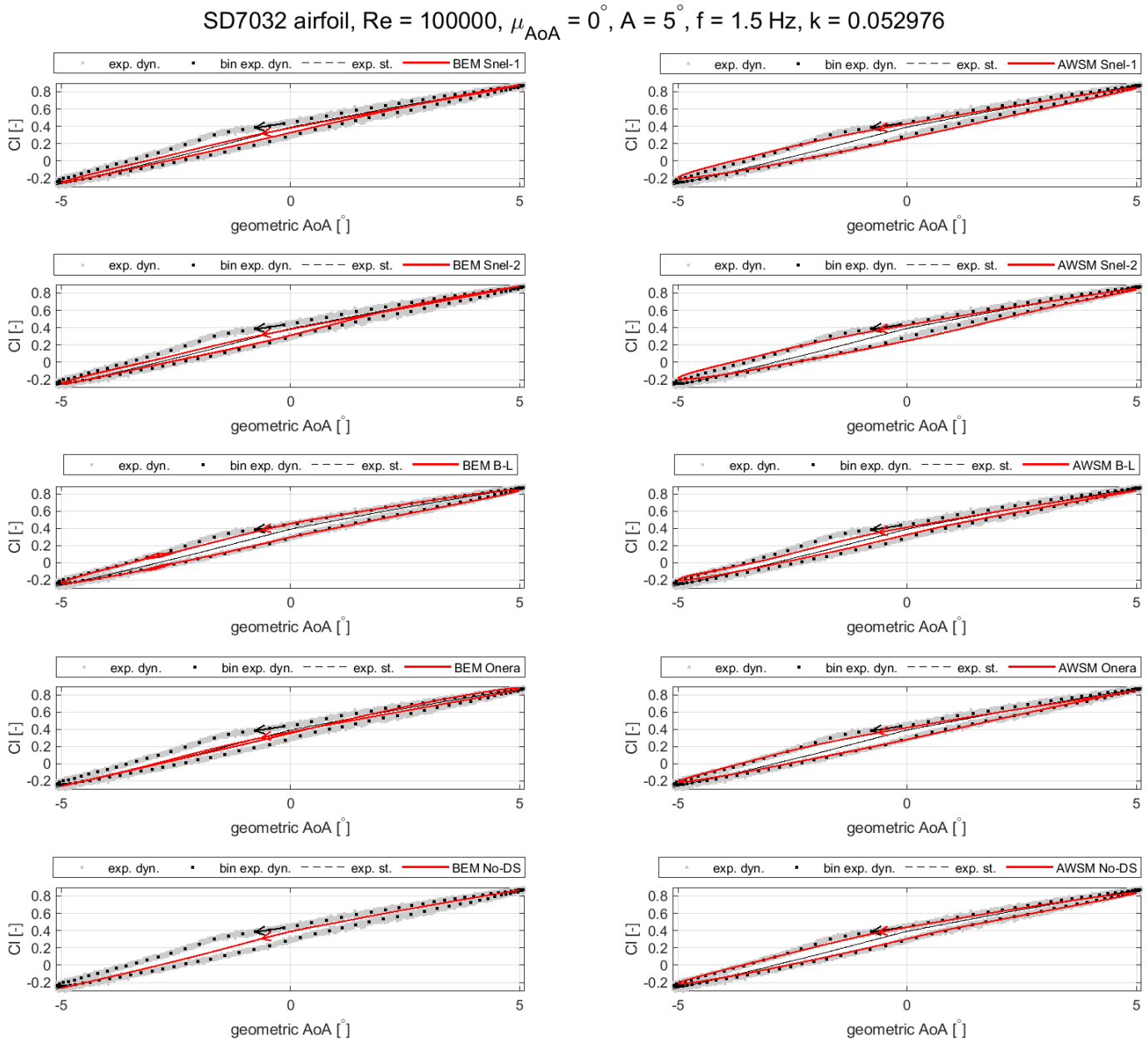

Figure A.10: Comparison between SD7032 airfoil's experimental dynamic lift coefficient (incuding the bin average) and that predicted by means of different unsteay airfoil aerodynamic models for a Reynolds number of 100000. Geometric angle of attack mean, μ_{AoA}, and amplitude, A, are respectively equal to 0° and 5.0°, while frequency, f, is 1.00 Hz. In the figure, k denotes the reduced frequency.

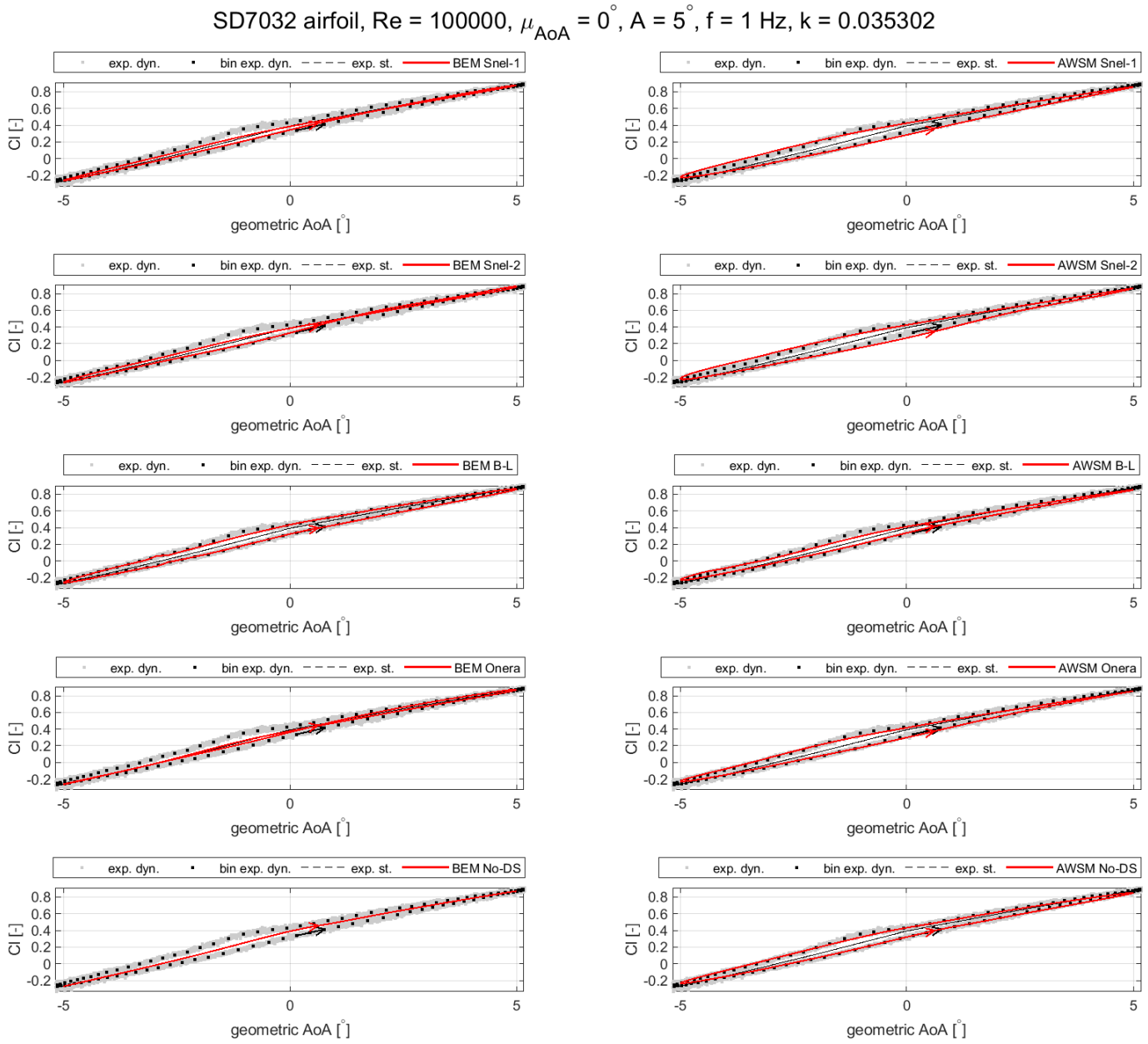

Figure A.11: Comparison between SD7032 airfoil's experimental dynamic lift coefficient (incuding the bin average) and that predicted by means of different unsteay airfoil aerodynamic models for a Reynolds number of 100000. Geometric angle of attack mean, μ_{AoA}, and amplitude, A, are respectively equal to 0° and 5.0°, while frequency, f, is 2.00 Hz. In the figure, k denotes the reduced frequency.

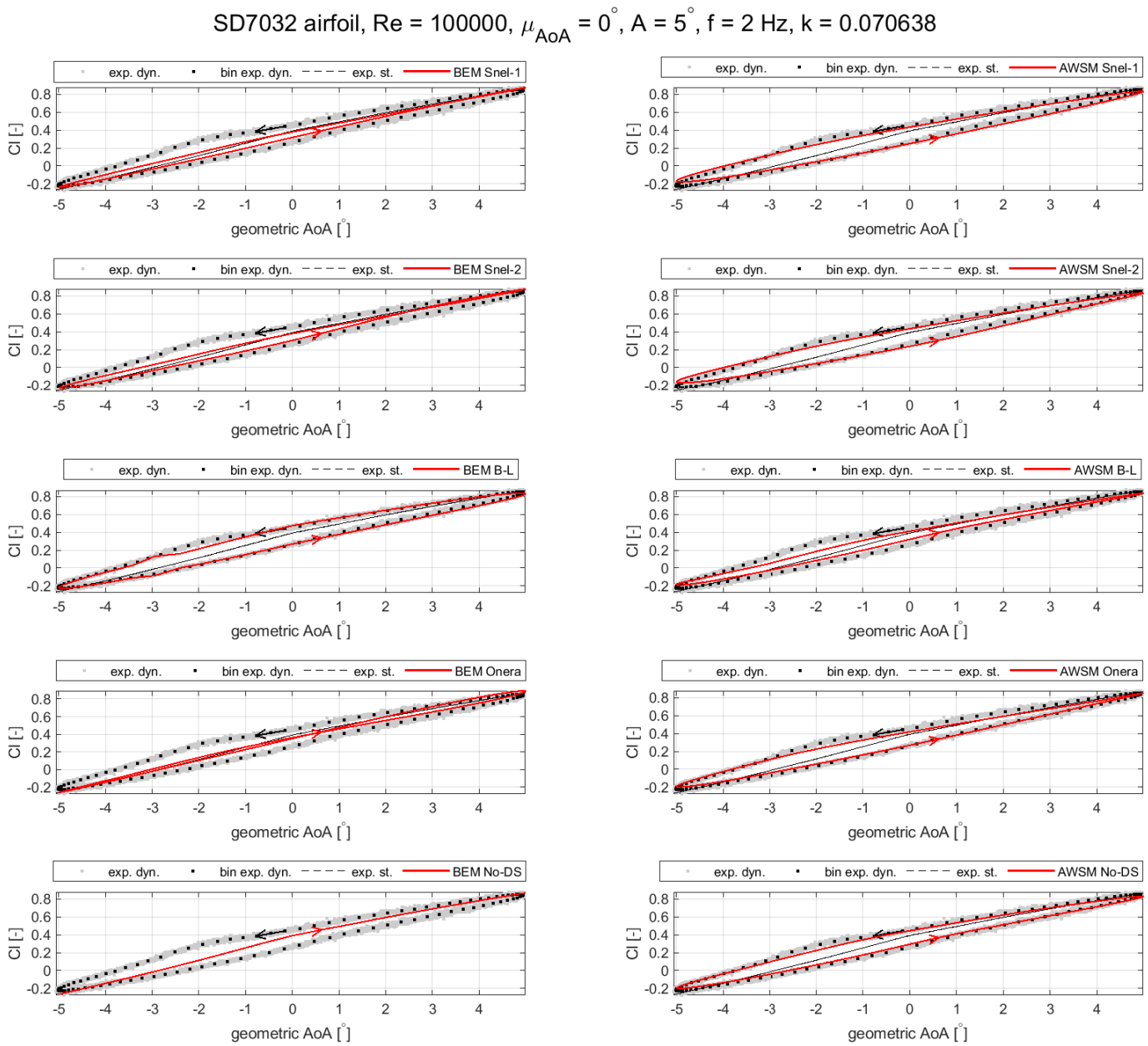

Figure A.12: Comparison between SD7032 airfoil's experimental dynamic lift coefficient (incuding the bin average) and that predicted by means of different unsteay airfoil aerodynamic models for a Reynolds number of 100000. Geometric angle of attack mean, μ_{AoA}, and amplitude, A, are respectively equal to 0° and 5.0°, while frequency, f, is 3.00 Hz. In the figure, k denotes the reduced frequency.

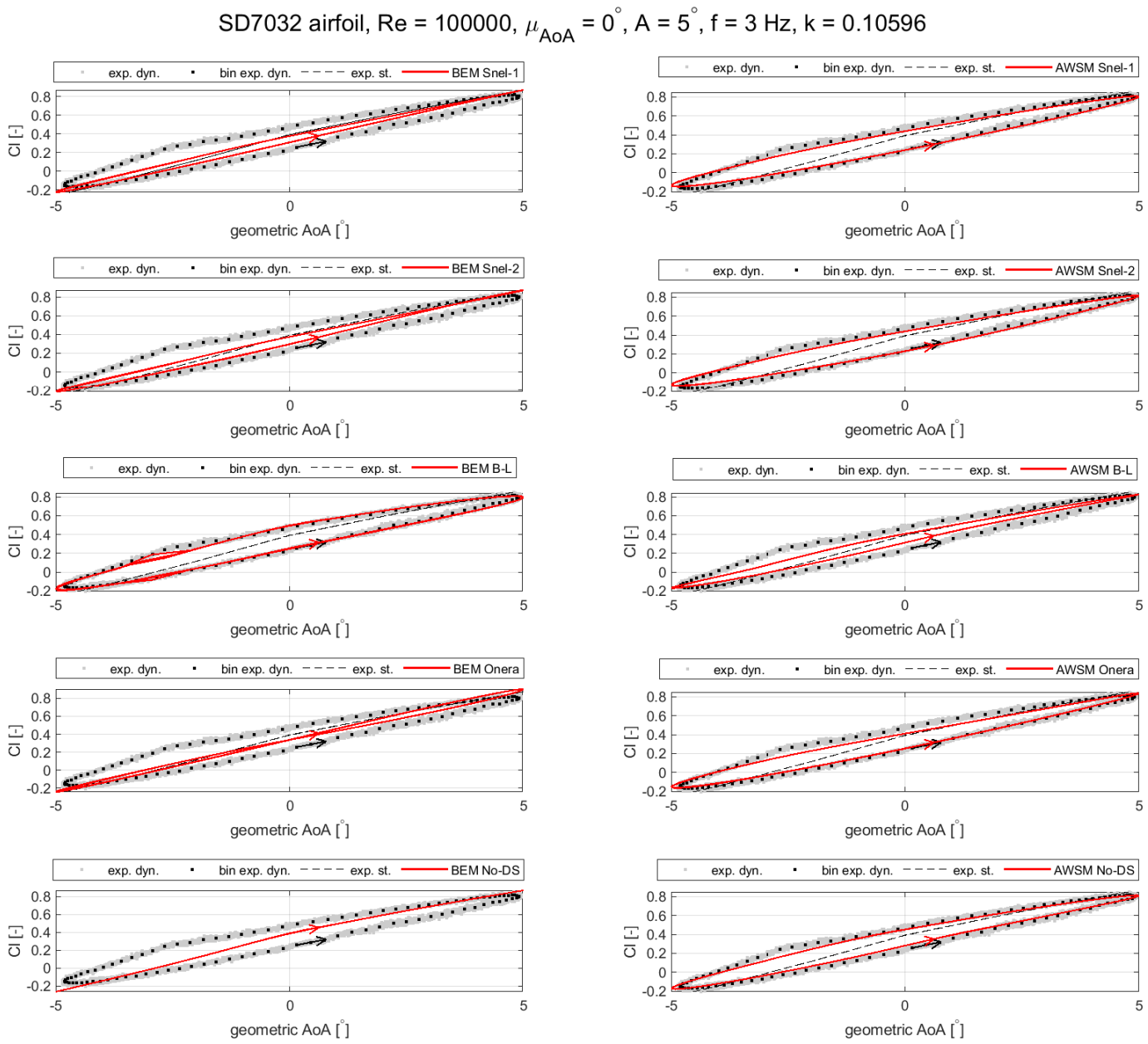

Figure A.13: Comparison between SD7032 airfoil's experimental dynamic lift coefficient (incuding the bin average) and that predicted by means of different unsteay airfoil aerodynamic models for a Reynolds number of 100000. Geometric angle of attack mean, μ_{AoA}, and amplitude, A, are respectively equal to 3° and 0.5°, while frequency, f, is 0.25 Hz. In the figure, k denotes the reduced frequency.

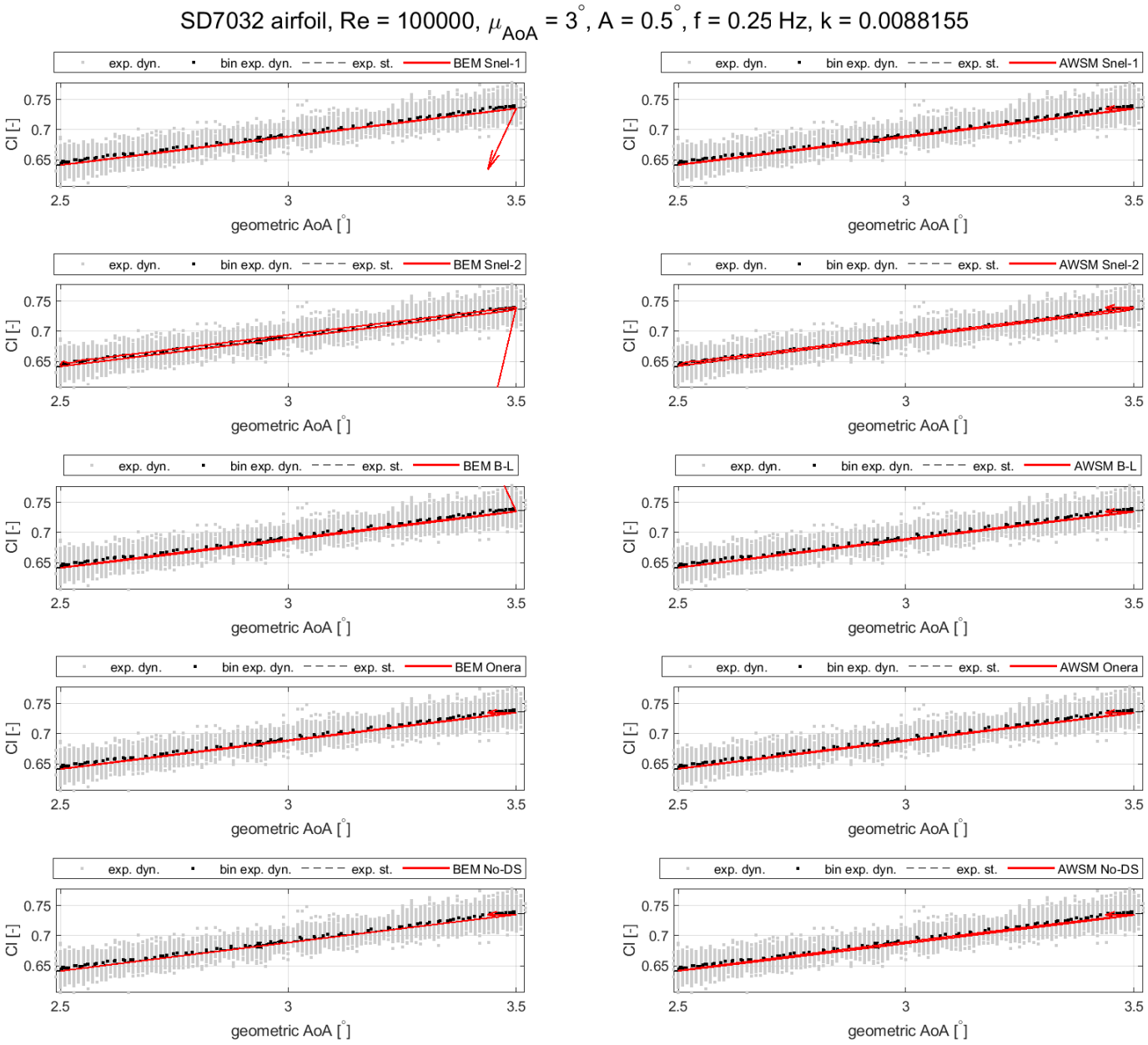

Figure A.14: Comparison between SD7032 airfoil's experimental dynamic lift coefficient (incuding the bin average) and that predicted by means of different unsteay airfoil aerodynamic models for a Reynolds number of 100000. Geometric angle of attack mean, μ_{AoA}, and amplitude, A, are respectively equal to 3° and 0.5°, while frequency, f, is 0.50 Hz. In the figure, k denotes the reduced frequency.

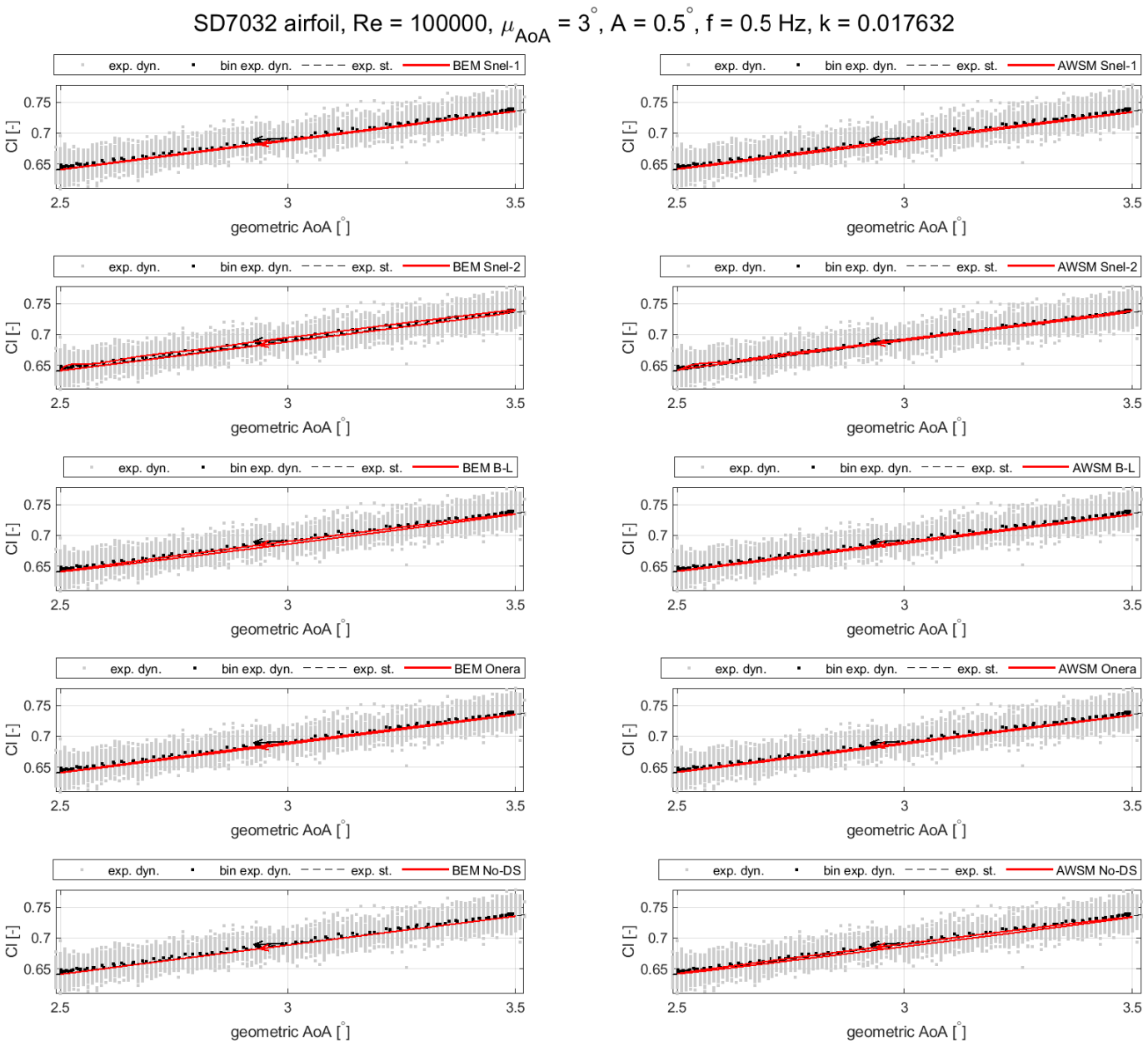

Figure A.15: Comparison between SD7032 airfoil's experimental dynamic lift coefficient (incuding the bin average) and that predicted by means of different unsteay airfoil aerodynamic models for a Reynolds number of 100000. Geometric angle of attack mean, μ_{AoA}, and amplitude, A, are respectively equal to 3° and 0.5°, while frequency, f, is 1.50 Hz. In the figure, k denotes the reduced frequency.

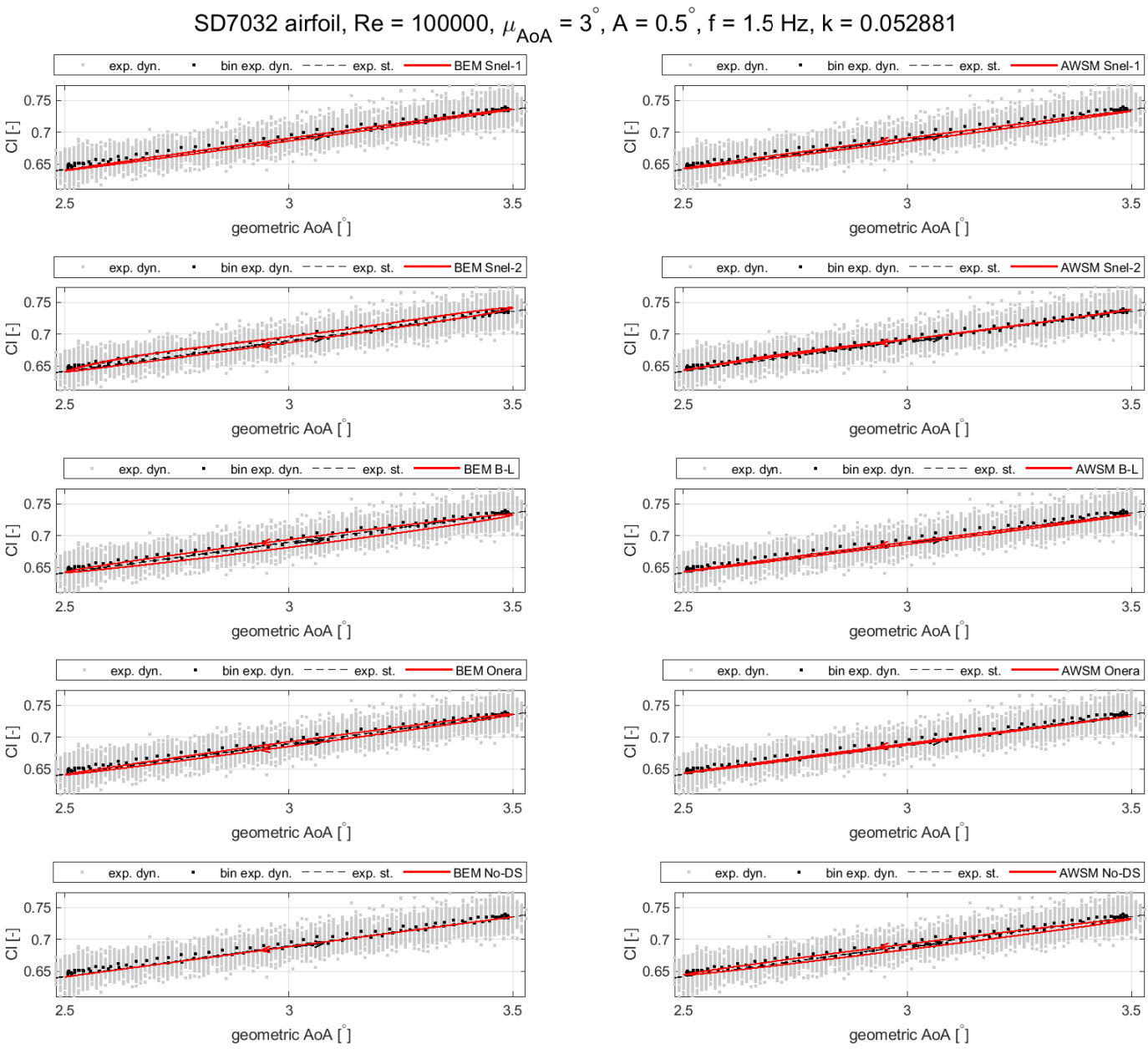

Figure A.16: Comparison between SD7032 airfoil's experimental dynamic lift coefficient (incuding the bin average) and that predicted by means of different unsteay airfoil aerodynamic models for a Reynolds number of 100000. Geometric angle of attack mean, μ_{AoA}, and amplitude, A, are respectively equal to 3° and 0.5°, while frequency, f, is 1.00 Hz. In the figure, k denotes the reduced frequency.

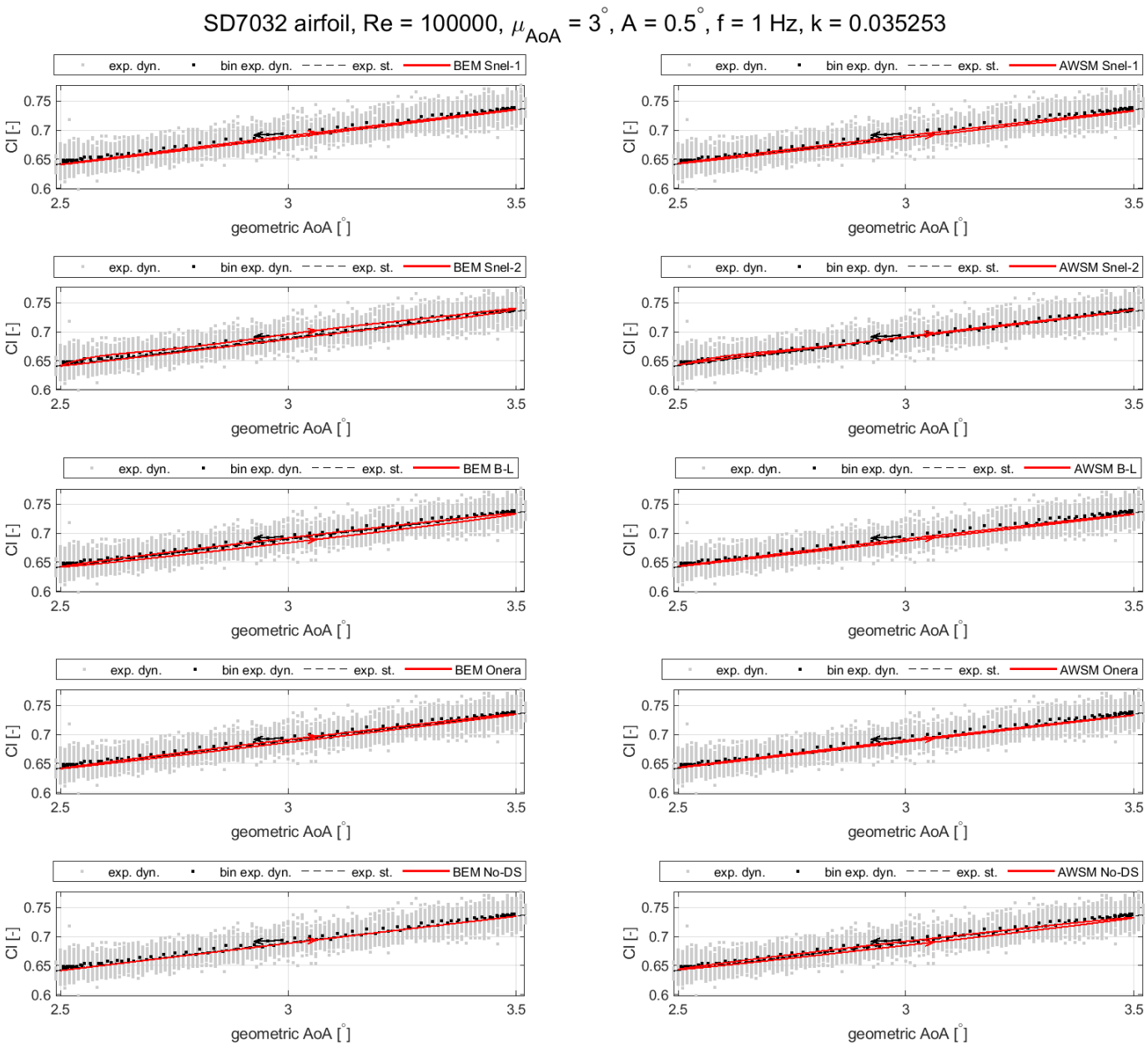

Figure A.17: Comparison between SD7032 airfoil's experimental dynamic lift coefficient (incuding the bin average) and that predicted by means of different unsteay airfoil aerodynamic models for a Reynolds number of 100000. Geometric angle of attack mean, μ_{AoA}, and amplitude, A, are respectively equal to 3° and 0.5°, while frequency, f, is 2.00 Hz. In the figure, k denotes the reduced frequency.

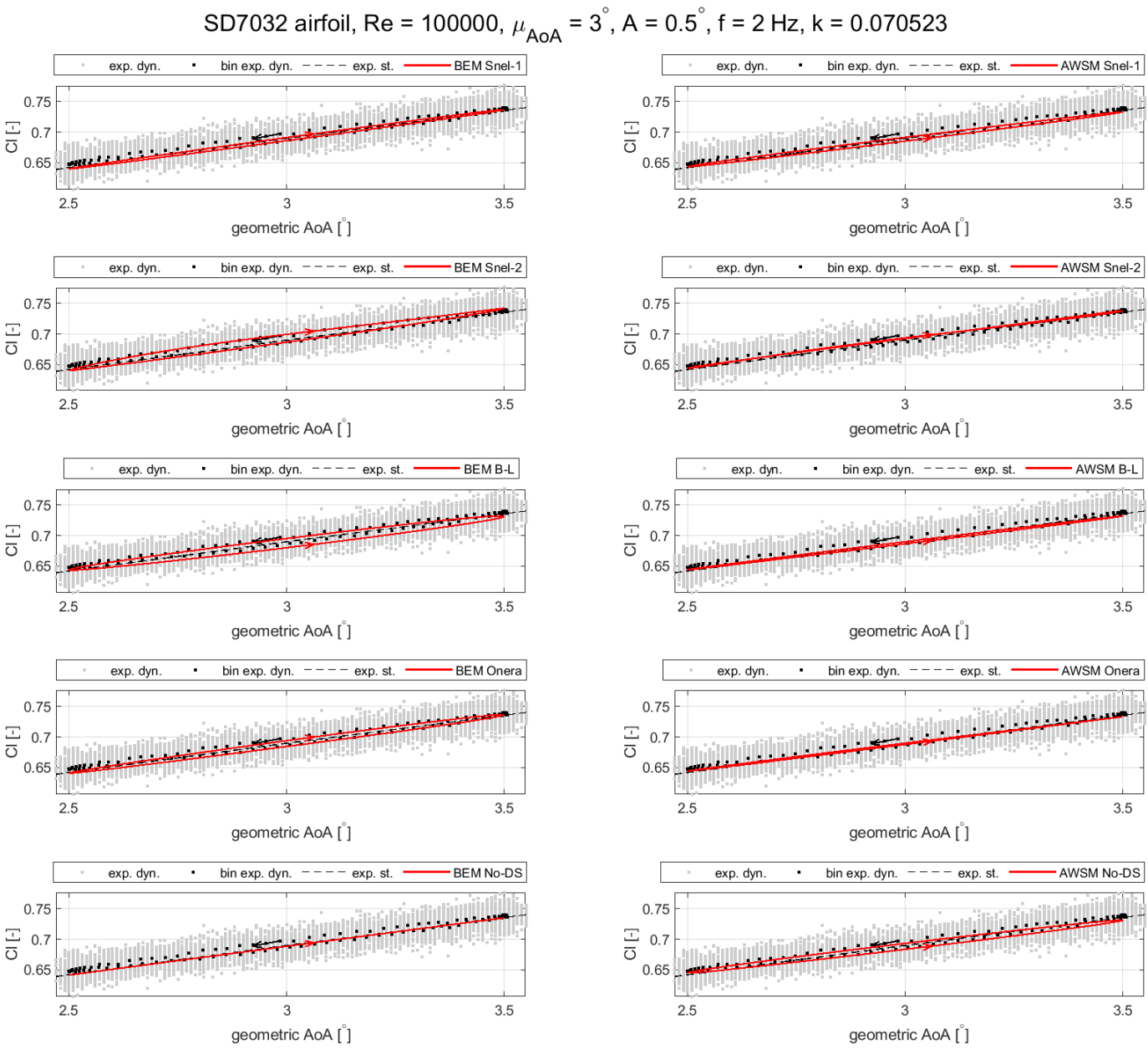

Figure A.18: Comparison between SD7032 airfoil's experimental dynamic lift coefficient (incuding the bin average) and that predicted by means of different unsteay airfoil aerodynamic models for a Reynolds number of 100000. Geometric angle of attack mean, μ_{AoA}, and amplitude, A, are respectively equal to 3° and 0.5°, while frequency, f, is 3.00 Hz. In the figure, k denotes the reduced frequency.

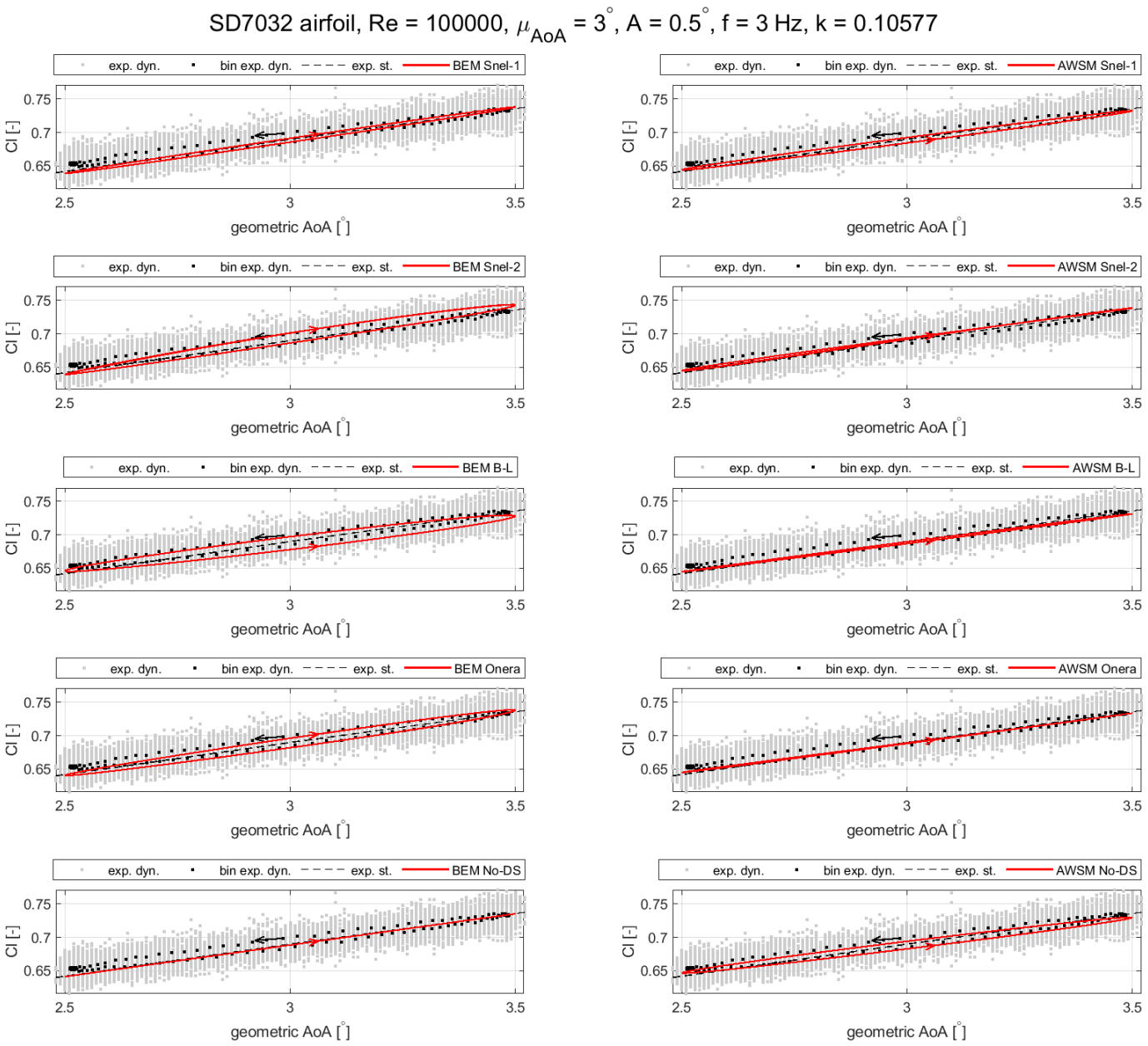

Figure A.19: Comparison between SD7032 airfoil's experimental dynamic lift coefficient (incuding the bin average) and that predicted by means of different unsteay airfoil aerodynamic models for a Reynolds number of 100000. Geometric angle of attack mean, μ_{AoA}, and amplitude, A, are respectively equal to 3° and 5.0°, while frequency, f, is 0.25 Hz. In the figure, k denotes the reduced frequency.

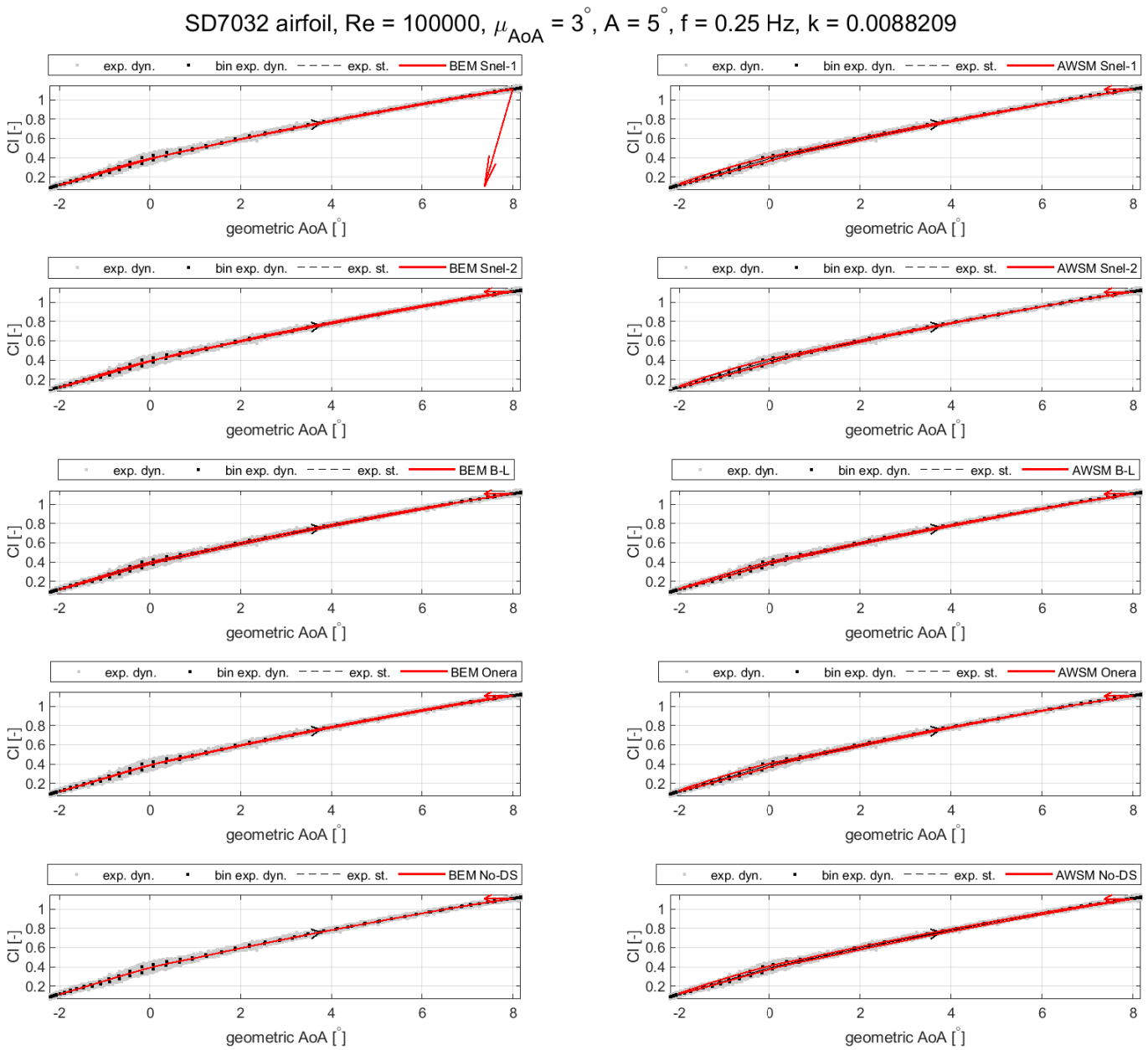

Figure A.20: Comparison between SD7032 airfoil's experimental dynamic lift coefficient (incuding the bin average) and that predicted by means of different unsteay airfoil aerodynamic models for a Reynolds number of 100000. Geometric angle of attack mean, μ_{AoA}, and amplitude, A, are respectively equal to 3° and 5.0°, while frequency, f, is 0.50 Hz. In the figure, k denotes the reduced frequency.

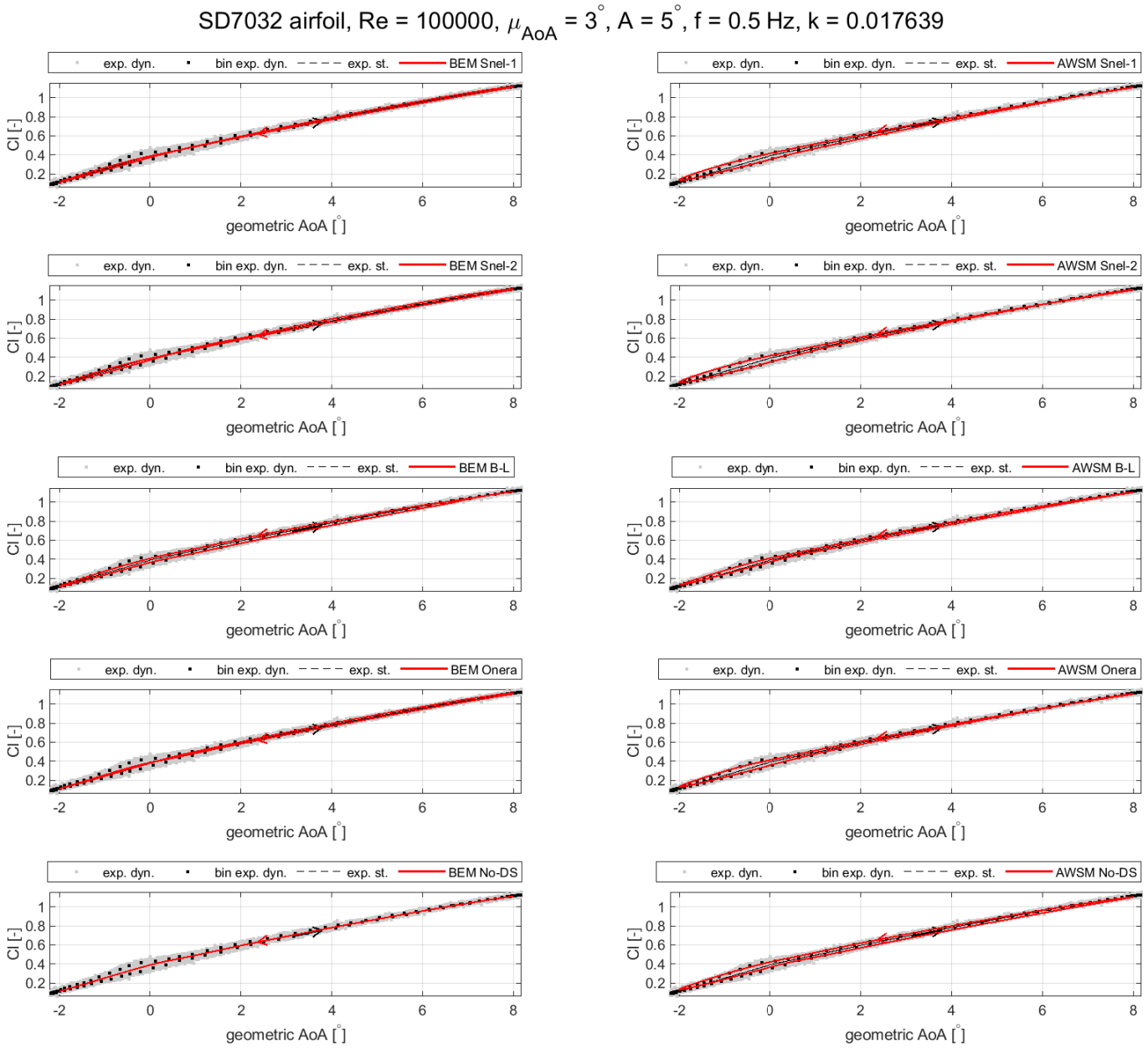

Figure A.21: Comparison between SD7032 airfoil's experimental dynamic lift coefficient (incuding the bin average) and that predicted by means of different unsteay airfoil aerodynamic models for a Reynolds number of 100000. Geometric angle of attack mean, μ_{AoA}, and amplitude, A, are respectively equal to 3° and 5.0°, while frequency, f, is 1.50 Hz. In the figure, k denotes the reduced frequency.

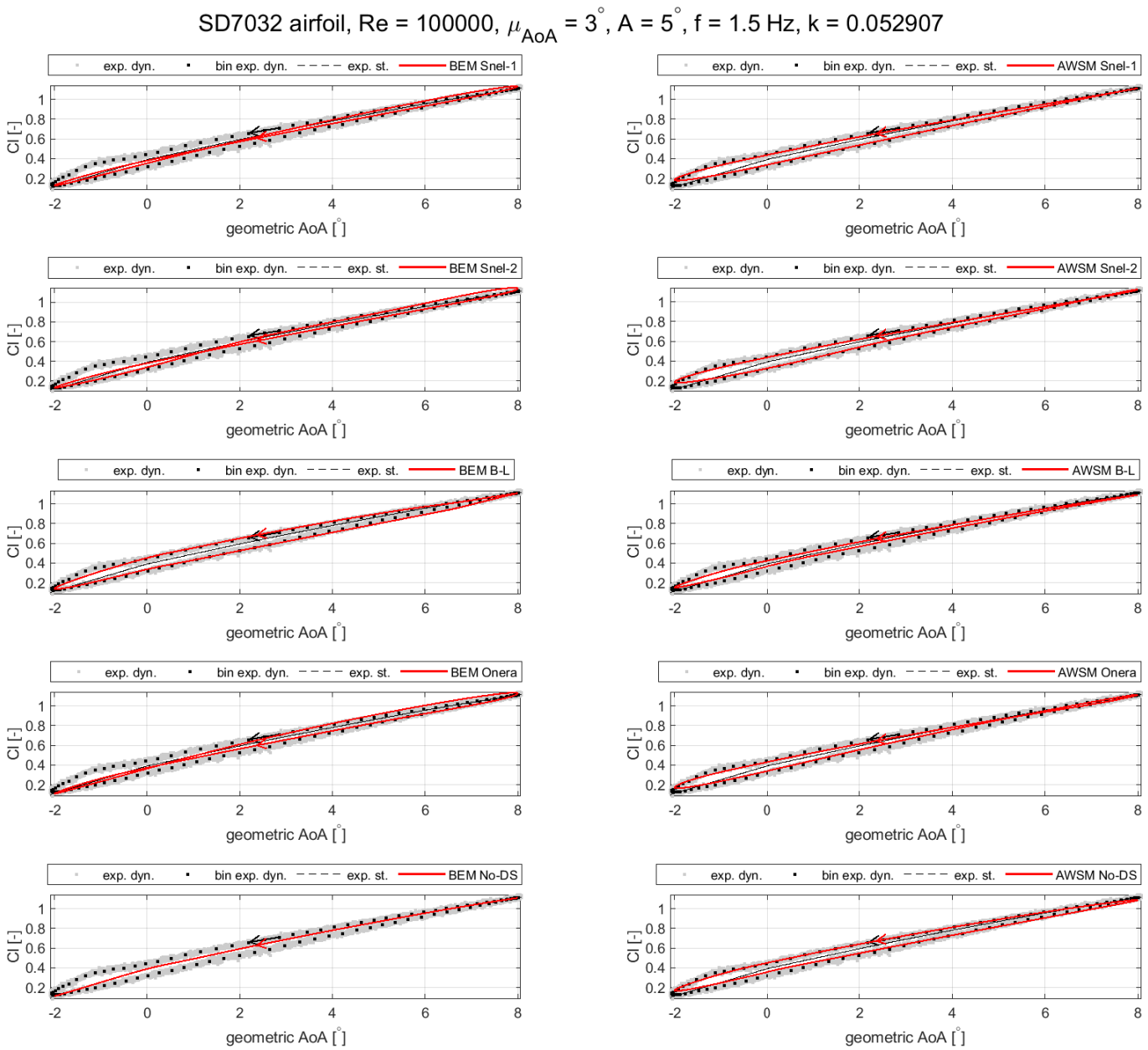

Figure A.22: Comparison between SD7032 airfoil's experimental dynamic lift coefficient (incuding the bin average) and that predicted by means of different unsteay airfoil aerodynamic models for a Reynolds number of 100000. Geometric angle of attack mean, μ_{AoA}, and amplitude, A, are respectively equal to 3° and 5.0°, while frequency, f, is 1.00 Hz. In the figure, k denotes the reduced frequency.

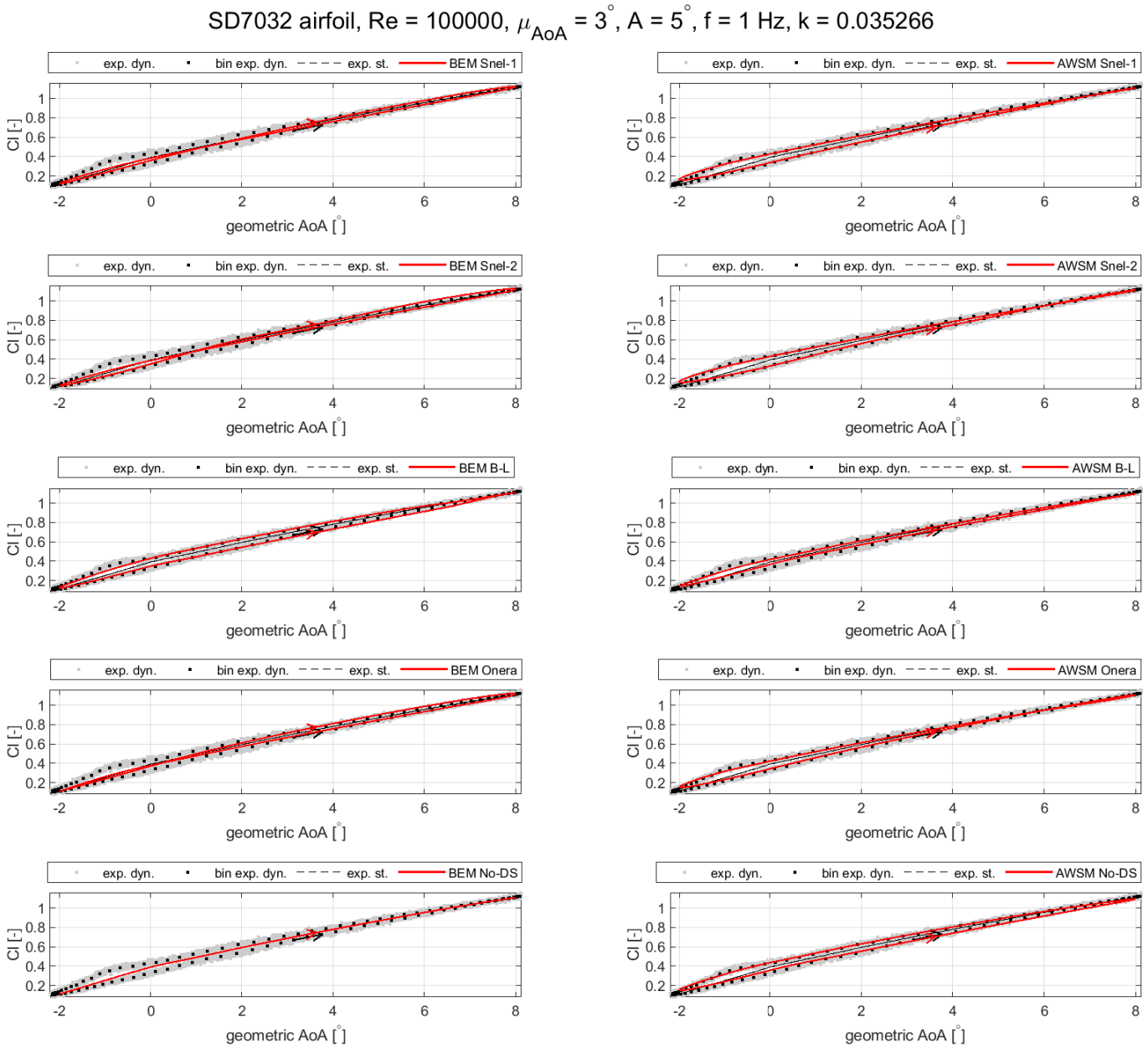

Figure A.23: Comparison between SD7032 airfoil's experimental dynamic lift coefficient (incuding the bin average) and that predicted by means of different unsteay airfoil aerodynamic models for a Reynolds number of 100000. Geometric angle of attack mean, μ_{AoA}, and amplitude, A, are respectively equal to 3° and 5.0°, while frequency, f, is 2.00 Hz. In the figure, k denotes the reduced frequency.

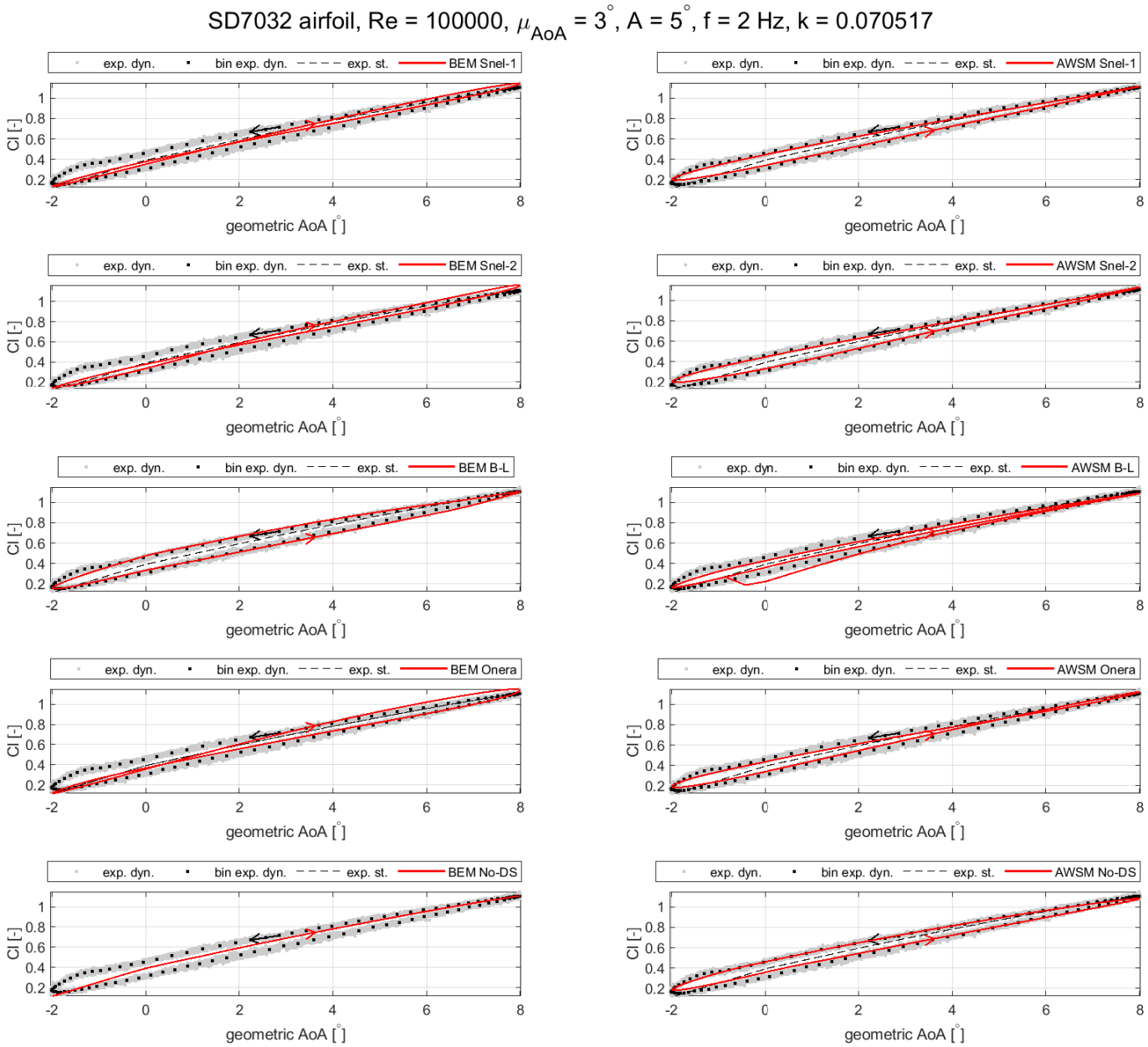

Figure A.24: Comparison between SD7032 airfoil's experimental dynamic lift coefficient (incuding the bin average) and that predicted by means of different unsteay airfoil aerodynamic models for a Reynolds number of 100000. Geometric angle of attack mean, μ_{AoA}, and amplitude, A, are respectively equal to 3° and 5.0°, while frequency, f, is 3.00 Hz. In the figure, k denotes the reduced frequency.

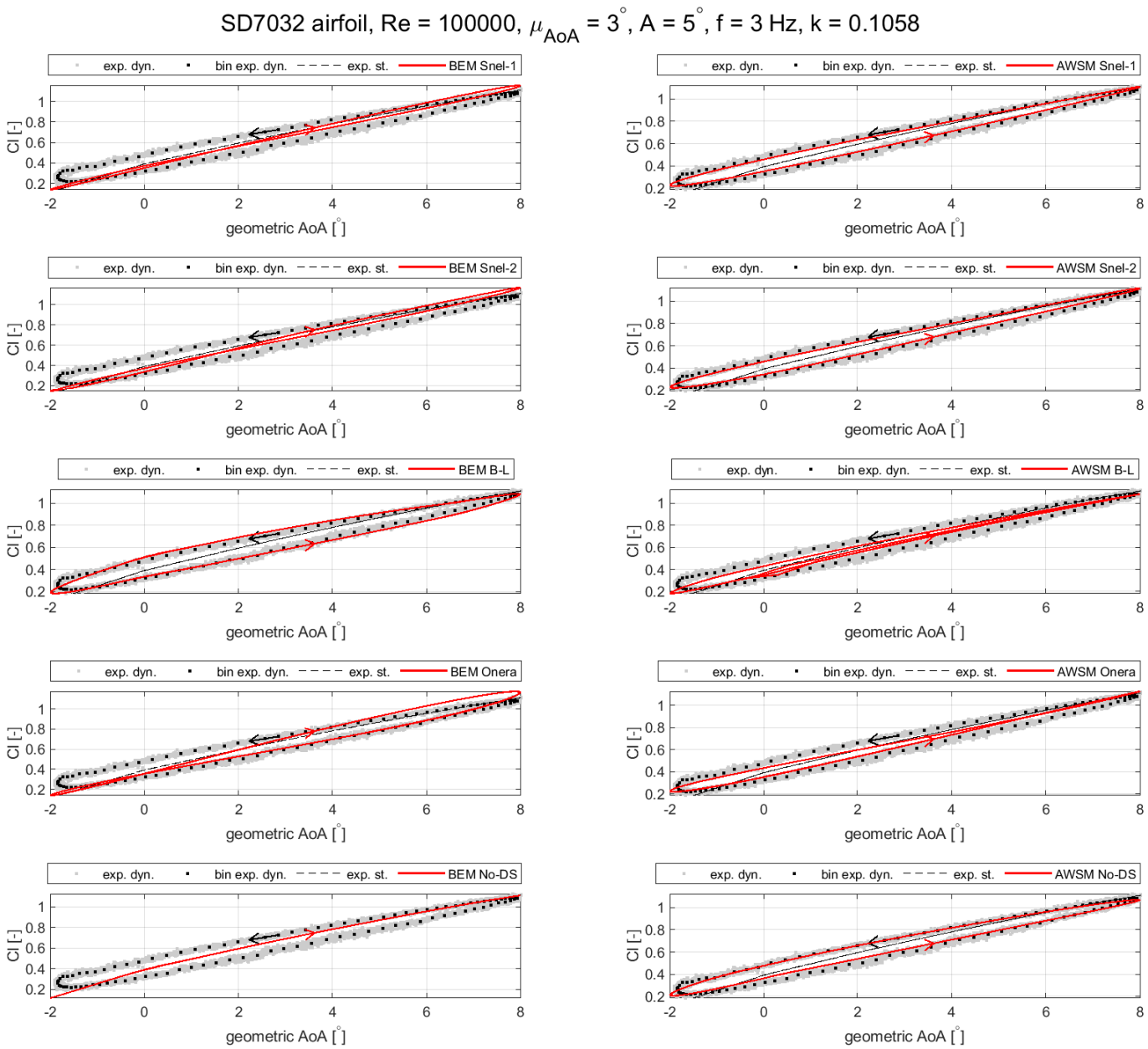

Figure A.25: Comparison between SD7032 airfoil's experimental dynamic lift coefficient (incuding the bin average) and that predicted by means of different unsteay airfoil aerodynamic models for a Reynolds number of 100000. Geometric angle of attack mean, μ_{AoA}, and amplitude, A, are respectively equal to 6° and 0.5°, while frequency, f, is 0.25 Hz. In the figure, k denotes the reduced frequency.

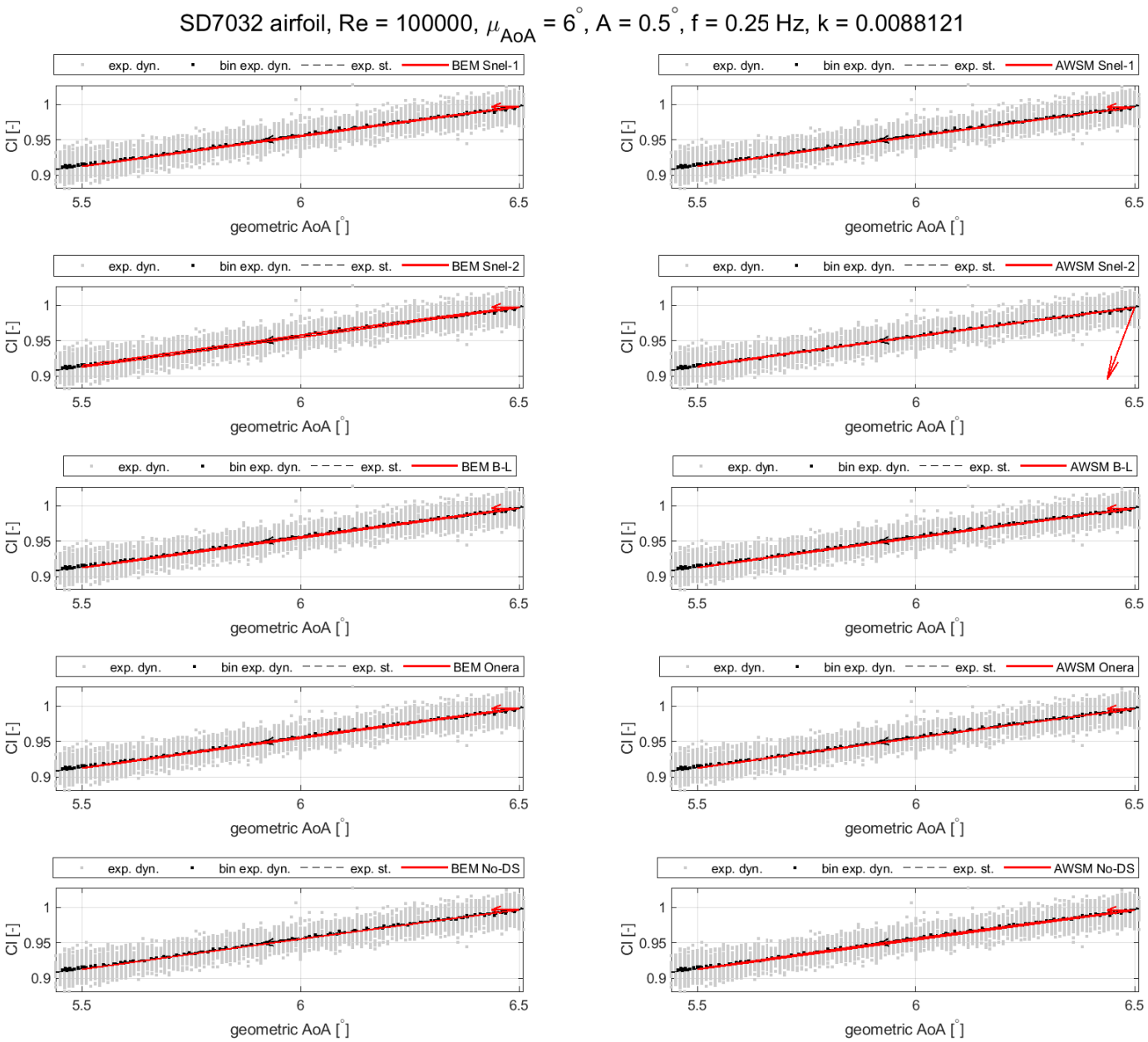

Figure A.26: Comparison between SD7032 airfoil's experimental dynamic lift coefficient (incuding the bin average) and that predicted by means of different unsteay airfoil aerodynamic models for a Reynolds number of 100000. Geometric angle of attack mean, μ_{AoA}, and amplitude, A, are respectively equal to 6° and 0.5°, while frequency, f, is 0.50 Hz. In the figure, k denotes the reduced frequency.

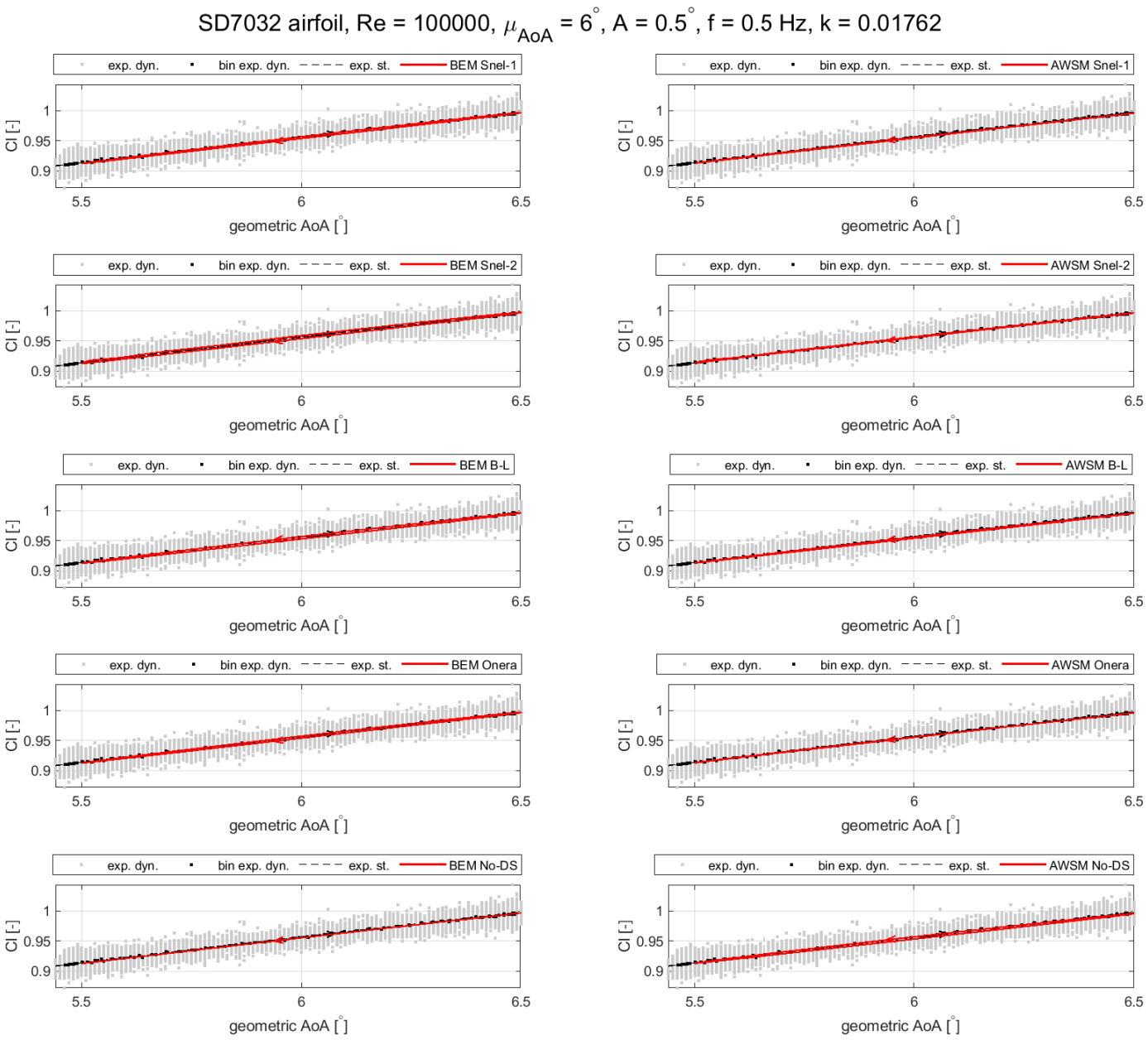

Figure A.27: Comparison between SD7032 airfoil's experimental dynamic lift coefficient (incuding the bin average) and that predicted by means of different unsteay airfoil aerodynamic models for a Reynolds number of 100000. Geometric angle of attack mean, μ_{AoA}, and amplitude, A, are respectively equal to 6° and 0.5°, while frequency, f, is 1.50 Hz. In the figure, k denotes the reduced frequency.

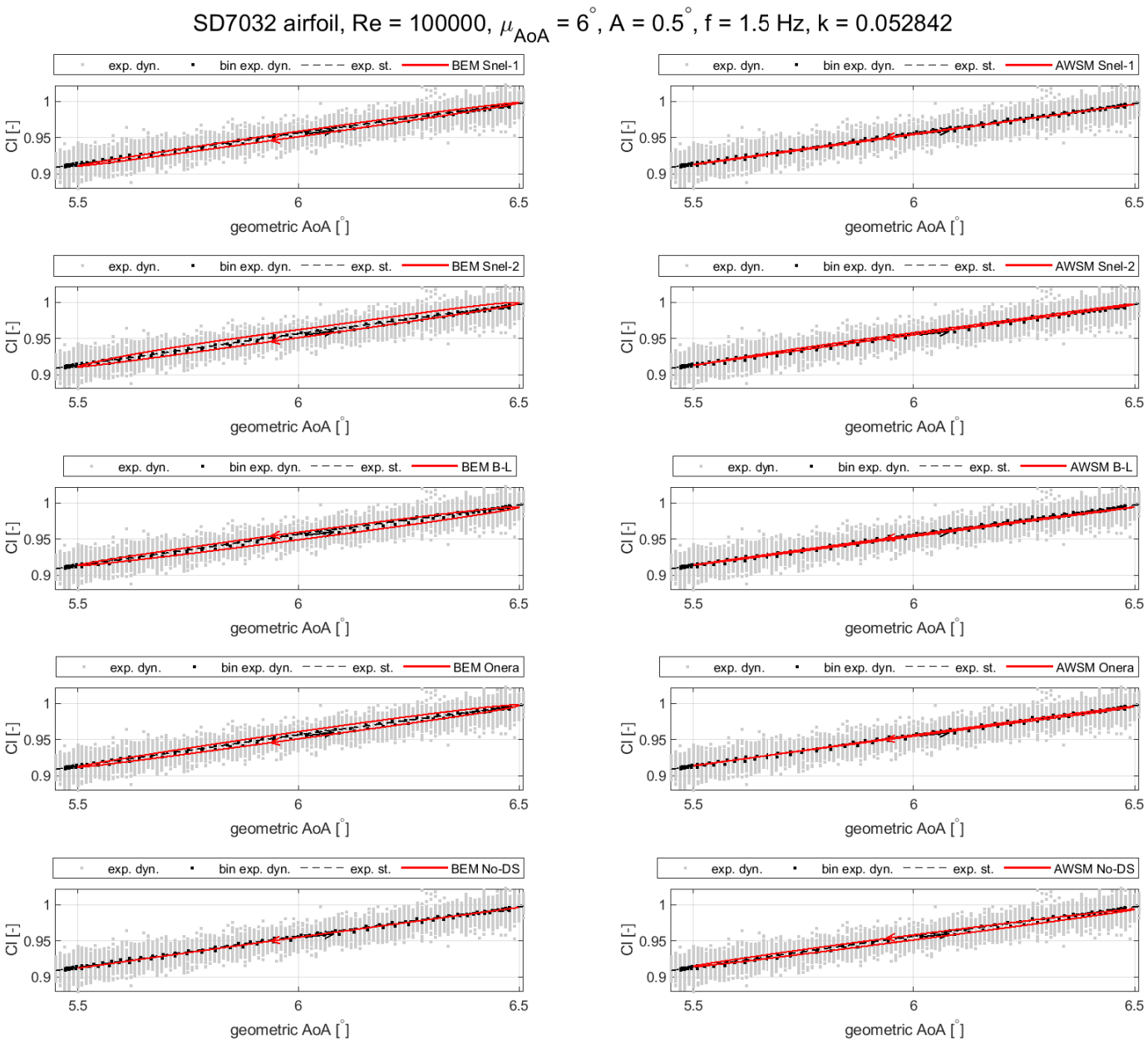

Figure A.28: Comparison between SD7032 airfoil's experimental dynamic lift coefficient (incuding the bin average) and that predicted by means of different unsteay airfoil aerodynamic models for a Reynolds number of 100000. Geometric angle of attack mean, μ_{AoA}, and amplitude, A, are respectively equal to 6° and 0.5°, while frequency, f, is 1.00 Hz. In the figure, k denotes the reduced frequency.

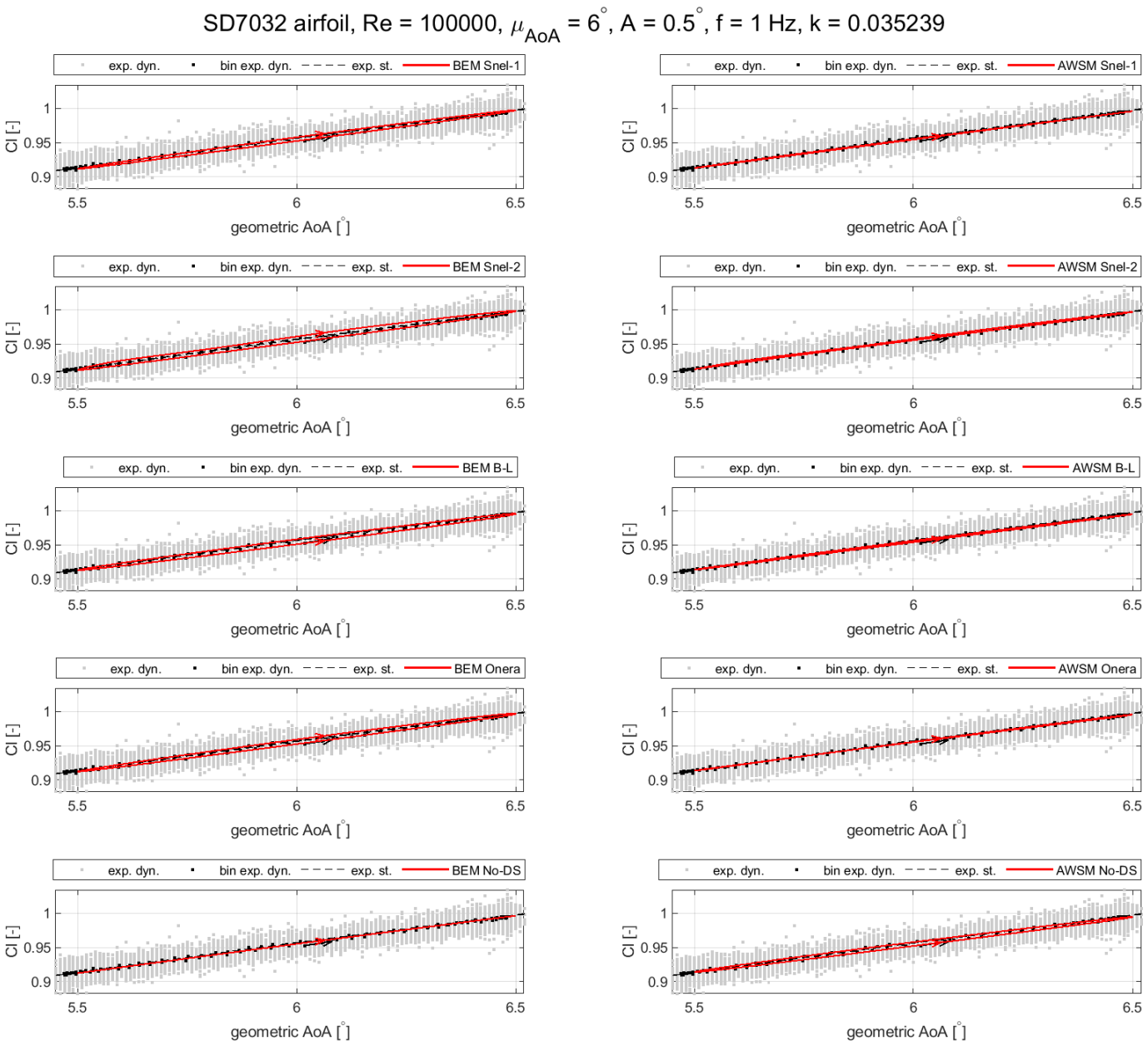

Figure A.29: Comparison between SD7032 airfoil's experimental dynamic lift coefficient (incuding the bin average) and that predicted by means of different unsteay airfoil aerodynamic models for a Reynolds number of 100000. Geometric angle of attack mean, μ_{AoA}, and amplitude, A, are respectively equal to 6° and 0.5°, while frequency, f, is 2.00 Hz. In the figure, k denotes the reduced frequency.

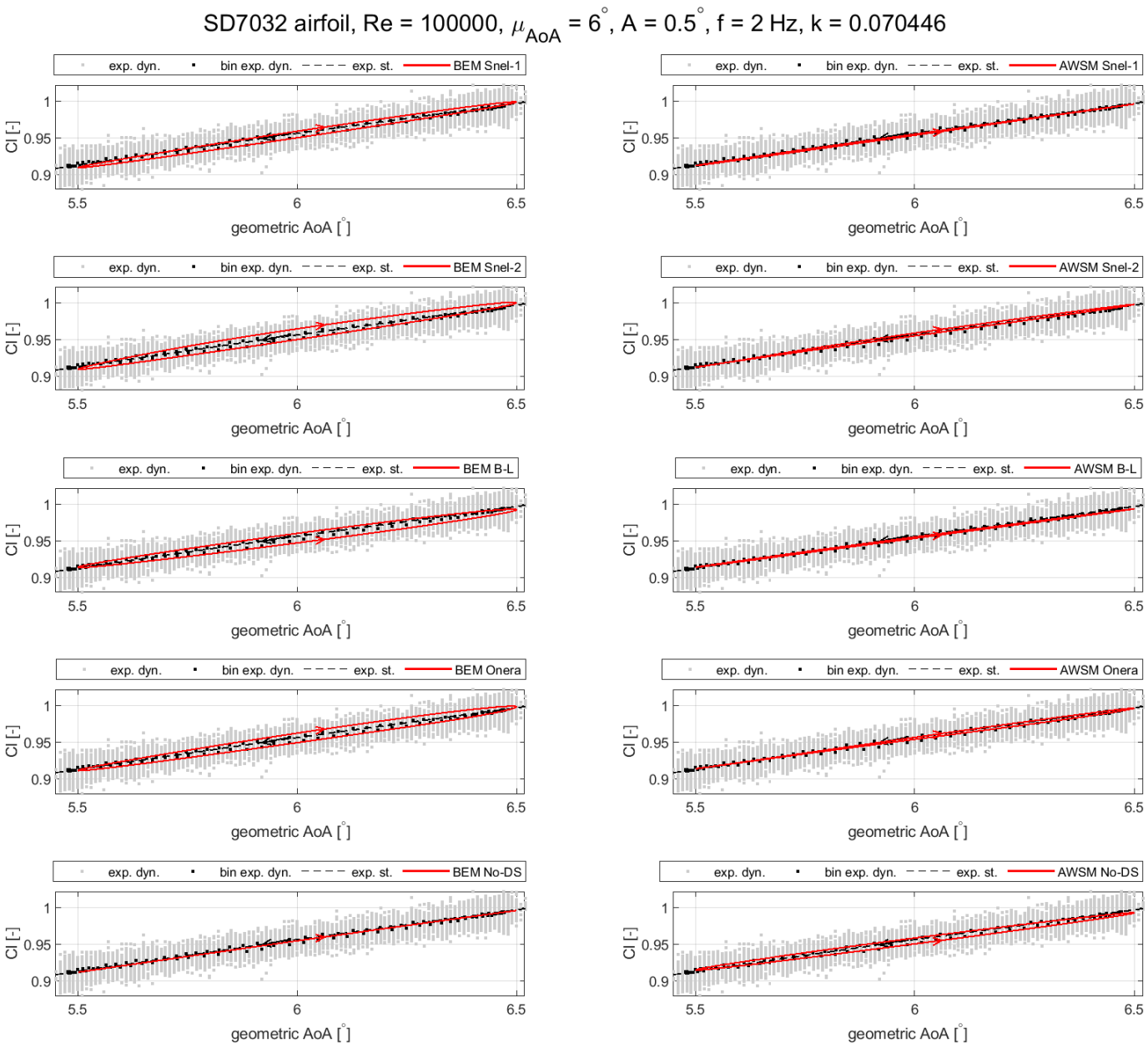

Figure A.30: Comparison between SD7032 airfoil's experimental dynamic lift coefficient (incuding the bin average) and that predicted by means of different unsteay airfoil aerodynamic models for a Reynolds number of 100000. Geometric angle of attack mean, μ_{AoA}, and amplitude, A, are respectively equal to 6° and 0.5°, while frequency, f, is 3.00 Hz. In the figure, k denotes the reduced frequency.

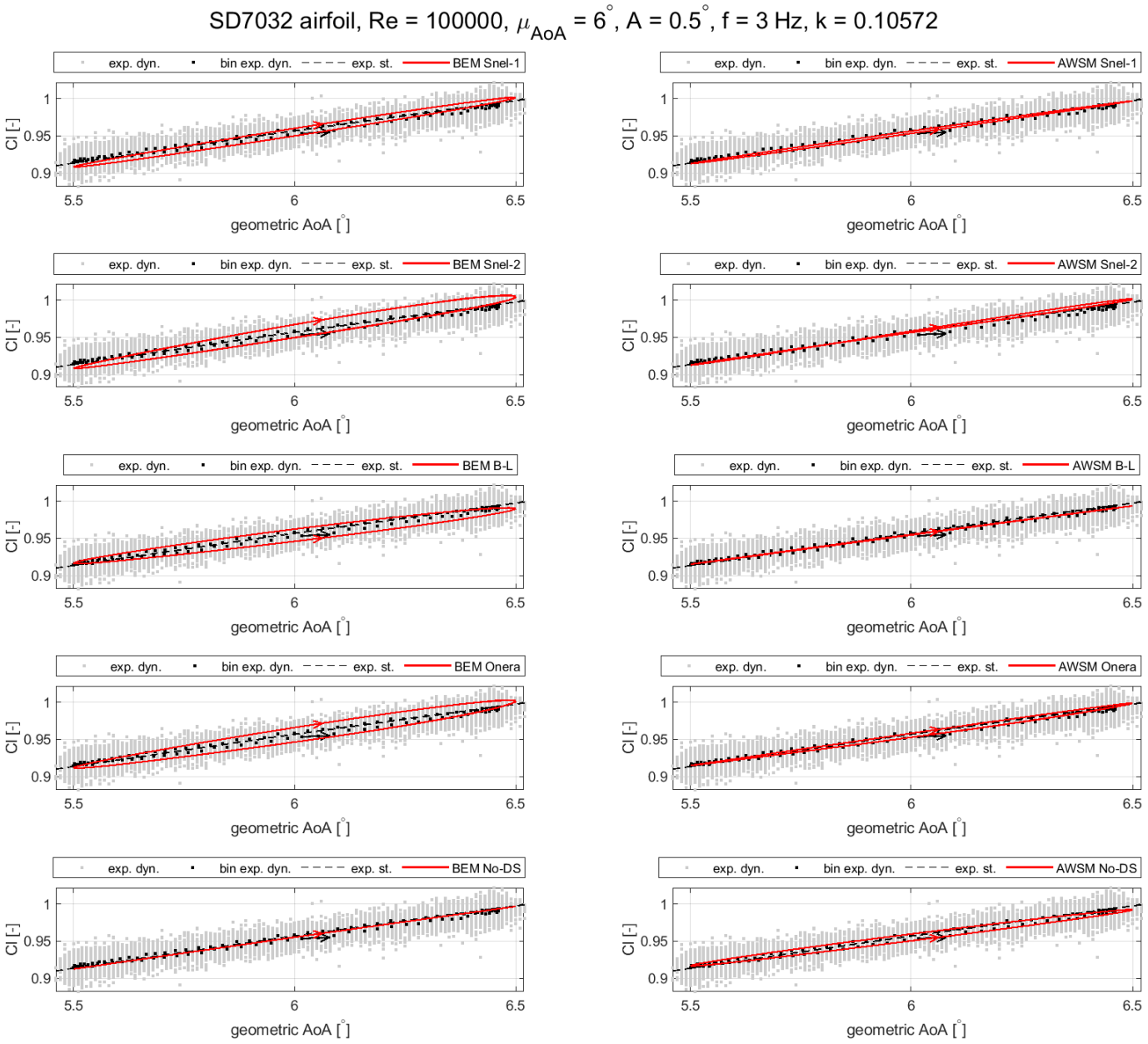

Figure A.31: Comparison between SD7032 airfoil's experimental dynamic lift coefficient (incuding the bin average) and that predicted by means of different unsteay airfoil aerodynamic models for a Reynolds number of 100000. Geometric angle of attack mean, μ_{AoA}, and amplitude, A, are respectively equal to 6° and 5.0°, while frequency, f, is 0.25 Hz. In the figure, k denotes the reduced frequency.

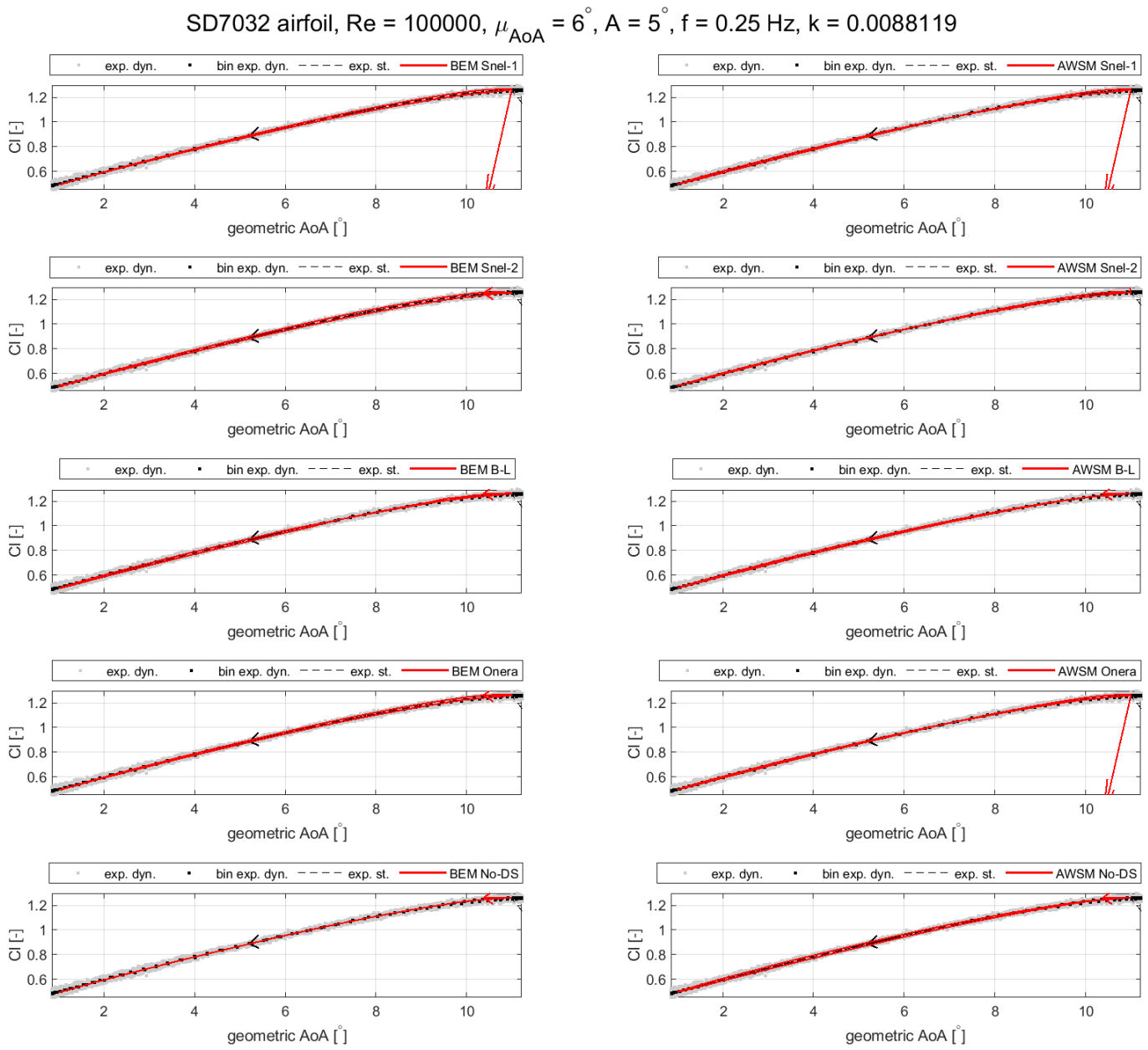

Figure A.32: Comparison between SD7032 airfoil's experimental dynamic lift coefficient (incuding the bin average) and that predicted by means of different unsteay airfoil aerodynamic models for a Reynolds number of 100000. Geometric angle of attack mean, μ_{AoA}, and amplitude, A, are respectively equal to 6° and 5.0°, while frequency, f, is 0.50 Hz. In the figure, k denotes the reduced frequency.

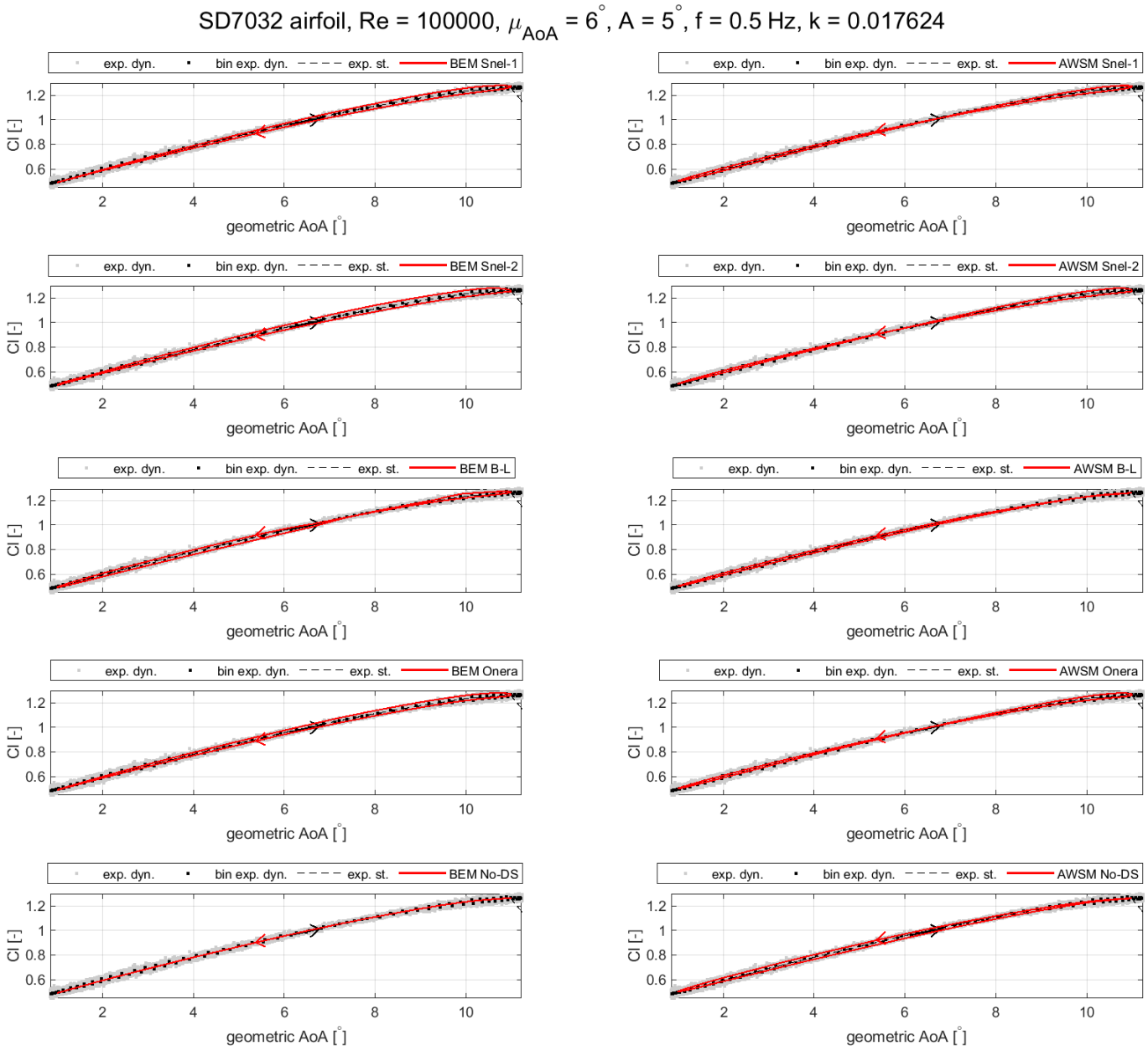

Figure A.33: Comparison between SD7032 airfoil's experimental dynamic lift coefficient (incuding the bin average) and that predicted by means of different unsteay airfoil aerodynamic models for a Reynolds number of 100000. Geometric angle of attack mean, μ_{AoA}, and amplitude, A, are respectively equal to 6° and 5.0°, while frequency, f, is 1.50 Hz. In the figure, k denotes the reduced frequency.

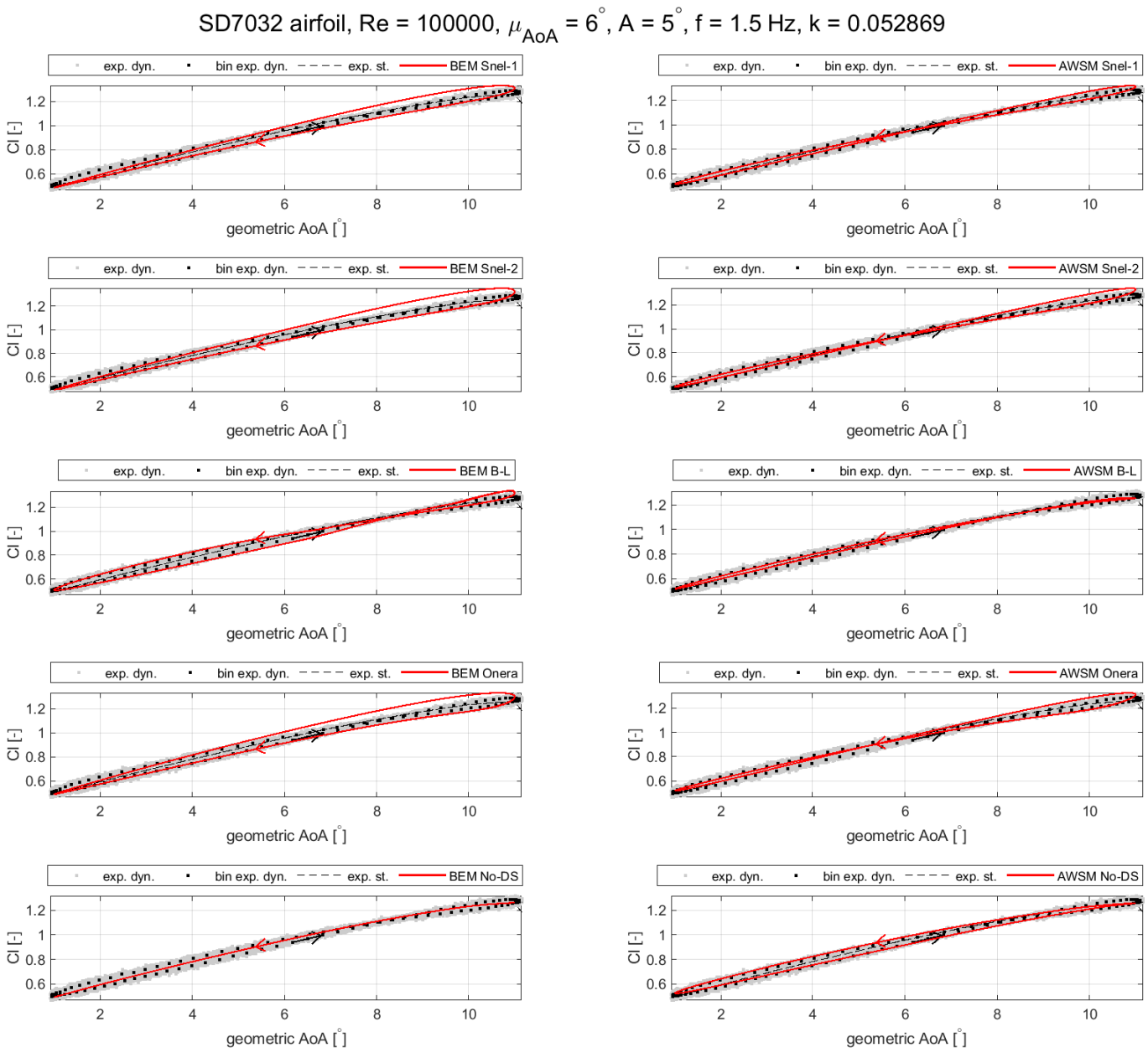

Figure A.34: Comparison between SD7032 airfoil's experimental dynamic lift coefficient (incuding the bin average) and that predicted by means of different unsteay airfoil aerodynamic models for a Reynolds number of 100000. Geometric angle of attack mean, μ_{AoA}, and amplitude, A, are respectively equal to 6° and 5.0°, while frequency, f, is 1.00 Hz. In the figure, k denotes the reduced frequency.

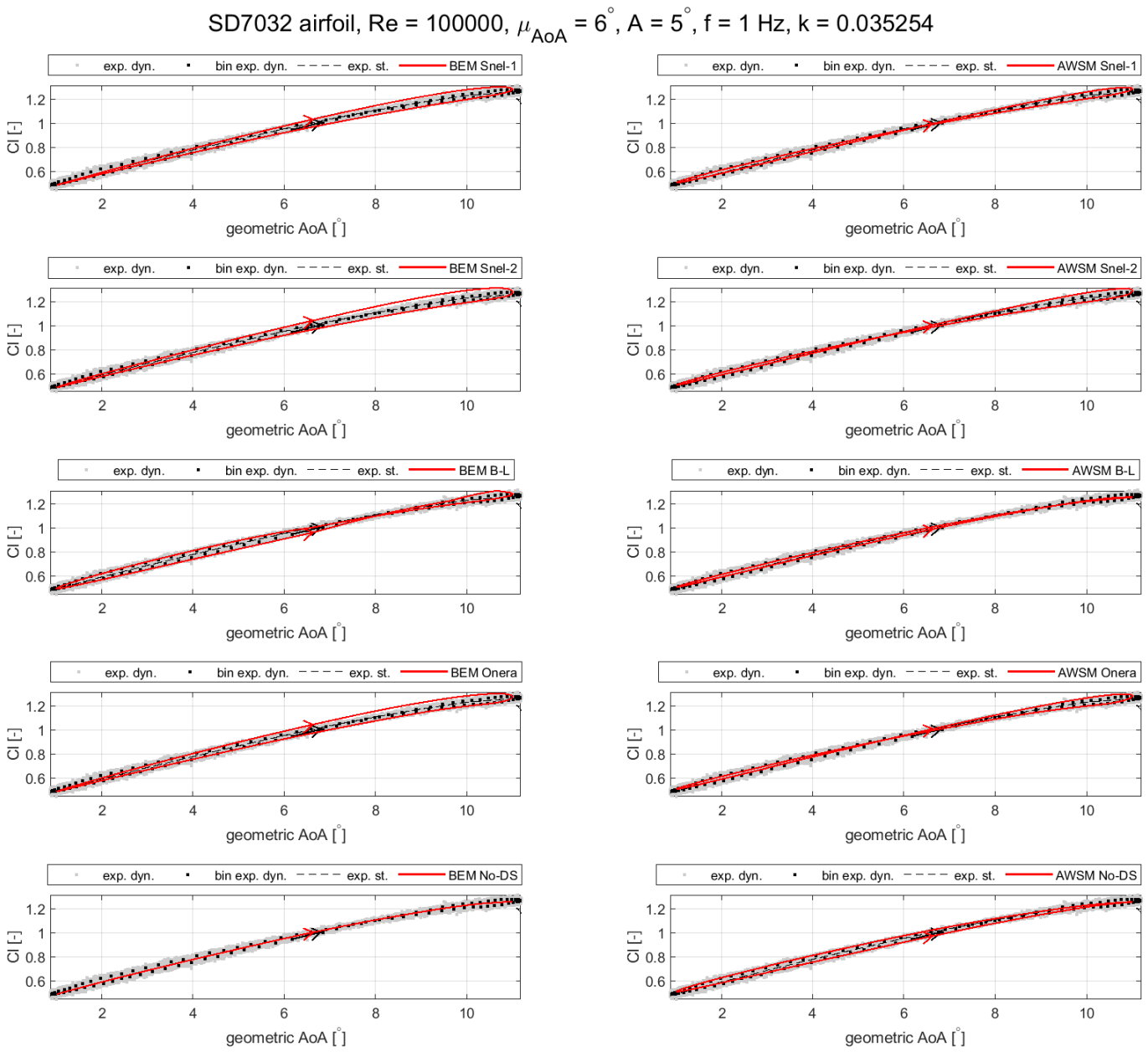

Figure A.35: Comparison between SD7032 airfoil's experimental dynamic lift coefficient (incuding the bin average) and that predicted by means of different unsteay airfoil aerodynamic models for a Reynolds number of 100000. Geometric angle of attack mean, μ_{AoA}, and amplitude, A, are respectively equal to 6° and 5.0°, while frequency, f, is 2.00 Hz. In the figure, k denotes the reduced frequency.

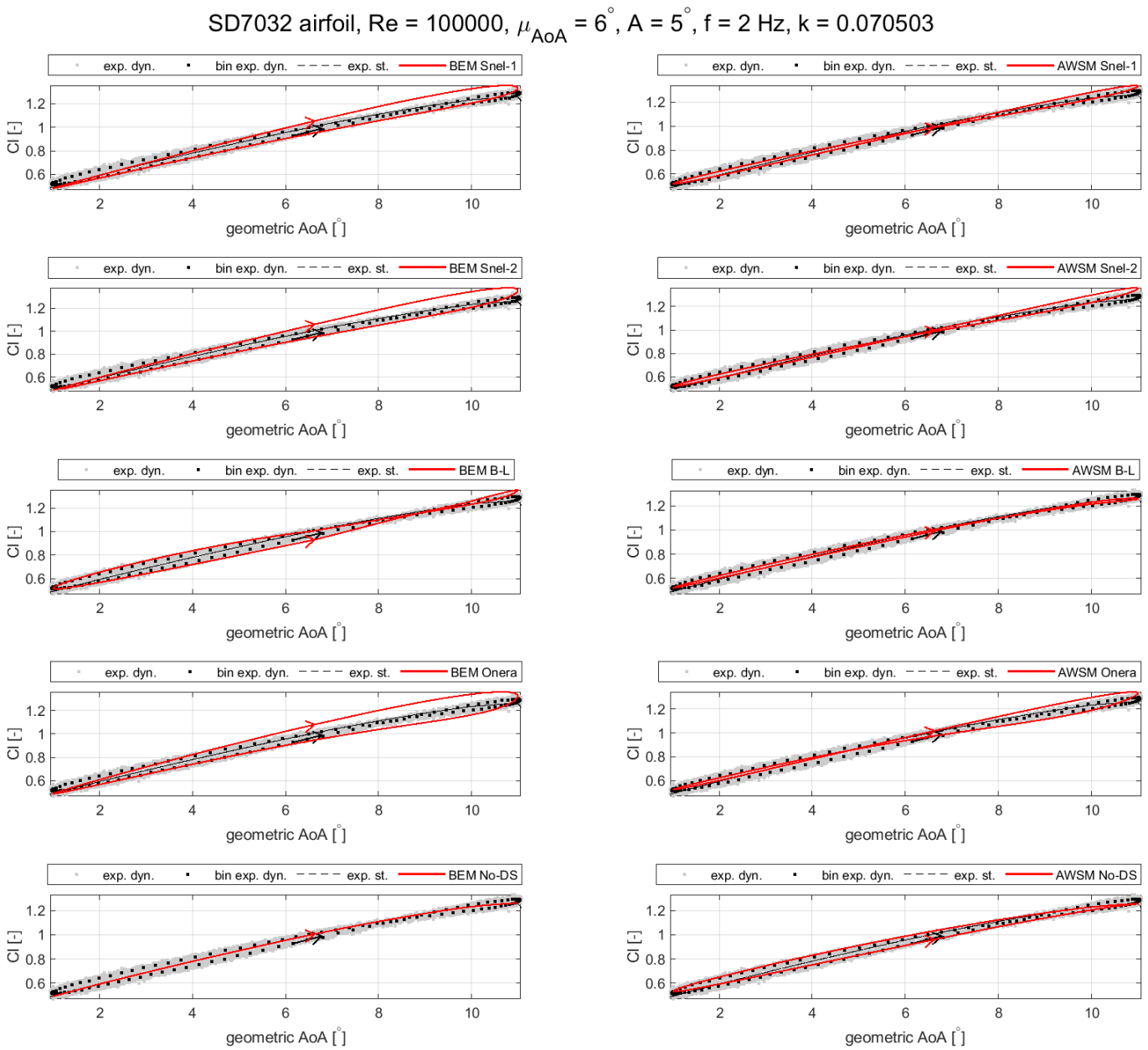

Figure A.36: Comparison between SD7032 airfoil's experimental dynamic lift coefficient (incuding the bin average) and that predicted by means of different unsteay airfoil aerodynamic models for a Reynolds number of 100000. Geometric angle of attack mean, μ_{AoA}, and amplitude, A, are respectively equal to 6° and 5.0°, while frequency, f, is 3.00 Hz. In the figure, k denotes the reduced frequency.

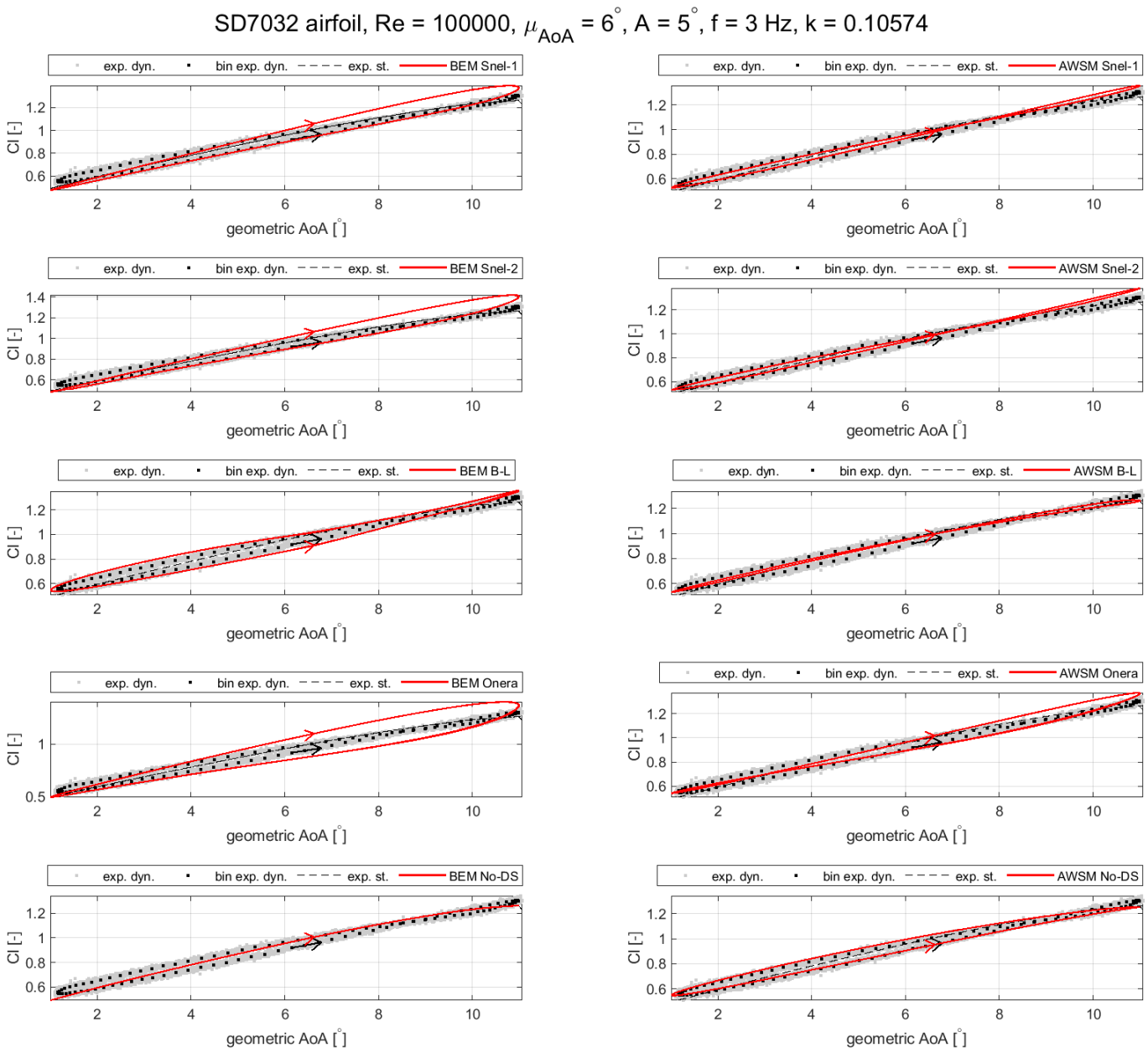

Figure A.37: Comparison between SD7032 airfoil's experimental dynamic lift coefficient (incuding the bin average) and that predicted by means of different unsteay airfoil aerodynamic models for a Reynolds number of 100000. Geometric angle of attack mean, μ_{AoA}, and amplitude, A, are respectively equal to 9° and 0.5°, while frequency, f, is 0.25 Hz. In the figure, k denotes the reduced frequency.

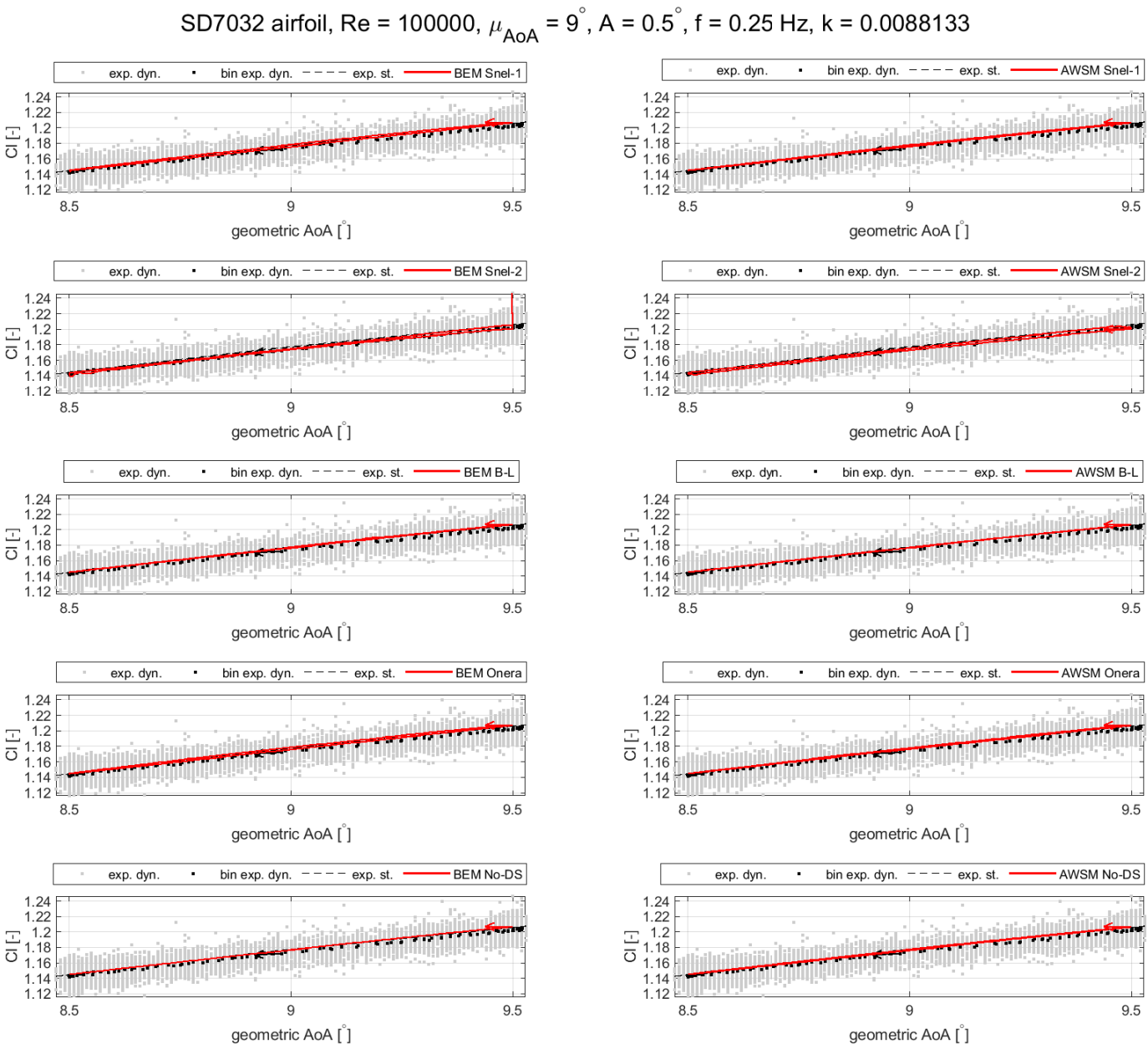

Figure A.38: Comparison between SD7032 airfoil's experimental dynamic lift coefficient (incuding the bin average) and that predicted by means of different unsteay airfoil aerodynamic models for a Reynolds number of 100000. Geometric angle of attack mean, μ_{AoA}, and amplitude, A, are respectively equal to 9° and 0.5°, while frequency, f, is 0.50 Hz. In the figure, k denotes the reduced frequency.

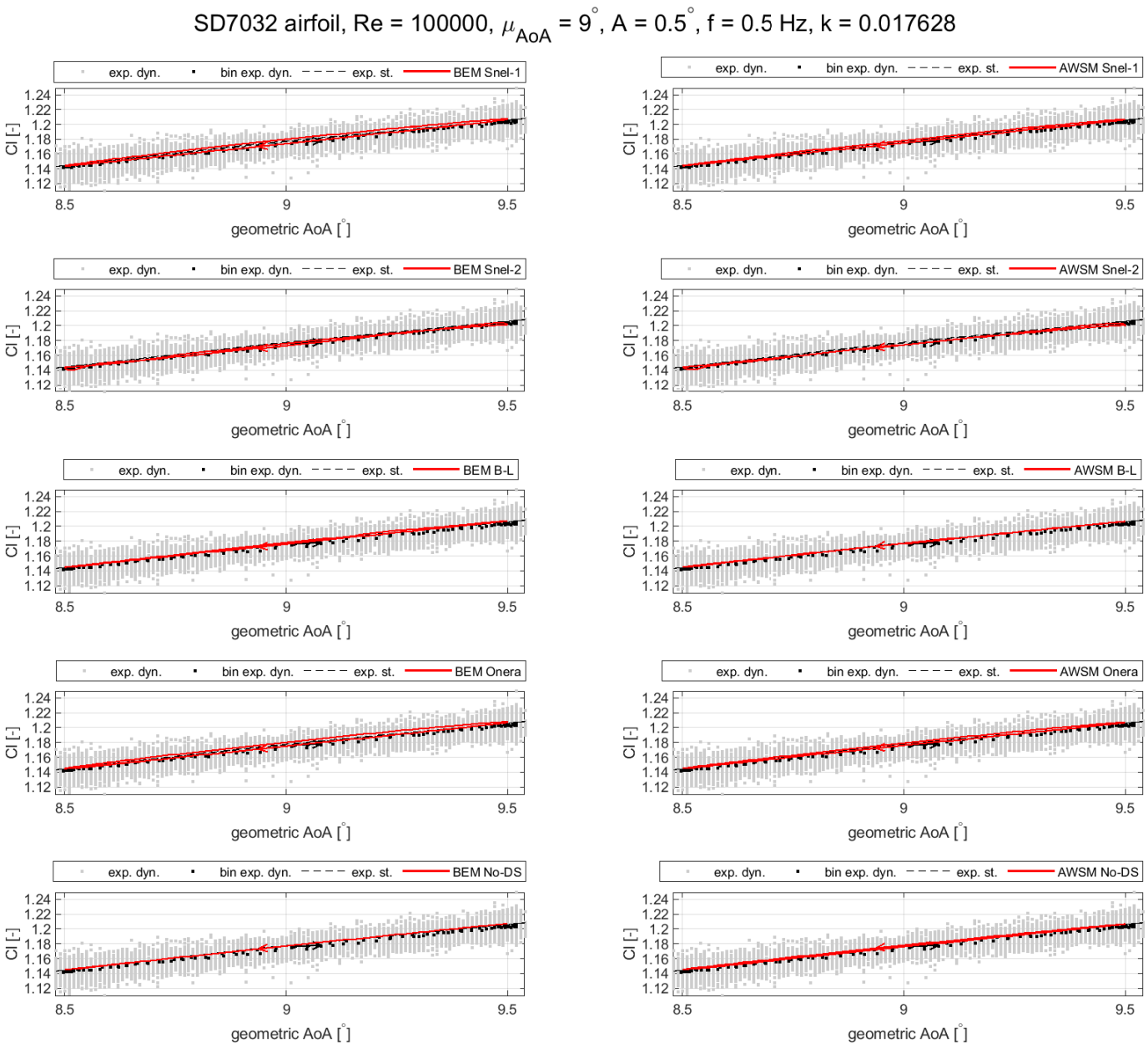

Figure A.39: Comparison between SD7032 airfoil's experimental dynamic lift coefficient (incuding the bin average) and that predicted by means of different unsteay airfoil aerodynamic models for a Reynolds number of 100000. Geometric angle of attack mean, μ_{AoA}, and amplitude, A, are respectively equal to 9° and 0.5°, while frequency, f, is 1.50 Hz. In the figure, k denotes the reduced frequency.

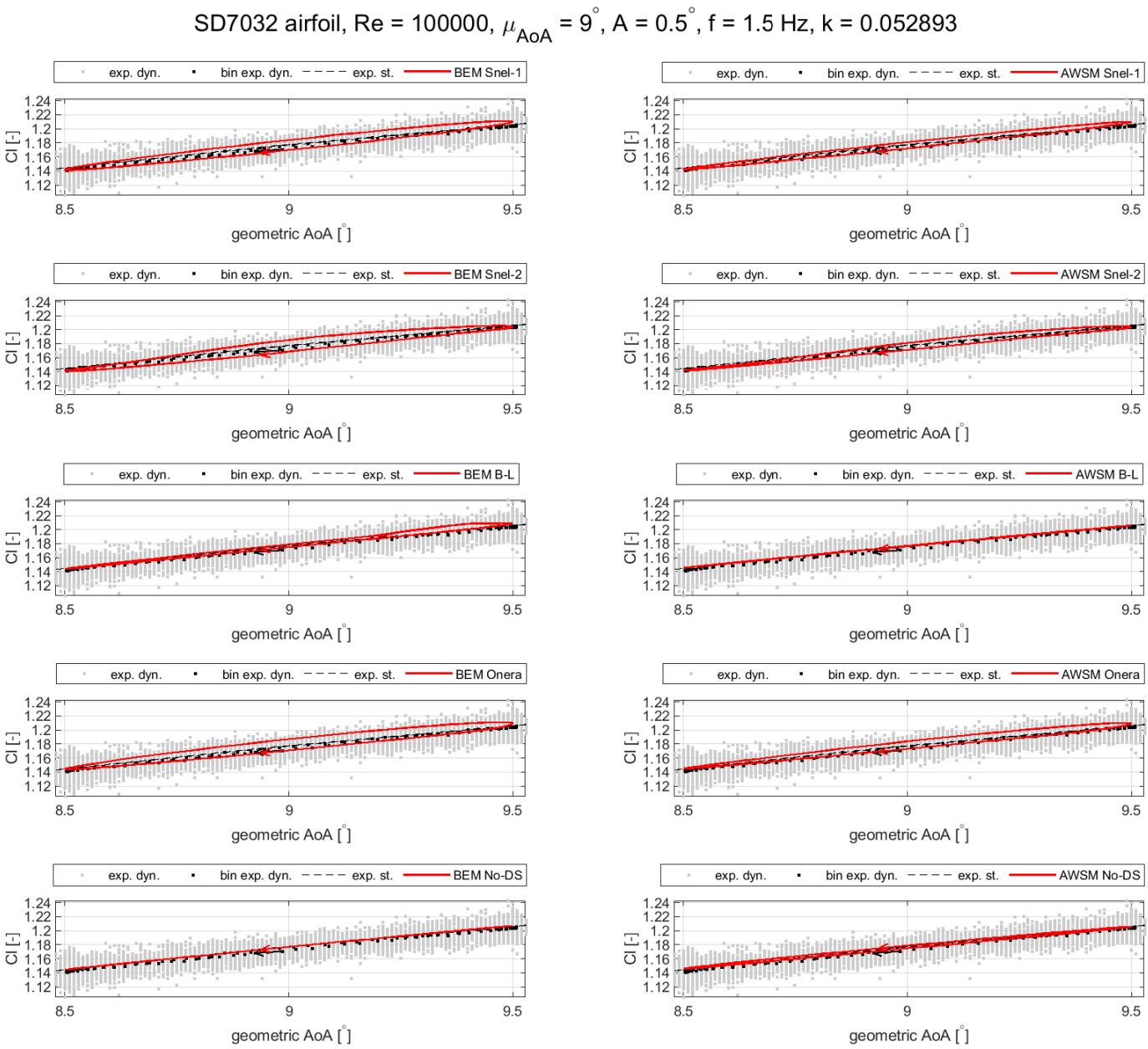

Figure A.40: Comparison between SD7032 airfoil's experimental dynamic lift coefficient (incuding the bin average) and that predicted by means of different unsteay airfoil aerodynamic models for a Reynolds number of 100000. Geometric angle of attack mean, μ_{AoA}, and amplitude, A, are respectively equal to 9° and 0.5°, while frequency, f, is 1.00 Hz. In the figure, k denotes the reduced frequency.

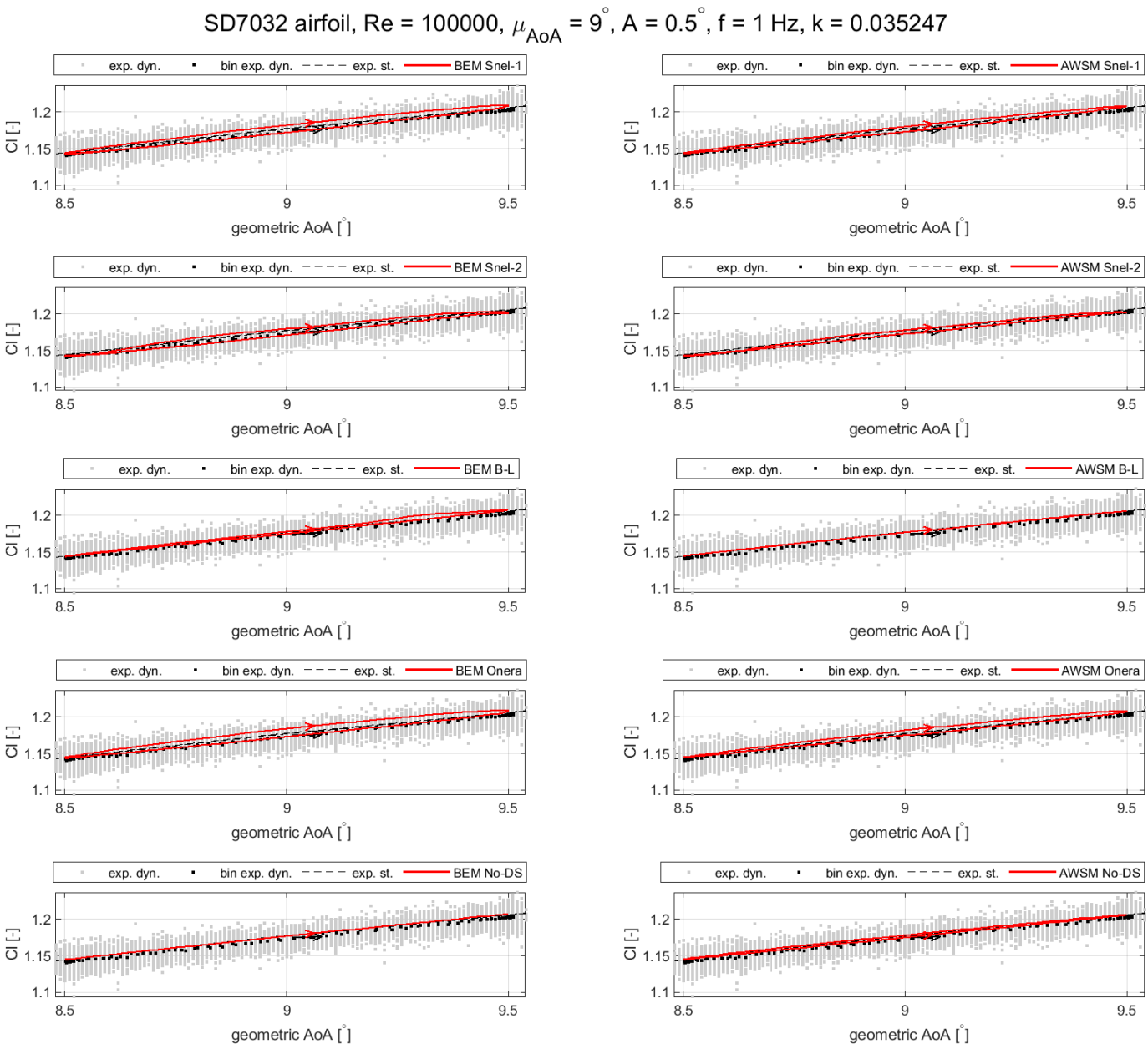

Figure A.41: Comparison between SD7032 airfoil's experimental dynamic lift coefficient (incuding the bin average) and that predicted by means of different unsteay airfoil aerodynamic models for a Reynolds number of 100000. Geometric angle of attack mean, μ_{AoA}, and amplitude, A, are respectively equal to 9° and 0.5°, while frequency, f, is 2.00 Hz. In the figure, k denotes the reduced frequency.

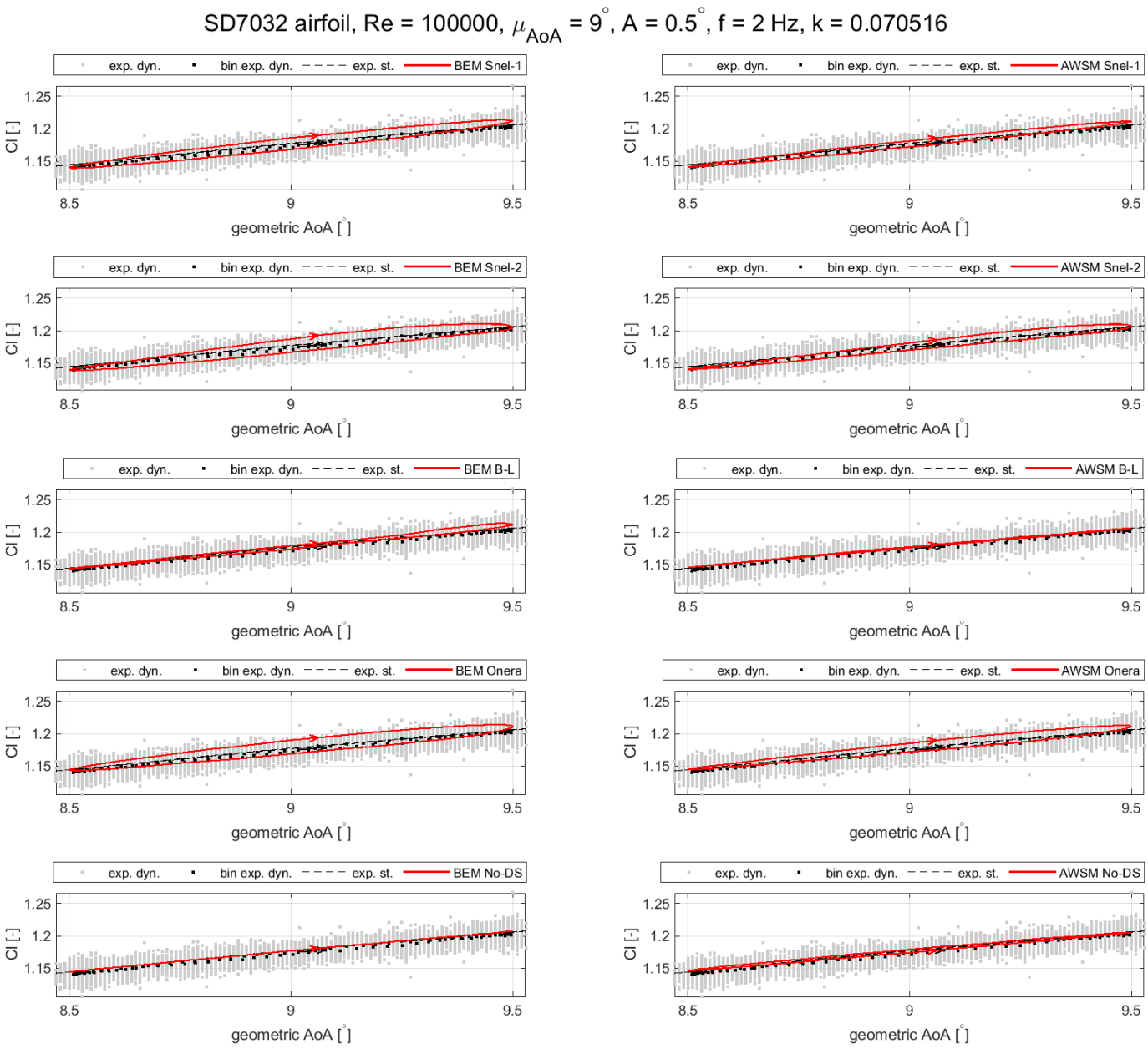

Figure A.42: Comparison between SD7032 airfoil's experimental dynamic lift coefficient (incuding the bin average) and that predicted by means of different unsteay airfoil aerodynamic models for a Reynolds number of 100000. Geometric angle of attack mean, μ_{AoA}, and amplitude, A, are respectively equal to 9° and 0.5°, while frequency, f, is 3.00 Hz. In the figure, k denotes the reduced frequency.

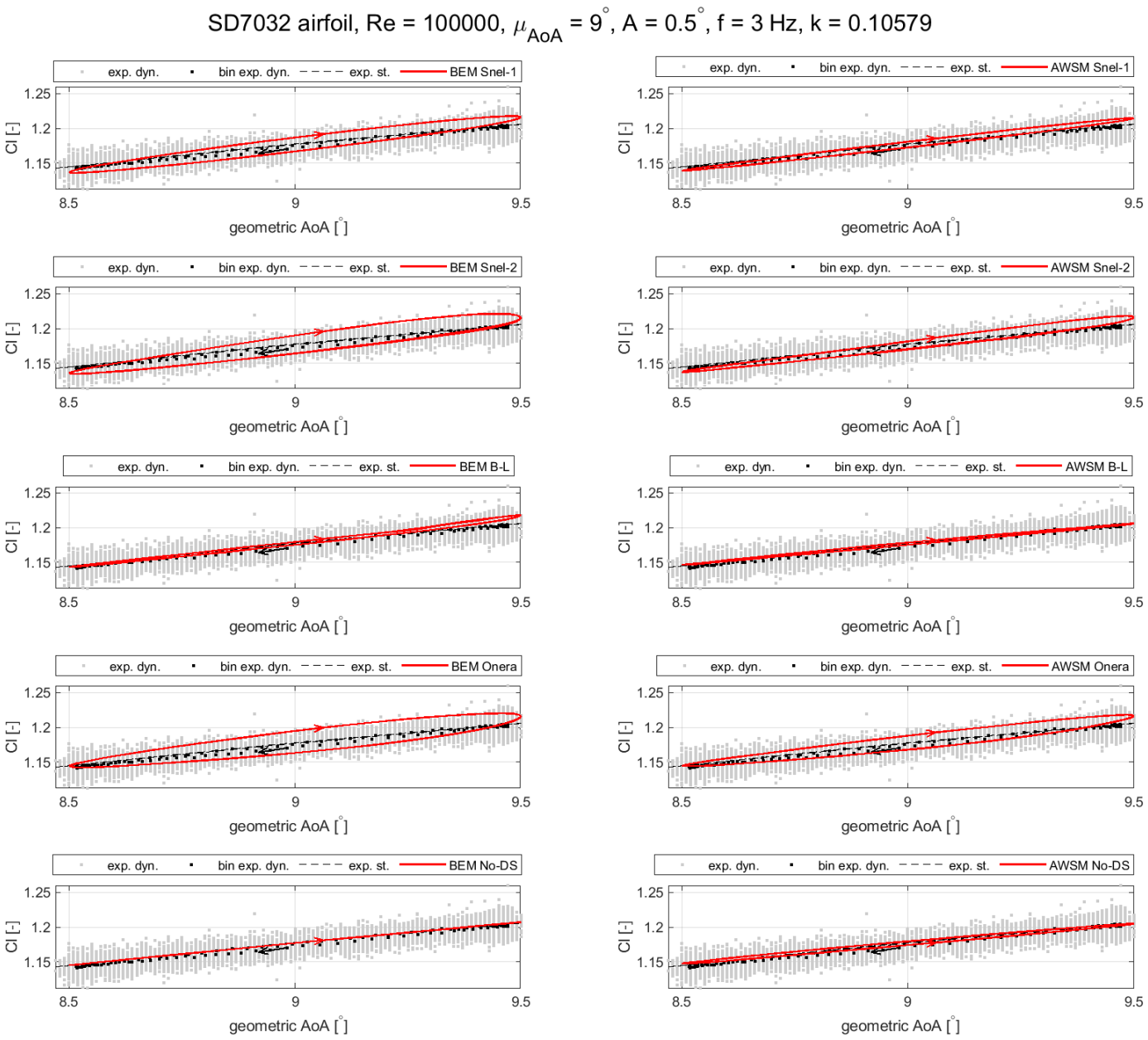

Figure A.43: Comparison between SD7032 airfoil's experimental dynamic lift coefficient (incuding the bin average) and that predicted by means of different unsteay airfoil aerodynamic models for a Reynolds number of 100000. Geometric angle of attack mean, μ_{AoA}, and amplitude, A, are respectively equal to 9° and 5.0°, while frequency, f, is 0.25 Hz. In the figure, k denotes the reduced frequency.

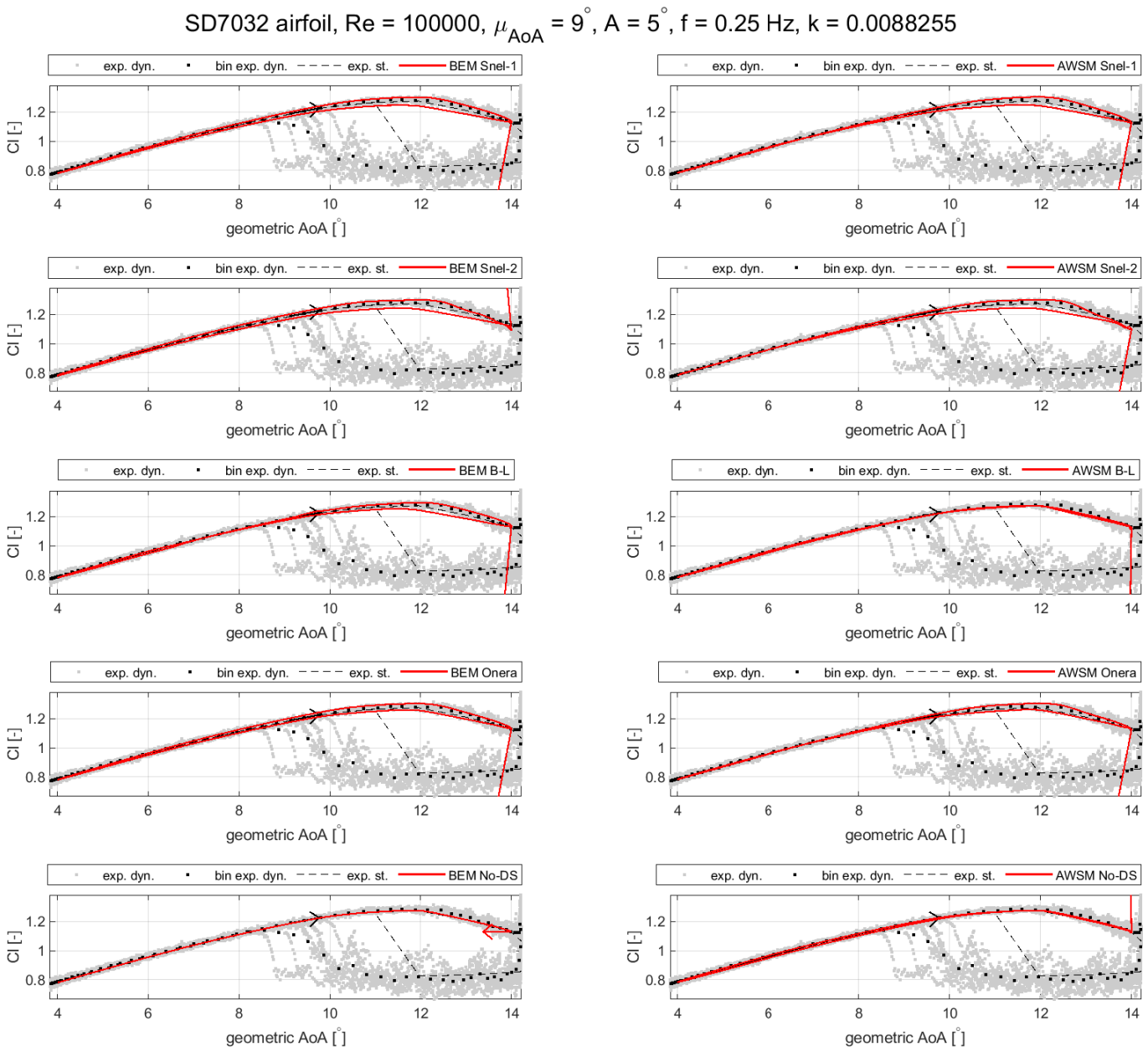

Figure A.44: Comparison between SD7032 airfoil's experimental dynamic lift coefficient (incuding the bin average) and that predicted by means of different unsteay airfoil aerodynamic models for a Reynolds number of 100000. Geometric angle of attack mean, μ_{AoA}, and amplitude, A, are respectively equal to 9° and 5.0°, while frequency, f, is 0.50 Hz. In the figure, k denotes the reduced frequency.

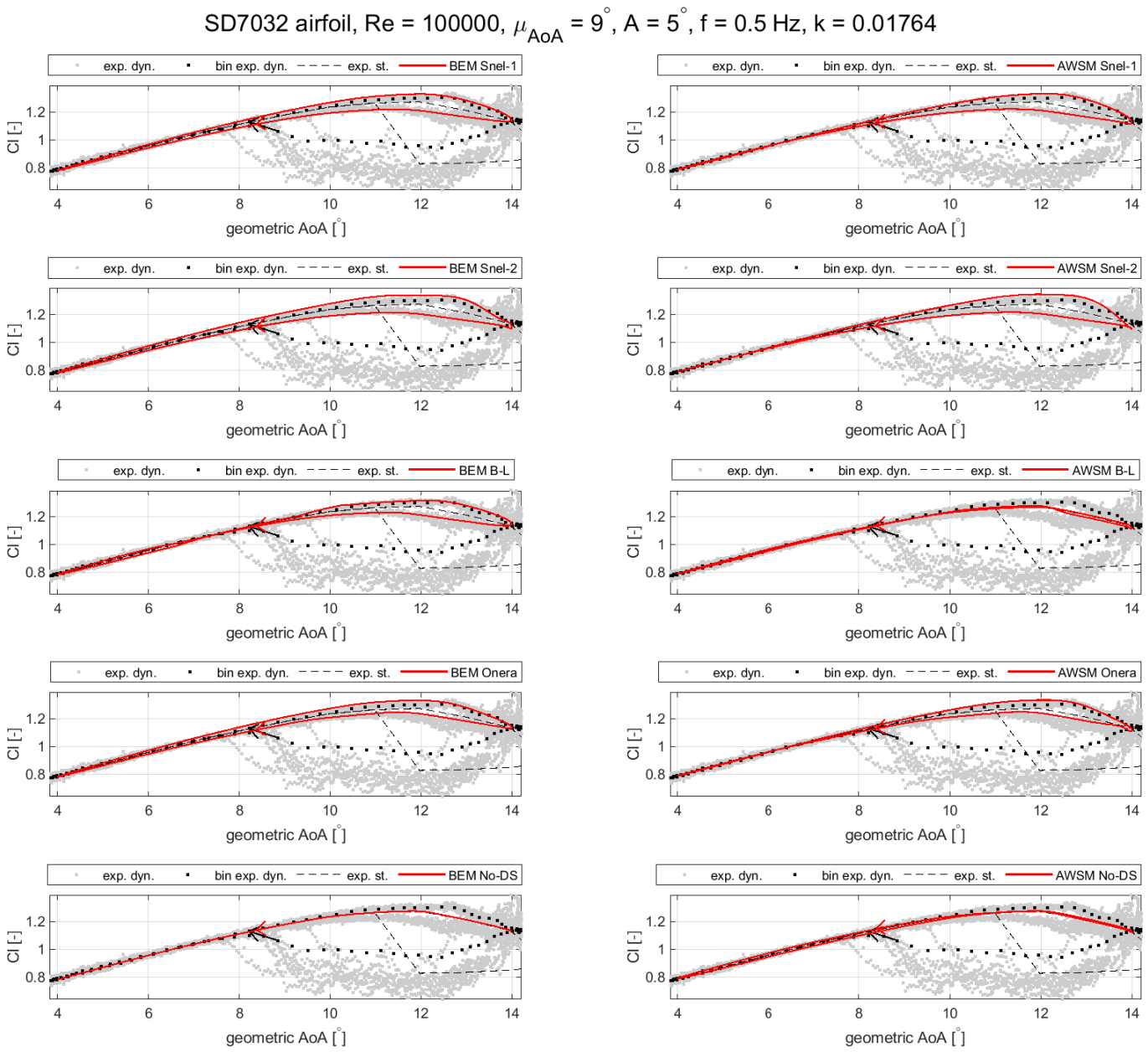

Figure A.45: Comparison between SD7032 airfoil's experimental dynamic lift coefficient (incuding the bin average) and that predicted by means of different unsteay airfoil aerodynamic models for a Reynolds number of 100000. Geometric angle of attack mean, μ_{AoA}, and amplitude, A, are respectively equal to 9° and 5.0°, while frequency, f, is 1.50 Hz. In the figure, k denotes the reduced frequency.

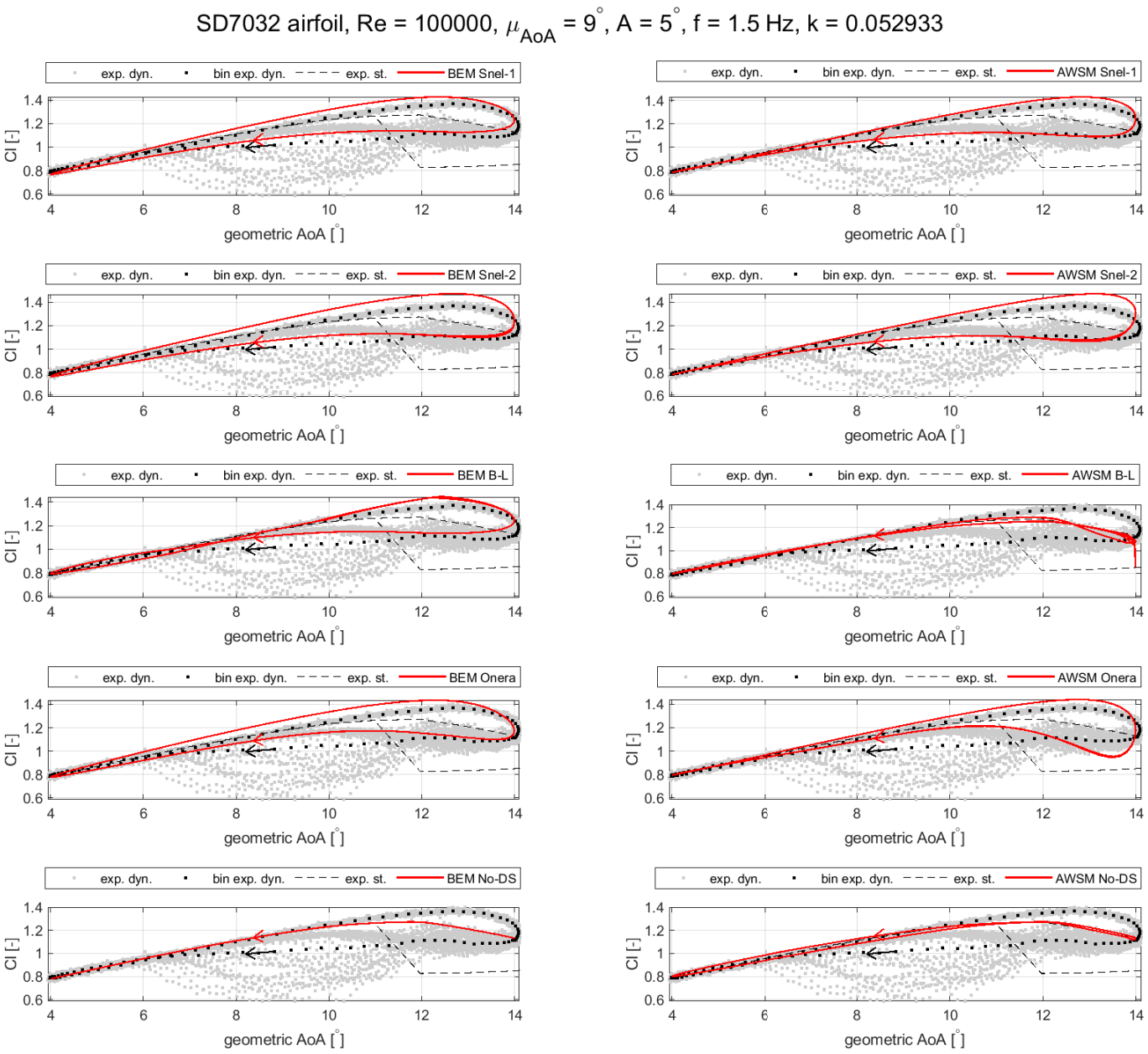

Figure A.46: Comparison between SD7032 airfoil's experimental dynamic lift coefficient (incuding the bin average) and that predicted by means of different unsteay airfoil aerodynamic models for a Reynolds number of 100000. Geometric angle of attack mean, μ_{AoA}, and amplitude, A, are respectively equal to 9° and 5.0°, while frequency, f, is 1.00 Hz. In the figure, k denotes the reduced frequency.

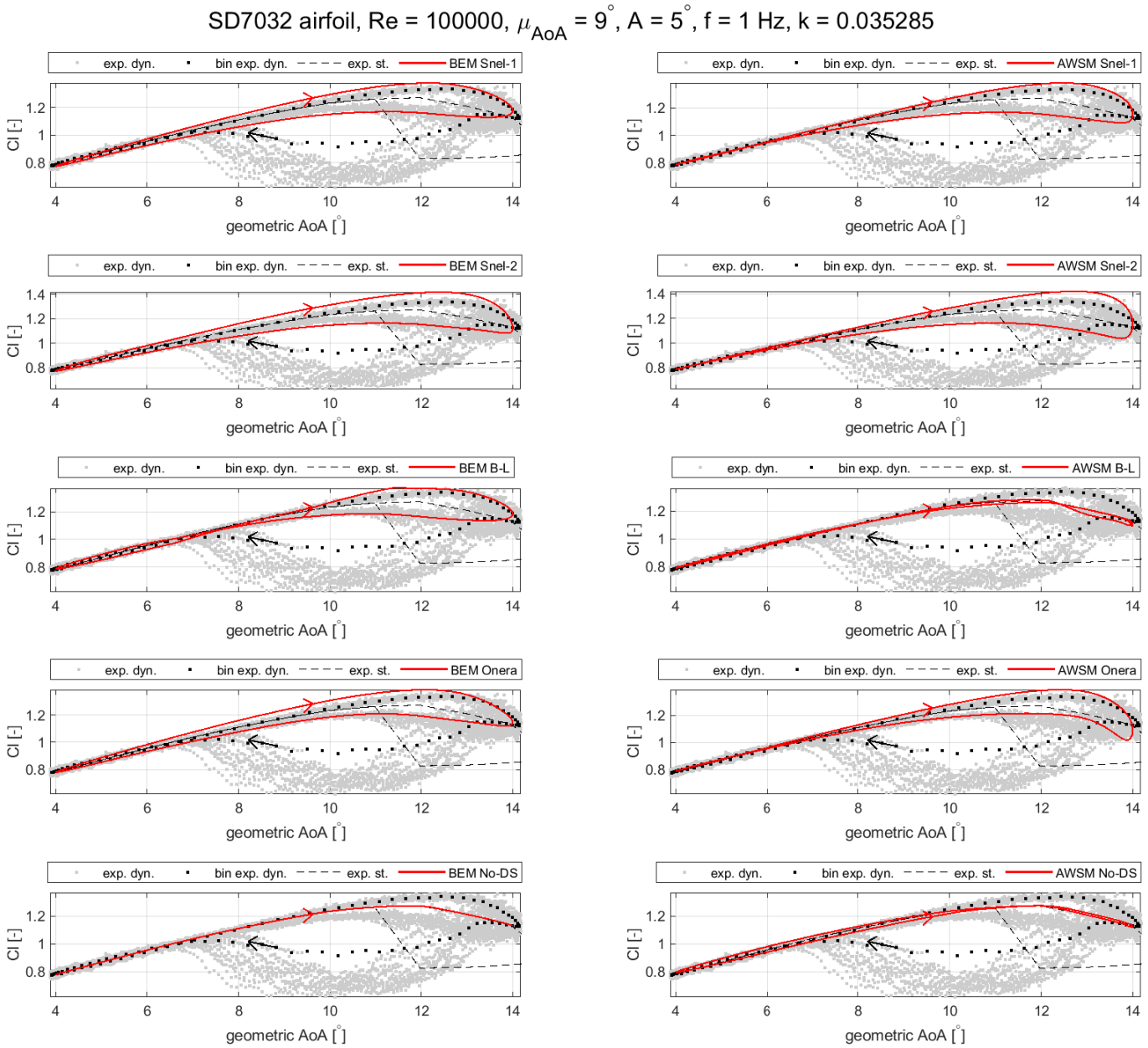

Figure A.47: Comparison between SD7032 airfoil's experimental dynamic lift coefficient (incuding the bin average) and that predicted by means of different unsteay airfoil aerodynamic models for a Reynolds number of 100000. Geometric angle of attack mean, μ_{AoA}, and amplitude, A, are respectively equal to 9° and 5.0°, while frequency, f, is 2.00 Hz. In the figure, k denotes the reduced frequency.

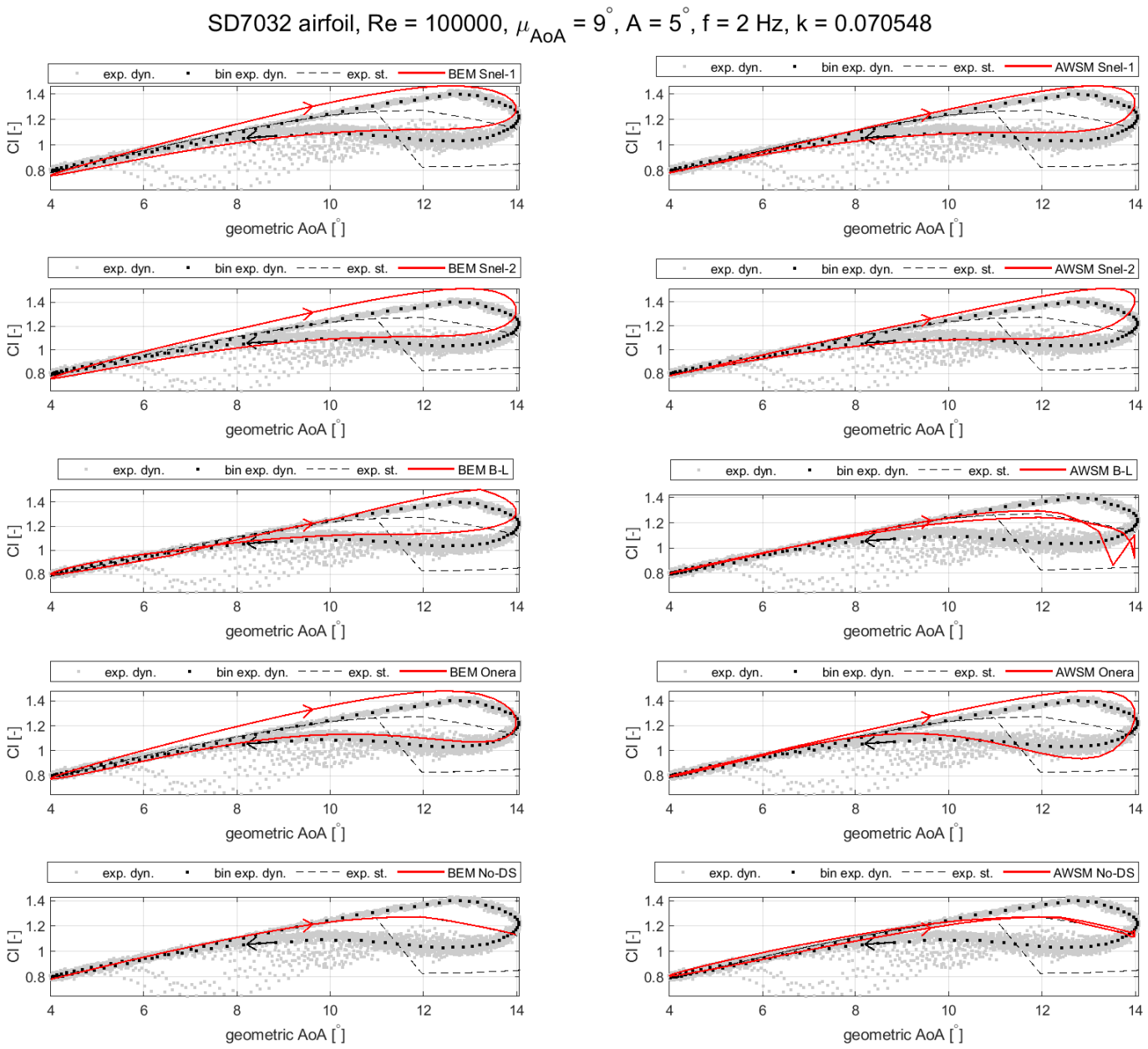

Figure A.48: Comparison between SD7032 airfoil's experimental dynamic lift coefficient (incuding the bin average) and that predicted by means of different unsteay airfoil aerodynamic models for a Reynolds number of 100000. Geometric angle of attack mean, μ_{AoA}, and amplitude, A, are respectively equal to 9° and 5.0°, while frequency, f, is 3.00 Hz. In the figure, k denotes the reduced frequency.

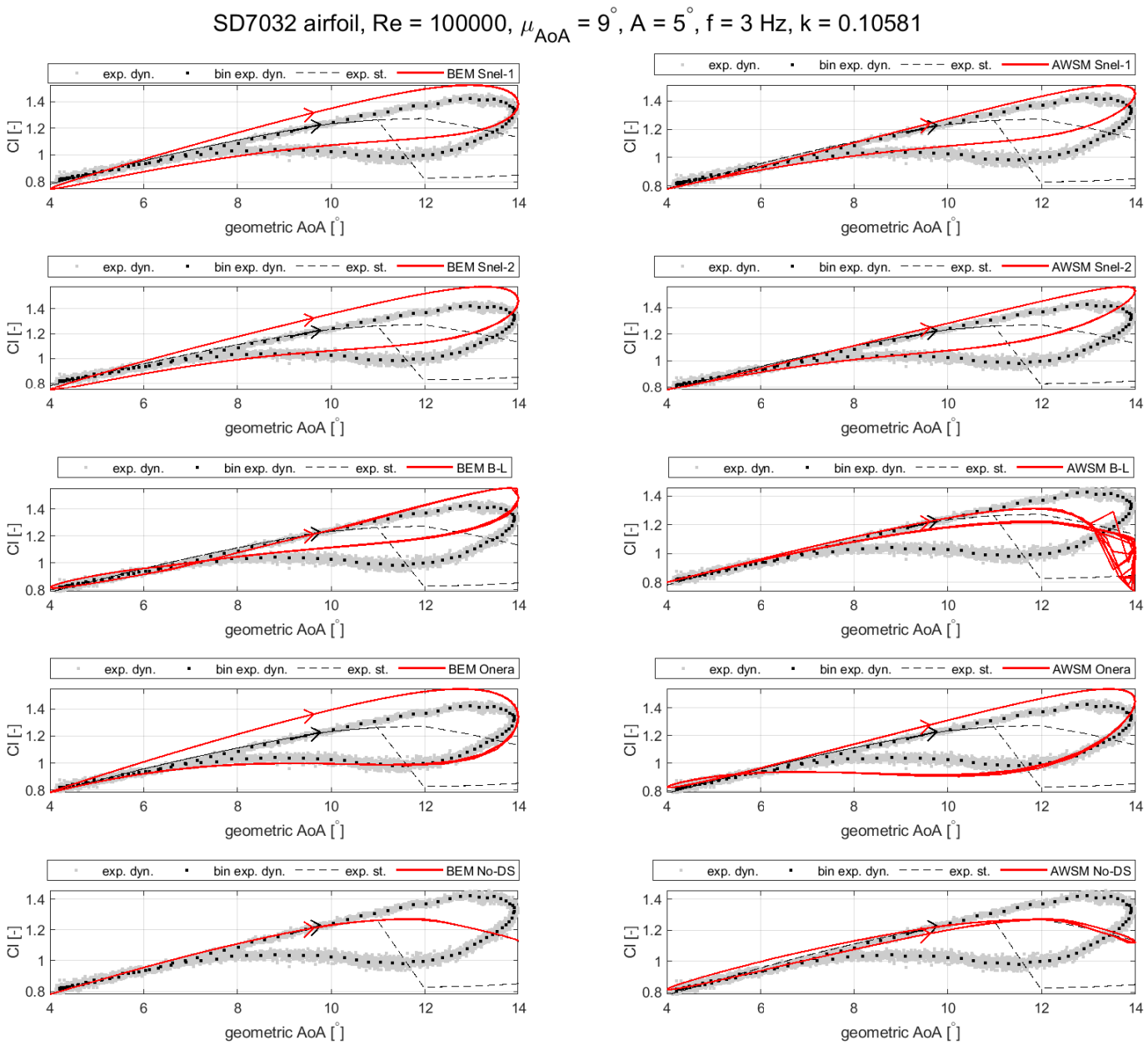

Figure A.49: Comparison between SD7032 airfoil's experimental dynamic lift coefficient (incuding the bin average) and that predicted by means of different unsteay airfoil aerodynamic models for a Reynolds number of 100000. Geometric angle of attack mean, μ_{AoA}, and amplitude, A, are respectively equal to 10° and 0.5°, while frequency, f, is 0.25 Hz. In the figure, k denotes the reduced frequency.

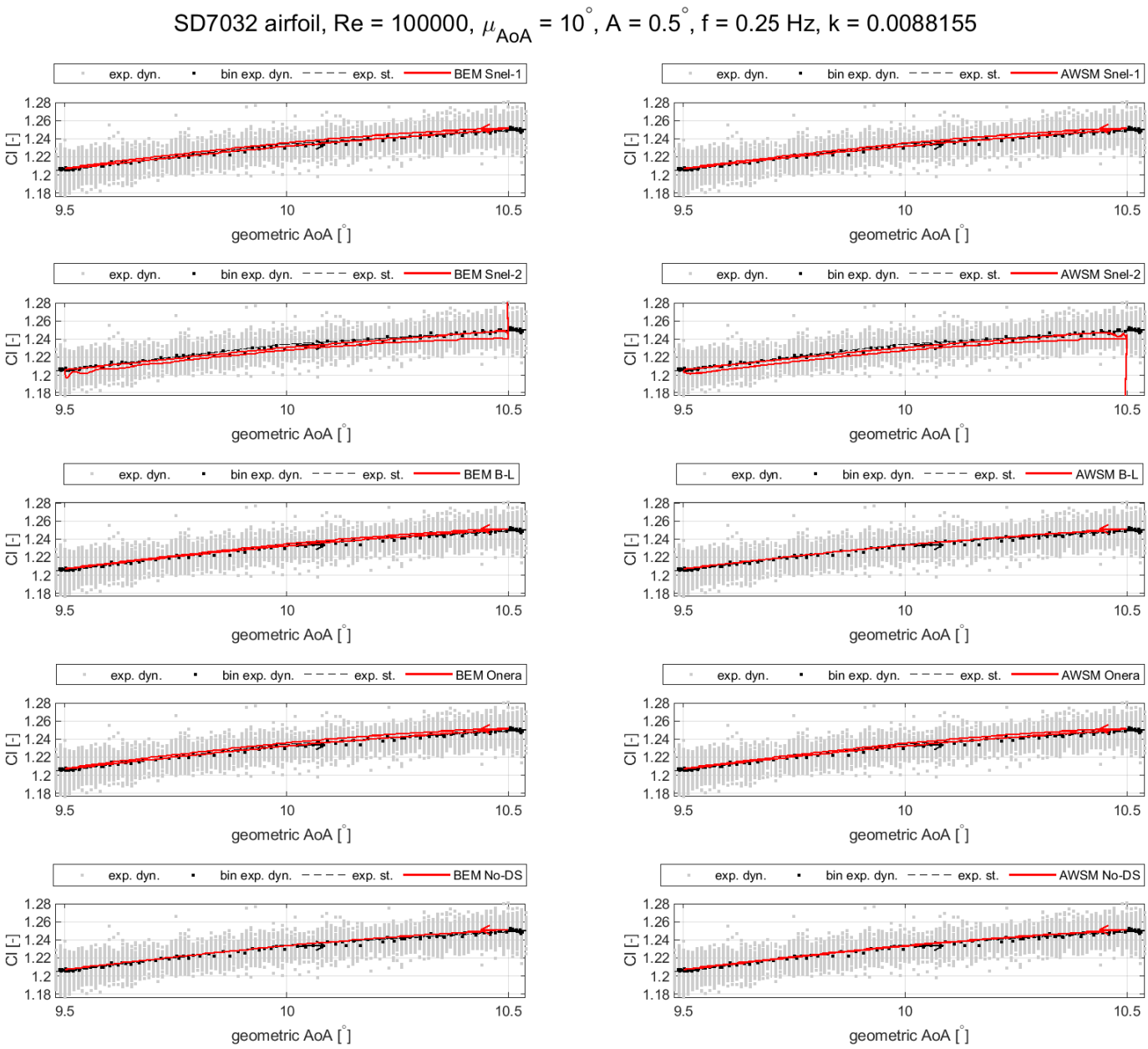

Figure A.50: Comparison between SD7032 airfoil's experimental dynamic lift coefficient (incuding the bin average) and that predicted by means of different unsteay airfoil aerodynamic models for a Reynolds number of 100000. Geometric angle of attack mean, μ_{AoA}, and amplitude, A, are respectively equal to 10° and 0.5°, while frequency, f, is 0.50 Hz. In the figure, k denotes the reduced frequency.

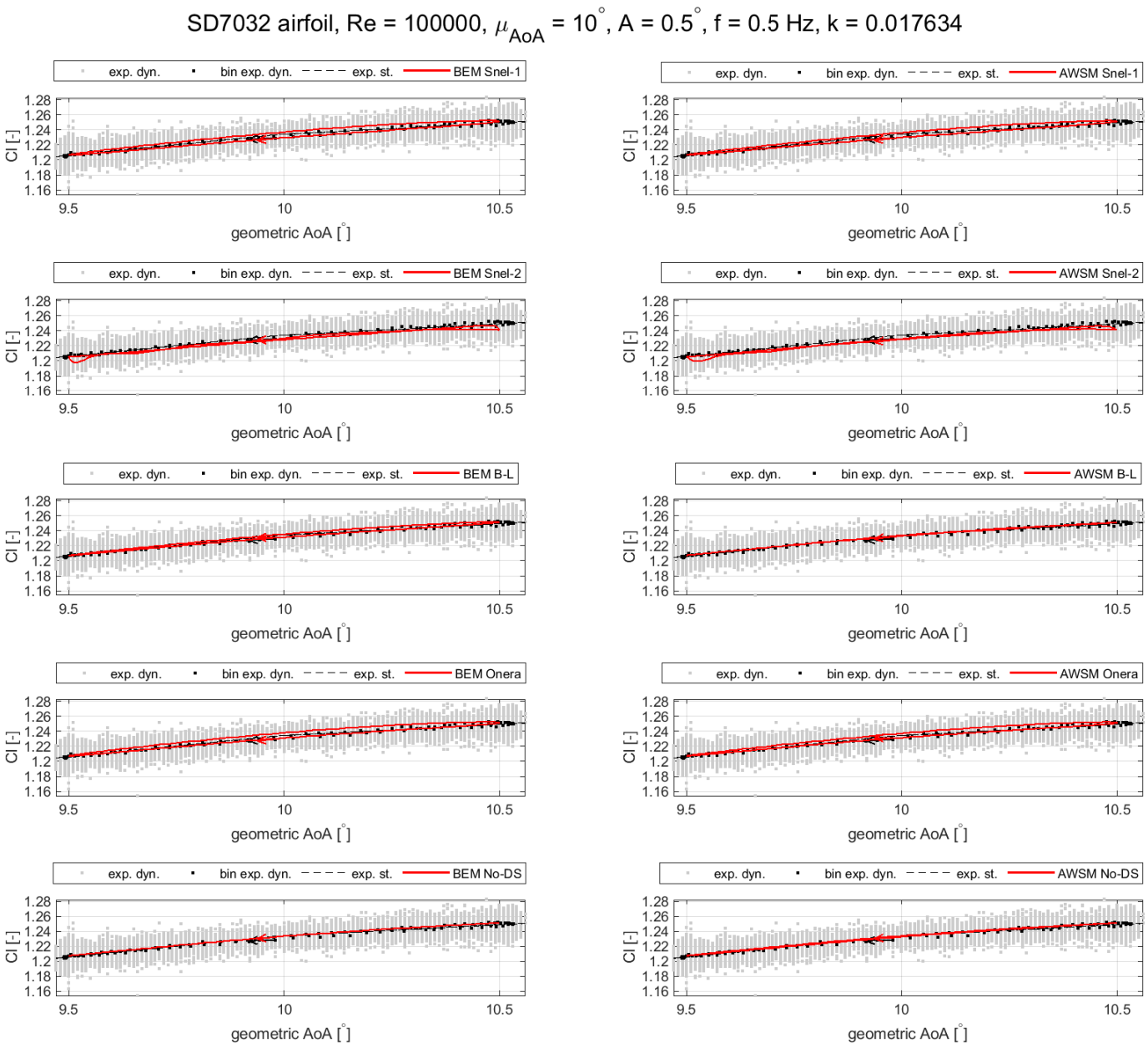

Figure A.51: Comparison between SD7032 airfoil's experimental dynamic lift coefficient (incuding the bin average) and that predicted by means of different unsteay airfoil aerodynamic models for a Reynolds number of 100000. Geometric angle of attack mean, μ_{AoA}, and amplitude, A, are respectively equal to 10° and 0.5°, while frequency, f, is 1.50 Hz. In the figure, k denotes the reduced frequency.

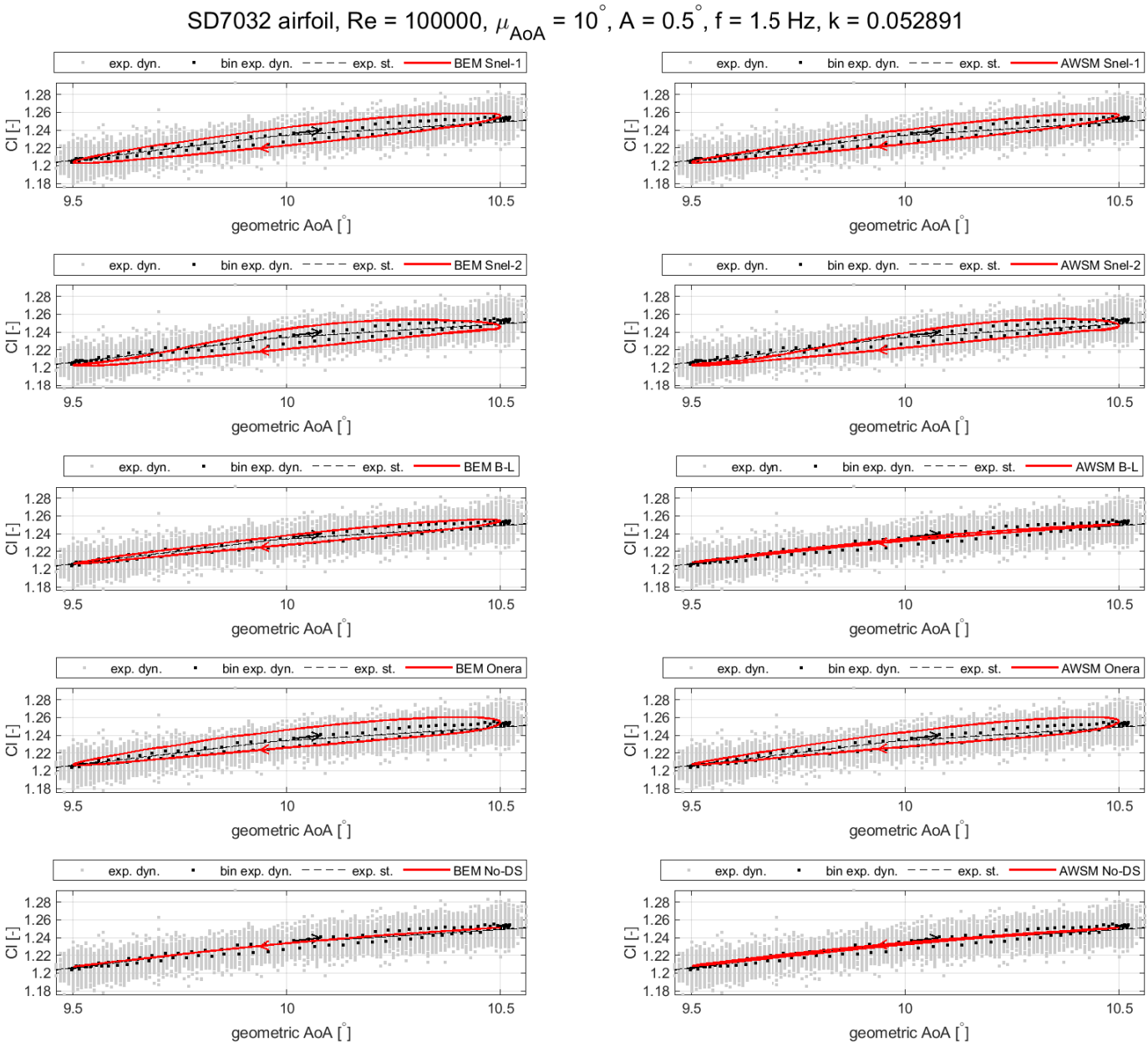

Figure A.52: Comparison between SD7032 airfoil's experimental dynamic lift coefficient (incuding the bin average) and that predicted by means of different unsteay airfoil aerodynamic models for a Reynolds number of 100000. Geometric angle of attack mean, μ_{AoA}, and amplitude, A, are respectively equal to 10° and 0.5°, while frequency, f, is 1.00 Hz. In the figure, k denotes the reduced frequency.

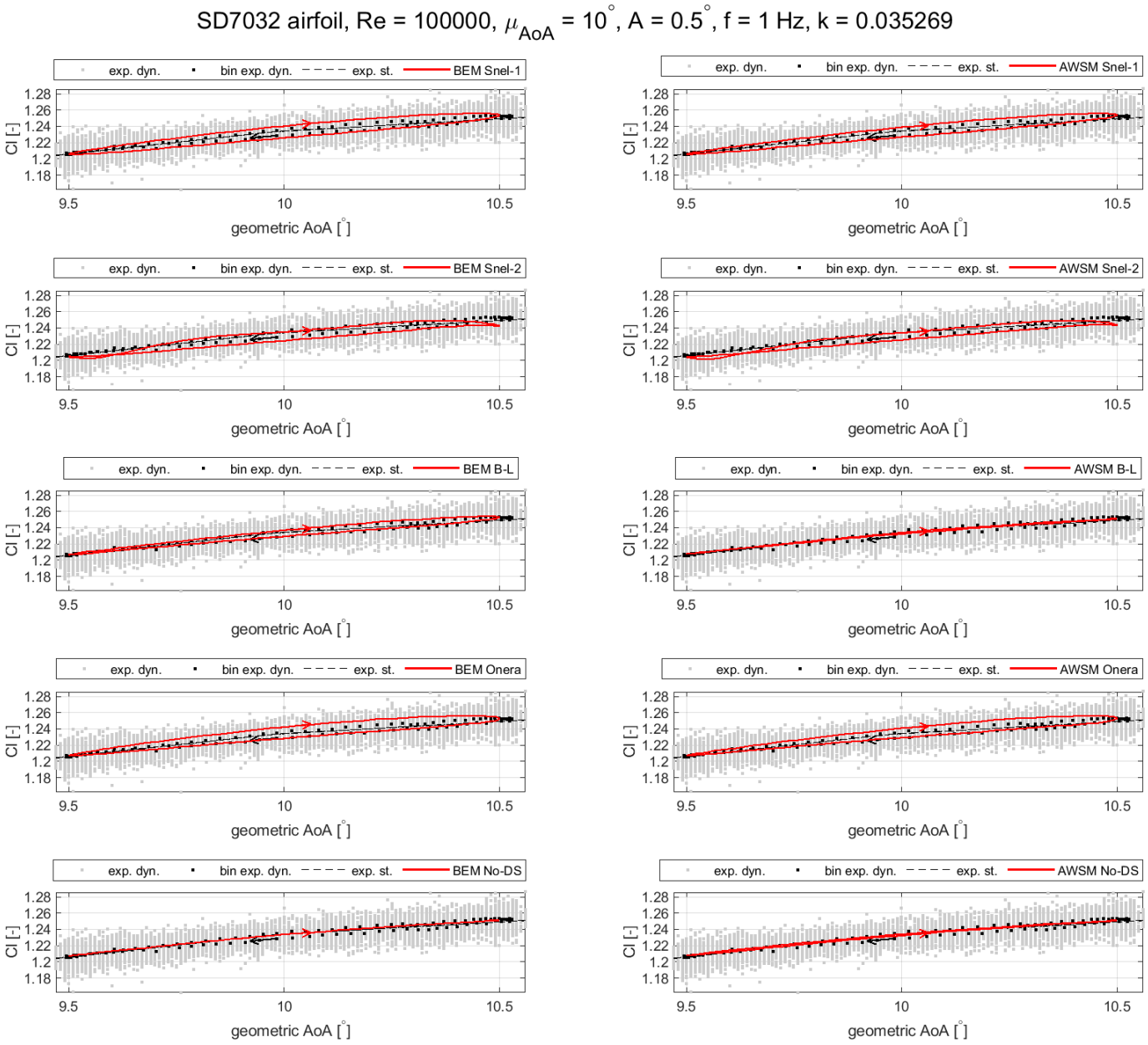

Figure A.53: Comparison between SD7032 airfoil's experimental dynamic lift coefficient (incuding the bin average) and that predicted by means of different unsteay airfoil aerodynamic models for a Reynolds number of 100000. Geometric angle of attack mean, μ_{AoA}, and amplitude, A, are respectively equal to 10° and 0.5°, while frequency, f, is 2.00 Hz. In the figure, k denotes the reduced frequency.

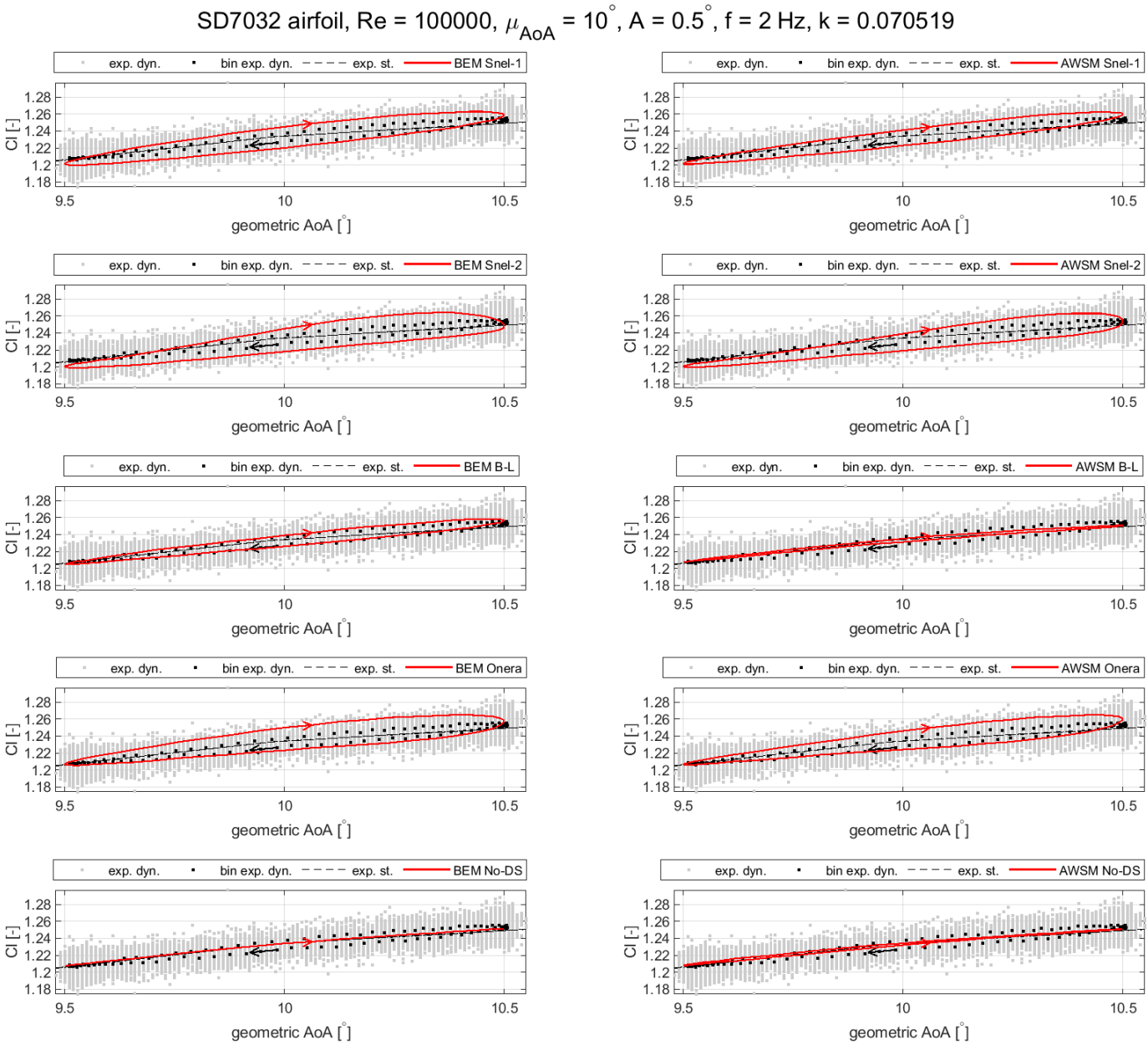

Figure A.54: Comparison between SD7032 airfoil's experimental dynamic lift coefficient (incuding the bin average) and that predicted by means of different unsteay airfoil aerodynamic models for a Reynolds number of 100000. Geometric angle of attack mean, μ_{AoA}, and amplitude, A, are respectively equal to 10° and 0.5°, while frequency, f, is 3.00 Hz. In the figure, k denotes the reduced frequency.

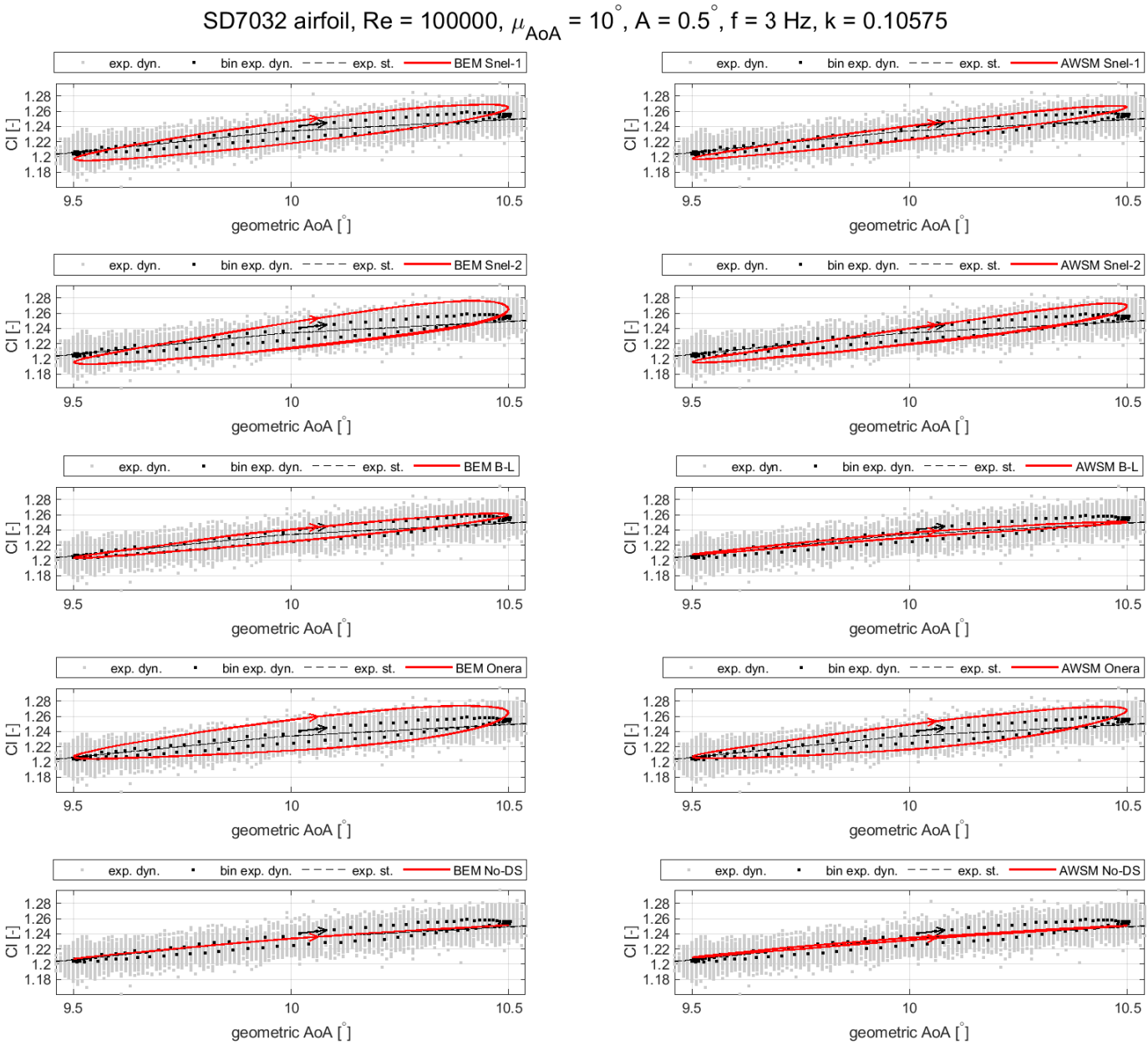

Figure A.55: Comparison between SD7032 airfoil's experimental dynamic lift coefficient (incuding the bin average) and that predicted by means of different unsteay airfoil aerodynamic models for a Reynolds number of 100000. Geometric angle of attack mean, μ_{AoA}, and amplitude, A, are respectively equal to 10° and 5.0°, while frequency, f, is 0.25 Hz. In the figure, k denotes the reduced frequency.

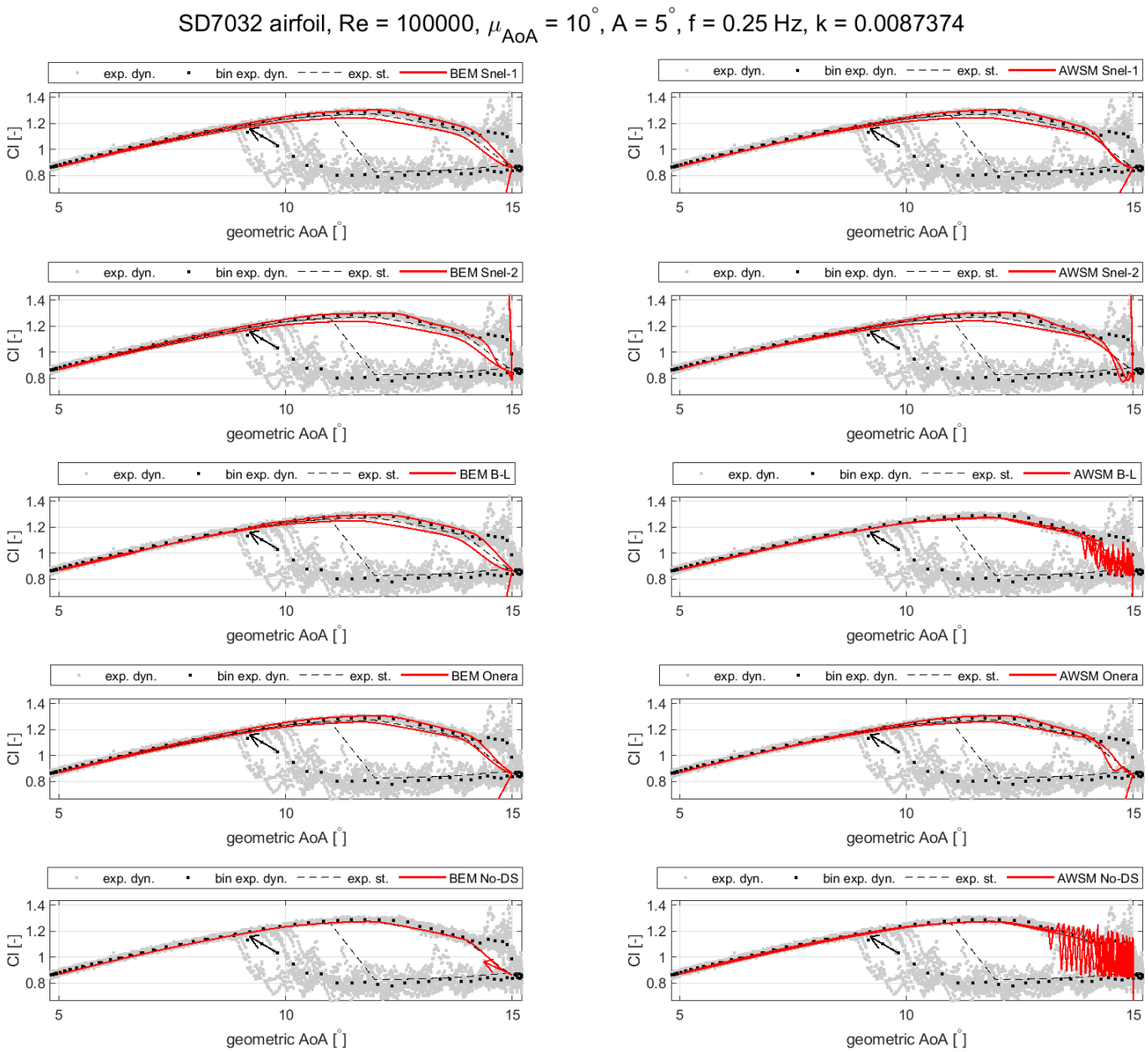

Figure A.56: Comparison between SD7032 airfoil's experimental dynamic lift coefficient (incuding the bin average) and that predicted by means of different unsteay airfoil aerodynamic models for a Reynolds number of 100000. Geometric angle of attack mean, μ_{AoA}, and amplitude, A, are respectively equal to 10° and 5.0°, while frequency, f, is 0.50 Hz. In the figure, k denotes the reduced frequency.

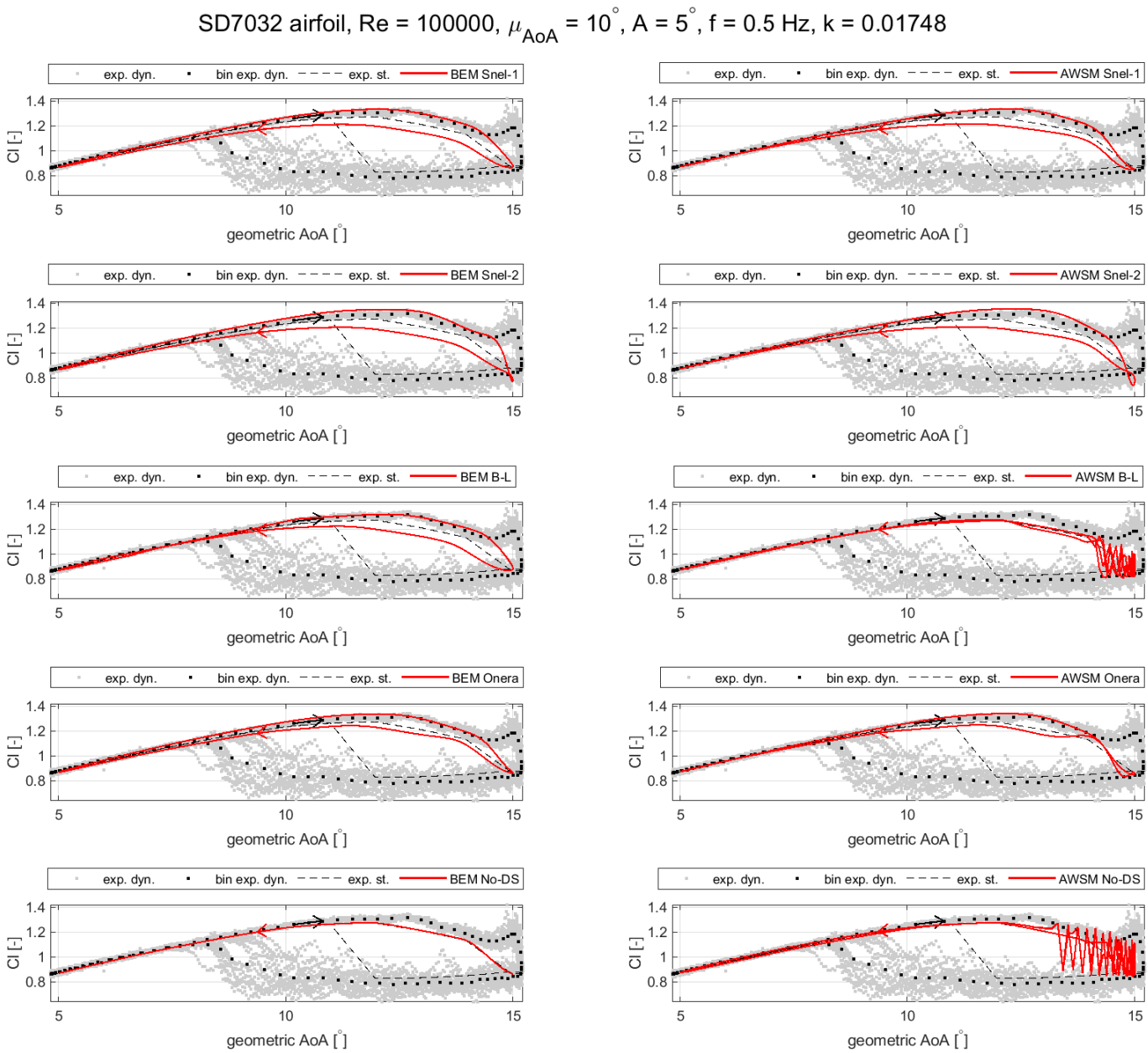

Figure A.57: Comparison between SD7032 airfoil's experimental dynamic lift coefficient (incuding the bin average) and that predicted by means of different unsteay airfoil aerodynamic models for a Reynolds number of 100000. Geometric angle of attack mean, μ_{AoA}, and amplitude, A, are respectively equal to 10° and 5.0°, while frequency, f, is 1.50 Hz. In the figure, k denotes the reduced frequency.

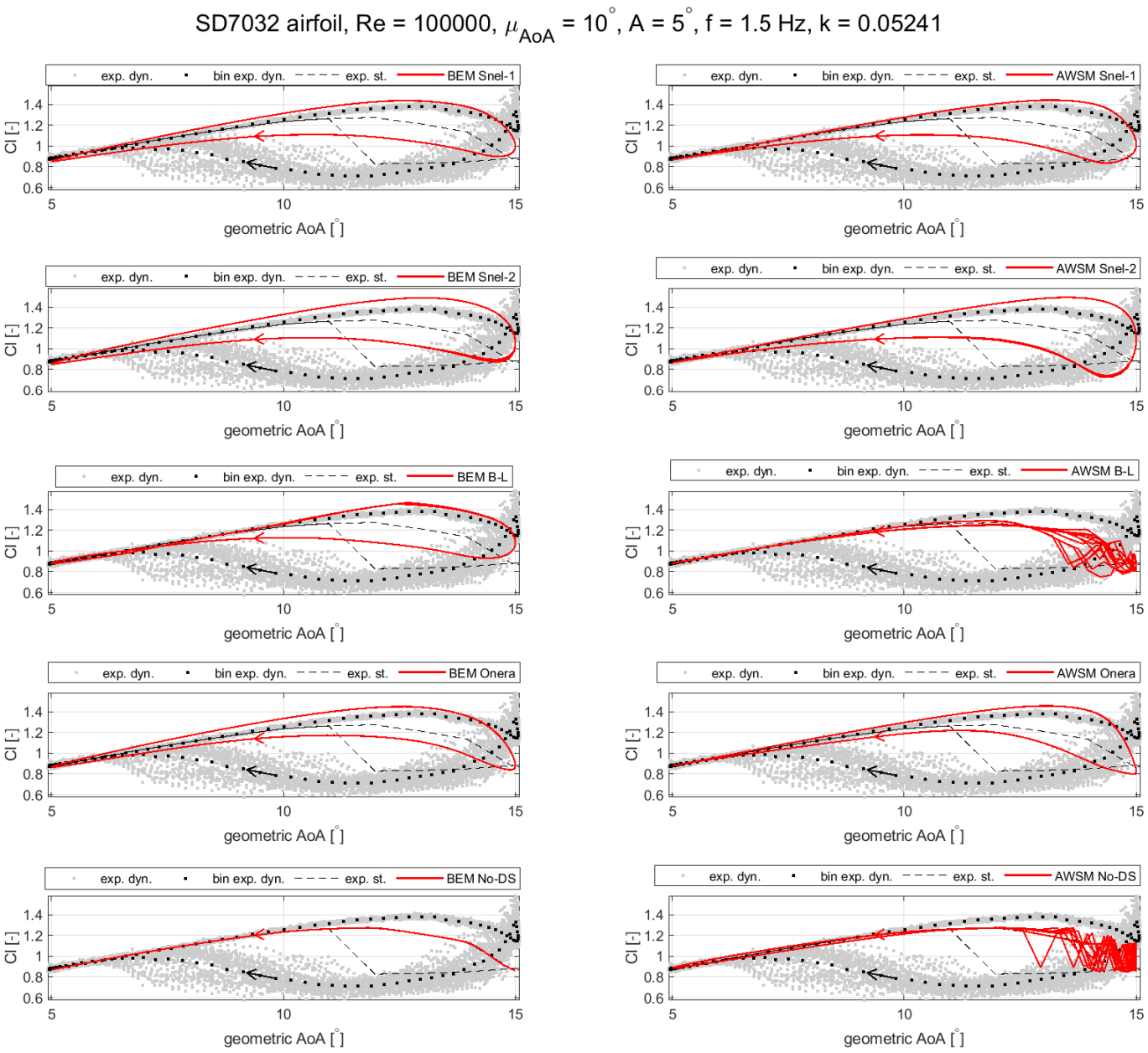

Figure A.58: Comparison between SD7032 airfoil's experimental dynamic lift coefficient (incuding the bin average) and that predicted by means of different unsteay airfoil aerodynamic models for a Reynolds number of 100000. Geometric angle of attack mean, μ_{AoA}, and amplitude, A, are respectively equal to 10° and 5.0°, while frequency, f, is 1.00 Hz. In the figure, k denotes the reduced frequency.

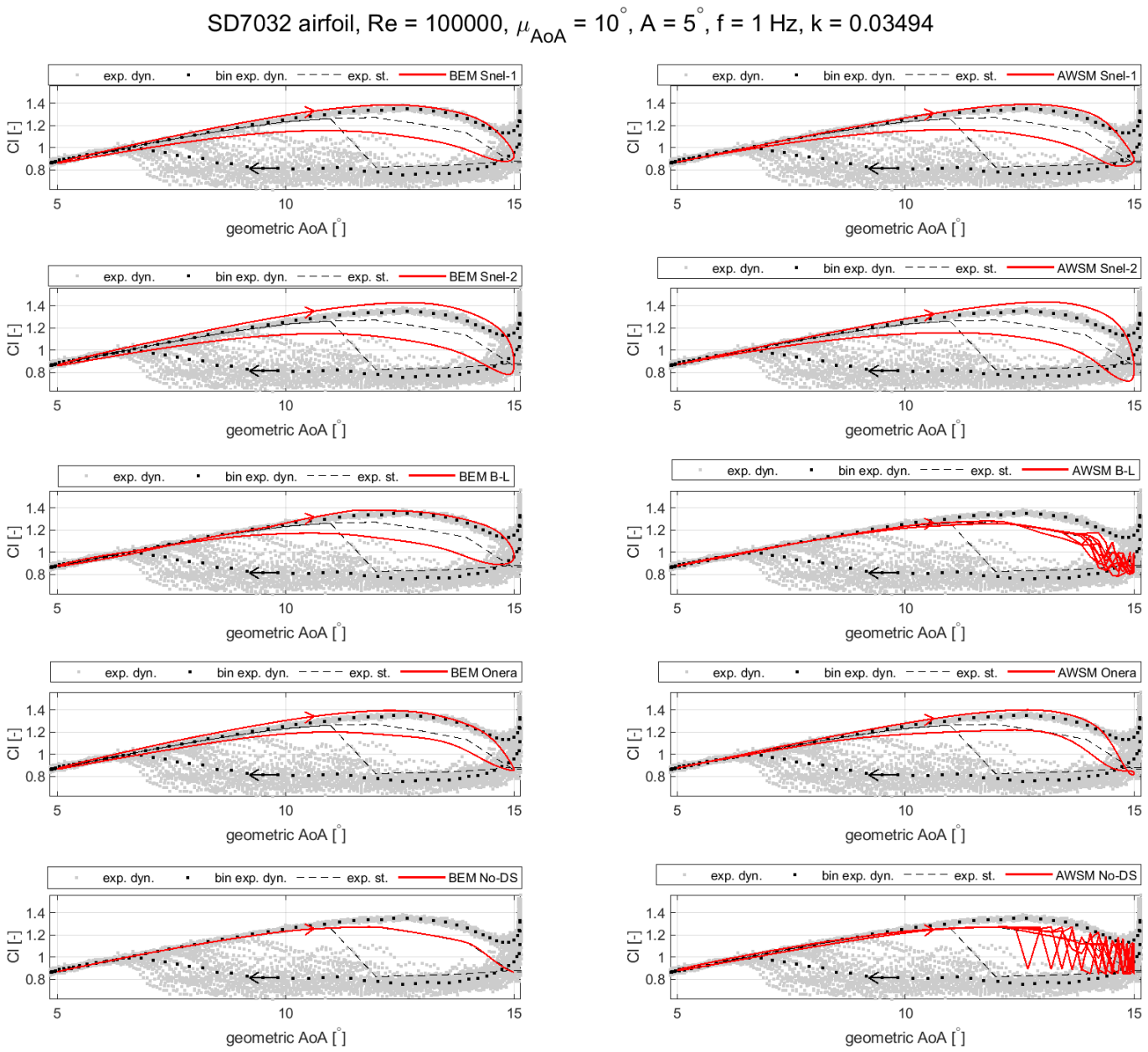

Figure A.59: Comparison between SD7032 airfoil's experimental dynamic lift coefficient (incuding the bin average) and that predicted by means of different unsteay airfoil aerodynamic models for a Reynolds number of 100000. Geometric angle of attack mean, μ_{AoA}, and amplitude, A, are respectively equal to 10° and 5.0°, while frequency, f, is 2.00 Hz. In the figure, k denotes the reduced frequency.

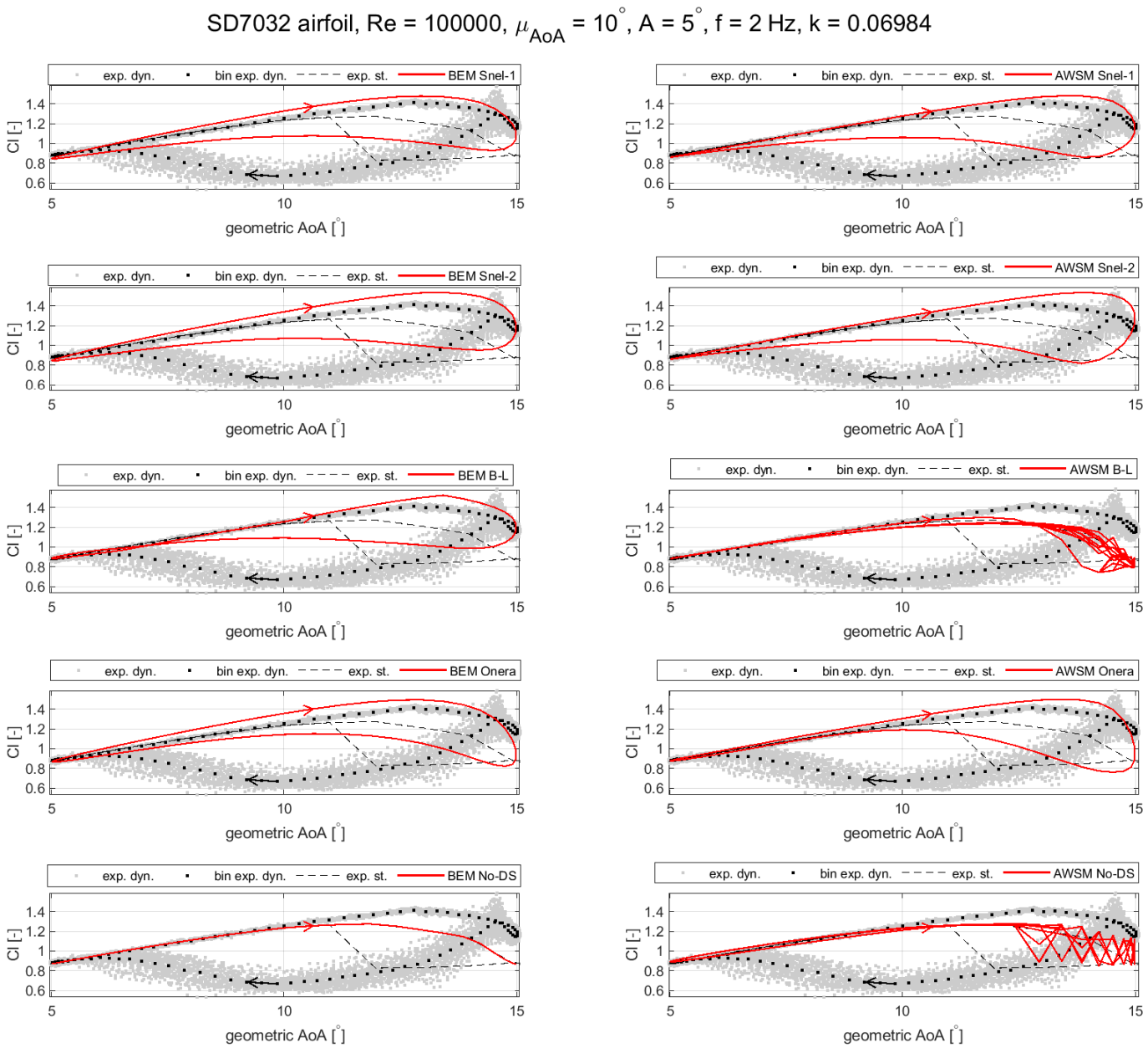

Figure A.60: Comparison between SD7032 airfoil's experimental dynamic lift coefficient (incuding the bin average) and that predicted by means of different unsteay airfoil aerodynamic models for a Reynolds number of 100000. Geometric angle of attack mean, μ_{AoA}, and amplitude, A, are respectively equal to 10° and 5.0°, while frequency, f, is 3.00 Hz. In the figure, k denotes the reduced frequency.

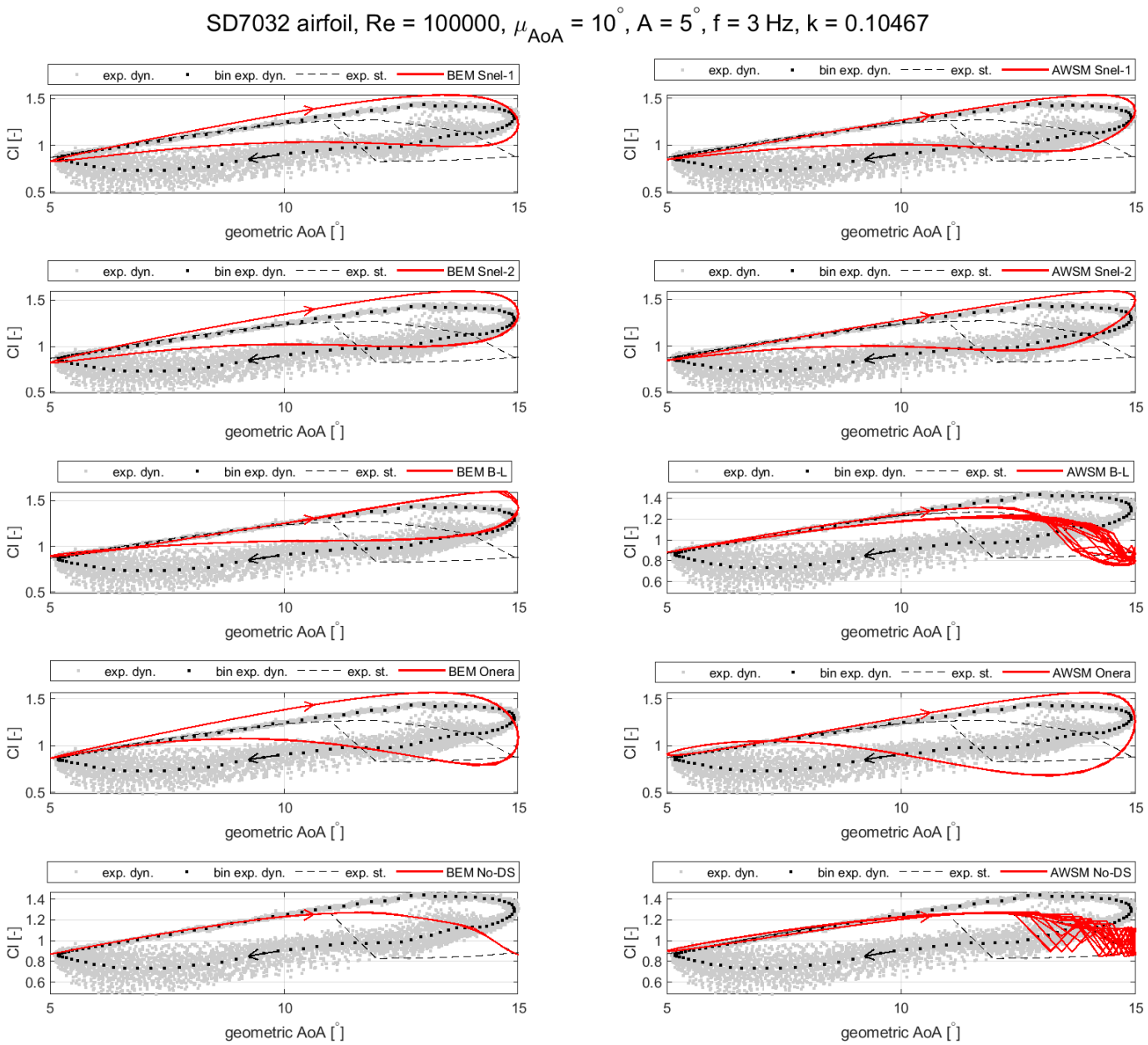

Figure A.61: Comparison between SD7032 airfoil's experimental dynamic lift coefficient (incuding the bin average) and that predicted by means of different unsteay airfoil aerodynamic models for a Reynolds number of 100000. Geometric angle of attack mean, μ_{AoA}, and amplitude, A, are respectively equal to 12° and 0.5°, while frequency, f, is 0.25 Hz. In the figure, k denotes the reduced frequency.

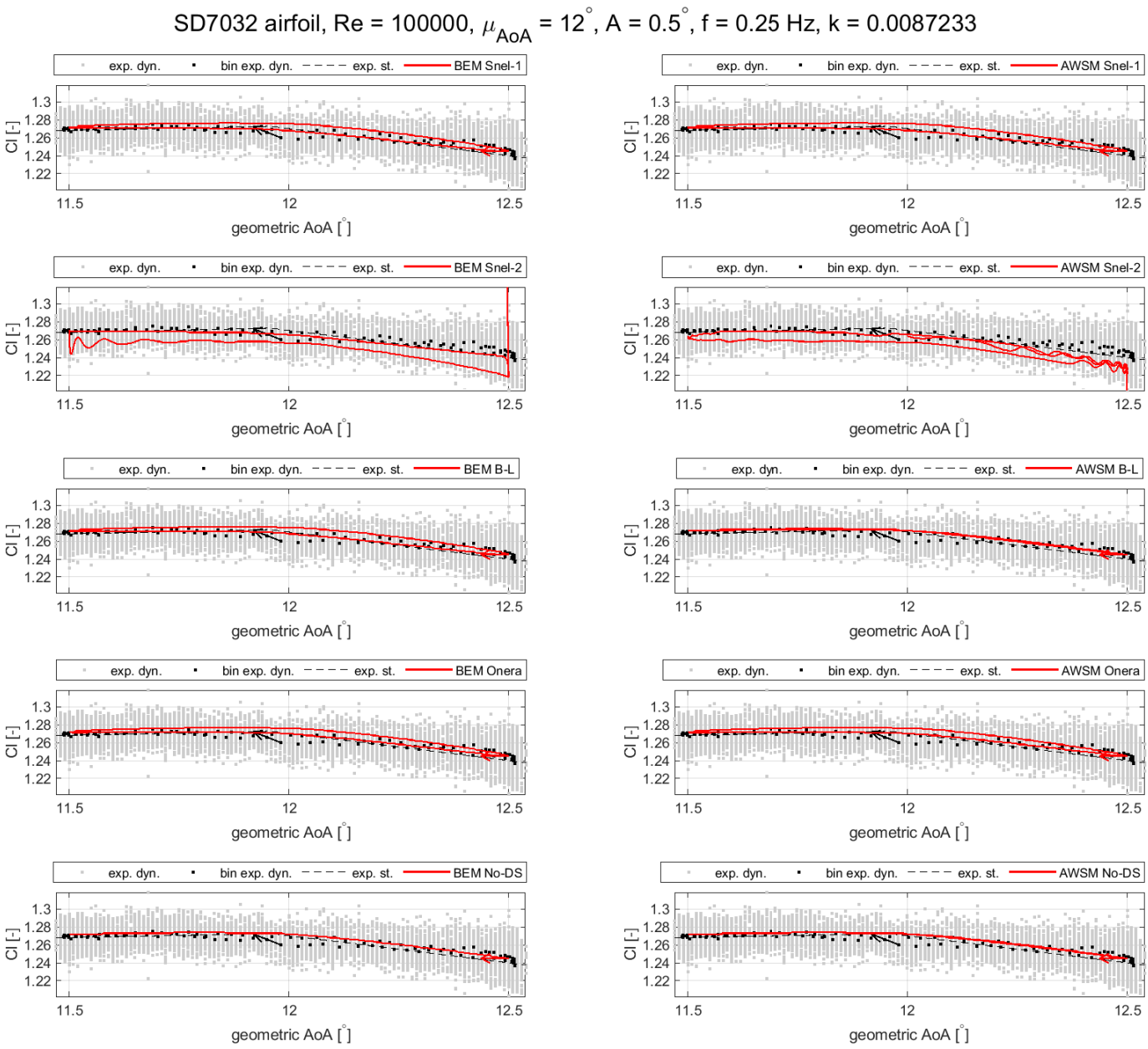

Figure A.62: Comparison between SD7032 airfoil's experimental dynamic lift coefficient (incuding the bin average) and that predicted by means of different unsteay airfoil aerodynamic models for a Reynolds number of 100000. Geometric angle of attack mean, μ_{AoA}, and amplitude, A, are respectively equal to 12° and 0.5°, while frequency, f, is 0.50 Hz. In the figure, k denotes the reduced frequency.

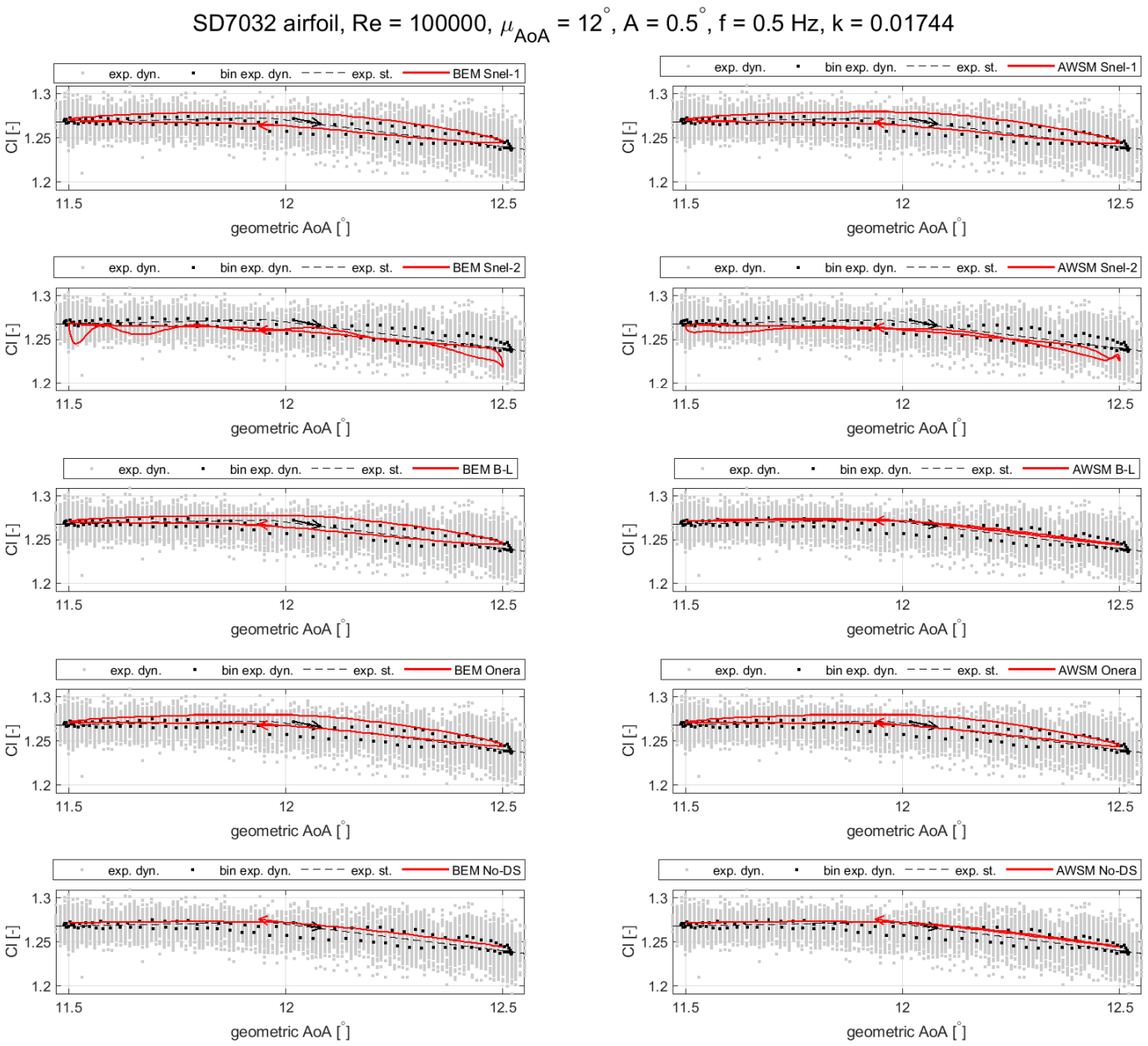

Figure A.63: Comparison between SD7032 airfoil's experimental dynamic lift coefficient (incuding the bin average) and that predicted by means of different unsteay airfoil aerodynamic models for a Reynolds number of 100000. Geometric angle of attack mean, μ_{AoA}, and amplitude, A, are respectively equal to 12° and 0.5°, while frequency, f, is 1.50 Hz. In the figure, k denotes the reduced frequency.

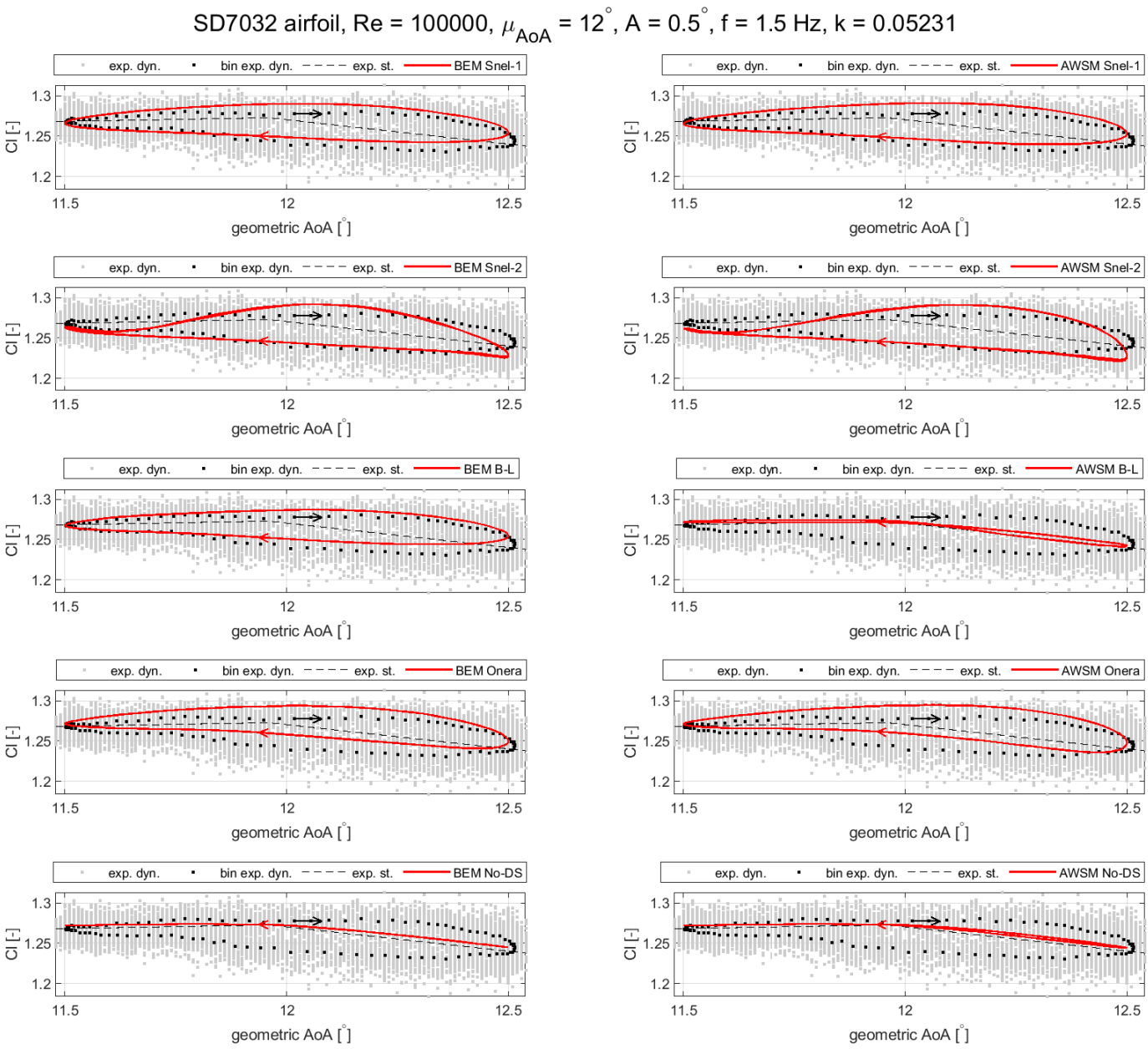

Figure A.64: Comparison between SD7032 airfoil's experimental dynamic lift coefficient (incuding the bin average) and that predicted by means of different unsteay airfoil aerodynamic models for a Reynolds number of 100000. Geometric angle of attack mean, μ_{AoA}, and amplitude, A, are respectively equal to 12° and 0.5°, while frequency, f, is 1.00 Hz. In the figure, k denotes the reduced frequency.

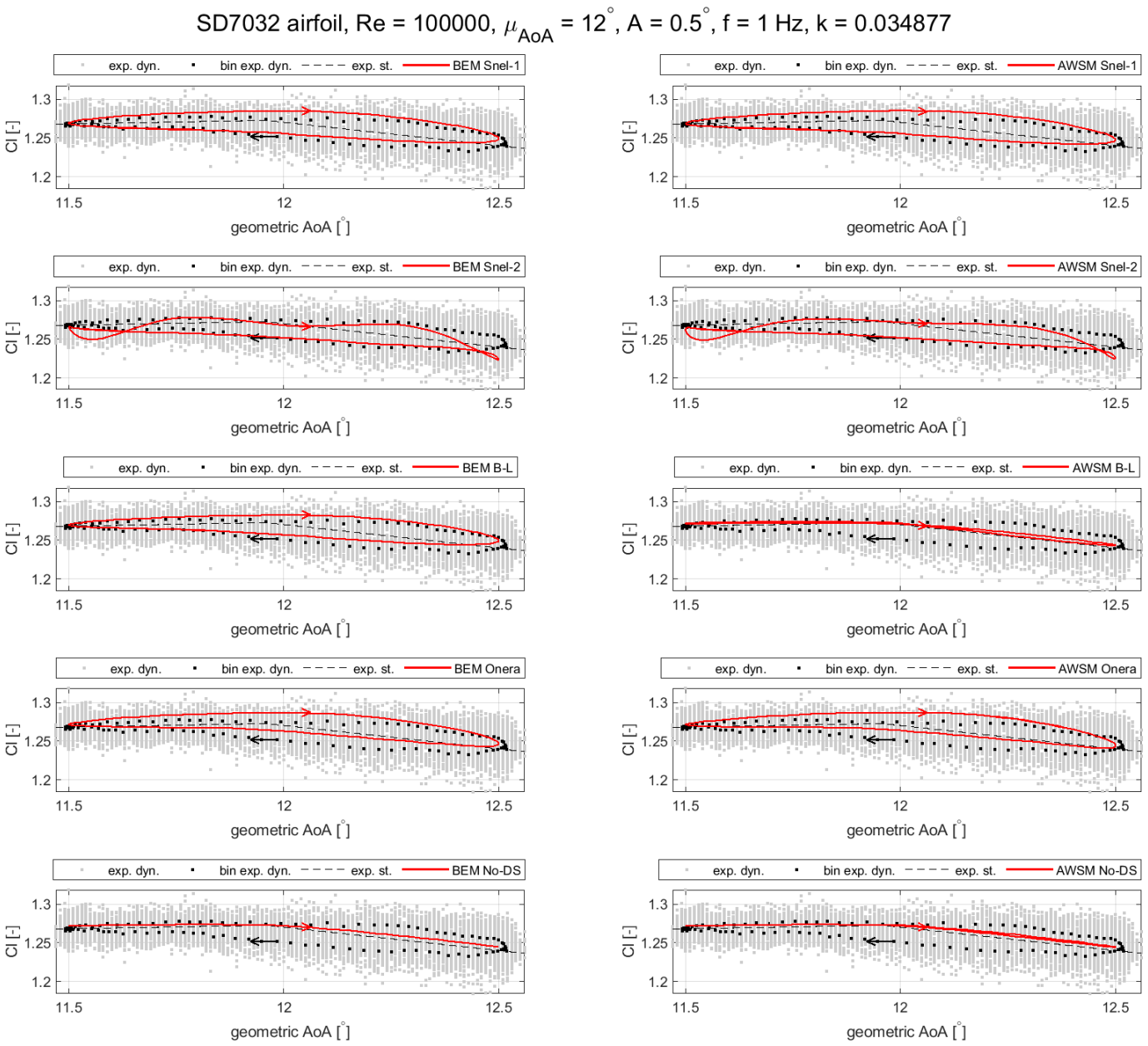

Figure A.65: Comparison between SD7032 airfoil's experimental dynamic lift coefficient (incuding the bin average) and that predicted by means of different unsteay airfoil aerodynamic models for a Reynolds number of 100000. Geometric angle of attack mean, μ_{AoA}, and amplitude, A, are respectively equal to 12° and 0.5°, while frequency, f, is 2.00 Hz. In the figure, k denotes the reduced frequency.

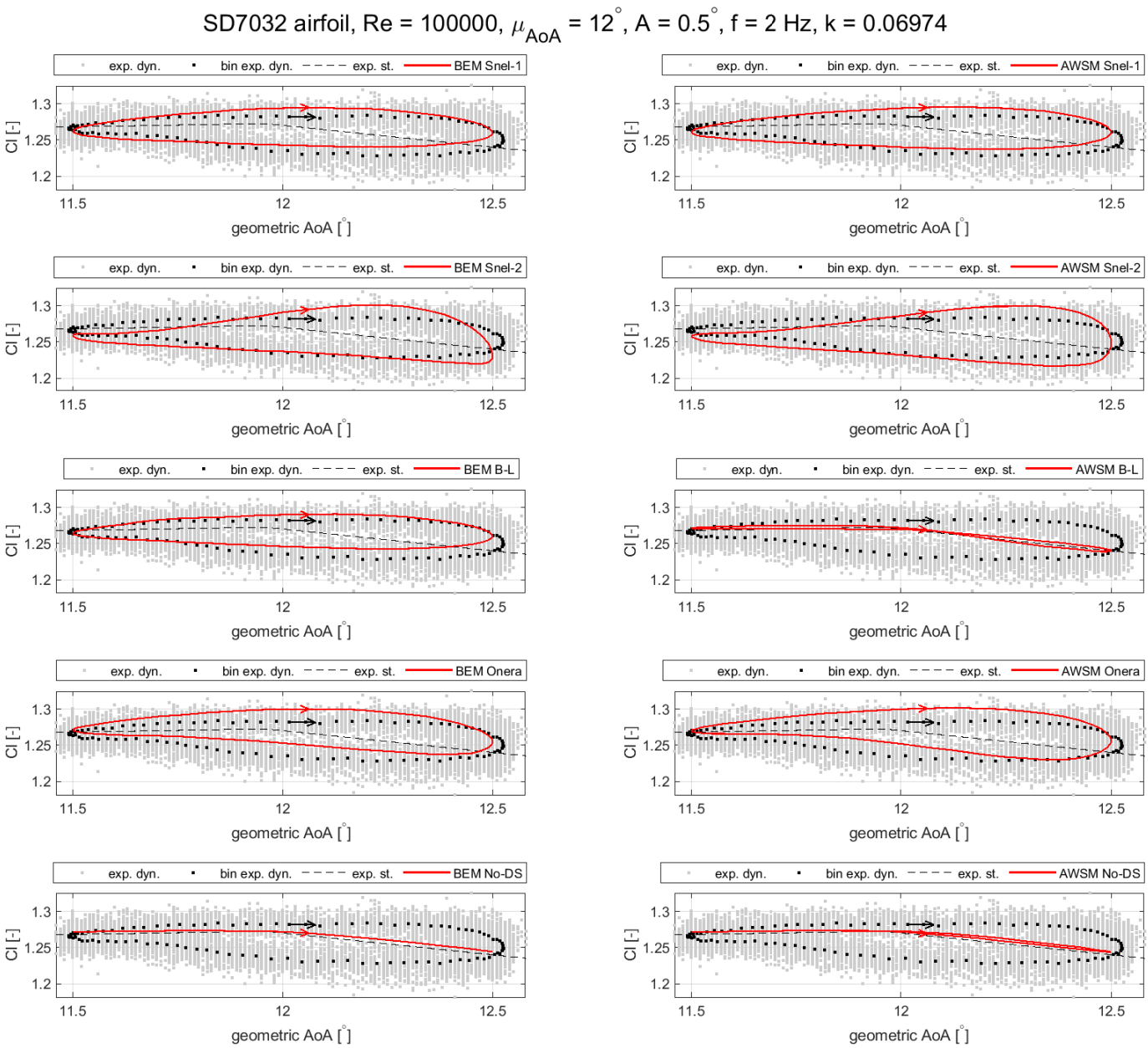

Figure A.66: Comparison between SD7032 airfoil's experimental dynamic lift coefficient (incuding the bin average) and that predicted by means of different unsteay airfoil aerodynamic models for a Reynolds number of 100000. Geometric angle of attack mean, μ_{AoA}, and amplitude, A, are respectively equal to 12° and 0.5°, while frequency, f, is 3.00 Hz. In the figure, k denotes the reduced frequency.

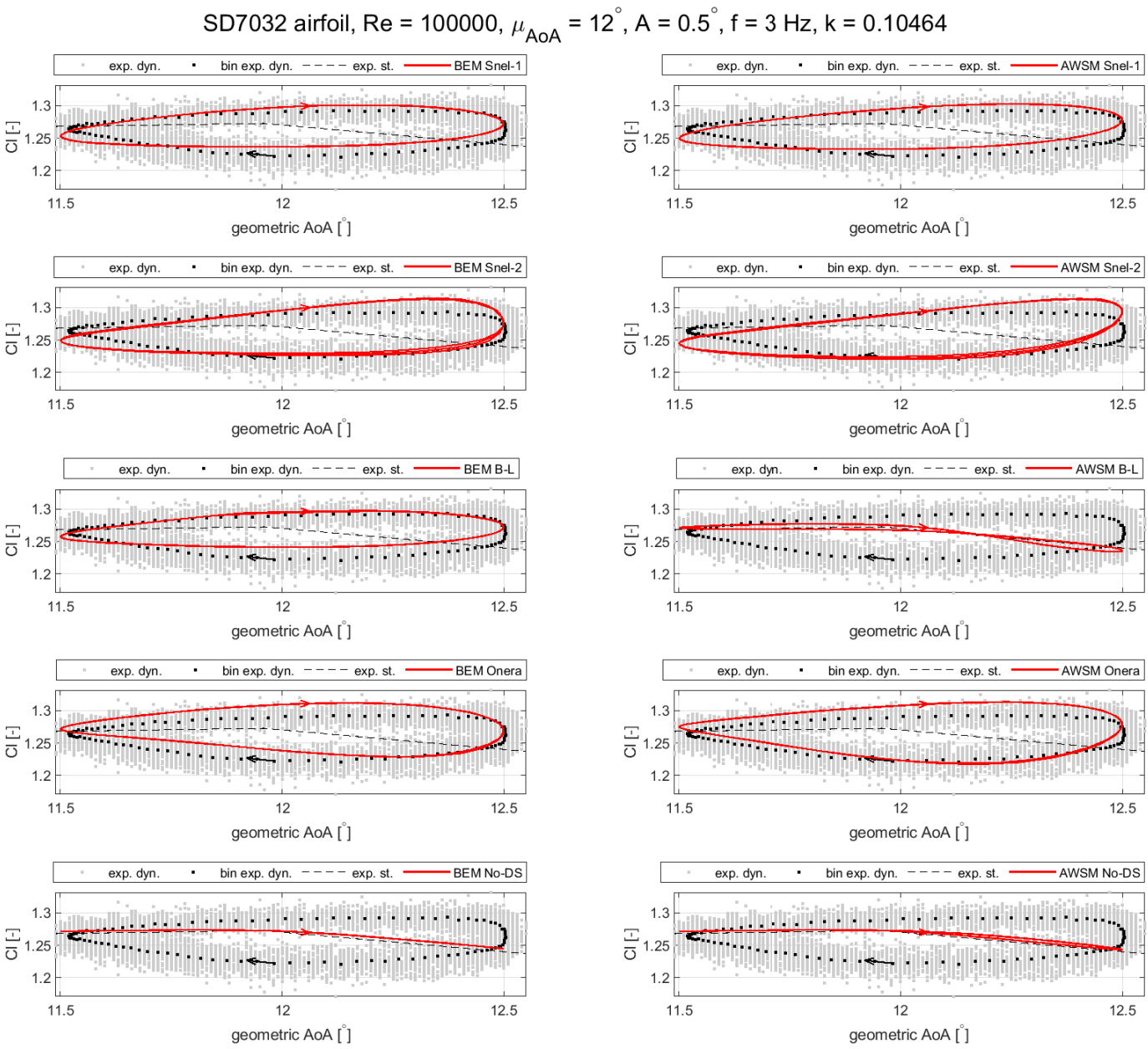

Figure A.67: Comparison between SD7032 airfoil's experimental dynamic lift coefficient (incuding the bin average) and that predicted by means of different unsteay airfoil aerodynamic models for a Reynolds number of 100000. Geometric angle of attack mean, μ_{AoA}, and amplitude, A, are respectively equal to 12° and 5.0°, while frequency, f, is 0.25 Hz. In the figure, k denotes the reduced frequency.

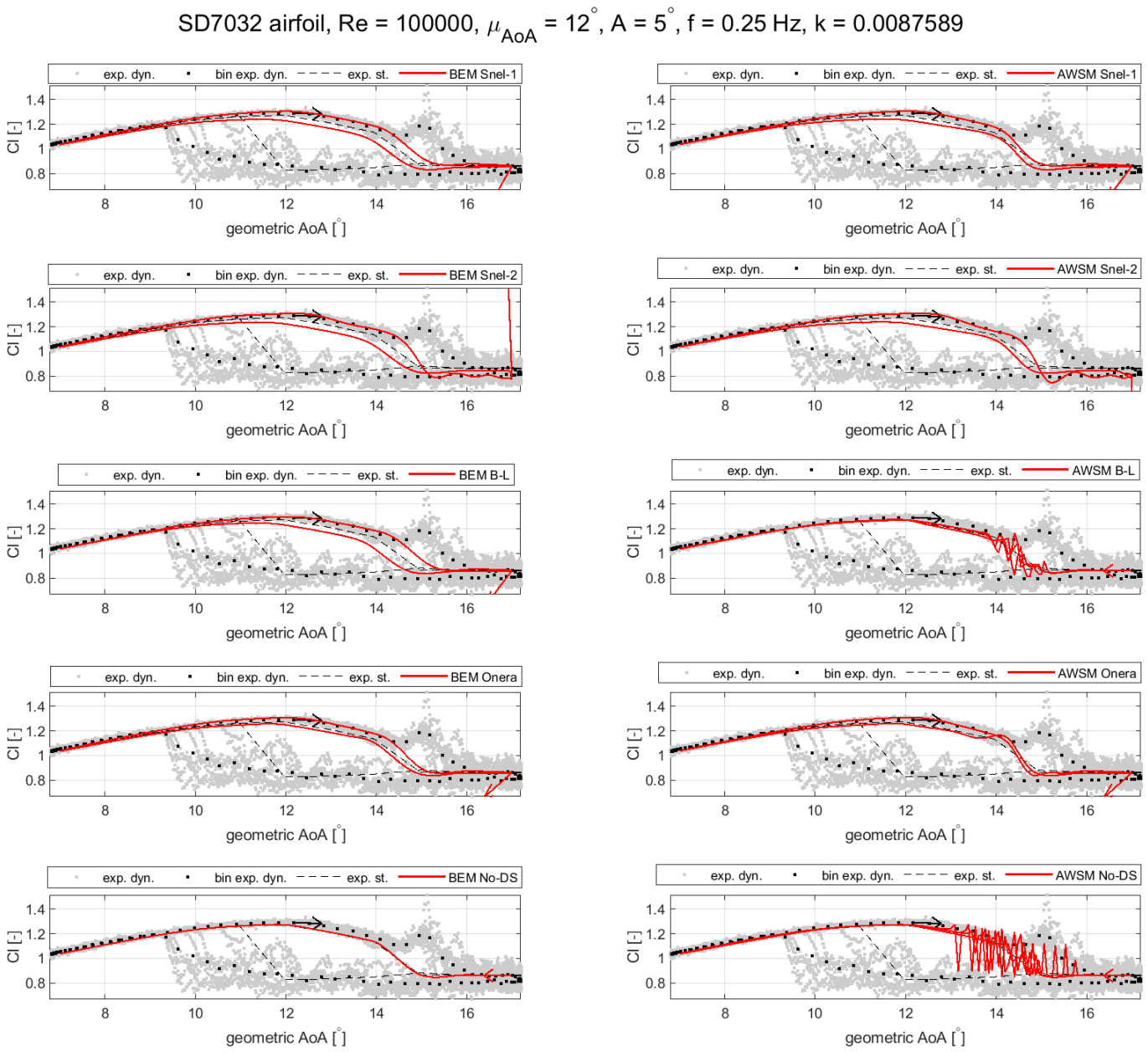

Figure A.68: Comparison between SD7032 airfoil's experimental dynamic lift coefficient (incuding the bin average) and that predicted by means of different unsteay airfoil aerodynamic models for a Reynolds number of 100000. Geometric angle of attack mean, μ_{AoA}, and amplitude, A, are respectively equal to 12° and 5.0°, while frequency, f, is 0.50 Hz. In the figure, k denotes the reduced frequency.

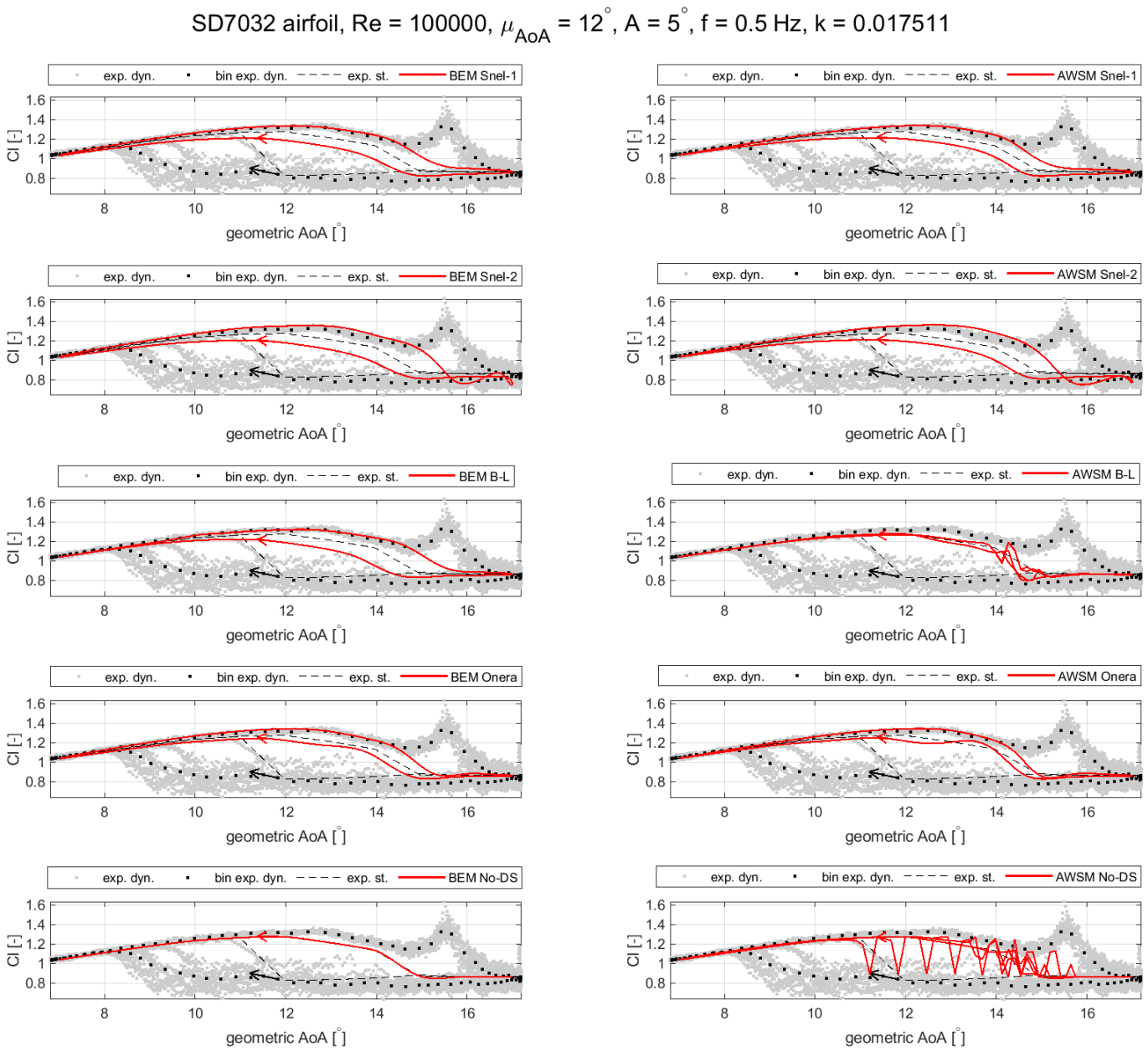

Figure A.69: Comparison between SD7032 airfoil's experimental dynamic lift coefficient (incuding the bin average) and that predicted by means of different unsteay airfoil aerodynamic models for a Reynolds number of 100000. Geometric angle of attack mean, μ_{AoA}, and amplitude, A, are respectively equal to 12° and 5.0°, while frequency, f, is 1.50 Hz. In the figure, k denotes the reduced frequency.

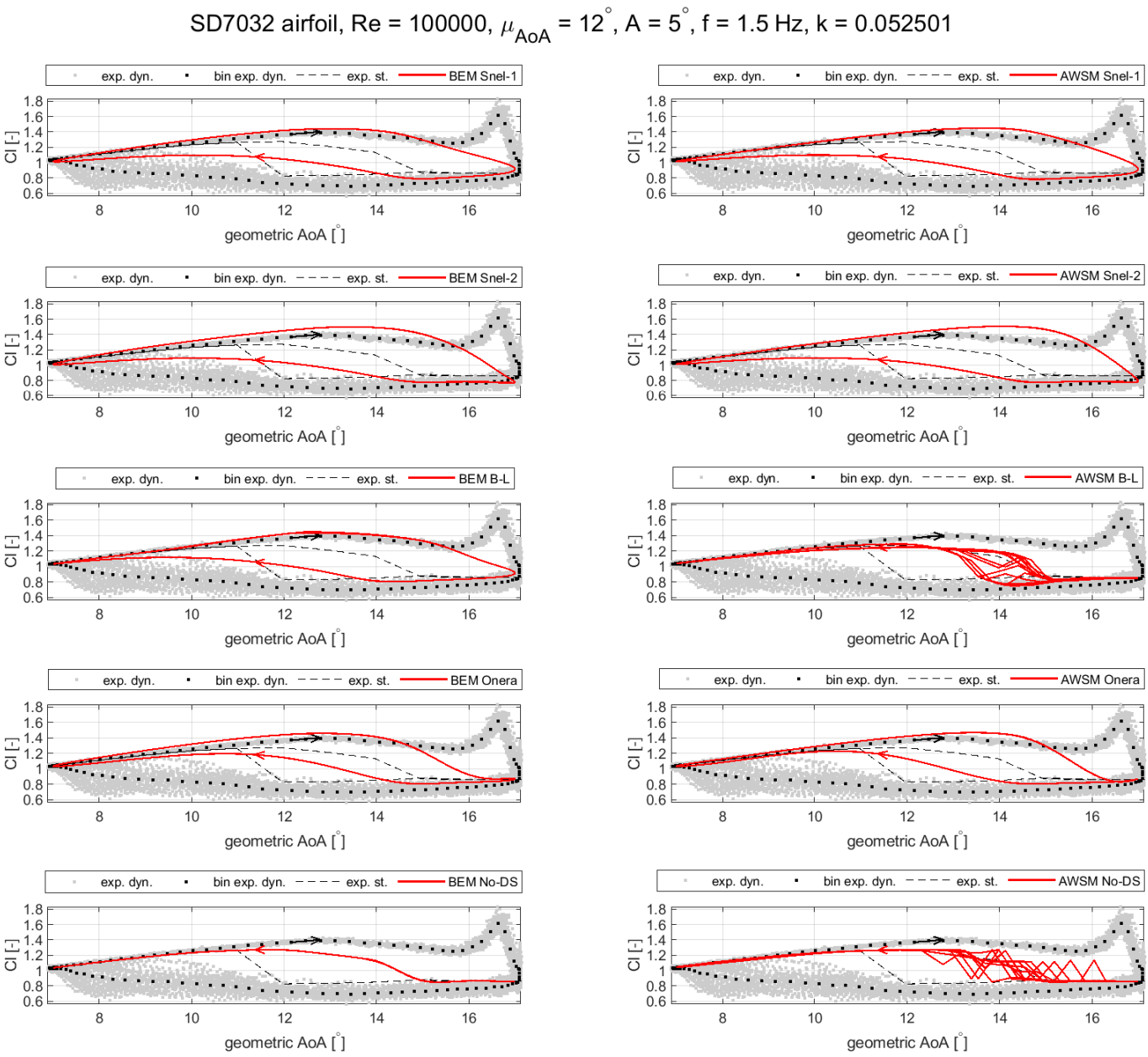

Figure A.70: Comparison between SD7032 airfoil's experimental dynamic lift coefficient (incuding the bin average) and that predicted by means of different unsteay airfoil aerodynamic models for a Reynolds number of 100000. Geometric angle of attack mean, μ_{AoA}, and amplitude, A, are respectively equal to 12° and 5.0°, while frequency, f, is 1.00 Hz. In the figure, k denotes the reduced frequency.

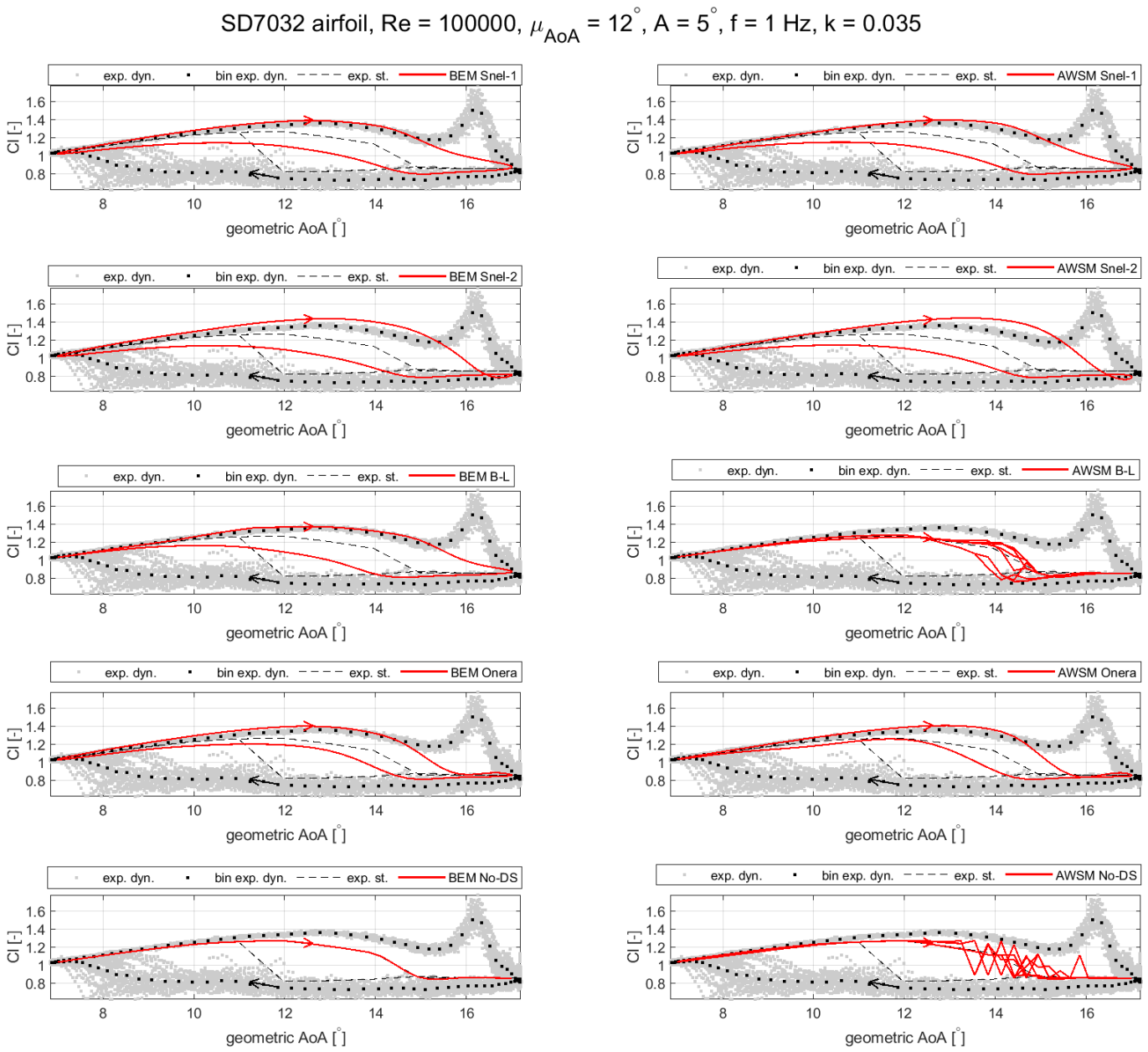

Figure A.71: Comparison between SD7032 airfoil's experimental dynamic lift coefficient (incuding the bin average) and that predicted by means of different unsteay airfoil aerodynamic models for a Reynolds number of 100000. Geometric angle of attack mean, μ_{AoA}, and amplitude, A, are respectively equal to 12° and 5.0°, while frequency, f, is 2.00 Hz. In the figure, k denotes the reduced frequency.

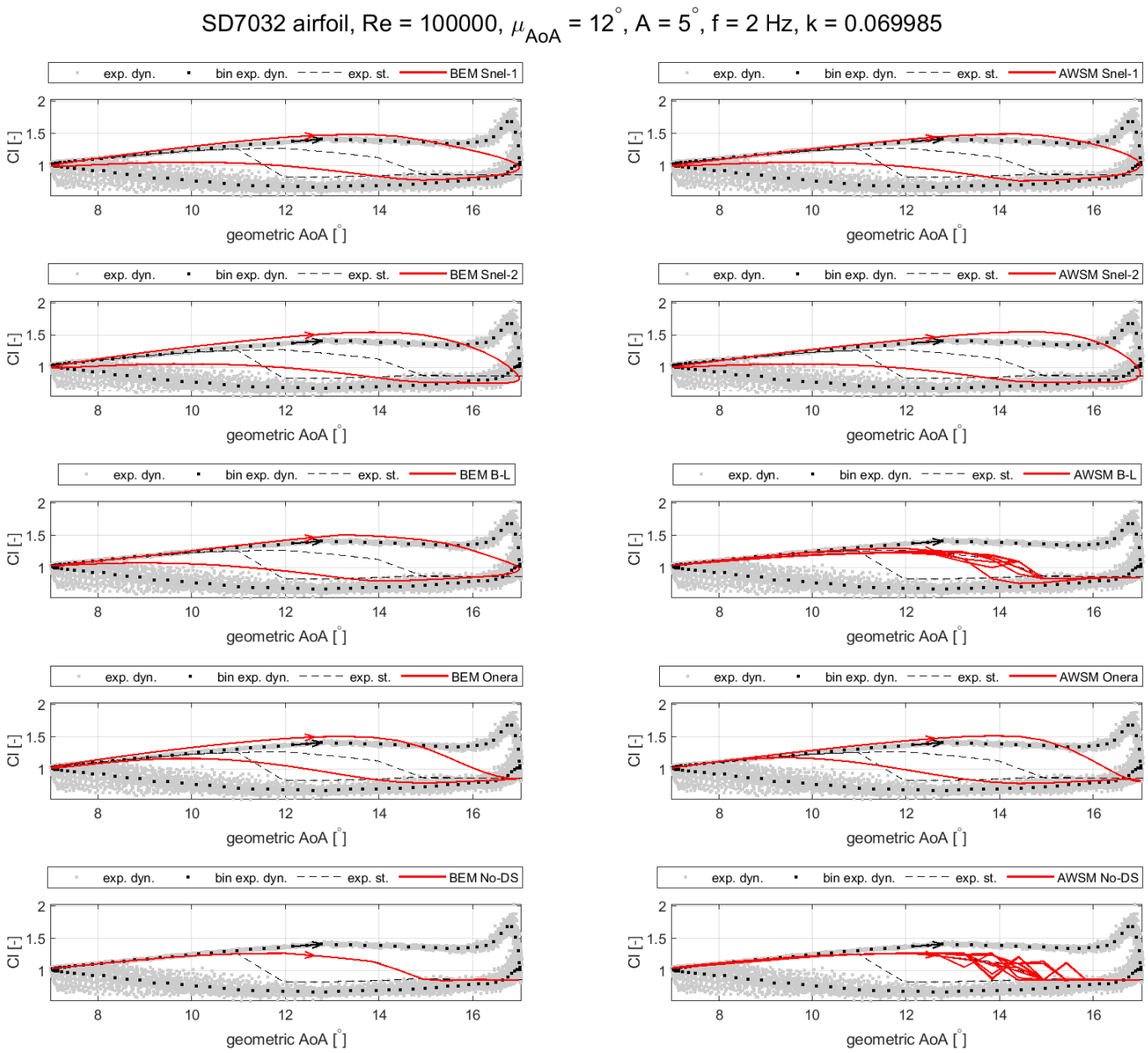

Figure A.72: Comparison between SD7032 airfoil's experimental dynamic lift coefficient (incuding the bin average) and that predicted by means of different unsteay airfoil aerodynamic models for a Reynolds number of 100000. Geometric angle of attack mean, μ_{AoA}, and amplitude, A, are respectively equal to 12° and 5.0°, while frequency, f, is 3.00 Hz. In the figure, k denotes the reduced frequency.

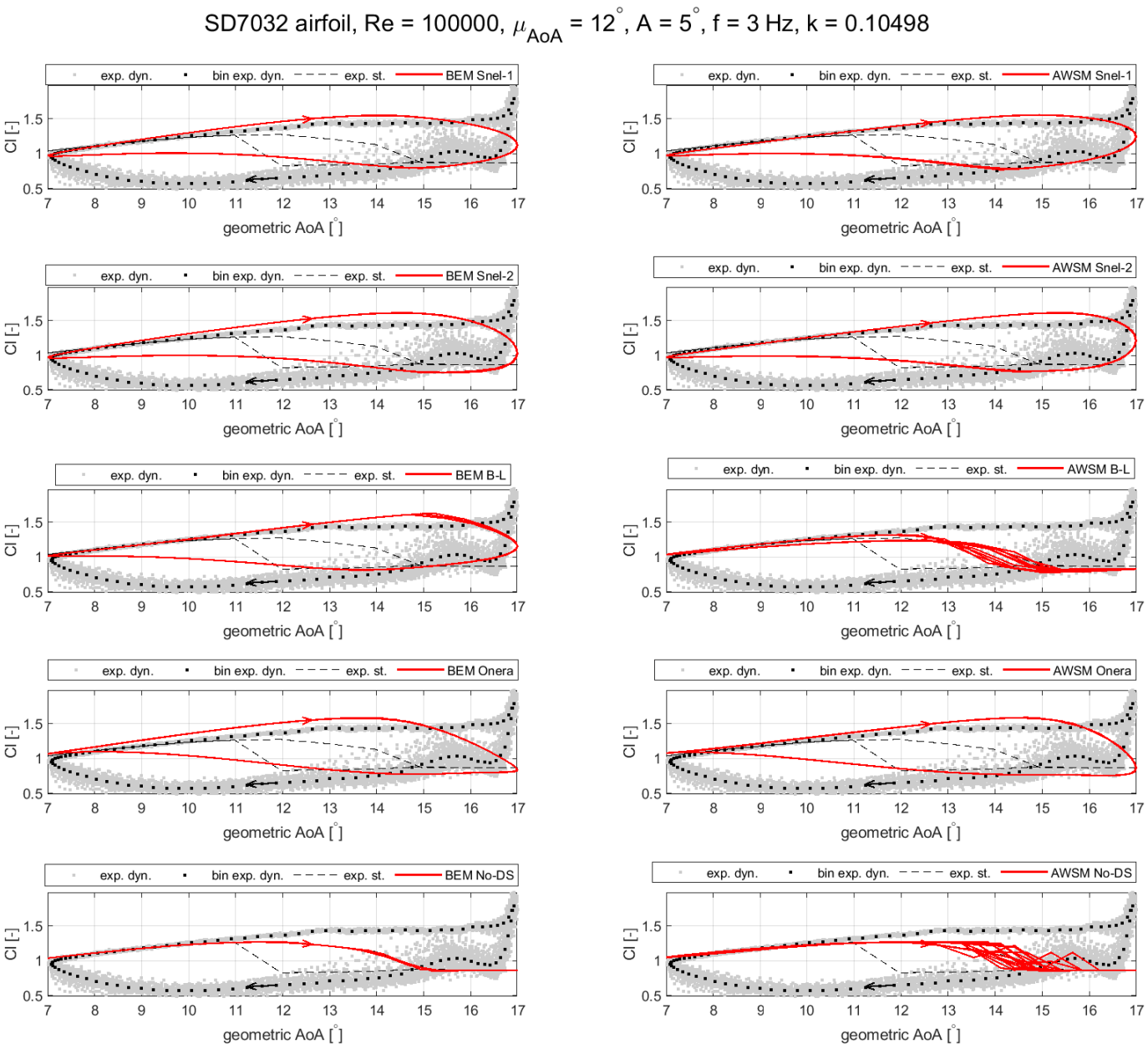

Figure A.73: Comparison between SD7032 airfoil's experimental dynamic lift coefficient (incuding the bin average) and that predicted by means of different unsteay airfoil aerodynamic models for a Reynolds number of 100000. Geometric angle of attack mean, μ_{AoA}, and amplitude, A, are respectively equal to 15° and 0.5°, while frequency, f, is 0.25 Hz. In the figure, k denotes the reduced frequency.

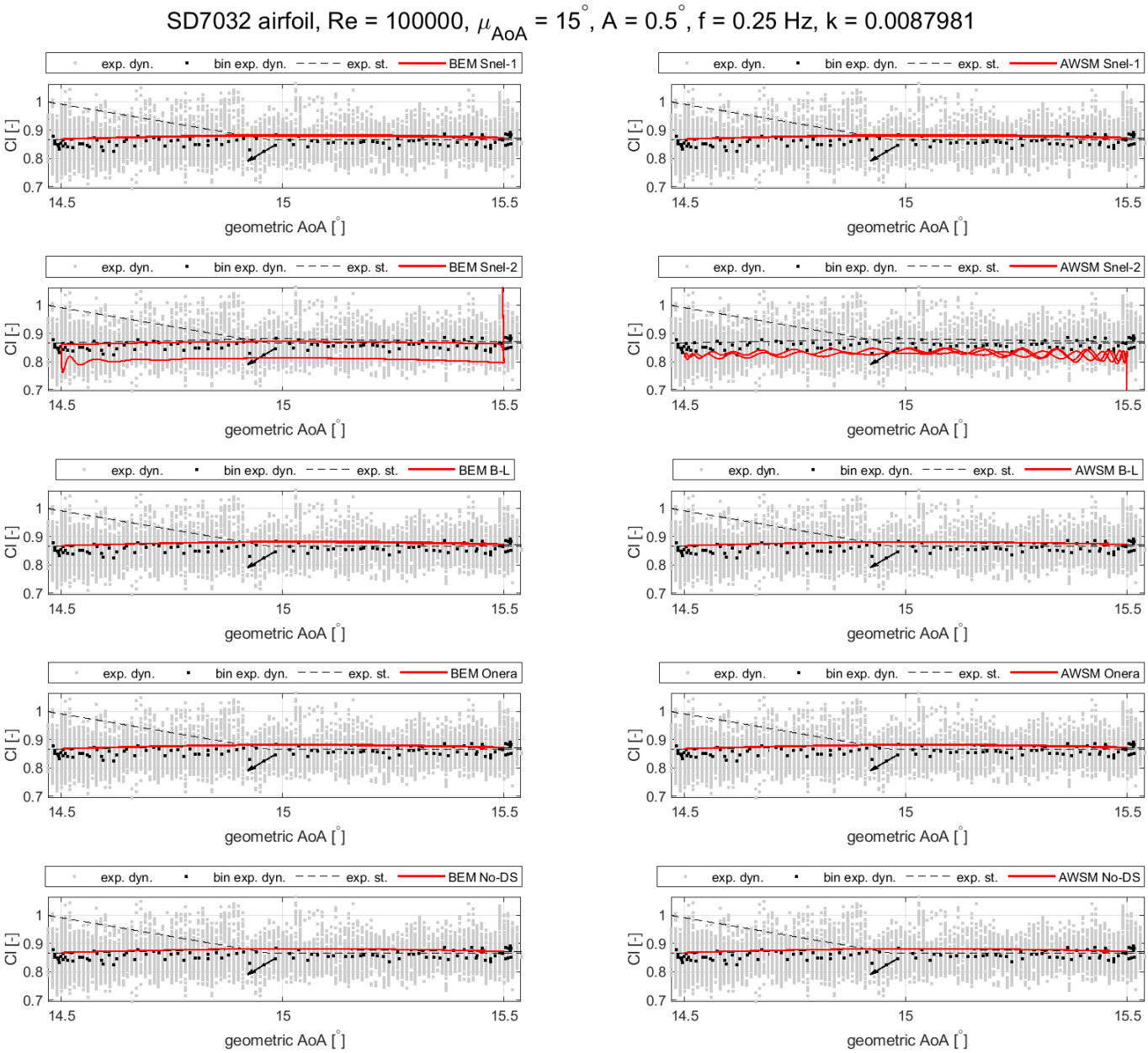

Figure A.74: Comparison between SD7032 airfoil's experimental dynamic lift coefficient (incuding the bin average) and that predicted by means of different unsteay airfoil aerodynamic models for a Reynolds number of 100000. Geometric angle of attack mean, μ_{AoA}, and amplitude, A, are respectively equal to 15° and 0.5°, while frequency, f, is 0.50 Hz. In the figure, k denotes the reduced frequency.

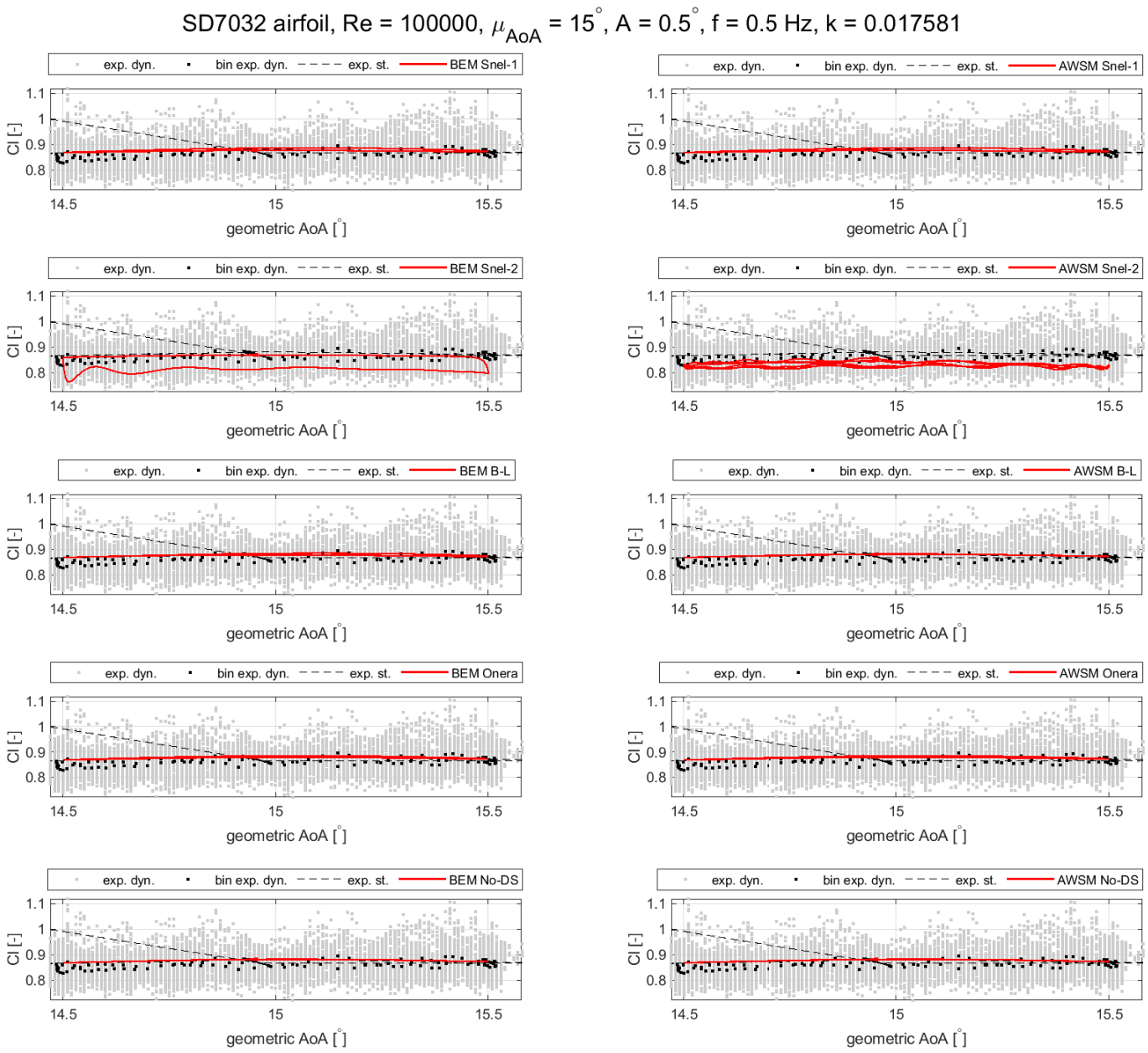

Figure A.75: Comparison between SD7032 airfoil's experimental dynamic lift coefficient (incuding the bin average) and that predicted by means of different unsteay airfoil aerodynamic models for a Reynolds number of 100000. Geometric angle of attack mean, μ_{AoA}, and amplitude, A, are respectively equal to 15° and 0.5°, while frequency, f, is 1.50 Hz. In the figure, k denotes the reduced frequency.

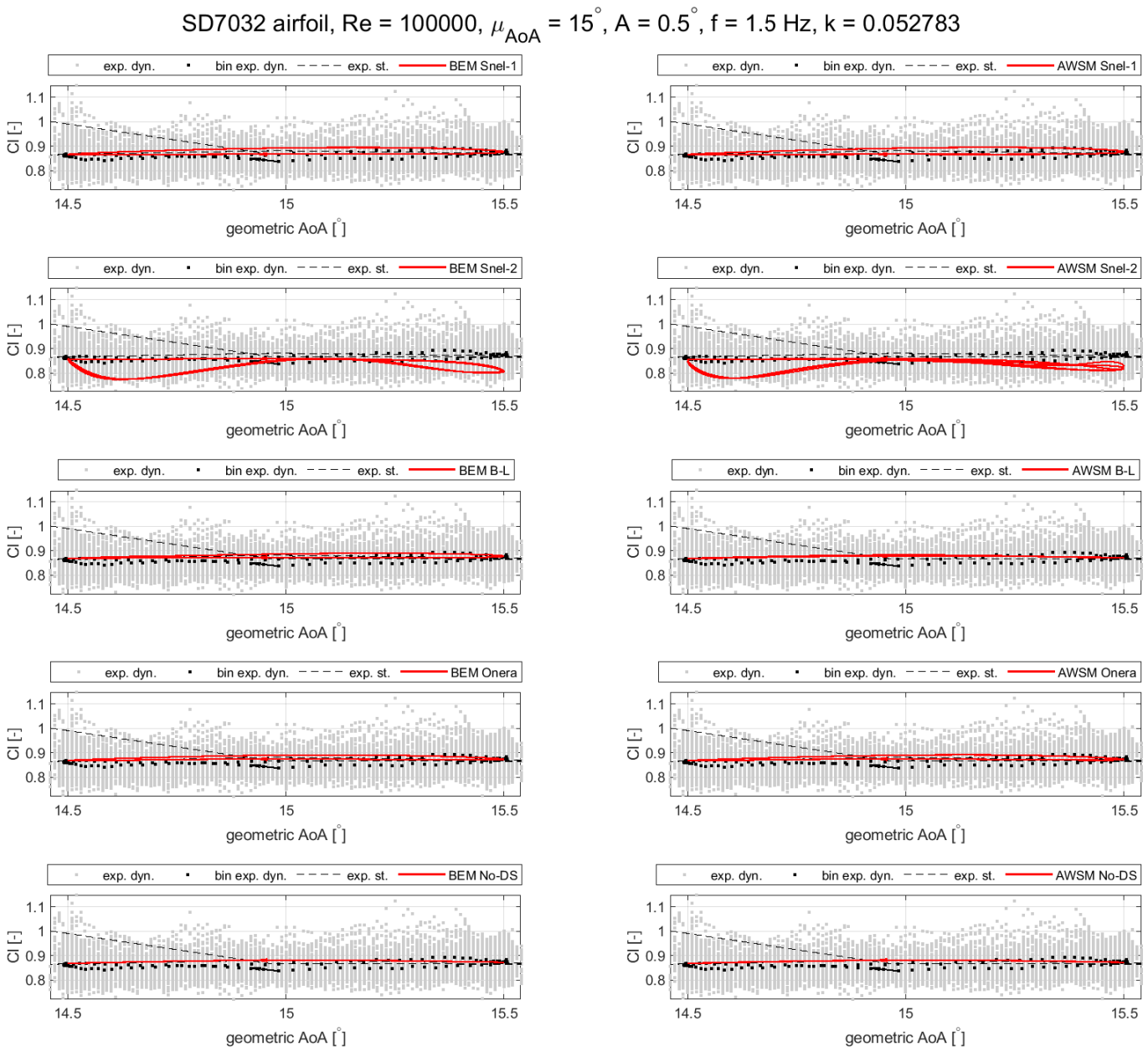

Figure A.76: Comparison between SD7032 airfoil's experimental dynamic lift coefficient (incuding the bin average) and that predicted by means of different unsteay airfoil aerodynamic models for a Reynolds number of 100000. Geometric angle of attack mean, μ_{AoA}, and amplitude, A, are respectively equal to 15° and 0.5°, while frequency, f, is 1.00 Hz. In the figure, k denotes the reduced frequency.

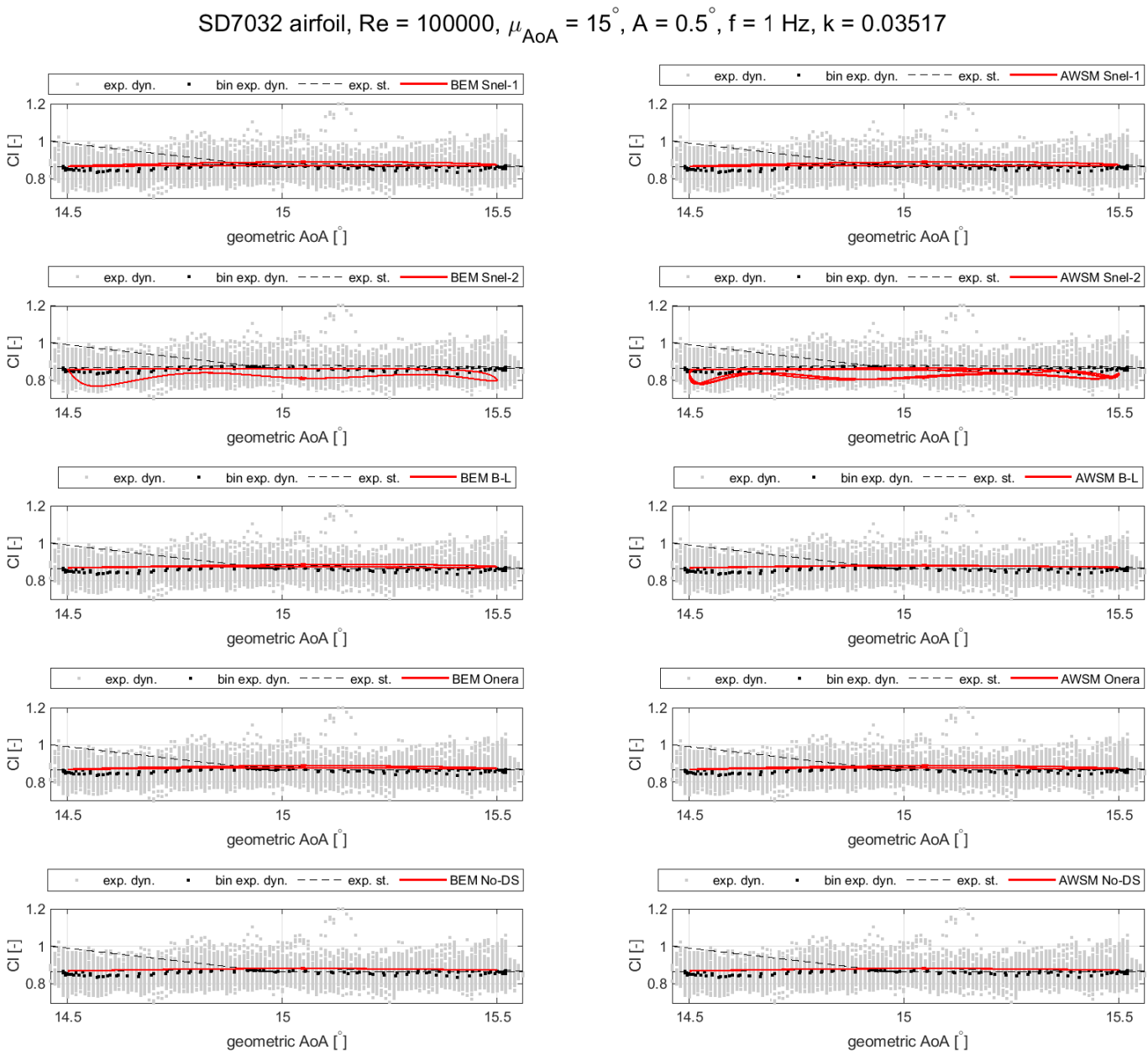

Figure A.77: Comparison between SD7032 airfoil's experimental dynamic lift coefficient (incuding the bin average) and that predicted by means of different unsteay airfoil aerodynamic models for a Reynolds number of 100000. Geometric angle of attack mean, μ_{AoA}, and amplitude, A, are respectively equal to 15° and 0.5°, while frequency, f, is 2.00 Hz. In the figure, k denotes the reduced frequency.

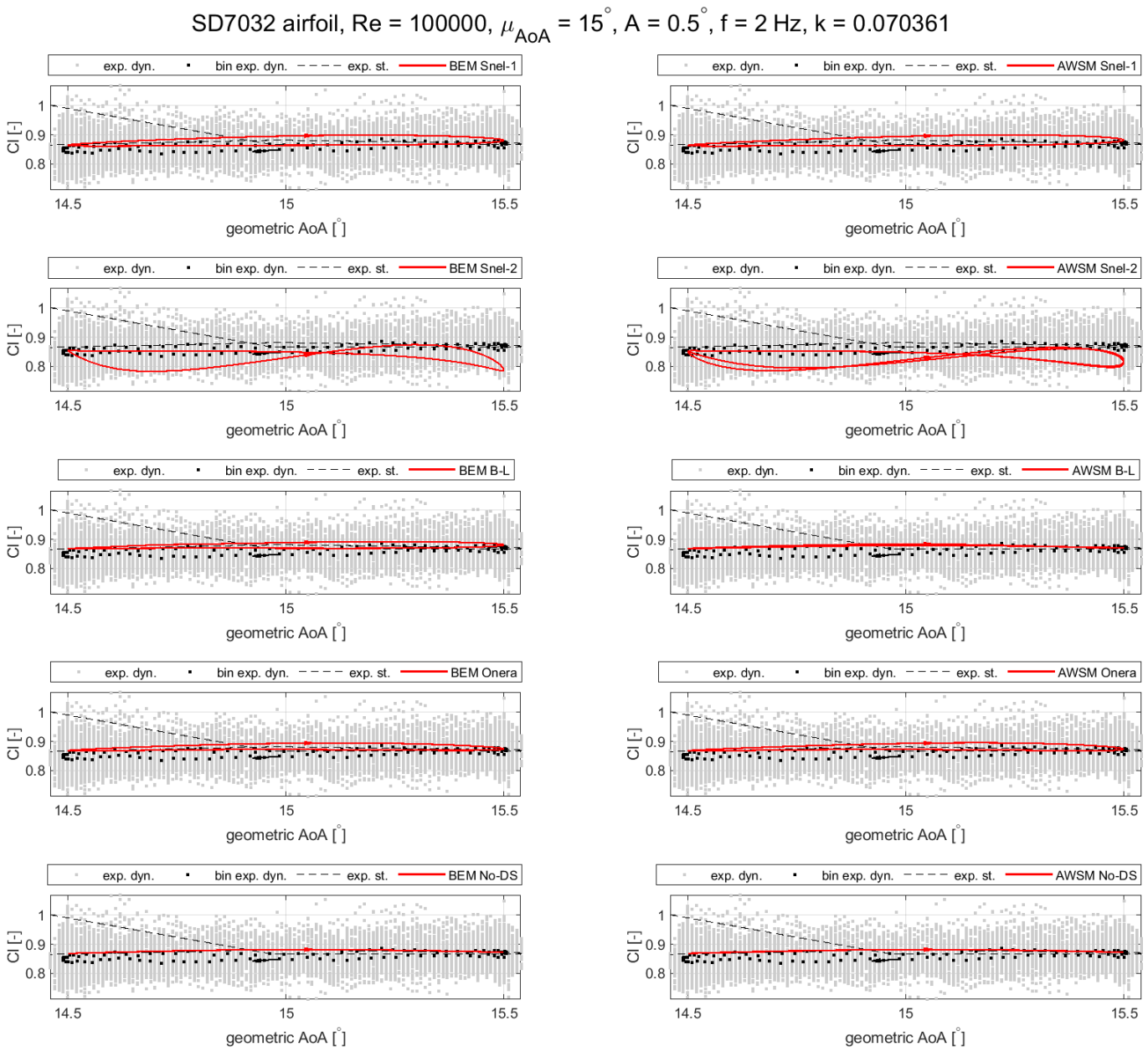

Figure A.78: Comparison between SD7032 airfoil's experimental dynamic lift coefficient (incuding the bin average) and that predicted by means of different unsteay airfoil aerodynamic models for a Reynolds number of 100000. Geometric angle of attack mean, μ_{AoA}, and amplitude, A, are respectively equal to 15° and 0.5°, while frequency, f, is 3.00 Hz. In the figure, k denotes the reduced frequency.

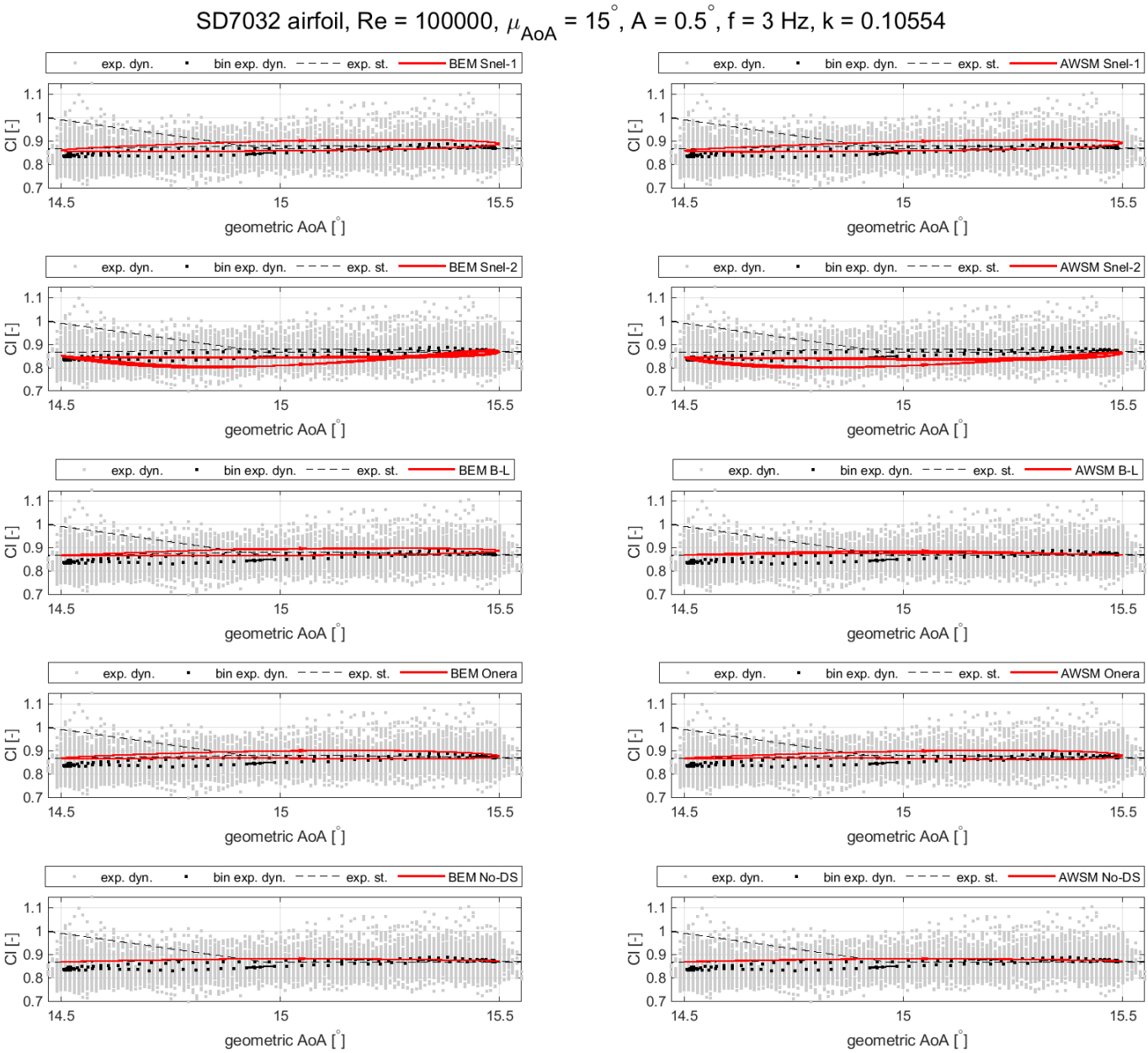

Figure A.79: Comparison between SD7032 airfoil's experimental dynamic lift coefficient (incuding the bin average) and that predicted by means of different unsteay airfoil aerodynamic models for a Reynolds number of 100000. Geometric angle of attack mean, μ_{AoA}, and amplitude, A, are respectively equal to 15° and 5.0°, while frequency, f, is 0.25 Hz. In the figure, k denotes the reduced frequency.

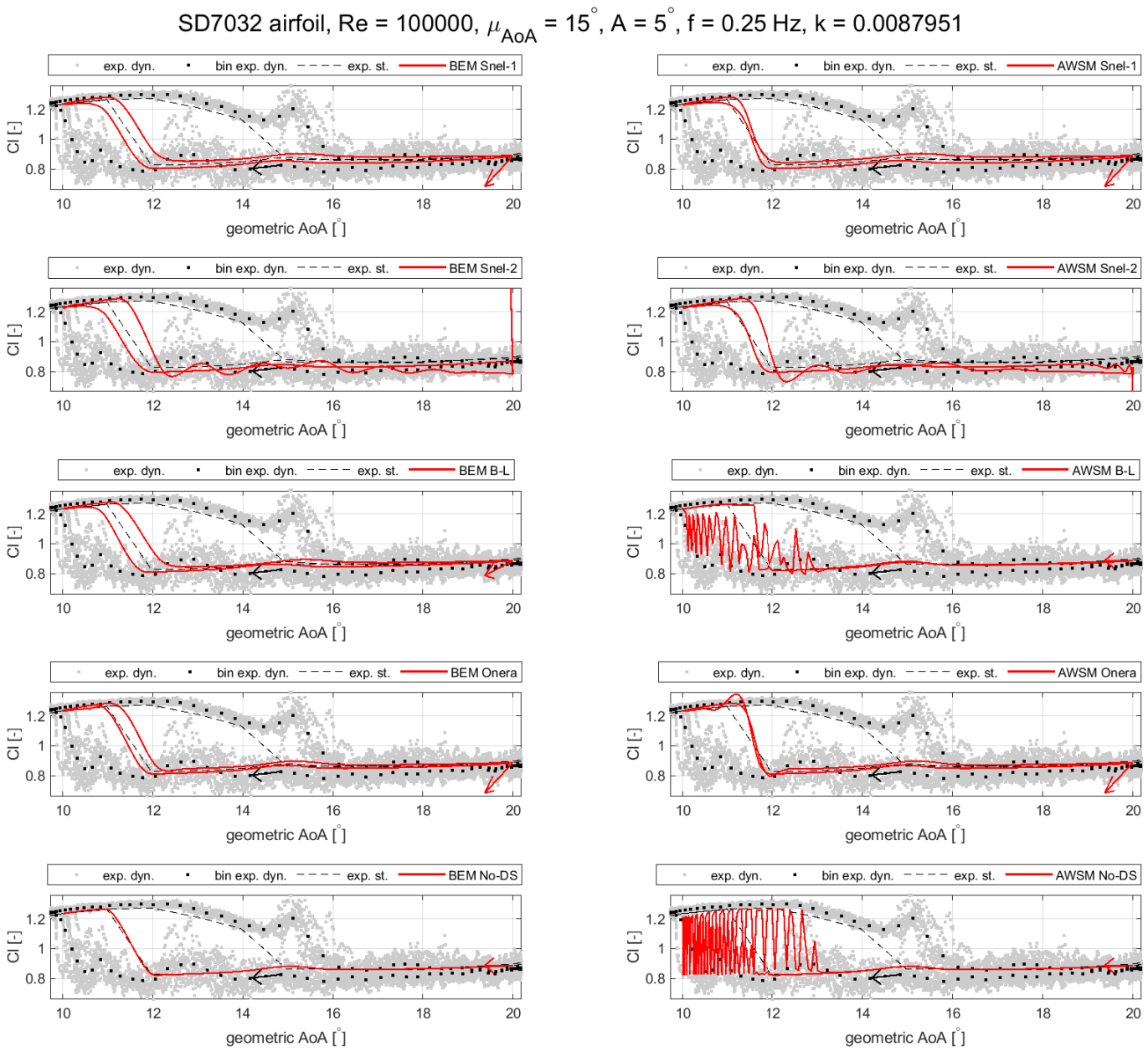

Figure A.80: Comparison between SD7032 airfoil's experimental dynamic lift coefficient (incuding the bin average) and that predicted by means of different unsteay airfoil aerodynamic models for a Reynolds number of 100000. Geometric angle of attack mean, μ_{AoA}, and amplitude, A, are respectively equal to 15° and 5.0°, while frequency, f, is 0.50 Hz. In the figure, k denotes the reduced frequency.

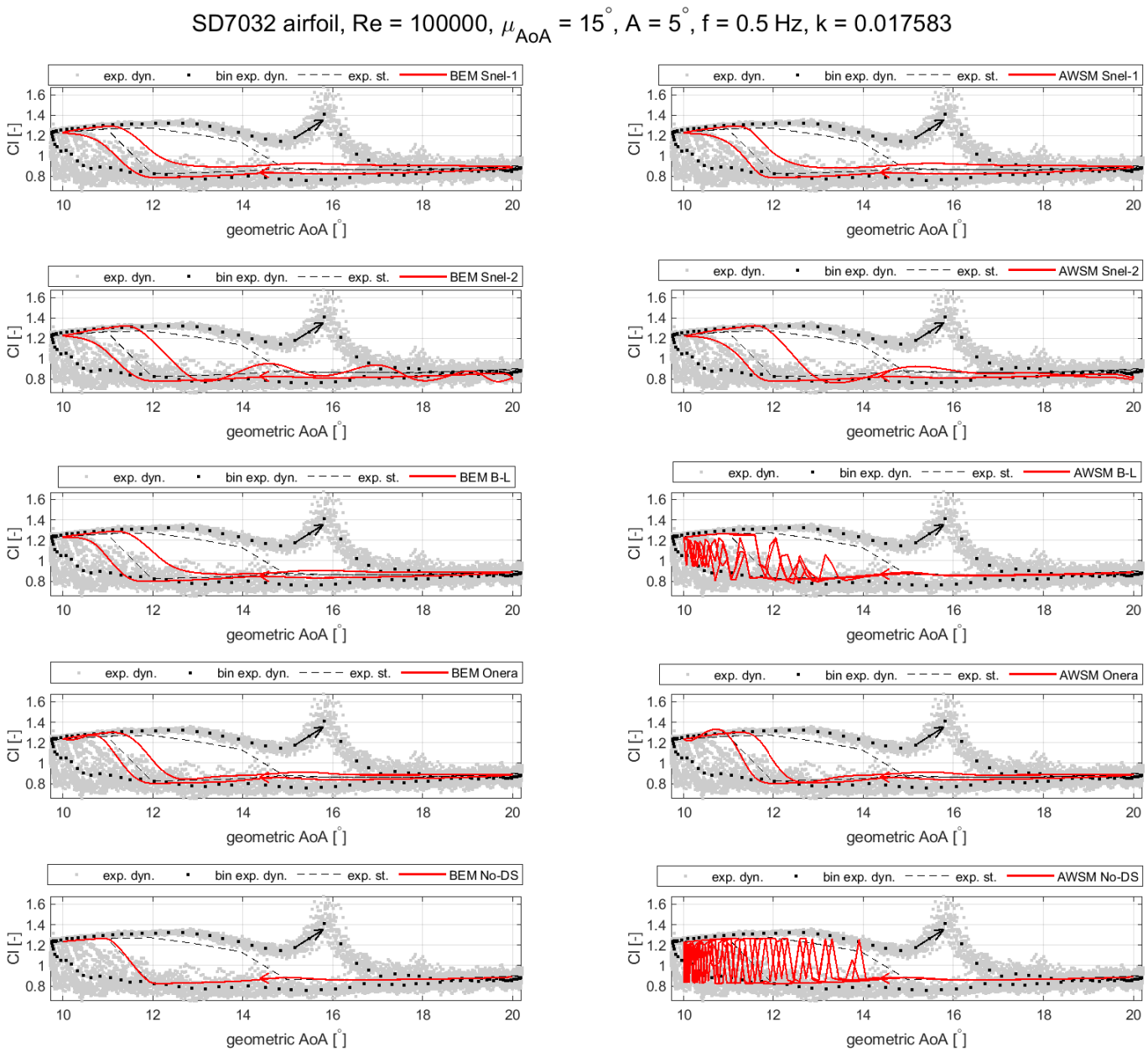

Figure A.81: Comparison between SD7032 airfoil's experimental dynamic lift coefficient (incuding the bin average) and that predicted by means of different unsteay airfoil aerodynamic models for a Reynolds number of 100000. Geometric angle of attack mean, μ_{AoA}, and amplitude, A, are respectively equal to 15° and 5.0°, while frequency, f, is 1.50 Hz. In the figure, k denotes the reduced frequency.

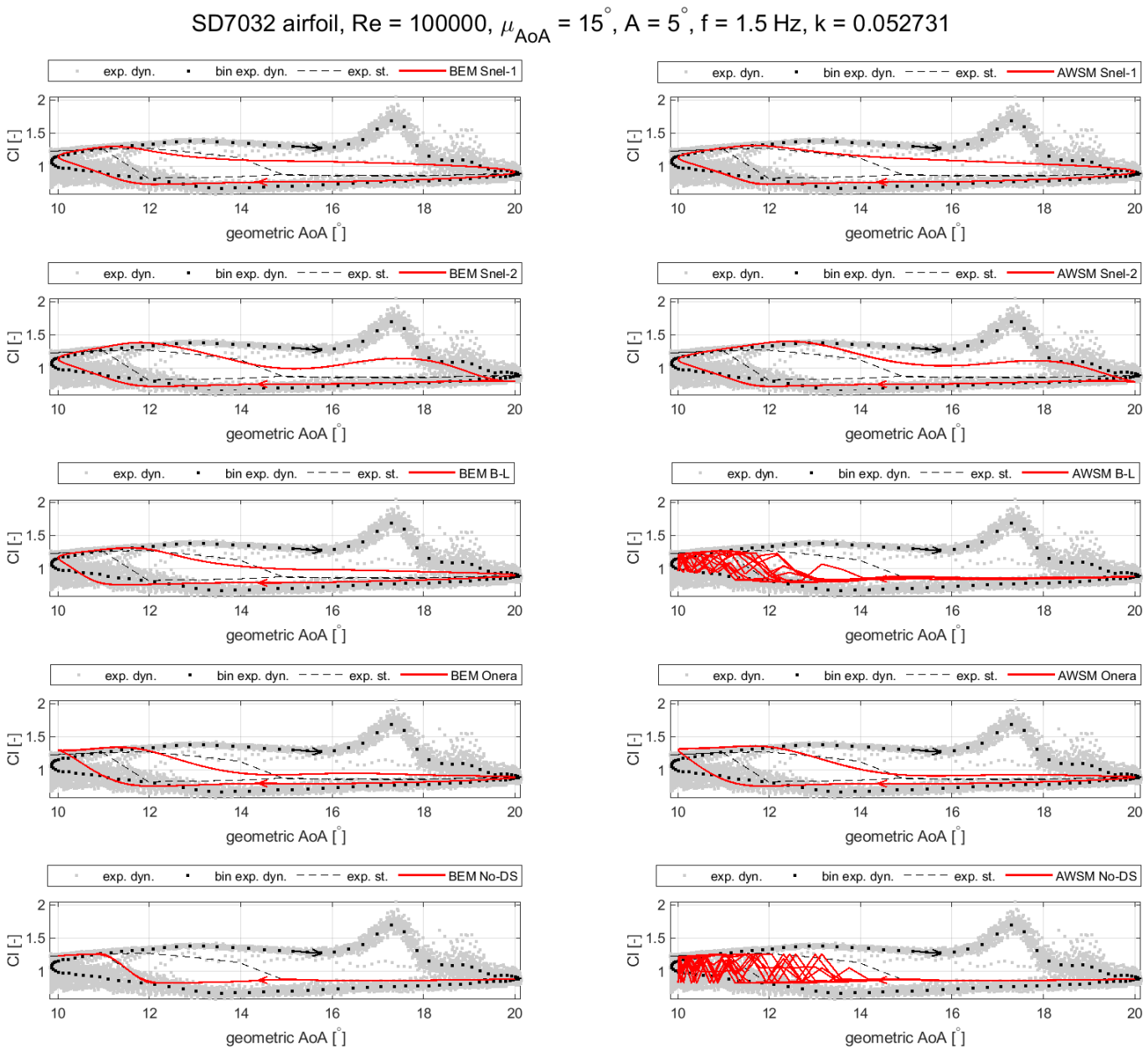

Figure A.82: Comparison between SD7032 airfoil's experimental dynamic lift coefficient (incuding the bin average) and that predicted by means of different unsteay airfoil aerodynamic models for a Reynolds number of 100000. Geometric angle of attack mean, μ_{AoA}, and amplitude, A, are respectively equal to 15° and 5.0°, while frequency, f, is 1.00 Hz. In the figure, k denotes the reduced frequency.

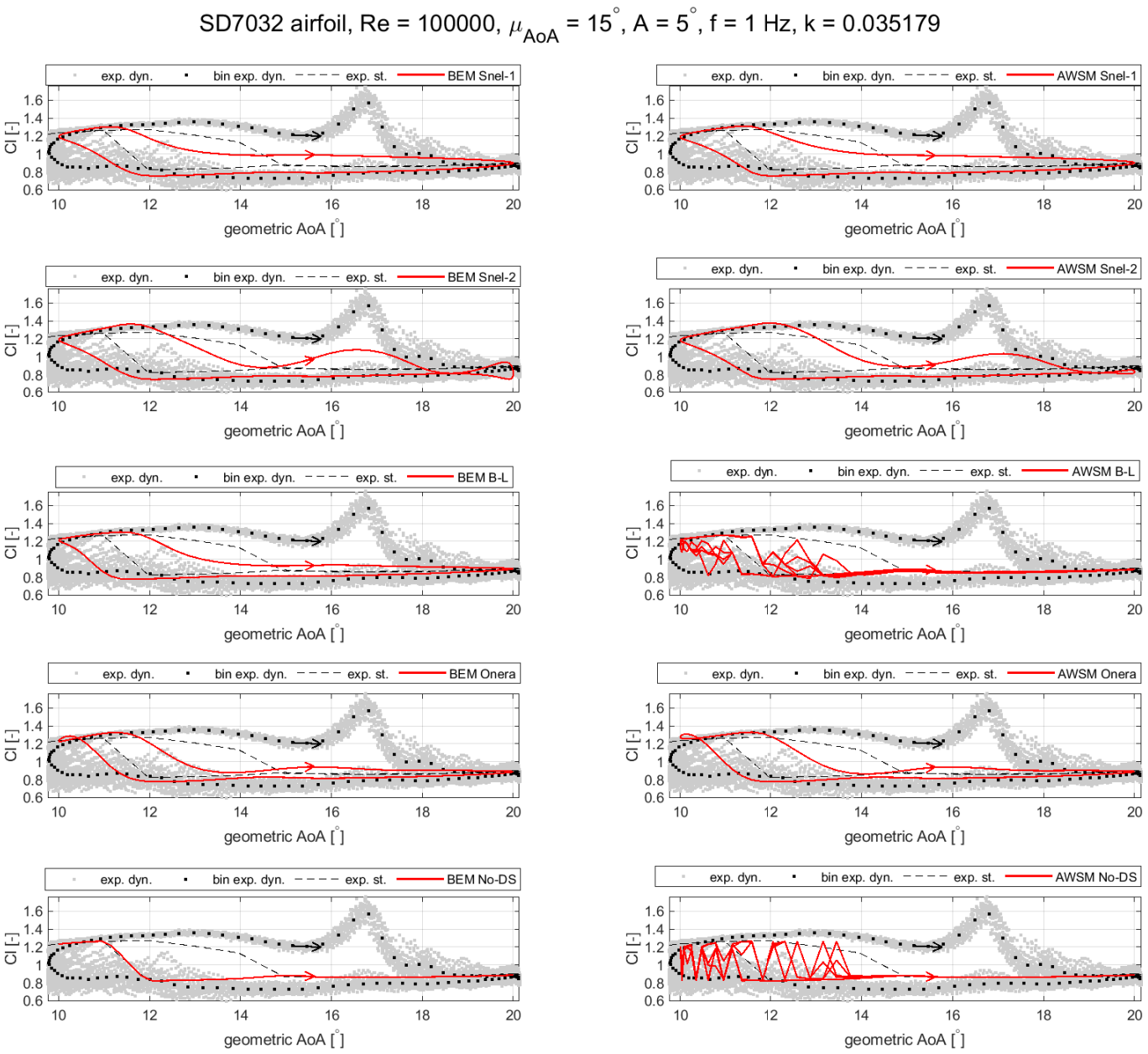

Figure A.83: Comparison between SD7032 airfoil's experimental dynamic lift coefficient (incuding the bin average) and that predicted by means of different unsteay airfoil aerodynamic models for a Reynolds number of 100000. Geometric angle of attack mean, μ_{AoA}, and amplitude, A, are respectively equal to 15° and 5.0°, while frequency, f, is 2.00 Hz. In the figure, k denotes the reduced frequency.

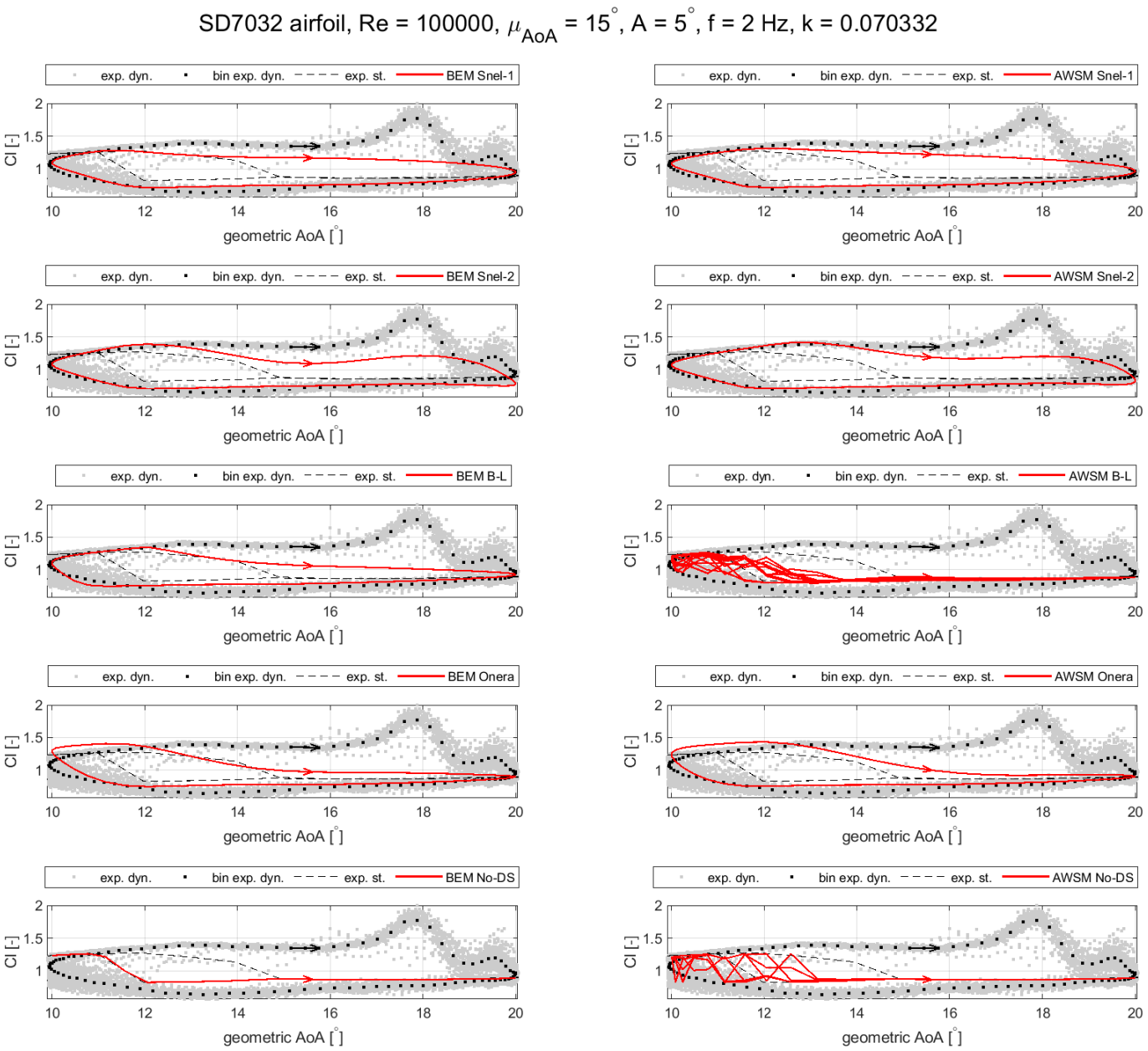

Figure A.84: Comparison between SD7032 airfoil's experimental dynamic lift coefficient (incuding the bin average) and that predicted by means of different unsteay airfoil aerodynamic models for a Reynolds number of 100000. Geometric angle of attack mean, μ_{AoA}, and amplitude, A, are respectively equal to 15° and 5.0°, while frequency, f, is 3.00 Hz. In the figure, k denotes the reduced frequency.

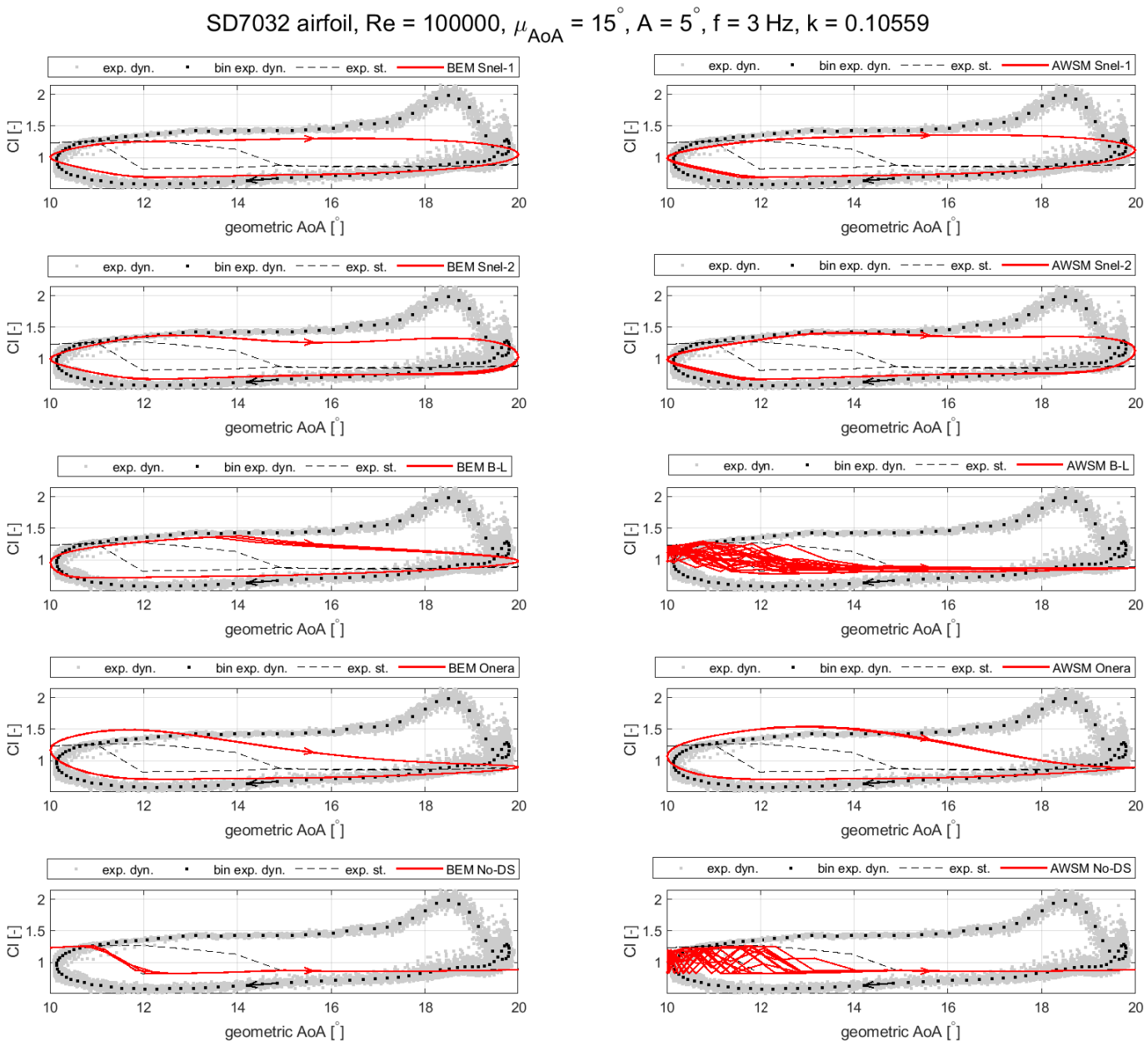

B Rotor plots

B.1 Surge cases with constant frequency

Figure B.1: Response of the angle of attack at 75% blade span, rotor thrust and rotor torque to a surge motion characterized by frequency of 0.5 Hz and amplitude 0.0325 m.

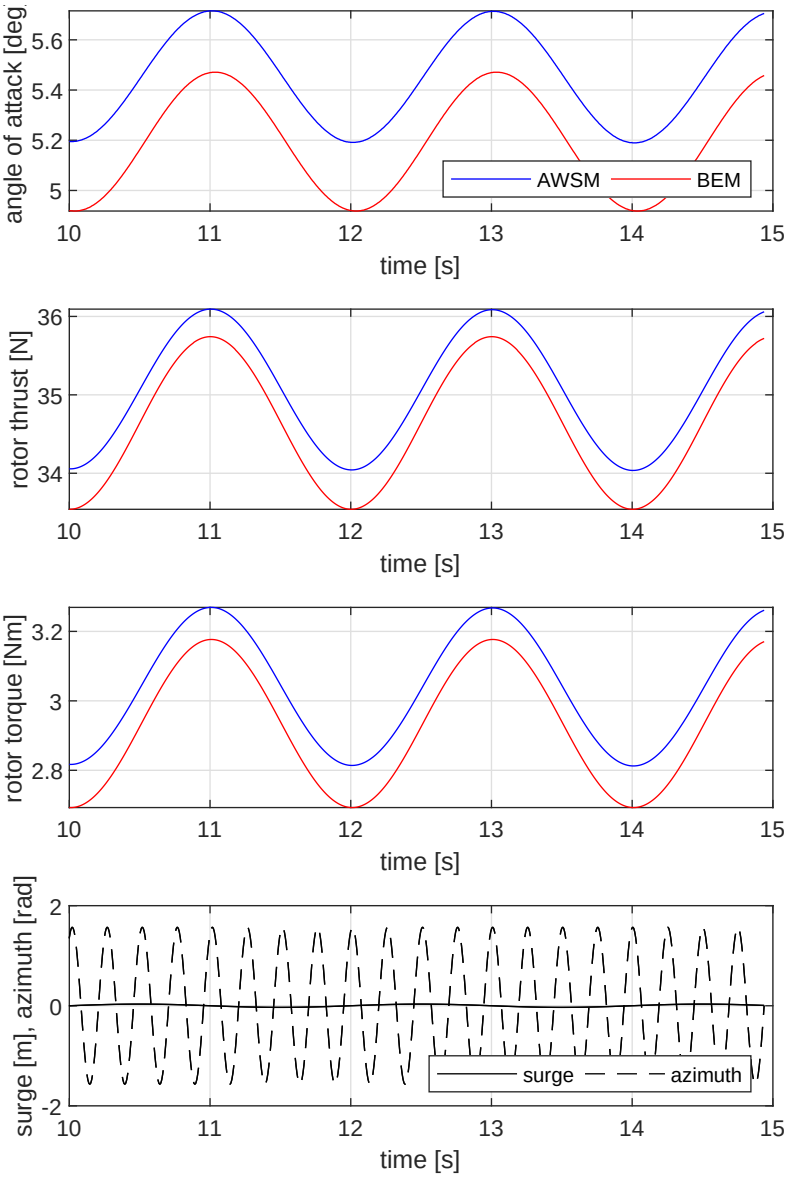

Figure B.2: Hysteresis loops of the angle of attack at 75% blade span, rotor thrust and rotor torque for a surge motion characterized by frequency of 0.5 Hz and amplitude 0.0325 m.

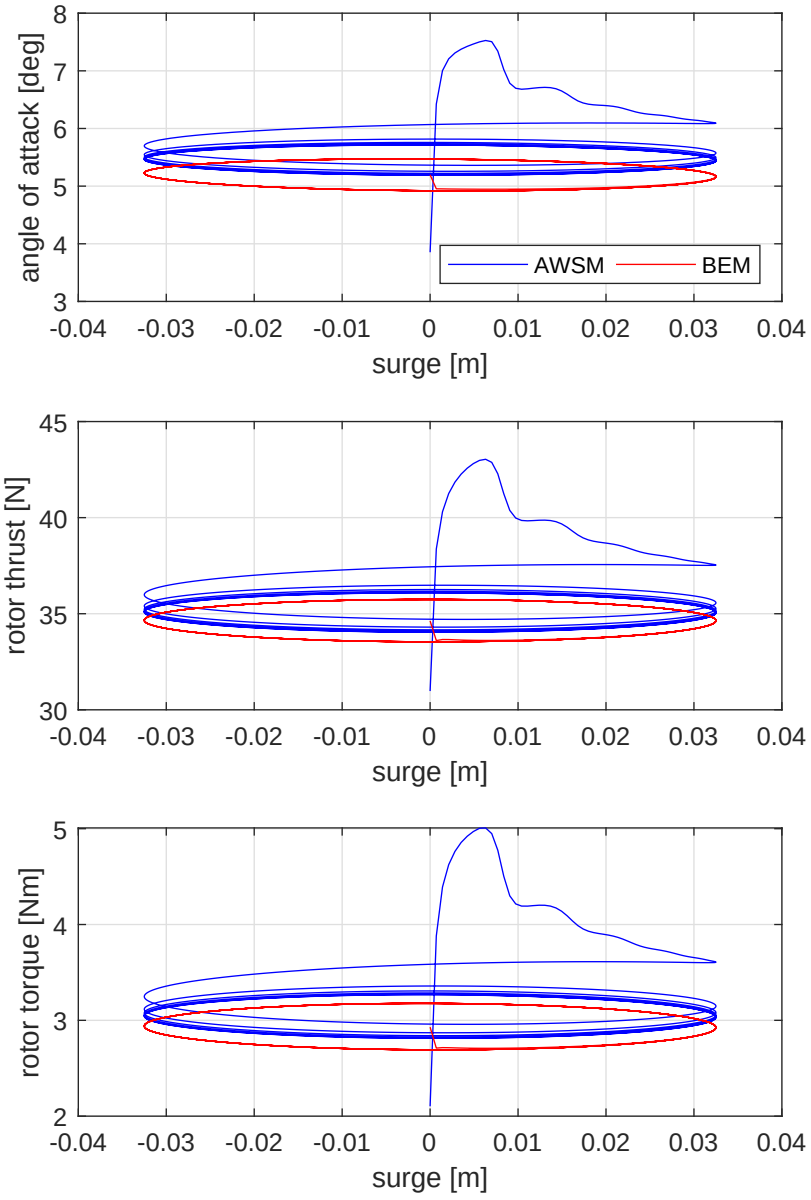

Figure B.3: Response of the angle of attack at 75% blade span, rotor thrust and rotor torque to a surge motion characterized by frequency of 0.5 Hz and amplitude 0.065 m.

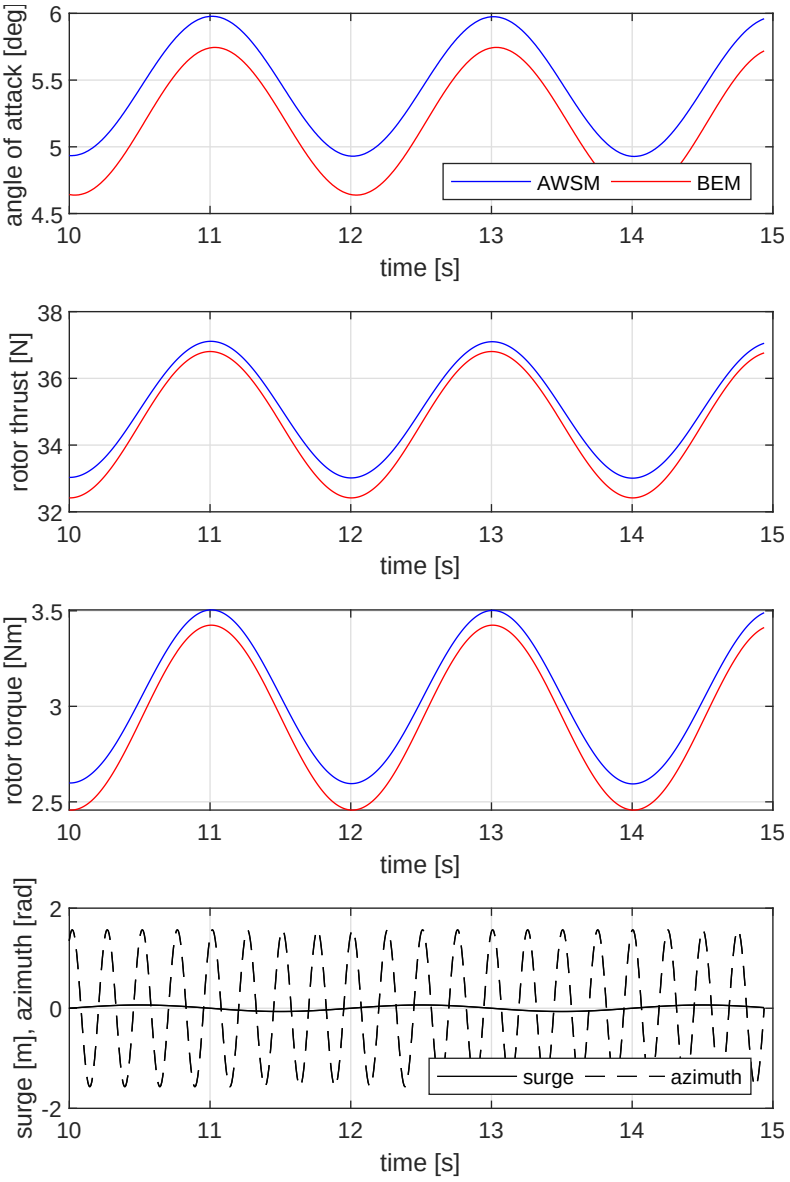

Figure B.4: Hysteresis loops of the angle of attack at 75% blade span, rotor thrust and rotor torque for a surge motion characterized by frequency of 0.5 Hz and amplitude 0.065 m.

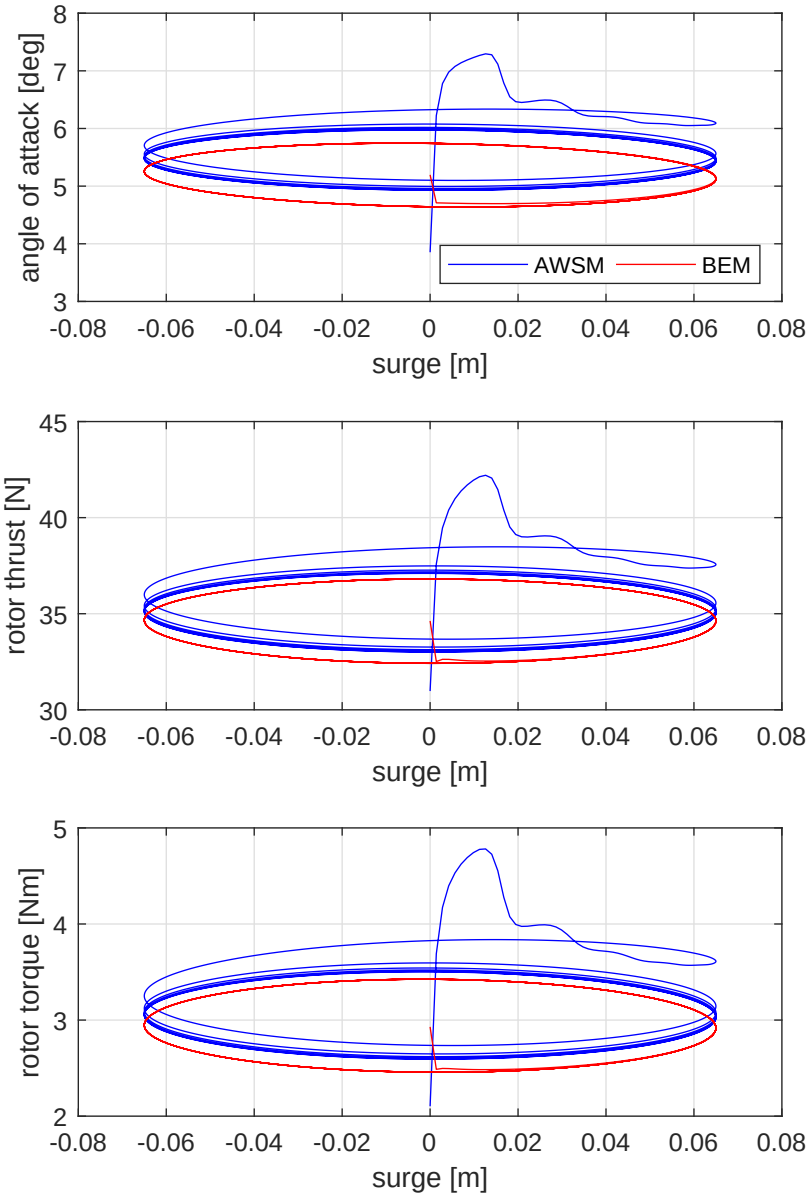

Figure B.5: Response of the angle of attack at 75% blade span, rotor thrust and rotor torque to a surge motion characterized by frequency of 0.5 Hz and amplitude 0.13 m.

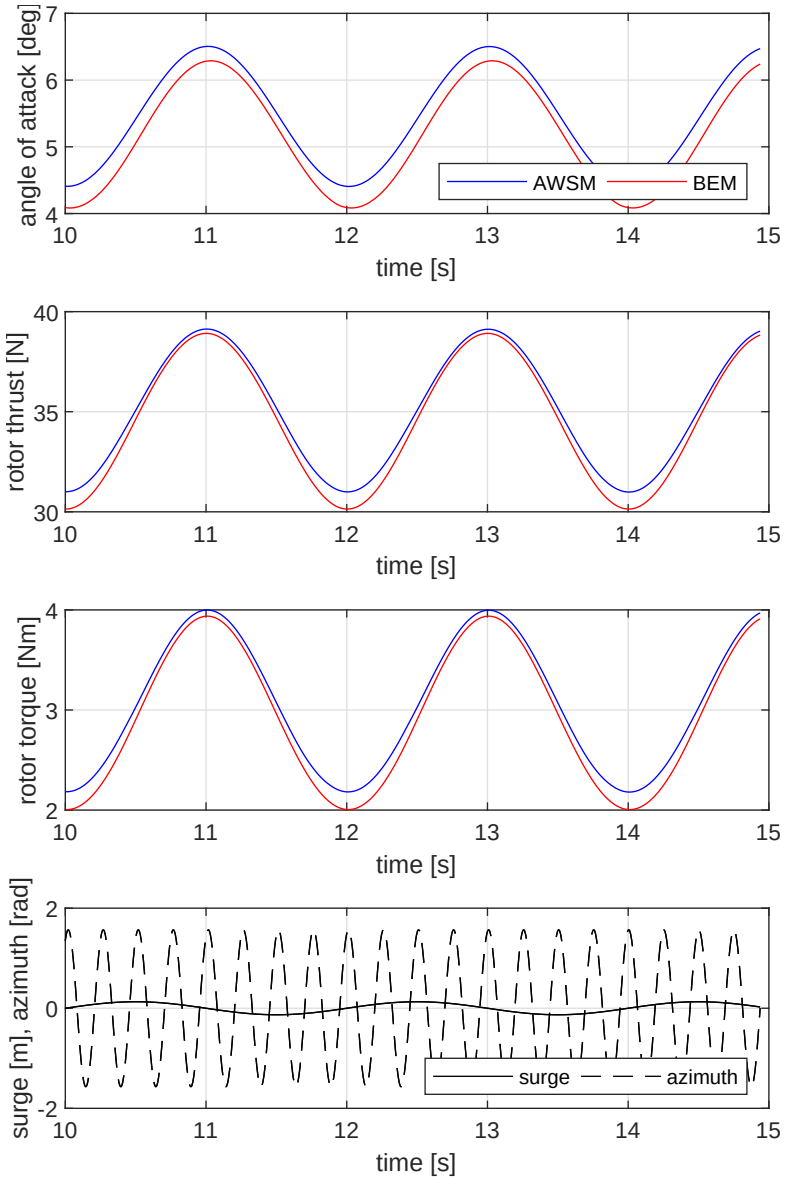

Figure B.6: Hysteresis loops of the angle of attack at 75% blade span, rotor thrust and rotor torque for a surge motion characterized by frequency of 0.5 Hz and amplitude 0.13 m.

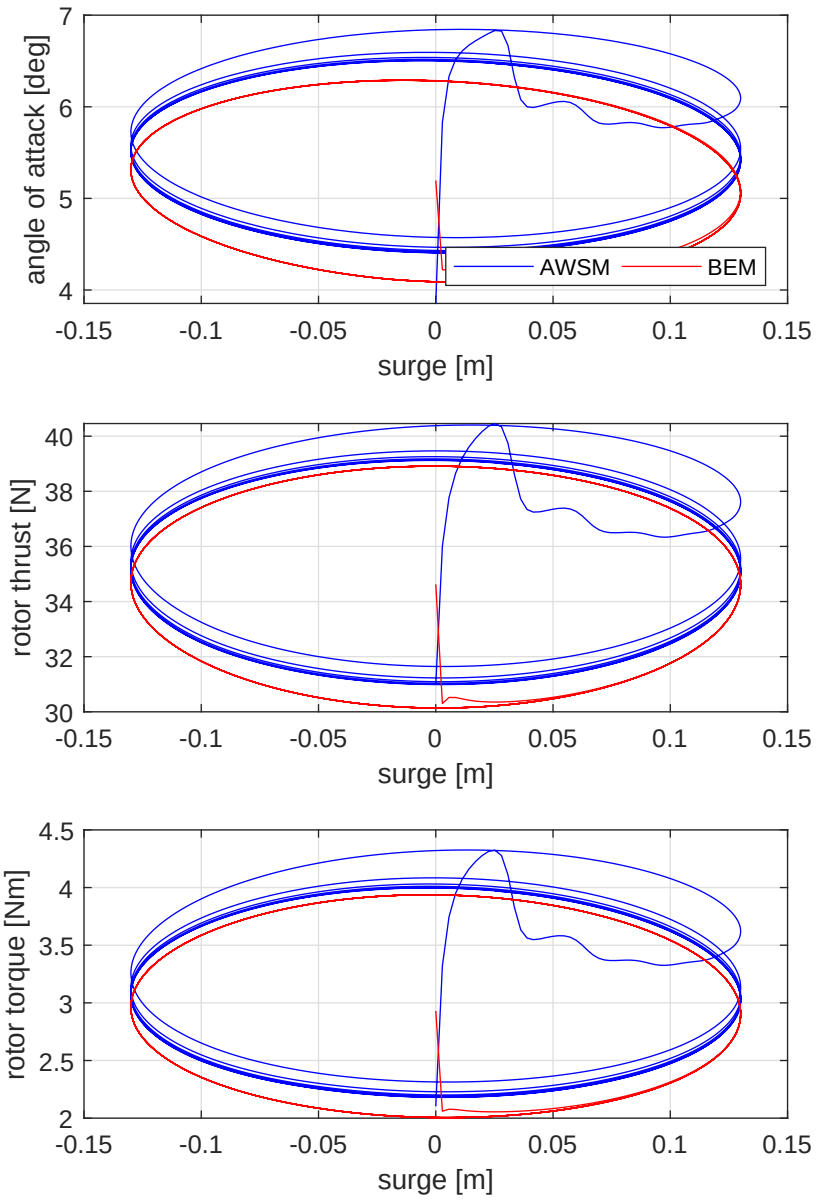

Figure B.7: Response of the angle of attack at 75% blade span, rotor thrust and rotor torque to a surge motion characterized by frequency of 0.5 Hz and amplitude 0.26 m.

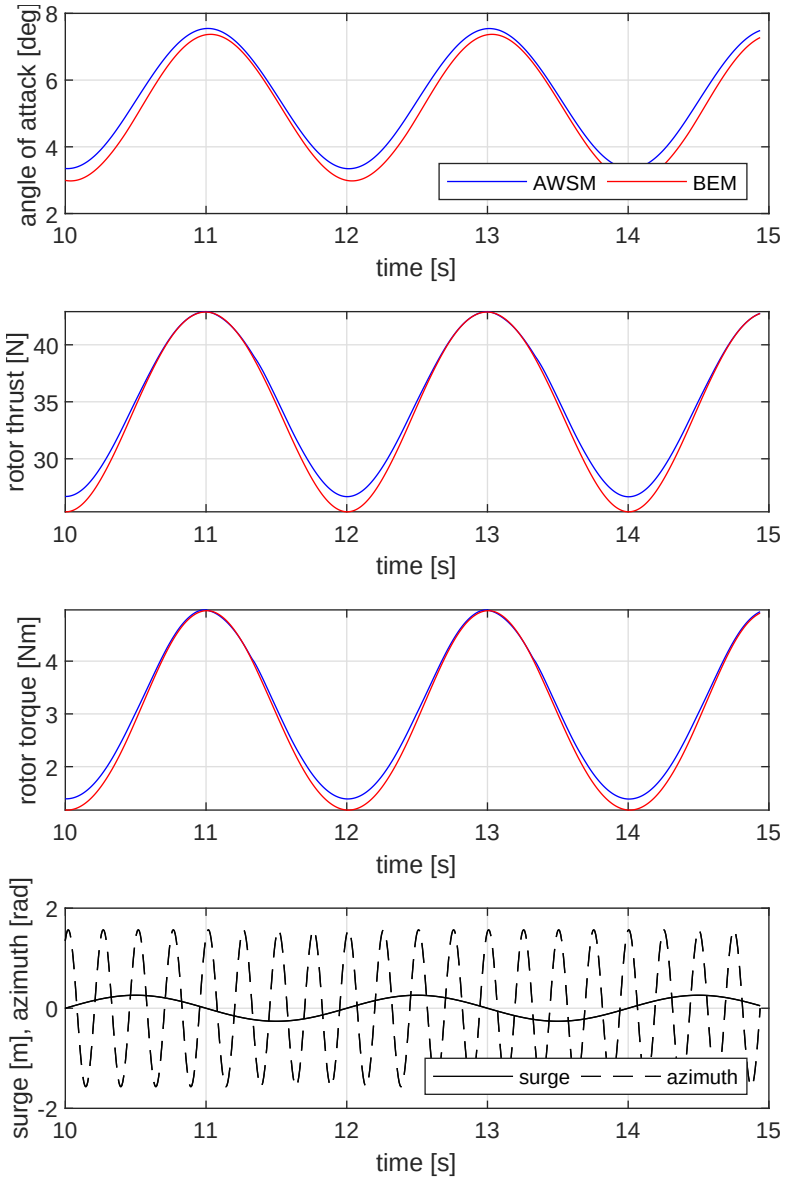

Figure B.8: Hysteresis loops of the angle of attack at 75% blade span, rotor thrust and rotor torque for a surge motion characterized by frequency of 0.5 Hz and amplitude 0.26 m.

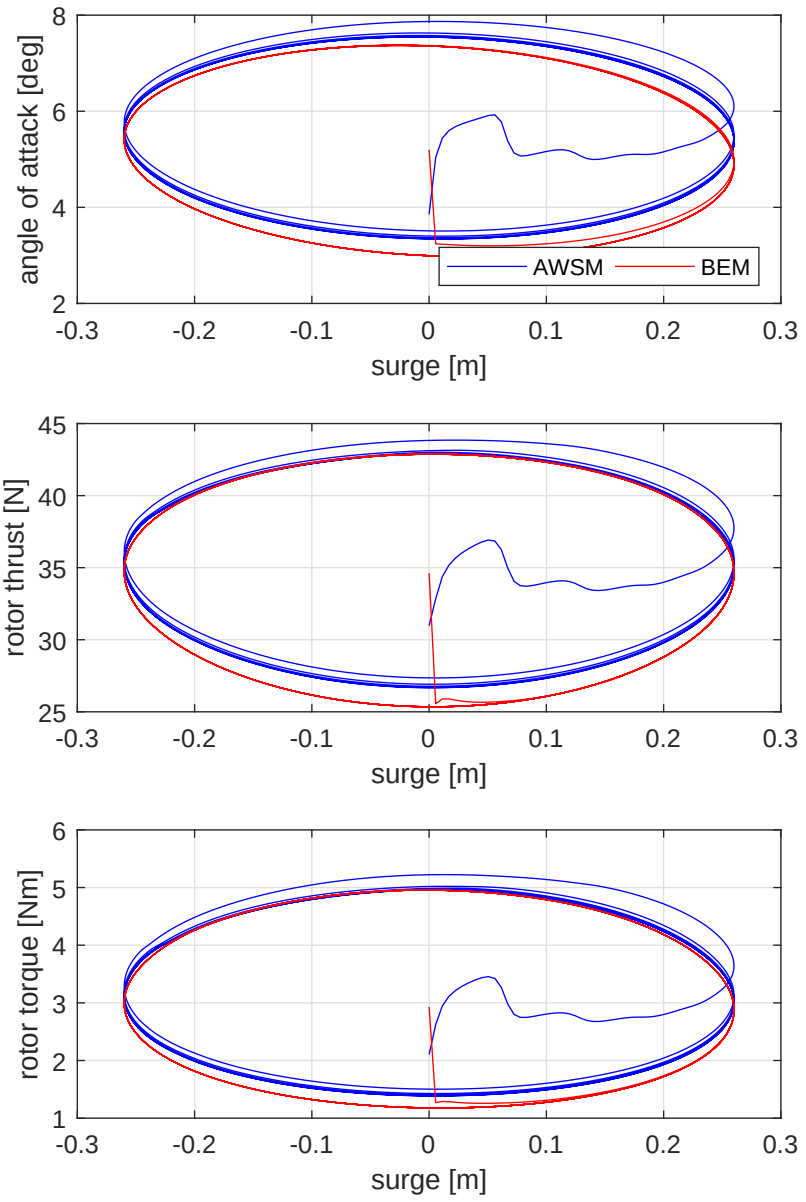

Figure B.9: Response of the angle of attack at 75% blade span, rotor thrust and rotor torque to a surge motion characterized by frequency of 0.5 Hz and amplitude 0.52 m.

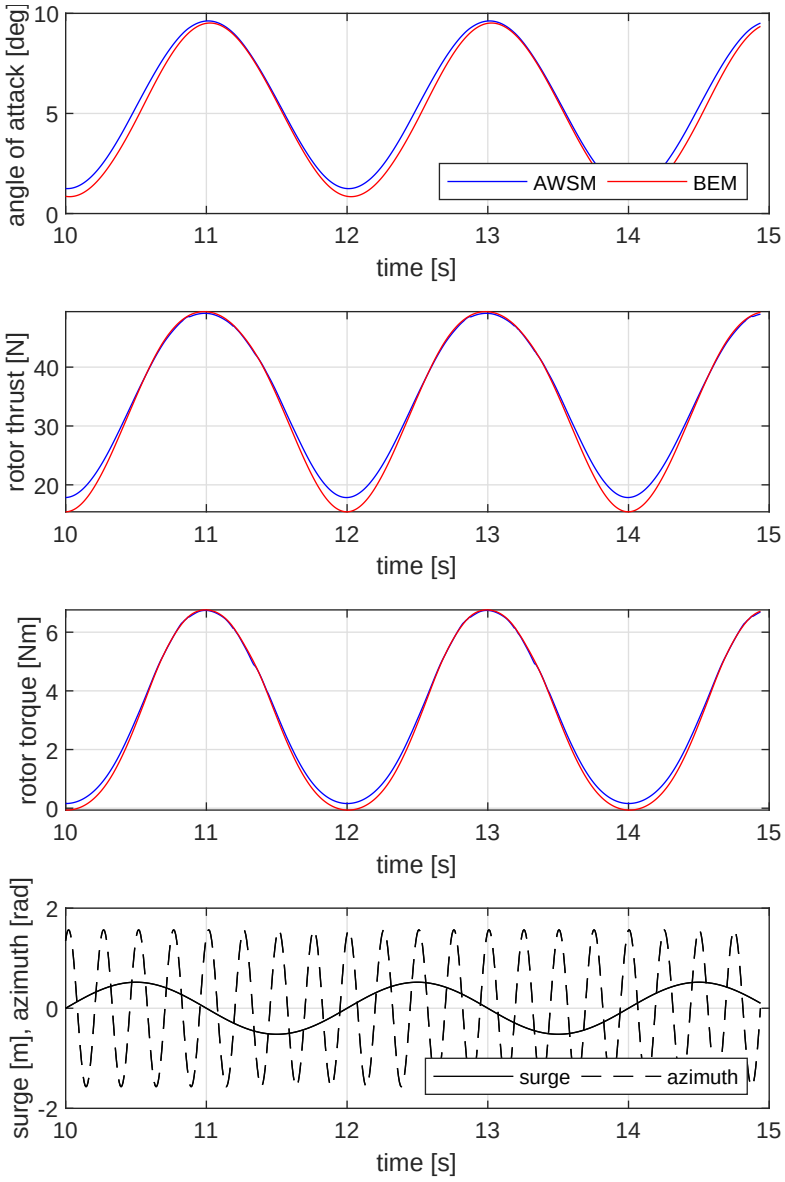

Figure B.10: Hysteresis loops of the angle of attack at 75% blade span, rotor thrust and rotor torque for a surge motion characterized by frequency of 0.5 Hz and amplitude 0.52 m.

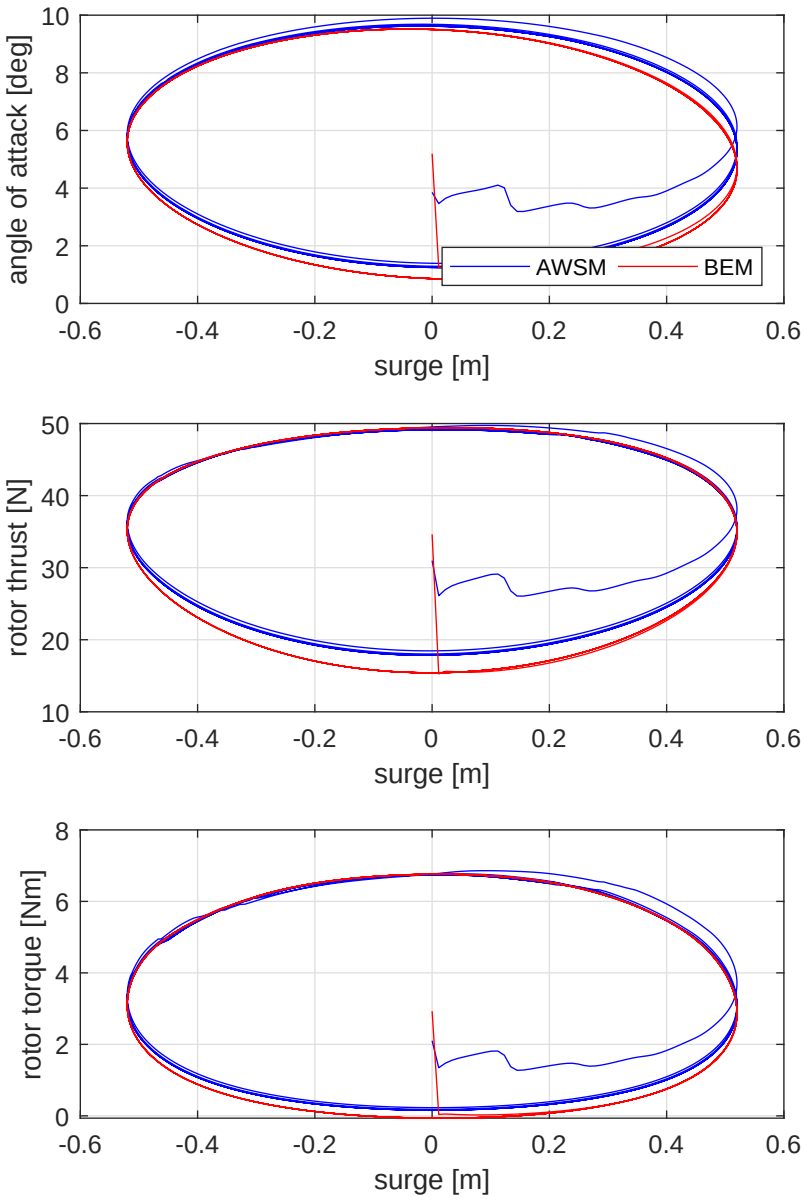

B.2 Surge cases with constant amplitude

Figure B.11: Response of the angle of attack at 75% blade span, rotor thrust and rotor torque to a surge motion characterized by frequency of 0.25 Hz and amplitude 0.13 m.

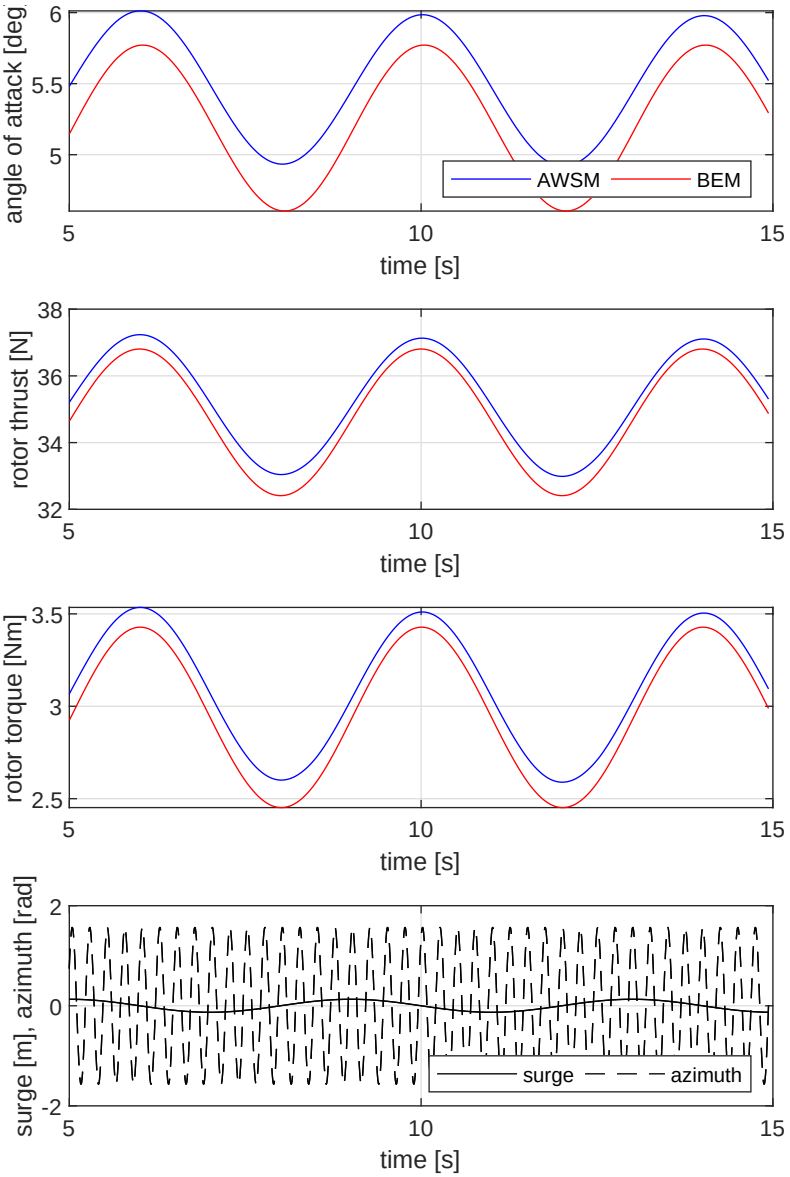

Figure B.12: Hysteresis loops of the angle of attack at 75% blade span, rotor thrust and rotor torque for a surge motion characterized by frequency of 0.25 Hz and amplitude 0.13 m.

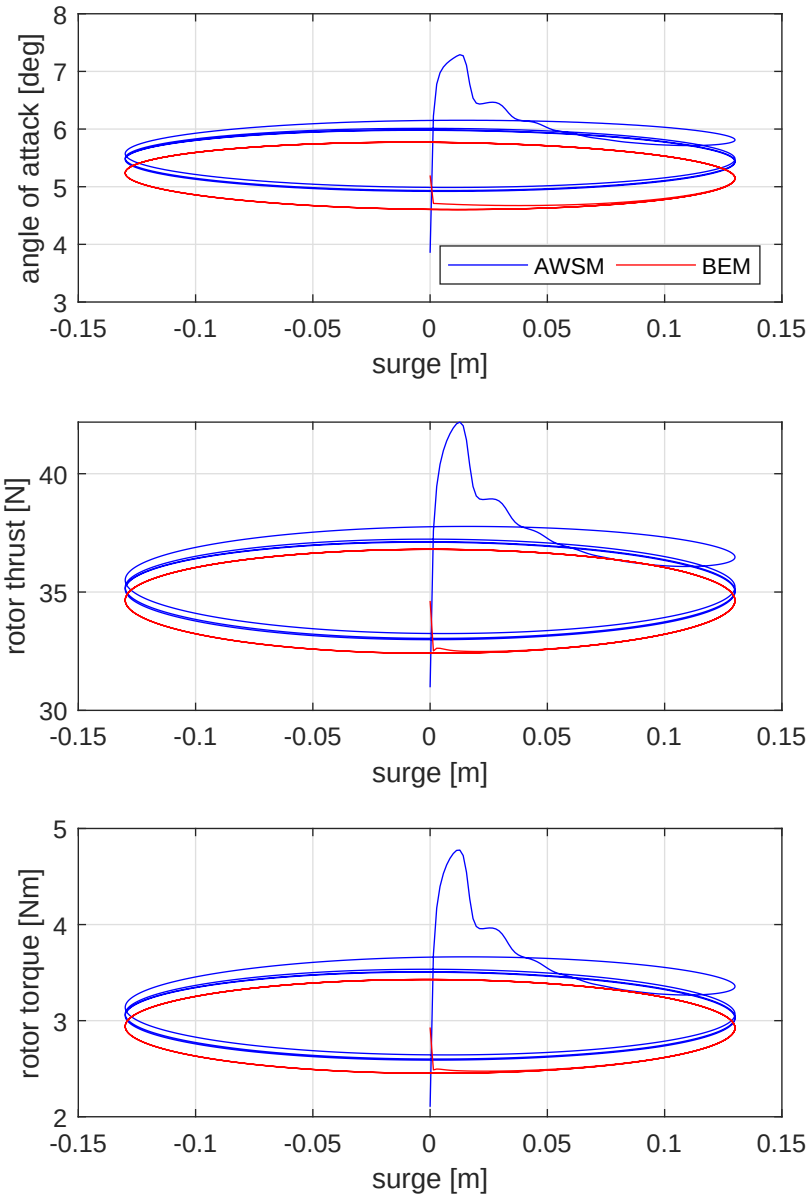

Figure B.13: Response of the angle of attack at 75% blade span, rotor thrust and rotor torque to a surge motion characterized by frequency of 1 Hz and amplitude 0.13 m.

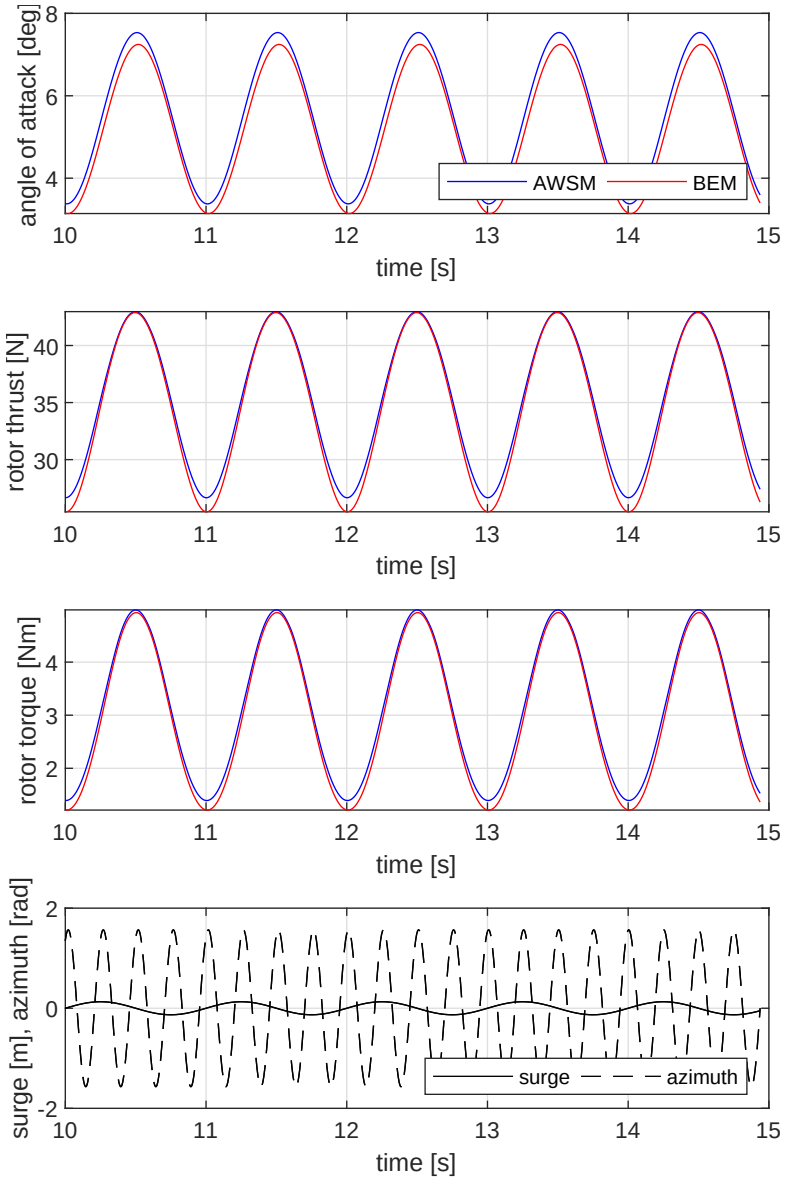

Figure B.14: Hysteresis loops of the angle of attack at 75% blade span, rotor thrust and rotor torque for a surge motion characterized by frequency of 1 Hz and amplitude 0.13 m.

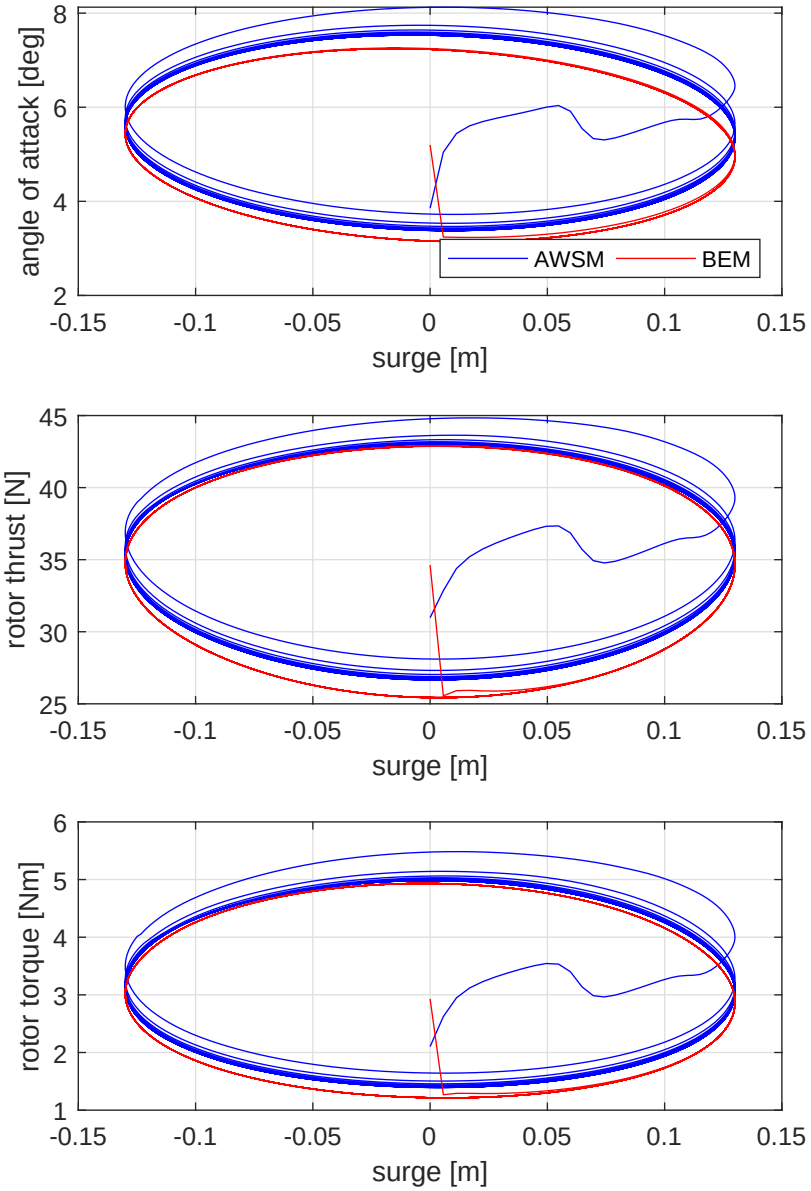

Figure B.15: Response of the angle of attack at 75% blade span, rotor thrust and rotor torque to a surge motion characterized by frequency of 2 Hz and amplitude 0.13 m.

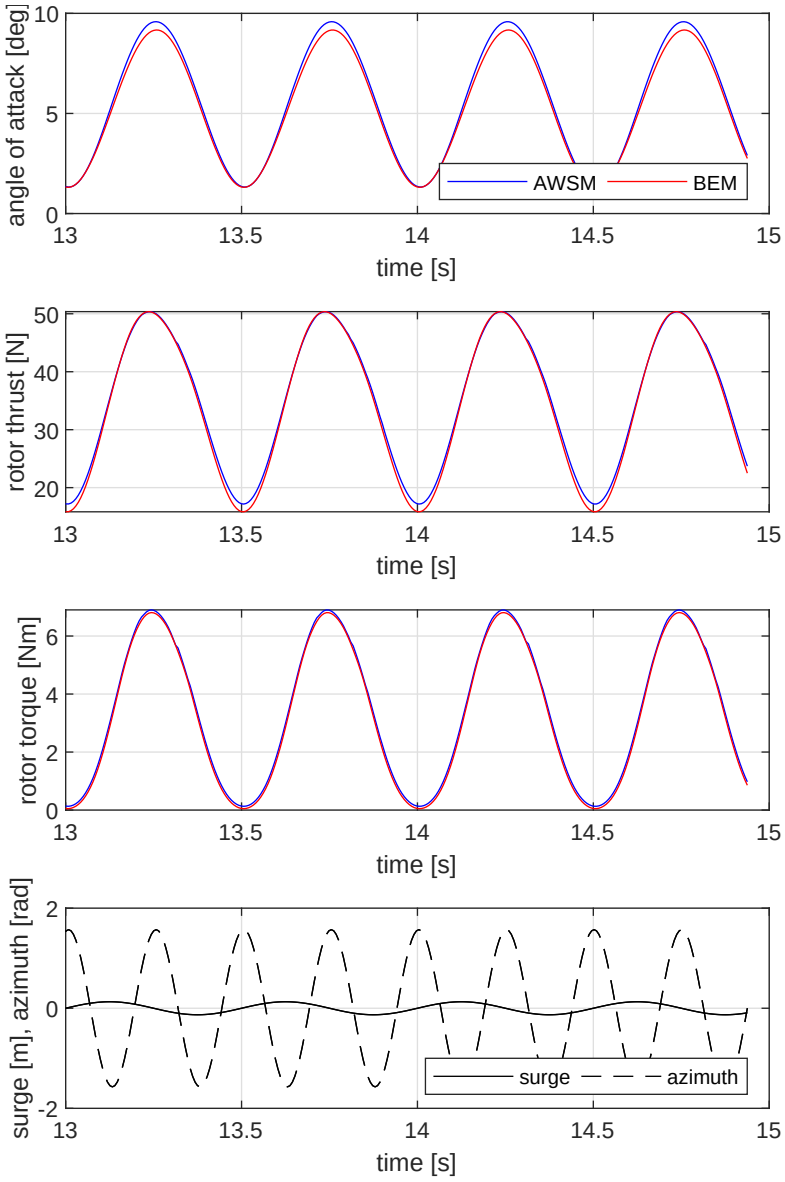

Figure B.16: Hysteresis loops of the angle of attack at 75% blade span, rotor thrust and rotor torque for a surge motion characterized by frequency of 2 Hz and amplitude 0.13 m.

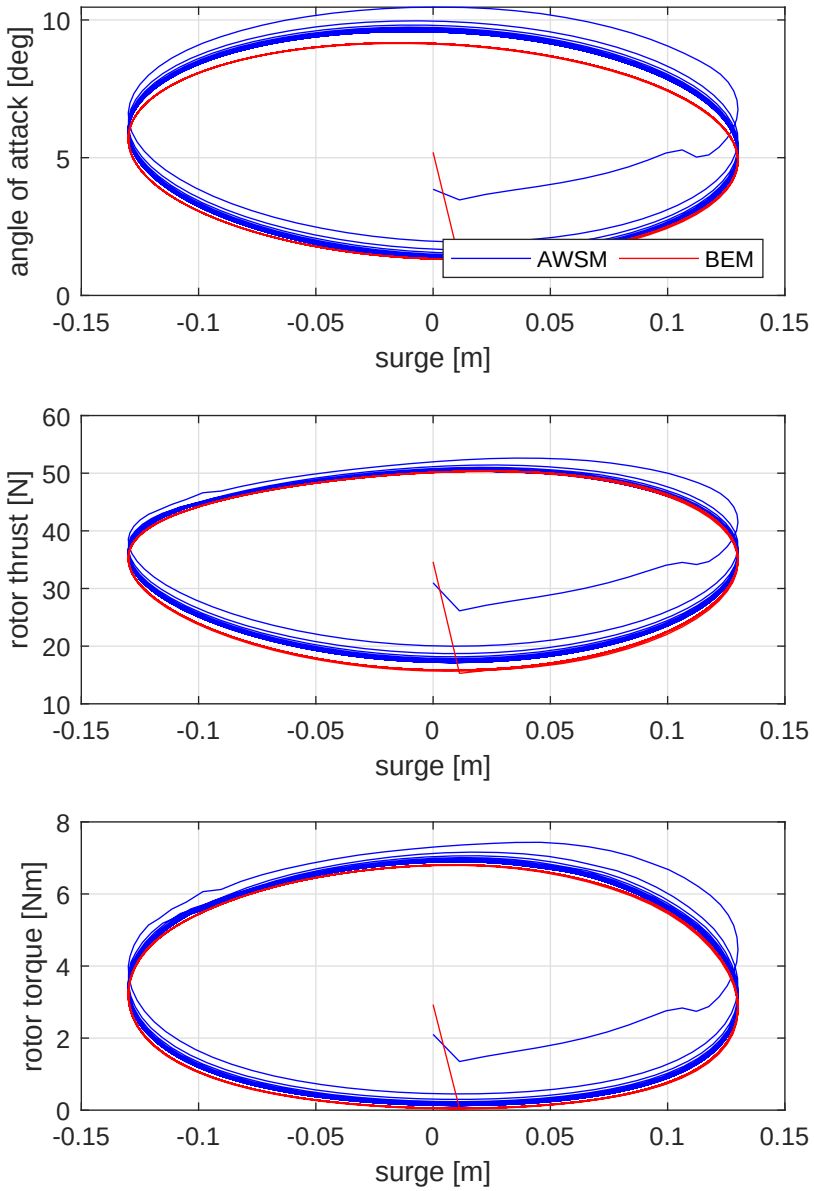

Figure B.17: Response of the angle of attack at 75% blade span, rotor thrust and rotor torque to a surge motion characterized by frequency of 4 Hz and amplitude 0.13 m.

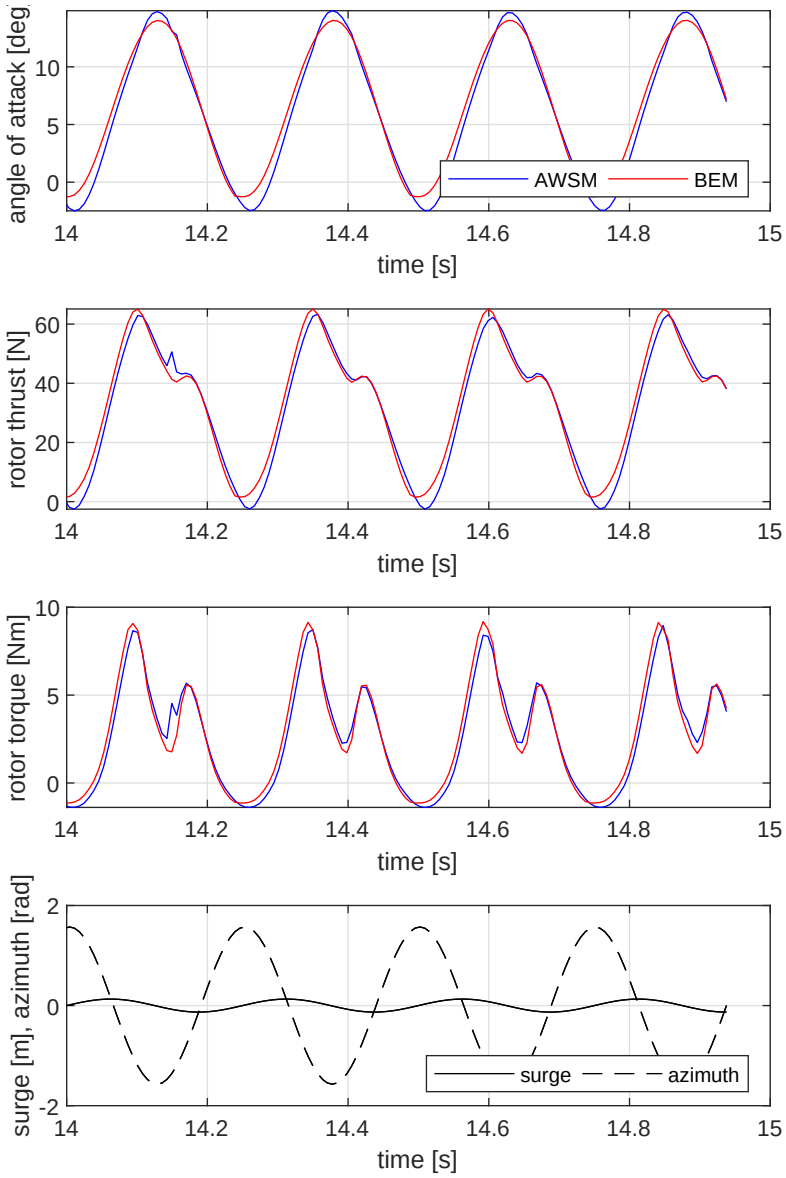

Figure B.18: Hysteresis loops of the angle of attack at 75% blade span, rotor thrust and rotor torque for a surge motion characterized by frequency of 4 Hz and amplitude 0.13 m.